Journal of Research of the National Bureau of Standards Vol. 47, No. 4, October 1951 Research Paper 2246

Spectrochemical Analysis of Bronze by a Porous Electrode Method

Bourdon F. Scribner and John C. Ballinger

A modification of Feldman's porous electrode method is described for the spectrochemical analysis of bronze (3 Sn, 3 Zn, 2 Pb, 2 Ni, 90 Cu). A 1-gram sample of bronze drillings is dissolved by the addition of 4 milliliters of hydrochloric acid and 16 milliliters of nitric acid, and after dilution to 40 milliliters with water, the solution is transferred to the hollow electrode for spark excitation. The analysis is made with reference to standard solutions prepared in a similar manner. Studies of the effect of electrode shape on the reproducibility of excitation led to the adoption of a porous electrode having a tip in the shape of a truncated cone. With this electrode the precision was greater by a factor of 1.2 to 2.1 over that obtained with a flat-tipped electrode. The precision of the method, determined as the coefficient of variation of a group of duplicate runs on 50 samples, ranged from 1.6 percent for nickel to 4.3 percent for lead. On the average, the results of routine spectrochemical determinations agree with the results of chemical determinations on the same samples to within ±5 percent.

1. Introduction

In spectrographic analyses of low-tin statuary bronze (3 Sn, 3 Zn, 2 Pb, 2 Ni, 90 Cu) by methods involving the direct sparking of the metal, certain unaccountable variations from the results of chemical analyses were observed. Although a group of samples prepared over a short period of time by a single manufacturer was found to give results entirely consistent within themselves, comparison of this group of samples with a group made at a later date, or by another manufacturer, revealed variations that could not be traced to the analytical method or technique. Others who have studied the analysis of copper alloys by direct spark methods have encountered similar difficulties and have placed considerable emphasis on preparation of the sample. It has been found necessary to exercise rigid control over the temperature of the melt, the rate of cooling, and the form of the sample [1].[1]

If samples from many sources were to be analyzed, it appeared advisable to adopt a method that would erase any effects of differences in metallurgical processing. It was also important to preserve the analytical speed made possible by the spectrochemical method. A procedure for obtaining physically identical electrodes by remelting the bronze under carefully controlled conditions is described by Palmer, Irwin, and Fogg [2]. In the search for a more rapid and flexible method, we considered the practicability of applying a solution technique. An excellent review of existing solution methods adaptable to spark excitation may be found in the paper by Feldman [3]. The method developed by him and described in his paper involved the use of a porous cup electrode. The possibility of applying this method to the analysis of bronze was tested with encouraging results.

Attention was then directed toward investigating details of the procedure to obtain maximum speed and precision with sufficient sensitivity. Several electrode shapes and sizes were investigated, as well as a variety of sparking conditions, with the result that an improved form of electrode was designed. Water-cooled copper electrode holders were found to be effective in preventing boiling of the solution as the spark energy was increased. Graphite bushings in the electrode holder were adopted to retard acid attack. Also, special sampling and dissolution methods were developed to give speed and facility to preparation of the solution. The standards consisted both of samples analyzed chemically and samples synthesized in acid solution by dissolving pure metals in the proper proportions. Calculating scales served to expedite and simplify the conversion of microphotometer readings to concentration values.

[1] Figures in brackets indicate the literature references at the end of this paper.

2. Preparation of Solutions

2.1. Sample Solutions

The bronze samples are prepared as drillings or millings to obtain material in convenient form for weighing and dissolution. In order to speed up the drilling operation a drill press is fitted with the jig assembly shown in figure 1. The test sample, which is generally in the form of a bar ½ by ½ by 4 in., is cleaned on two opposite long faces with a belt sander and is inserted in the jig. A clean, glass vial, fastened in the threaded opening on the underside of the jig, serves to collect the drillings. Sufficient material for test is obtained from one ¼-in. hole drilled through the middle of the bar from one cleaned surface to the other.

A 1.0-g portion of the sample is transferred to a 125-ml Erlenmeyer flask, to which is added 4 ml of hydrochloric acid (sp gr 1.19) followed by the addition of 16 ml of nitric acid (sp gr 1.42). When the reaction has ceased, 20 ml of water is added. Care is taken that dissolution is complete after addition of the water; this may be accelerated by gentle warming. Three self-leveling burettes serve for rapid dispensing of the acids and water. Because of the toxicity of the acid fumes, adequate ventilation must be maintained during both the preparation and storage of the solutions.

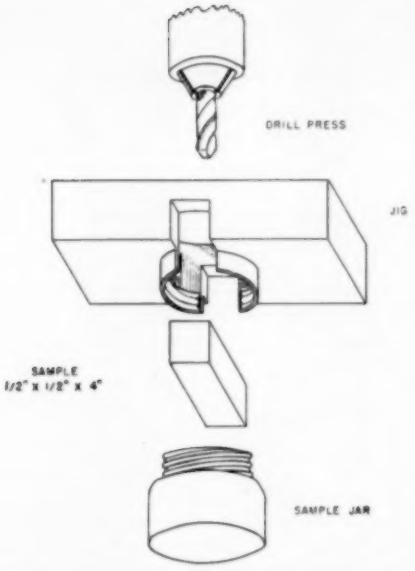

FIGURE 1. *Assembly for drilling and collecting sample.*

2.2. Standard Solutions

Chemically analyzed bronze samples serve as standards if selected so that concentrations of Pb, Ni, Sn, and Zn cover the desired ranges, and the concentration of copper is within 3 percent of that of the analytical samples. The latter condition is imposed to avoid the necessity of correcting for differences in the concentration of the internal standard copper between standards and analytical samples. Solutions of the metal standards are prepared in the manner described for the analytical samples. Synthetic standards may be prepared by dissolving pure metal constituents, provided that the resulting solutions match those of the analytical samples with respect to total metal concentration, concentration of copper, and concentration of acids. For the analysis of bronze in which copper varies from 89 to 91 percent, the copper may be held within this range by preparing solutions in which the compositions of the dissolved metals correspond to those of the alloys given in table 1.

The individual standard solutions of nickel, lead, and zinc may be prepared conveniently by dissolving the metals in a minimum of dilute nitric acid (1:1) and diluting with water to obtain a concentration of 0.01 g of metal per milliliter. For tin, dilute hydrochloric acid (1:1) is used and a solution of the same concentration is prepared. The set of bronze standard solutions is prepared by dissolving the required amount of copper in aqua regia (4 ml of hydrochloric acid plus 16 ml of nitric acid), and then adding water and metal solutions in the proper proportions.

Comparative testing of synthetically prepared standards and carefully analyzed chemical standards has indicated good agreement, as is shown on the analytical curve for nickel, figure 2.

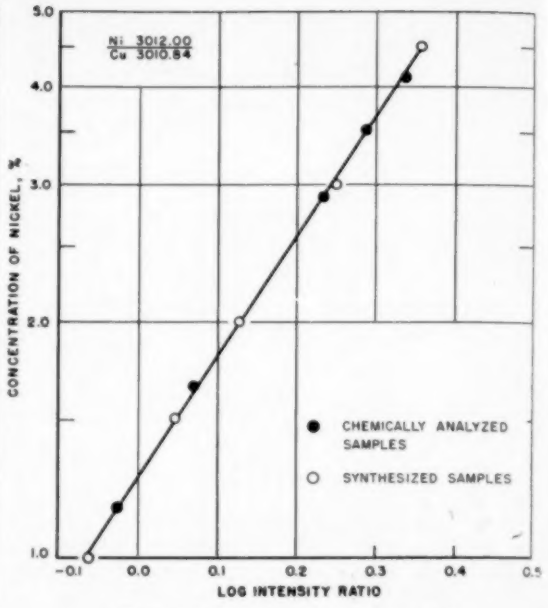

FIGURE 2. *Analytical curve for nickel.*

TABLE 1. *Compositions of alloys corresponding to standards prepared in solution*

Element	Standard				
	A	B	C	D	E
	%	%	%	%	%
Ni	6.0	3.0	2.0	1.0	0.5
Pb	0.5	5.0	2.0	3.0	1.0
Sn	1.0	0.5	5.0	3.0	2.0
Zn	2.0	1.0	0.5	3.0	6.0
Cu	90.5	90.5	90.5	90.0	90.5

3. Spark Excitation

3.1. Electrode System

The solution electrode, figure 3, is prepared from graphite rods of high purity, ¼ in. in diameter. Its form, with the exception of a truncated tip, is similar to that described by Feldman [3]. The upper (porous cup) electrode is 1⅜ in. long with a ⅛-in. hole drilled along its axis from one end to within 0.05 (±0.008) in., or 1.3 (±0.2) mm of the other end. A standard ⅛-in. twist drill is employed but, for ease in drilling, the grooves of the drill are ground wider to provide more space for carrying the chips away from the head of the drill. The sparking end of the electrode is beveled on the edge to an angle of 45°, resulting in a truncated cone with a tip diameter of ⅛ in. Tests of various electrode shapes showed a marked improvement in the precision of

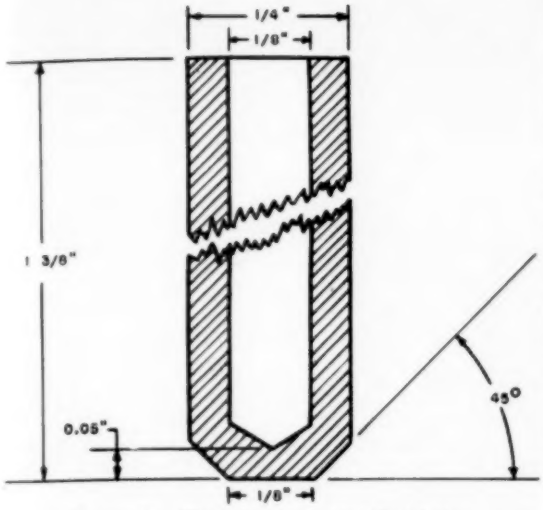

FIGURE 3. *Electrode for sparking the solution.*

results as the tip of the electrode was reduced in diameter. An electrode with a tip ⅛ in. in diameter was adopted with gains in precision amounting to a factor of 1.2 to 2.1, as shown in table 2.

TABLE 2. *Repeatability tests of two electrode tips*

Element	Concentration	Coefficient of variation *		Number of observations
		Truncated cone, tip diameter ⅛ in.	Flat end, tip diameter ¼ in.	
	%	%	%	
Ni	1.9	1.4	1.7	20
Pb	2.5	2.3	4.4	20
Sn	3.5	2.8	5.8	20
Zn	3.5	1.8	2.7	20

* $v=\frac{100\sigma}{C}=\frac{100}{C}\sqrt{\frac{\Sigma d^2}{n-1}}$, where v is the coefficient of variation; σ the standard deviation; C the concentration in percent; d the difference of a determination from the mean; n the number of determinations.

A pipette with an elongated tip 1½ in. long and less than ¼-in. outside diameter is used for filling the porous cup electrode in the manner illustrated by Feldman [3]. The tip of the pipette should touch the bottom of the electrode cavity, as the solution is expelled, to prevent the formation of bubbles within the electrode. The electrode is filled to the top (0.3 ml) immediately before sparking. The lower graphite electrode, ¼ in. in diameter, is shaped at the tip to a 120° cone and is clamped vertically in opposition to the upper electrode. The electrodes, separated by a 3-mm gap, are held in ½-in. split graphite bushings, which in turn are held in water-cooled copper clamps [4]. The water-cooled clamps were found effective in preventing boiling of the solution.

3.2. Excitation Conditions

The spark excitation conditions have an important effect upon both the sensitivity and repeatability of this method. A high-energy spark is desirable in that it provides high sensitivity. However, when the energy is raised considerably, the heat generated cannot be dissipated rapidly enough to prevent boiling of the solution within the electrode. This results in an erratic, irreproducible spark. A compromise of conditions has therefore been selected. Sensitivity is also affected by the inductance of the circuit, any considerable increase beyond 25 μh producing a high background intensity with a corresponding decrease in sensitivity. An Applied Research Laboratories' high-voltage spark unit was employed, although any unit capable of being adjusted to obtain a low-energy spark should be satisfactory. The settings used with this unit are as follows: Power setting, ⅝ kva; capacitance, 0.0073 μf; inductance, 25 μh; interrupter adjustment, set for a low-energy spark (26 volts on the indicating instrument furnished with the unit).

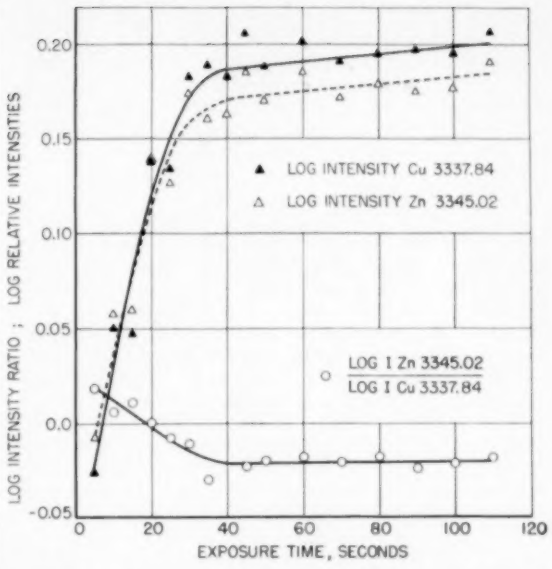

FIGURE 4. *Change of spectral line intensities with time of sparking.*

Under these conditions the spectrum assumes a fairly stable intensity level after the first 35 seconds and maintains it for well over 2 minutes, as shown in figure 4. On the basis of these observations it would appear preferable to allow a period of 35 seconds before making the exposure. However, in practice a shorter period was allowed in order to reduce the total time. A presparking period of 10 sec. and an exposure of 110 seconds were adopted.

4. Analytical Procedure

4.1. Spectrographic Procedure

A conventional large Littrow quartz spectrograph and illuminating system are employed to photograph the range 2650 to 3400 A [5]. With a lens (f_a=34

cm) at the slit, the arrangement is such that the resulting spectrum represents radiant energy from all parts of the spark. A step sector or other variation of exposure is not needed for this analysis. In routine work, the spectrum of each sample is photographed in duplicate, but on separate plates for higher accuracy. On each plate one exposure is made for each of 18 samples and 2 standards. In addition, an exposure of the iron spark spectrum is made on the plate for calibrating the emulsion with the following exposure conditions: Power setting, 4/3 kva; capacitance, 0.014 μf; inductance (none added), 3 μh; interrupter adjustment, set for spark of moderate energy (40 volts on the indicating instrument furnished with the unit); electrode form, two electrodes of commercially pure rods ¼ in. in diameter each tipped with a 150° cone; electrode separation, 3 mm; exposure time, 30 sec.

The copper spectrum obtained displays a sufficient number of lines of varying intensities in the range from 2650 to 3400 A to eliminate the need for a stepped sector or other variation of exposure. Analytical line pairs used in this method are listed in table 3. The only interference observed was that caused by Na 3302.32 A with Zn 3302.59 A. This was attributed to contamination of the sample during the sampling or dissolution procedures and was eliminated entirely when adequate precautions were taken. Good ventilation of the spark stand during the sparking procedure was found advisable to prevent serious corrosive attack by the acid fumes on neighboring apparatus and toxic effects on the operator.

TABLE 3. *Analytical Line pairs*

Element to be determined	Wavelength of element line [a]	Wavelength of copper line [a]	Concentration range	Concentration index [b]
	A	*A*	*%*	*%*
Ni	3057.64	3063.42	1.0 to 5.0	2.1
	3012.00	3010.84	0.5 to 2.5	1.3
	3050.82	3073.80	.5 to 0.7	0.3
Pb	2833.07	3010.84	.5 to 5.0	2.9
	3683.47	3684.67	.5 to 1.2	0.4
Sn	3009.15	3010.84	1.5 to 5.0	3.0
	3175.05	3194.10	0.6 to 2.5	1.3
	3175.05	3169.68	.5 to 1.0	0.4
Zn	3302.59	3279.82	2.5 to 5.5	4.0
	3345.02	3337.84	0.7 to 3.0	1.7
	3345.02	3349.29	.5 to 1.5	0.6

[a] All wavelengths are from neutral atoms.
[b] The concentration index is the concentration at which the intensity ratio is unity.

4.2. Photometry

The emulsion is calibrated by photometric measurement of the iron spark exposure for the selected group of iron lines listed in table 4, the relative intensities of which were determined by a primary method, using a step sector.[2] These lines are used in preparing a plate calibration curve as outlined by Vincent and Sawyer [6]. Transmittance measurements of analytical line pairs and lines of the calibration spectrum are made with a projection microphotometer. Analytical line pairs appropriate to the concentration ranges encountered are selected from the list in table 3. The transmittances of the analytical lines and the internal standard lines are converted to log intensity ratios by means of the plate calibration curve. This procedure, carried through for standard samples, serves to establish an analytical curve relating log intensity ratio and log concentration for each line pair. A typical analytical curve, that for nickel, is illustrated in figure 2. Log intensity ratios of analytical determinations may then be converted to concentrations by reference to the appropriate analytical curve. The average of two determinations, each made on a separate plate, and corrected by a control standard in duplicate on each plate, is reported for each element. In view of the fact that the principal alloying constituents of the bronze other than copper are determined directly by the method, a reasonably accurate value of the copper concentration is obtained by subtracting the sum of the concentrations of tin, zinc, lead, and nickel from 100.

[2] The calibration procedure, established by C. H. Corliss, is common to several analytical methods employed in this laboratory.

TABLE 4. *Iron wavelengths* (Fe II) *for emulsion calibration*

Angstroms			
2770.51	2811.27	2875.35	2892.83
2774.69	2827.43	2876.80	2897.26
2793.89	2837.30	2879.24	2904.38
2799.29	2861.19	[a] 2880.8	2910.76
2805.79	2864.97	2885.93	2934.49

[a] Double line.

When samples are to be analyzed on a routine basis, the procedure is simplified by the use of analytical scales or of both analytical and calibration scales. The scales are prepared from the established analytical and calibration curves by projecting the curve to its intensity axis. The scales are then used in the manner described by Churchill [7] for the Dunn-Lowry calculator.

5. Discussion

5.1. Precision and Accuracy

Calculations of the precision of the method were made in two ways, first, by comparing a group of determinations on a single sample made under identical conditions, and second, by comparing duplicate determinations made on a large number of samples. In the first case a single solution was used in making all of the determinations, and care was taken to maintain the observing conditions constant. Coefficients of variation (defined in table 2) were computed for each plate (20 determinations) and the results averaged to give the values shown in table 5.

In the second case actual routine test data were used involving 50 samples, where two exposures were made each on a separate plate. The values for coefficient of variation were calculated for the pairs of determinations with the results shown in table 6. As one would expect, the coefficients of variation

TABLE 5. *Results of repeatability tests on a single sample*

Element	Concentration	Coefficient of variation [a]	Number of observations [b]
	%	%	
Ni	1.9	1.9	100
Pb	2.5	2.8	100
Sn	3.5	3.9	100
Zn	3.5	1.8	80

[a] See footnote a, table 2.
[b] Treated in groups of 20 and the results averaged.

are larger here than in the first case and may be expected to represent a more realistic measure of the precision of the method. It is of interest to note the convenience of calculating precision from routine analytical data, thus obviating the necessity of making a large number of runs on a single sample under the somewhat improbable restriction of "constant conditions." However, the method of employing pairs of determinations is a reliable measure of the precision of the method only when the single determinations can be considered independent, that is, observed on different plates and preferably on different days.

The precision found for nickel is considerably better than that for lead, tin, and zinc. This is probably the result of a combination of factors that may include the close match between Ni I 3012.00A and Cu I 3010.84A in wavelength and excitation energy, as well as a close similarity in the physical properties of nickel and copper and their salts.

TABLE 6. *Results of repeatability tests based on duplicate routine determinations made on 50 samples*

Element	Average concentration	Coefficient of variation [a]	Number of pairs of observations
	%	%	
Ni	1.6	1.6	50
Pb	2.3	4.3	50
Sn	3.6	4.2	50
Zn	3.2	2.4	50

[a] $v = \frac{100\sigma}{C} = \frac{100}{C}\sqrt{\frac{\Sigma D^2}{2p}}$, where v is the coefficient of variation; σ the standard deviation; C the average concentration in percent; D the difference between duplicate runs; p the number of pairs of observations.

An expression for the accuracy of this method may be obtained by comparing the spectrochemical with chemical results.[3] The differences between the averages of two sets of results for each element are given in column 4 of table 7. The differences were found not to be significant, indicating that a bias was not observed. The average differences between determinations by the two methods, calculated without regard to sign, are given in column 5 of table 7; these give a measure of the expected random differences between determinations by the two methods. The differences, of course, include any errors in chemical analysis as well as those in the spectrographic determination. It is significant that the determinations of copper, made by difference in the spectrographic method, show good agreement with the chemical determinations that were made directly by electrodeposition.

[3] The chemical analyses were made by R. K. Bell, E. E. Maczkowske, and K. M. Sappenfield of the Bureau's Analytical Chemistry Section. In the chemical method Cu, Sn, Pb, and Ni are determined directly, and Zn is determined by difference.

5.2. Advantages and Limitations

This method is particularly advantageous for the analysis of samples for which the metallurgical preparation, size, or shape cannot be controlled sufficiently well to permit application of a self-electrode method. It is useful also in the absence of bronze metal standards covering the required concentration ranges. Because of continuous supply of sample solution to the electrode tip, there is negligible intensity variation after the first 25 or 30 sec of exposure (fig. 4); consequently the time of exposure may be changed considerably without appreciable effect on the intensity ratios. Furthermore, the intensity ratios are not critically affected by variations (up to a factor of 2) in the concentration of the sample in solution.

TABLE 7. *Comparison of chemical and spectrochemical results*

Element	Average of chemical determinations	Average of spectrochemical determinations	Difference between averages	Average absolute difference between determinations	Number of determinations
	%	%	%	%	
Ni	1.55	1.55	0.0	0.04	50
Pb	2.46	2.41	+.05	.12	50
Sn	3.43	3.47	−.04	.14	50
Zn	[a] 2.65	2.73	−.08	.12	50
Cu	89.84	[a] 89.81	+.03	.18	50

[a] Determined by difference.

The speed of the method is obviously less than that for methods using spark excitation of metal electrodes. However, in routine analyses one operator can maintain a rate of 50 samples analyzed per week, which is a time requirement of a little less than 10 man-minutes per determination (each determination being the average of two runs). An appreciable gain in the precision of analytical results is observed (table 2) for the truncated-tip electrode of our design when compared with Feldman's flat-tip electrode [3], both electrodes being tested with the same solutions of bronze. The accuracy of the method is sufficient for control testing at the concentration levels encountered, but if the method were to be extended to concentrations higher than 5 percent for the elements determined directly, the accuracy might be insufficient for close control. Limitations in the method are encountered in extending the concentration ranges for analyses beyond those given in table 3. To extend the lower limits would involve either excessively long exposures or increasing the metal-to-acid ratio. The latter may be feasible, provided the sample can be dissolved completely. Similarly, the extension of concentration ranges to higher values is limited by the solubility of lead or tin in the acid mixture, although adjustment of relative concentrations of the acids used may provide suitable conditions.

Methods of this nature offer considerable promise in spectochemical analysis in permitting the use of standards synthesized from pure metals or salts so that calibration of the method becomes independent of other analytical methods.

The assistance of Doward M. Bouchette, Jr. in making many of the analyses is acknowledged.

6. References

[1] R. A. Wolfe and E. J. Jemal, Am. Soc. Testing Materials Bull. **129,** 45 (1944)
[2] E. W. Palmer, J. P. Irwin, and C. C. Fogg, Am. Soc. Testing Materials Bull. **160,** 41 (1949).
[3] C. Feldman, Anal. Chem. **21,** 1041 (1949).
[4] B. F. Scribner and C. H. Corliss, J. Opt. Soc. Am. **33,** 515 (1943).
[5] B. F. Scribner, J. Research NBS **28,** 165 (1942) RP1451.
[6] H. B. Vincent and R. A. Sawyer, J. Applied Phys. **8,** 163 (1937).
[7] J R. Churchill, Ind. Eng. Chem., Anal. Ed. **16,** 653 (1944).

Washington, March 28, 1951

Journal of Research of the National Bureau of Standards Vol. 47, No. 4, October 1951 Research Paper 2247

Correcting for Density and Viscosity of Incompressible Fluids in Float-Type Flowmeters

Montgomery R. Shafer, Ernest F. Fiock, Harry L. Bovey, and Ross B. Van Lone

The theory of the flow of incompressible fluids through float-type flowmeters is developed by the methods of dimensional analysis. The relations thus derived have been verified experimentally for the specific cases of five flowmeter tubes with 11 liquid hydrocarbons of different physical properties. Parameters that are suggested to describe the performance of any float-type flowmeter may be evaluated by measuring the float density and the mass rate of flow of fluids of known density and viscosity. Procedures are described whereby, after calibration of a metering tube with a few fluids of known physical properties, accurate corrections may be calculated for any fluid whose properties lie within the range embraced by the calibration fluids. Application of the proposed method of calibration and correction to the five metering tubes studied gave corrected values of flow that were always within one-quarter percent of the true values of flow.

1. Introduction

In the course of a program of research on the metering of fuels to aircraft engines, conducted under sponsorship of the Bureau of Aeronautics, the effects of the physical properties of the fluid upon metering devices have been studied extensively. Those results that pertain to the basic instrument used in establishing actual flow rates are considered of sufficient general interest to warrant separate presentation here.

Float-type flowmeters are convenient for flow testing various fuel metering accessories of both reciprocating and jet engines because they indicate flow rate directly. In such applications there is a growing demand for meters that can be used with various liquids and for increased accuracy under test conditions in which the density and viscosity of the test liquid may change with time from such causes as evaporation of light ends, admixture with heavier hydrocarbons, or inadequate control of temperature.

The word fluid appears frequently throughout this paper, although only liquid hydrocarbons were used in the experiments. This choice of terms was made for two reasons. First, the liquid used in testing the metering accessories of engines is referred to almost universally as the test fluid; and second, the results of the present study are believed to apply also to the metering of gases, provided the pressure drop at the float is negligible with respect to the absolute static pressure.

The flowmeter under consideration is of the variable-area, constant-pressure-drop type frequently referred to as a Rotameter. In such an instrument the metering takes place at an opening between a movable float and a surrounding tube so shaped that the metering area increases as the float rises. Tapered tubes of circular cross section and cylindrical tubes with tapered flutes have been used with greatest success. The instrument used in the present study was of the latter type.

Most published discussions of float-type flowmeters [1 to 5][1] have been concerned primarily with the basic theory and with mechanical means for reducing the sensitivity to density and viscosity of the fluid metered. The theory involves a dimensionless coefficient, analogous to the coefficient of discharge of an orifice but more difficult to evaluate and apply, since the metering area and the upstream and downstream flow conditions change with float position.

By choosing approximate values of the coefficient, the theory may be applied in designing metering tubes to have desired ranges when used with specified fluids. Due partly to lack of knowledge of the coefficient and partly to manufacturing tolerances, it has been found desirable to calibrate each meter with the same fluid later to be metered. It has not been feasible to calculate accurately the corrections that are necessary when the fluid metered has properties differing from those of the calibration fluid.

The present paper describes a method whereby, if any float-type flowmeter is calibrated with a limited number of fluids having different densities and viscosities, accurate values of the actual flow rate of any fluid having properties in the ranges of the calibration fluids can be calculated. A meter so calibrated might have a linear scale, in which case the results could be expressed in the form of calibration curves; or it might have a scale indicating the mass rate of flow of some specific fluid, with correction curves applicable to fluids having different properties. The meter thus becomes a more versatile instrument, since it can be used for accurate measurement of the actual flow rates of fluids embracing a considerable range of physical properties, without an individual calibration for each fluid.

The scale of the meter used in the present work reads directly in pounds per hour of fluid of specified density and viscosity, since it is common practice to express the rate of flow of fuel to an aircraft engine in this way. It is likewise common practice to express density and absolute viscosity in grams per cubic centimeter and in centipoises, respectively.

[1] Figures in brackets indicate the literature references at the end of this paper.

These units are used throughout this paper, despite the fact that the employment of mixed systems is objectionable in principle. Since numerical values of conversion factors are not required for present purposes, no confusion can arise from adherence to units with which the user is most familiar.

2. Description of the Flowmeter

The instrument used in this study is one of a lot purchased by the Navy in 1944 for use on Stromberg aircraft carburetor flow benches. It has seven tubes connected in series, so that when the range of one is exceeded, the next automatically meters the flow, in the range from 5 to 4,000 lb of naphtha per hour. Either the first four or the first six tubes may be bypassed by means of two valves to reduce the drop in pressure, which would otherwise occur within the instrument at high flow rates.

Each cylindrical glass tube has four tapered flutes, symmetrically spaced and parallel to its axis. These flutes were so designed that indicated values of flow can be observed with the same percentage accuracy throughout the entire range of the meter. Within each tube is a spool-shaped float of stainless steel having a density of 7.589 g/cm³.

The meter was calibrated at the factory with a hydrocarbon having a density of 0.733 ± 0.002 g/cm³ and a viscosity of 0.544 ± 0.011 centipoise, and from these data a scale in pounds per hour was ruled for each tube. Since the guaranteed accuracy was ± 1 percent, errors up to this magnitude are to be expected in the original scales. As will be seen later, these errors in the original calibration and in the ruling of the scales therefrom introduce some complications in the present effort to obtain values of flow that are accurate to within a few tenths of 1 percent. However, this difficulty can be avoided in other instruments by specifying the accuracy of calibration and scaling that is desired.

3. Description of the Test Fluids

For practical reasons the properties of the fluids used in this investigation were restricted to the ranges of interest in testing aircraft engines and their fuel accessories. In all, 11 different liquid hydrocarbons, ranging in density from 0.68 to 0.80 g/cm³ and in viscosity from 0.39 to 1.83 centipoises, were used. The pertinent properties of each are given in table 1. Fluids 2, 3, 4, 8, and 9 were furnished by the Phillips Petroleum Co., and fluid 10 was supplied by the Anderson-Prichard Oil Corp. The cooperation of these firms is hereby gratefully acknowledged.

TABLE 1. *Properties of the test fluids*

Test fluid No.	Description	Test temperature	Density, ρ	Absolute viscosity, μ
		°F	g/cm³	Centipoises
1	Navy test bench fluid (used)	73	0.736	0.538
2	Soltrol-100 [a]	75	.742	1.064
3	Commercial isooctanes [a]	70	.742	0.554
4	60% Soltrol+40% isooctanes [a]	73	.741	.703
5	Varsol	83.5	.770	.821
6	Varsol+hydraulic oil (I)	77	.792	1.278
7	Varsol+hydraulic oil (II)	77	.787	1.135
8	ASTM n-heptane [a]	80	.681	0.386
9	Commercial n-heptane [a]	80	.710	.439
10	Apco-467 [b]	80	.803	1.827
11	Kerosine	77	.791	1.661

[a] Supplied by courtesy of the Phillips Petroleum Co.
[b] Supplied by courtesy of the Anderson-Prichard Oil Corp.

4. Experimental Procedure

The two smallest tubes of the flowmeter, covering the range from 5 to 45 lb/hr, were not used because the accuracy with which the actual flows could be measured at these low rates was not sufficiently high with available equipment. In each of the remaining five tubes, actual flow rates were determined with all test fluids at positions of the float near the

TABLE 2. *Summary of experimental results*

Tube	Indicated flow, M_i	Actual flow, M, (lb/hr) of test fluid number—										
		1	2	3	4	5	6	7	8	9	10	11
	lb/hr											
3	55	54.72	49.54	54.52	52.12	52.99	49.81	50.75	54.88	55.06	46.15	47.78
3	85	85.10	79.27	84.86	82.07	83.58	80.25	81.30	84.34	85.29	77.48	78.30
3	120	120.2	114.2	120.0	117.0	118.9	116.2	117.2	117.7	119.8	113.7	113.5
4	140					140.0				139.9	133.8	
4	160	160.4	154.2	160.2	157.8	159.9	157.6	158.6	157.3	159.7	153.9	155.1
4	180					180.9				180.2	174.9	
4	210	211.7	204.1	211.6	208.3	211.7	208.7	209.8	206.8	210.3	205.3	206.0
4	260					261.0				258.9	254.0	
4	310	309.9	300.3	309.7	305.7	310.8	308.1	309.1	303.2	307.9	302.5	303.1
4	340					341.7				338.3	332.3	
5	400	401.8	389.0	402.5	395.9	403.0	398.0	399.8	391.2	398.3	391.0	391.3
5	520	522.9	507.8	523.8	515.0	523.7	520.1	521.2	508.6	517.5	512.4	513.8
5	700	701.9	686.2	703.3	694.7	706.9	703.9	705.2	682.4	693.6	696.8	697.4
6	900	902.5	886.3	905.1	898.1	912.5	907.1	909.2	880.6	893.9	894.2	896.7
6	1200	1208	1188	1211	1200	1221	1214	1219	1178	1197	1201	1202
6	1600	1606	1578	1609	1594	1621	1614	1620	1570	1597	1599	1601
7	2000	2002	1962	2007	1989	2020	2004	2013	1947	1984	1979	1980
7	2600	2601	2558	2608	2588	2627	2621	2624	2522	2572	2596	2593
7	3400	3395	3346	3408			3421	3433	3291	3352	3396	3390

bottom, center, and top of the tube. Tube 4 was calibrated in considerably greater detail, including four additional float positions with three test fluids, in addition to a reference calibration at intervals of 1 cm. Each measurement was repeated at least twice, and examination of the data leads to the belief that the error in an individual observation seldom exceeded 0.25 percent. The temperature of the fluid entering the meter was controlled to within ± 1 deg F of the values listed in table 1 under test temperature.

Three sets of equipment were used for determining actual flow rates. In earlier work with fluids 1 through 5, when these left the meter at rates between 50 and 320 lb/hr, they were directed over a weir into volumetric flasks. Time, volume, and density were measured for each sample. Larger flows were determined by weighing and manual timing. In later work with fluids 6 through 11, a gravimetric calibrating stand with automatic timing was used throughout the entire flow range.

Densities of the test fluids were obtained from accurate hydrometer readings and the data of NBS Circular 410; their viscosities were determined by R. C. Hardy of this Bureau, whose assistance is hereby acknowledged.

The average results of all flow measurements are given in tables 2 and 3.

TABLE 3. *Results of reference calibration of tube 4*

Scale reading		Actual flow rate, M_r	Scale reading		Actual flow rate, M_r
cm	M_t, *lb/hr*	*lb/hr*	*cm*	M_t, *lb/hr*	*lb/hr*
1	----------	129.9	24	219.0	220.6
2	123.3	132.4	25	224.1	225.9
3	135.5	135.4	26	229.3	231.1
4	138.7	138.7	27	234.8	236.8
5	141.9	141.6	28	240.2	242.0
6	145.1	145.0	29	245.9	247.6
7	148.5	148.9	30	251.7	253.4
8	151.9	152.3	31	257.8	259.3
9	155.4	155.7	32	263.9	265.3
10	159.1	159.4	33	270.0	271.6
11	162.9	163.4	34	276.4	277.9
12	166.6	167.2	35	282.9	284.4
13	170.3	171.3	36	289.2	290.8
14	174.1	175.4	37	296.1	297.4
15	178.2	179.4	38	303.2	304.6
16	182.3	183.4	39	310.5	311.8
17	186.6	187.8	40	317.9	319.5
18	191.0	192.4	41	325.5	327.1
19	195.4	196.8	42	333.3	335.3
20	199.8	201.3	43	341.3	343.3
21	204.5	206.0	44	349.0	351.8
22	209.1	210.9	45	----------	361.0
23	214.0	215.9			

5. Analytical Considerations

The problems of interest in this study may be stated as follows. It is desired to consider those quantities that affect the performance of float-type flowmeters under steady flow conditions; to derive expressions relating these quantities; to check these relations experimentally; and to establish the limitations that apply to the final solutions. It is desired also to determine the effects of density and viscosity of the fluid upon the performance of a flowmeter, and to develop procedures whereby, after calibration with a few fluids of known physical properties, accurate corrections can be calculated and applied when other fluids are used.

Previous investigators have developed relations pertaining to the performance of these meters by deriving expressions based upon Bernoulli's equation, Torricelli's theorem, and the laws of resistance to flow. Although most of these derivations are sound, certain important limitations to their practical application have been overlooked at times. The method of dimensional analysis has been chosen from among the various methods by which the theory of float-type flowmeters could be presented. This method does not in itself provide a complete solution. Rather, it yields functional relations that become explicit only when combined with appropriate experimental data. Equations derived in this manner may then be used to predict and explain the effects of the various quantities upon the over-all performance of the meter.

5.1. Theory

Consider the float-type flowmeter shown schematically in figure 1, consisting of a vertical tapered tube, the area of which increases from bottom to top, through which a fluid of density ρ and viscosity μ is flowing upward at a constant mass rate, M. Within the tube is an object that is free to move in the vertical direction and that may be called a float, although its density, ρ_b, is greater than ρ. The exact configurations of the tube and float need not be specified. Thus the consideration will apply to a variety of shapes, including tubes that are fluted, beaded and circular, and floats that are shaped like plumb bobs, spools, and disks. All of these have found application in practical flowmeters.

As a first step, it is necessary to select those quantities that may affect the drag or resistance force, R, acting between the flowing fluid and the stationary float. Experience indicates that R may be affected by the velocity, density, viscosity, and compressibility of the fluid and by the various geometrical dimensions pertaining to the configuration of the tube and float and to the orientation and position of the float. Among these dimensions, one may be selected as a characteristic length, D, designating the size of the meter, and all other lengths may be expressed in terms of this characteristic length as the dimensionless ratios, r_1, r_2, . . . r_l. Practically, it is simpler to use the mass flow rate, M, through the tube than to express the rate of flow in terms of velocity, since M is measured directly and questions as to what velocity is under consideration are avoided.

The assumption is made here that the fluid is incompressible, since primary interest here is in liquids, and since the derivation is simplified by omitting the effects of compressibility. This does not mean that the results are never applicable to the flow of gases, but rather that the range of applicability is limited to those cases in which the fluid undergoes a

UNIVERSITY OF MICHIGAN LIBRARIES

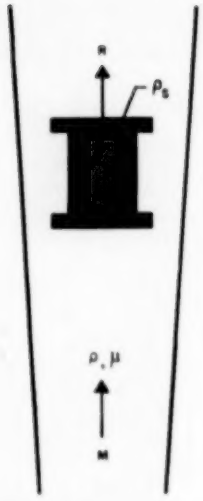

FIGURE 1. *Schematic sketch of a float-type flowmeter.*

negligible change in density as it passes the float. In other words, the analysis does apply to gases, provided that the drop in pressure across the float is only a small fraction of the absolute pressure.

Subject to this limitation, and under the assumption that only those factors discussed above contribute significantly to the drag force, their interdependence can be expressed in the form

$$F(R, M, \rho, \mu, D, r_1, r_2, \ldots r_i)=0, \quad (1)$$

where F denotes "function of."

This equation contains five dimensional quantities and an unspecified number, i, of dimensionless length ratios. The dimensional quantities involved can be expressed in terms of three fundamental physical dimensions; mass (m), length (l), and time (t). In accordance with Buckingham's Pi theorem [6, 7] eq 1 can be expressed in terms of $(i+5)-3=i+2$ dimensionless quantities. Of these, i are merely length ratios, r_i, which define the shape of the meter. Thus eq 1 may be written

$$f(\Pi_1, \Pi_2, r_1, r_2, \ldots r_i)=0. \quad (2)$$

Various methods can be used to form the dimensionless variables Π_1 and Π_2, which contain only the physical quantities R, M, ρ, μ, and D. One procedure is to select any three of the latter that are independent, that is, no one of which can be formed merely by combining the other two in any way, and to associate these three in turn with each of the other two quantities so as to obtain the two dimensionless variables. To this end it is necessary to recall that the dimensions are as follows: $[R]=[mlt^{-2}]$; $[M]=[mt^{-1}]$; $[\rho]=[ml^{-3}]$; $[\mu]=[ml^{-1}t^{-1}]$; and $[D]=[l]$.

Since the primary interest is in the effects of viscosity upon the mass rate of flow, it seemed desirable to derive Π_1 and Π_2 in such a way that one and only one would contain M, while the other alone would contain μ. This left R, ρ, and D as the three quantities that may be involved in both Π_1 and Π_2. On this basis the quantities were arranged in the form of quotients such that the physical dimensions cancelled, giving the following: $\Pi_1=M/D\sqrt{R\rho}$; and $\Pi_2=\mu/\sqrt{R\rho}$.

Substitution of these values in eq 2 gives

$$f(M/D\sqrt{R\rho}, \quad \mu/\sqrt{R\rho}, r_1, r_2, \ldots r_i)=0, \quad (3)$$

or

$$M/D\sqrt{R\rho}=\phi(\mu/\sqrt{R\rho}, r_1, r_2, \ldots r_i). \quad (4)$$

Subject only to the aforementioned limitation as to compressibility, eq 4 should hold for all float-type flowmeters, regardless of the configurations of the parts or of the densities and viscosities of the fluids. The function ϕ may have an infinite number of forms depending on the configurations of the various parts of the meters, that is upon the r_i ratios. As these ratios may vary in countless ways from meter to meter, it is concluded that no single form of ϕ, and therefore no single equation, will represent the performance of flowmeters of different shapes. Even along a single metering tube with a given float, the shape factors that influence the motion of the fluid as it passes the float do not remain constant. Thus it is also concluded that no single form of ϕ, and therefore no single equation, can be expected to represent accurately the performance throughout the length of a single flowmeter tube.

However, if the consideration be restricted to a single float shape at one given float position in a particular metering tube, eq 4 reduces to

$$M/D\sqrt{R\rho}=\phi(\mu/\sqrt{R\rho}). \quad (5)$$

As the stationary float is unrestrained in the vertical direction, the drag force must exactly balance the force of gravity. Thus

$$R=gv(\rho_s-\rho), \quad (6)$$

in which g and v are the acceleration of gravity and the volume of the float, respectively.

Substitution of this value of R in eq 5 gives

$$M/D\sqrt{gv(\rho_s-\rho)\rho}=\phi(\mu/\sqrt{gv(\rho_s-\rho)\rho}), \quad (7)$$

or

$$M/X=\phi_1(\mu/X), \quad (8)$$

in which X is used to replace the quantity $\sqrt{(\rho_s-\rho)\rho}$. The quantities D, g, and v are constant for any given float, so they may be omitted and their effects absorbed in the new function ϕ_1.

For reasons that will be appreciated later, it is convenient to express the relation of eq 5 in the form

$$M/\mu=\phi_2(X/\mu). \quad (9)$$

This transformation is valid since only dimensionless quantities are being treated. Thus, referring to eq 5, it is legitimate to multiply $M/D\sqrt{R\rho}$ by $\sqrt{R\rho}/\mu$, giving $M/D\mu$ for the left-hand member, and to invert the right-hand member. Again R

is replaced by its equivalent from eq 6, and the constant quantities D, g, and v are omitted as before.

All quantities in the arguments of eq 8 and 9 can be measured by experiment. If the equations are correct, plots of M/X versus μ/X and of M/μ versus X/μ should give smooth curves, the shapes of which constitute empirical determinations of the functions ϕ_1 and ϕ_2 for the selected float position.

To make a comprehensive test of these equations, the actual flow rates of 11 test liquids, varying in density from 0.68 to 0.80 g/cm³ and in viscosity from 0.39 to 1.83 centipoises, were measured at three selected positions of the floats in each of five different flowmeter tubes, designated as tubes 3 through 7 of the seven-tube meter. Measurements were also made at four additional float positions in tube 4. These experimental data are summarized in table 2.

Each of the floats was a spool of stainless steel having a density of 7.589 g/cm³. Since X appears in both eq 8 and 9, and since ρ_s was constant, a curve of X as a function of ρ, as shown in figure 2, proved convenient in the reduction of the results.

Figures 3 through 7 show M/X as a function of μ/X for the five metering tubes. Figure 8 shows M/μ as a function of X/μ for tube 4. Each figure applies for three or more float positions, which are designated by means of numbers on the existing scales of the meters.

In every case the experimental points for all test fluids at any one float position lie on a single curve, with no value deviating from its curve by more than the experimental error of a few tenths of one percent. Thus the validity of eq 1, 8, and 9 is demonstrated over the range of densities and viscosities studied. This means that no factors that significantly affect the flow past the float have been omitted in the dimensional analysis, that the application of the results is limited only as stated above, and that the present tests were made within these and no other limitations.

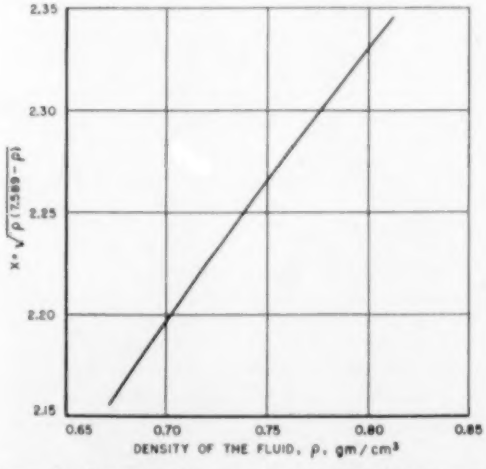

FIGURE 2. *Relation of parameter X to fluid density when* $\rho_s = 7.589$ *g/cm³.*

The curves shown could be used for calculating the actual flow rate of any fluid having physical properties within the ranges embraced by the test liquids, provided the float came to rest at one of the isolated

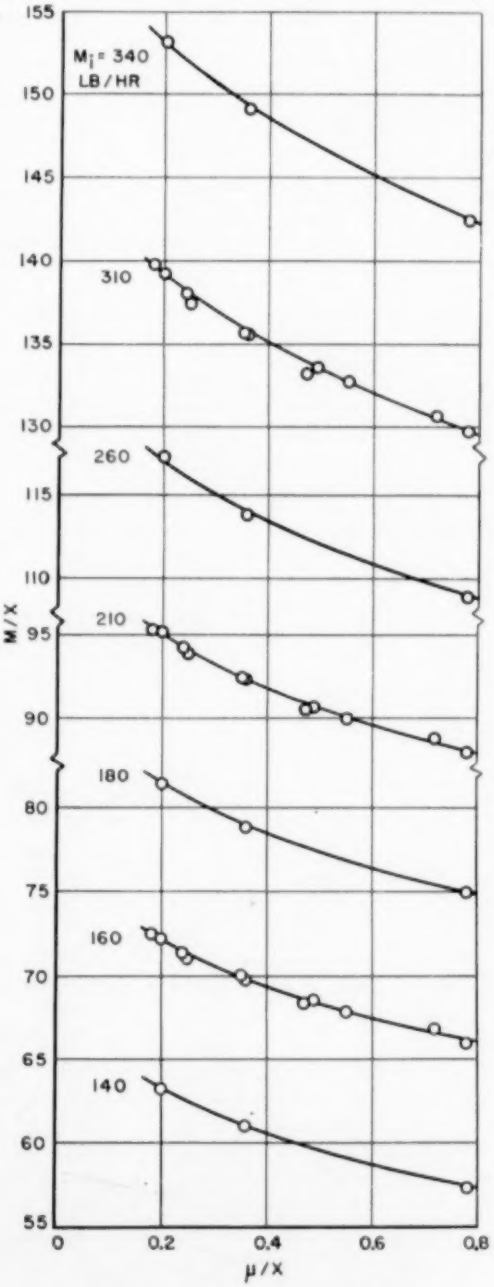

FIGURE 3. *Plot of* M/X *versus* μ/X *for tube 4.*

UNIVERSITY OF MICHIGAN LIBRARIES

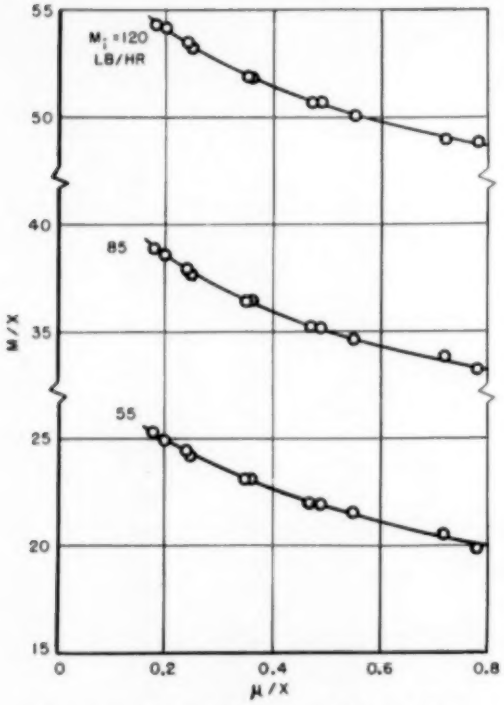

FIGURE 4. *Plot of M/X versus μ/X for tube 3.*

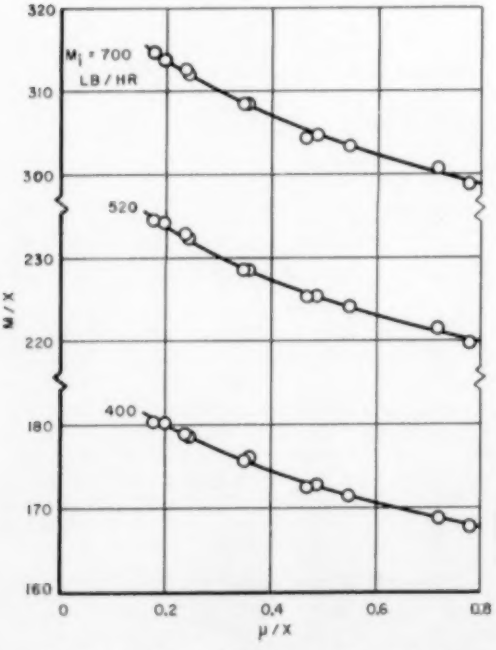

FIGURE 5. *Plot of M/X versus μ/X for tube 5.*

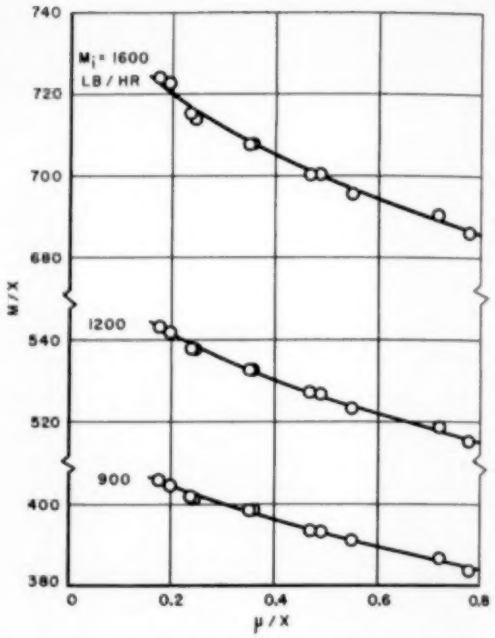

FIGURE 6. *Plot of M/X versus μ/X for tube 6.*

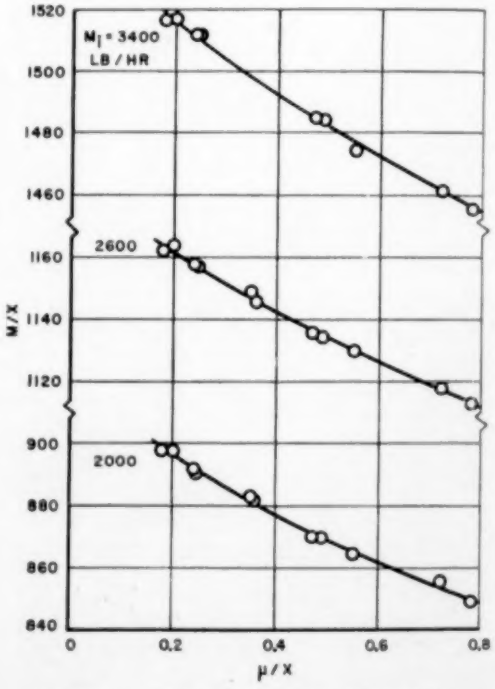

FIGURE 7. *Plot of M/X versus μ/X for tube 7.*

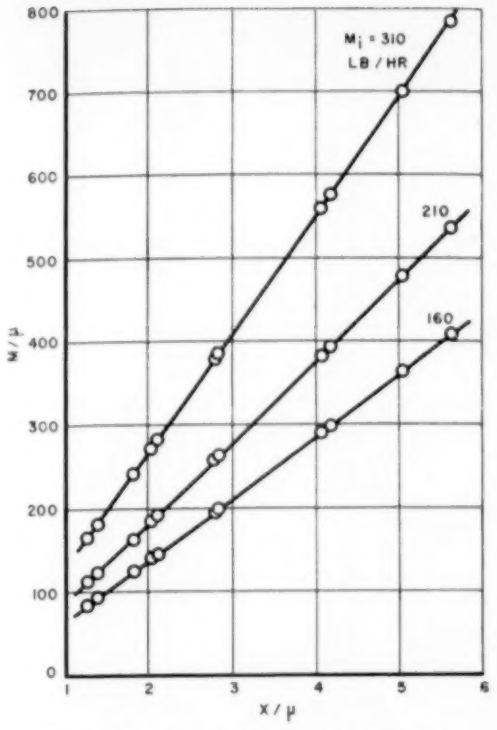

FIGURE 8. *Plot of M/μ versus X/μ for tube 4.*

positions for which the curves apply. Since this is unlikely, a more general interpretation of the results is essential to their practical application. However, before proceeding with this, the application of the data in evaluating the separate effects of density and viscosity on meter performance will be discussed. Such information has practical importance in establishing permissible tolerances in fluid properties for any desired accuracy of metering and in evaluating changes designed to reduce the sensitivity of the meter to the physical properties of the fluid by modifying the constituent parts.

5.2. Effects of Changes in Viscosity, Density Remaining Constant

The effects of changes in fluid viscosity upon the performance of the meter, provided the density of the fluid remains constant, can be obtained directly from figures 3 to 7. The curves in these figures give the empirical evaluations of the function ϕ_1 of eq 8.

If the fluid density is held constant at a value ρ_c, X will have a corresponding constant value X_c, and eq 8 becomes

$$M_\rho/X_c=\phi_1(\mu_\rho/X_c), \tag{8a}$$

in which the subscript ρ indicates that the density is constant. Since X_c is constant, M_ρ varies with μ_ρ alone and eq 8a can be written as

$$M_\rho=\phi_1(\mu_\rho). \tag{8b}$$

The functions ϕ_1 of eq 8, 8a, and 8b are identical, and for any particular float position the form is given by the appropriate curve in figures 3 through 7.

In order to show how M_ρ varies with μ_ρ, any arbitrary value ρ_c may be selected. Here the value $\rho_c=0.750$ g/cm³ is used. Compute the corresponding value of X_c, and for assumed values of μ_ρ over the range of interest, compute values of the ratio μ_ρ/X_c. Read the corresponding values of M_ρ/X_c from one of the curves of figures 3 through 7, and finally compute $M_\rho=(M_\rho/X_c)X_c$ for each assumed value of μ_ρ.

Typical results obtained in this way, applicable specifically to three float positions in tube 4, are shown as curves of M_ρ versus μ_ρ in figure 9. If the

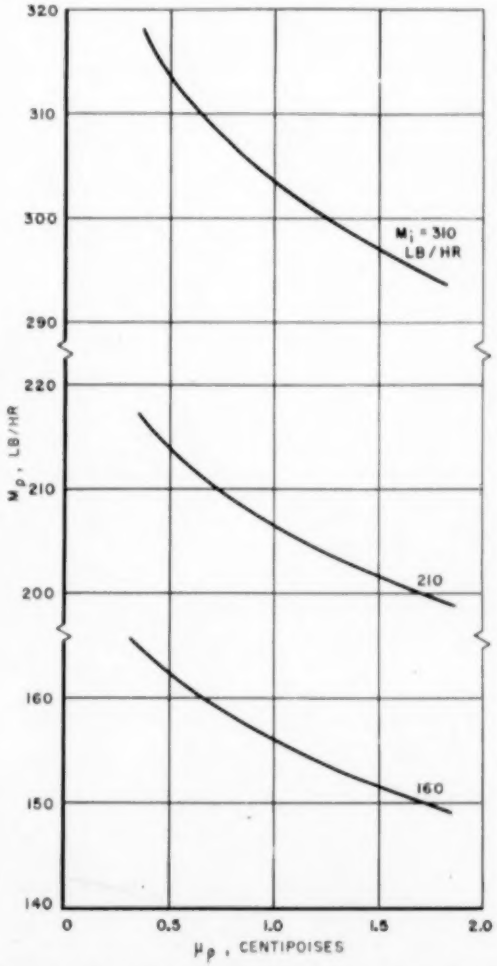

FIGURE 9. *Effects of viscosity upon the flow rate at certain float positions in tube 4, when $\rho_c=0.75$ g/cm³ and $\rho_s=7.589$ g/cm³.*

UNIVERSITY OF MICHIGAN LIBRARIES

instrument were completely insensitive to changes in viscosity, the curves in this figure would be horizontal straight lines.

The significance of the date of figure 9 can be illustrated by a numerical example. Suppose that two fluids having a density of 0.750 g/cm³ were used as follows. The meter was calibrated with fluid A, having a viscosity of 0.4 centipoise, and later fluid B having a viscosity of 1.8 centipoises was metered. If no viscosity correction is applied, the observed flow rate of fluid B will be approximately 8 percent too high over the entire length of the metering tube. Due to the large difference in viscosity that was assumed, this figure represents a maximum that would seldom be approached in conventional applications.

5.3. Effects of Changes in Density, Viscosity Remaining Constant

Equation 9 and figure 8 may be used to show the effects of changes in density when the viscosity remains constant. Using the same conventions and reasoning as before, eq 9 becomes

$$M_\mu/\mu_c = \phi_2(X_\mu/\mu_c) = \phi_2[\sqrt{(\rho_s-\rho_\mu)\rho_\mu}/\mu_c], \qquad (9a)$$

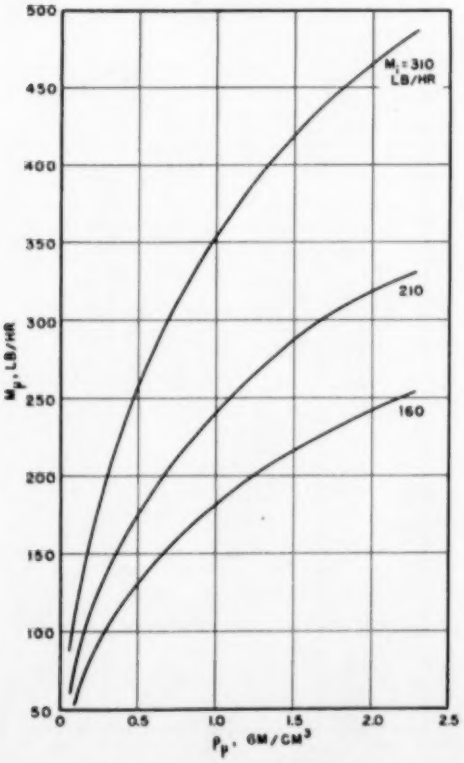

FIGURE 10. *Effects of fluid density upon the flow rate at certain float positions in tube 4 when μ_c=0.60 centipoise and ρ_s=7.589 g/cm³.*

or

$$M_\mu = \phi_2'(\rho_\mu), \qquad (9b)$$

in which the function ϕ_2' depends upon ϕ_2, ρ_s, and the selected value of μ_c.

Proceeding as before, an arbitrary value is assigned to μ_c, the value 0.600 centipoise being used here. For assumed values of ρ_μ over the range of interest, compute $X_\mu = \sqrt{(\rho_s-\rho_\mu)\rho_\mu}$, then calculate X_μ/μ_c, read the corresponding values of M_μ/μ_c from a curve in figure 8, and finally compute $M_\mu = (M_\mu/\mu_c)\mu_c$ for each assumed value of ρ_μ. Results applicable to three float positions in tube 4 are shown in figure 10. At any constant float position in tube 4, the actual flow of two liquids having densities of 0.6 and 0.8 g/cm³, each having a viscosity of 0.6 centipoise, differs by about 15 percent.

It is to be noted that the effect of increased viscosity on flow rate is in the opposite direction from that of increased density. For hydrocarbons in general, light liquids have low viscosities and heavy liquids are more viscous. Also, for such liquids a given change in temperature causes both density and viscosity to change in the same direction. Therefore, the effects of changes in these physical properties upon the metering will normally be of opposite sign. This means that the metering error due to a change in density is usually compensated in part by that from the accompanying change in viscosity.

6. Application of the Results

The previous analysis shows the effects of density and viscosity on the performance of the meter at selected, isolated float positions. To be generally useful, it is necessary to develop procedures whereby this analysis can be applied at all float positions along the metering tube. It is desired to evaluate corrections, preferably in the form of difference charts, applicable to either a single fluid of known density and viscosity, or to all fluids whose physical properties fall within the range embraced by the calibration fluids.

Conventional flowmeters are usually equipped with either linear scales, reading in centimeters or inches, or flow rate scales, graduated in mass flow rate units of a liquid of specified properties. Before these scale readings can be utilized in applying corrections for different fluids at any float position, a final reference calibration is required.

6.1. Reference Calibration

Errors that may arise from imperfections in the tube, from the factory calibration, and from the ruling and positioning of the scale can be eliminated by an accurate calibration with a single liquid whose physical properties need not be known. Since differences obtained with other fluids are reckoned from this calibration, it is termed a reference calibration.

A reference calibration of tube 4, equipped with a linear scale as well as the factory scale graduated

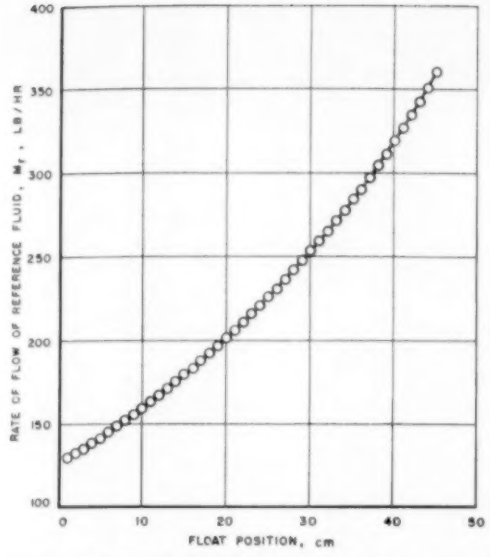

FIGURE 11. *Reference calibration of tube 4 in terms of float position.*

in pounds per hour, was made at 45 float positions, that is, at intervals of 1 cm on the linear scale. At each float position the actual flow rate, M_r, was determined, the linear scale was read, and the indicated flow, M_i, was observed. The results are summarized in table 3.

For a meter with a linear scale, this calibration can be represented by the curve of figure 11, in which M_r is shown as a function of the position of the float in centimeters above an arbitrary zero. Drawn to a large enough scale, such a curve may be used to read flow rates with an accuracy of about 0.1 percent.

For a meter graduated in terms of flow, it is convenient to express the reference calibration in the form of a difference curve such as that shown in figure 12, which is applicable to tube 4. In this figure the difference $M_r - M_i$ is called a composite error, E, as it involves both accidental errors and systemmatic differences. Actually, the density and viscosity of the reference fluid differed considerably from the corresponding properties of the fluid with which the meter was calibrated originally, so that the values of E should not be confused with the smaller errors in the original calibration from which the scale was ruled.

6.2. Combined Correction Procedure for a Single Fluid

Suppose that a given meter is to be used with a single fluid of known density and viscosity. It is desired to devise a procedure and develop a correction chart from which the actual flow rate, M, of this particular fluid may be calculated accurately at any indicated flow rate, M_i.

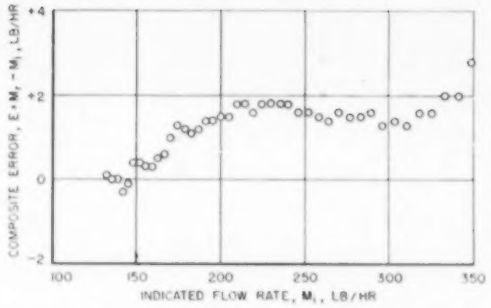

FIGURE 12. *Composite error from the reference calibration of tube 4.*

It has been shown that two corrections must be considered, namely one for errors in the existing scale, and one for the density and viscosity of the fluid to be metered. Determination of the composite error, E, as illustrated in figure 12, provides a possible means of correcting for the scale errors. From this figure any observed value of indicated flow, M_i, can be converted into the actual flow of the reference fluid by the relation $M_r = E + M_i$. Having obtained the value of M_r at any indicated flow reading, the difference between the actual flow rate of the fluid to be metered and the actual flow rate of the reference fluid, that is, $(M - M_r)$, is due solely to effects of differences in density and viscosity of the test and reference fluids.

The actual flow rate, M, of the fluid being metered is the sum of the quantities $M_r = E + M_i$ and $M - M_r$. The value of E corresponding to any observed value of M_i can be read from figure 12, so that M_r is known. To calculate M requires in addition a correction chart from which the quantity $M - M_r$ can be read. The development of such a chart will now be discussed.

For this illustration, suppose it is desired to use tube 4 of the present instrument to meter a fluid having a density of 0.745 g/cm³ and a viscosity of 0.924 centipoise at the temperature prevailing in the meter.

From figure 2 the value of X corresponding to $\rho = 0.745$ is seen to be 2.258. The corresponding value of μ/X for our example is $0.924/2.258 = 0.409$. These, as well as the following computations, are tabulated in table 4.

TABLE 4. *Computation of $(M - M_r)$ in tube 4 when $\rho = 0.745$ g/cm³ and $\mu = 0.924$ centipoise*

$X = 2.258$; $\mu/X = 0.409$

M_i, lb/hr	140	160	180	210	260	310	340
Float position, cm	4.4	10.2	15.4	22.2	31.4	39.0	42.8
$E = M_r - M_i$, lb/hr	−0.2	+0.4	+1.1	+1.7	+1.5	+1.4	+2.2
$M_r = M_i + E$, lb/hr	139.8	160.4	181.1	211.7	261.5	311.4	342.2
M/X	60.6	69.3	78.4	91.6	113.2	134.7	148.2
$M = 2.258(M/X)$, lb/hr	136.8	156.5	177.0	206.8	255.6	304.2	334.6
$M - M_r$, lb/hr	−3.0	−3.9	−4.1	−4.9	−5.9	+7.2	−7.6

The first line of table 4 lists the seven float positions, that is, values of M_i, at which the calibration curves of figure 3 were determined. The same float

UNIVERSITY OF MICHIGAN LIBRARIES

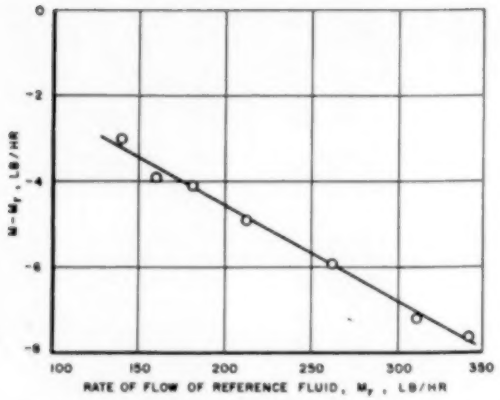

FIGURE 13. *Correction curve for tube 4, assuming $\rho=0.745$ g/cm³ and $\mu=0.924$ centipoise.*

positions, as indicated on a linear scale above an arbitrary zero, are given in the next line. The appropriate values of E, as read from figure 12, and the values of $M_r=M_t+E$ are listed in the next two horizontal lines.

Referring again to figure 3, the tabulated values of M/X corresponding to the constant value $\mu/X=0.409$ were read from each of the seven curves. The actual flow rates, M, were then obtained by multiplying each value of M/X by 2.258, that is, by the X for this particular example. Having thus found seven corresponding values of M and M_r, the desired correction, $M-M_r$ can be plotted as a function of M_r, as is done in figure 13.

For the fluid chosen as an illustration, the corrections ($M-M_r$) range from 3.0 to 7.6 lb/hr, and none of the seven points deviates from the smooth curve by more than 0.2 percent. Hence the combined effect of density and viscosity is to produce regular, rather than stepwise, changes in metering over the length of the tube.

Any indicated flow reading obtained with a fluid having the selected properties may now be corrected as follows by using figures 12 and 13. For any indicated flow reading, M_t, the corresponding value of E is read from figure 12 and the value of $M_r=E+M_t$ is computed. The corresponding value of ($M-M_r$) is then obtained from figure 13. Finally, the actual flow rate is obtained by adding M_r to $M-M_r$.

For a meter having a linear scale, M_r is read from figure 11 at a number of float positions, and the corresponding values of M are determined by use of figure 13. A calibration curve applicable to this specific fluid may then be plotted in terms of M as a function of the position of the float in centimeters.

6.3. Combined Correction Procedure for Any Fluid

Application of the procedure outlined above requires a correction chart or calibration curve for each fluid to be metered. If several different fluids are to be metered, a more general method of correction is desirable, that is, one which is applicable to any float position and to any fluid for which the value of μ/X lies within the range embraced by the calibration fluids.

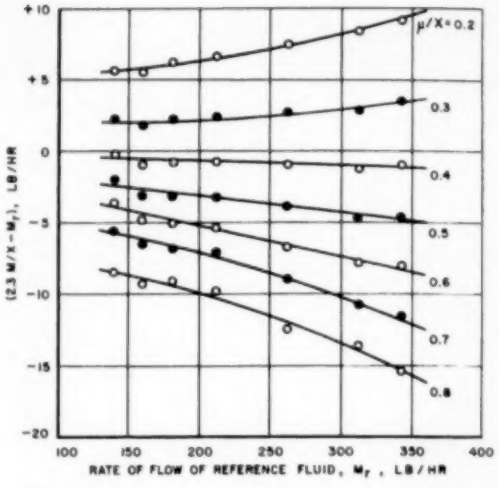

FIGURE 14. *Generalized correction chart for table 4.*

As in the previous example, corrections for both the composite error and the properties of the fluid must be considered. The composite error may be treated as before, by converting indicated flow rates, M_t, to actual flow rates, M_r, of the reference fluid through the use of figure 12. It is then necessary only to develop a chart to correct for differences between the densities and viscosities of the reference fluid and any other fluid that may be metered. The development of such a chart will now be discussed.

For the present consideration of a float of constant shape, regardless of its position within a single metering tube, eq 7 may be written as

$$M/DX\sqrt{g\rho}=\phi(\mu/X\sqrt{g\rho}, r), \qquad (10)$$

in which the dimensionless ratio r is used as an indication of the float position.

With any constant value of the parameter $\mu/X\sqrt{g\rho}$, the product $M/DX\sqrt{g\rho}$ will be a function of r alone. For this particular condition it is permissible to write

$$(M/DX\sqrt{g\rho})-r=\phi_3(r) \qquad (10a)$$

where the form of the function ϕ_3 will be different for each value of $\mu/X\sqrt{g\rho}$.

The dimensionless ratio r has been used to define float position. As will be seen in figure 11, this can also be defined by M_r; thus, r may be replaced by M_r. Also, it is useful and permissible to multiply $M/DX\sqrt{g\rho}$ by a dimensionless number A. Equation 10a may now be written as

$$(AM/X)-M_r=\phi_4(M_r). \qquad (10b)$$

TABLE 5. *Computation of* $[2.3(M/X) - M_r]$ *in tube 4 at assumed values of* μ/X

M_t		M_r	$\mu/X=$	0.2	0.3	0.4	0.5	0.6	0.7	0.8
lb/hr	*cm*	*lb/hr*								
140	4.4	139.8	M/X from fig. 3	63.20	61.72	60.70	59.90	59.20	58.40	57.10
			$2.3\ M/X$	145.4	142.0	139.6	137.8	136.2	134.3	131.3
			$2.3\ M/X-M_r$	5.6	2.2	−0.2	−2.0	−3.6	−5.5	−8.5
160	10.2	160.4	M/X	72.15	70.52	69.35	68.40	67.65	66.90	65.70
			$2.3\ M/X$	165.9	162.2	159.5	157.3	155.6	153.9	151.1
			$2.3\ M/X-M_r$	5.5	1.8	−0.9	−3.1	−4.8	−6.5	−9.3
180	15.4	181.1	M/X	81.45	79.70	78.45	77.40	76.55	75.80	74.80
			$2.3\ M/X$	187.3	183.3	180.4	178.0	176.1	174.3	172.0
			$2.3\ M/X-M_r$	6.2	2.2	−0.7	−3.1	−5.0	−6.8	−9.1
210	22.2	211.7	M/X	94.93	93.10	91.73	90.62	89.72	88.95	87.80
			$2.3\ M/X$	218.3	214.1	211.0	208.4	206.4	204.6	201.9
			$2.3\ M/X-M_r$	6.6	2.4	−0.7	−3.3	−5.3	−7.1	−9.8
260	31.4	261.5	M/X	116.9	114.8	113.3	112.0	110.8	109.8	108.6
			$2.3\ M/X$	268.9	264.2	260.6	257.6	254.8	252.5	249.8
			$2.3\ M/X-M_r$	7.4	2.7	−0.9	−3.9	−6.7	−9.0	−12.5
310	39.0	311.4	M/X	139.0	136.6	134.8	133.4	132.0	130.8	129.5
			$2.3\ M/X$	319.8	314.2	310.2	306.8	303.6	300.7	297.8
			$2.3\ M/X-M_r$	8.4	2.8	−1.2	−4.6	−7.8	−10.7	−13.6
340	42.8	342.2	M/X	152.8	150.3	148.8	146.8	145.3	143.8	142.1
			$2.3\ M/X$	351.4	345.7	341.3	337.6	334.2	330.7	326.8
			$2.3\ M/X-M_r$	9.2	3.5	−0.9	−4.6	−8.0	−11.5	−15.4

Neither D, v, or g varies for any particular float, so that they may be omitted if their effects are absorbed in the new function ϕ_4.

Restating the limitations, Equation 10b applies to a constant float shape, regardless of position within a single metering tube, for any constant value of μ/X. By arbitrarily choosing values of μ/X in the range of interest, a family of curves of $(AM/X - M_r)$ versus M_r can be obtained, as has been done in figure 14.

Although the constant A may be assigned any arbitrary value, it is desirable that the quantity $AM/X - M_r$ be kept small so that correction curves made therefrom can be read to a high percentage accuracy. This situation prevails when A is approximately equal to the average value of X for the calibration fluids, which, in the present case was 2.3. This value was therefore used in computing table 5, from which figure 14 is plotted.

The development of this table and figure, again applicable to tube 4, will now be explained. Column 1 of table 5 lists the seven values of M_t at which the calibration curves of figure 3 were determined. These same float positions, as indicated on a linear scale above an arbitrary zero, are given in column 2. Corresponding flow rates, M_r, of the reference fluid may be obtained from either figure 11 or 12, and are listed in column 3.

Values of μ/X from 0.2 to 0.8, in intervals of 0.1 were chosen arbitrarily. For each of these, seven values of M/X were read from the curves of figure 3, and the quantities 2.3 M/X and 2.3 $M/X - M_r$ were computed and tabulated. The latter values were plotted versus M_r in figure 14 for each of the chosen, constant values of μ/X. From this family of curves, used in conjunction with figure 12 when the meter has been scaled to read in terms of flow rate, any indicated value of the latter can be converted into actual flow rate, provided only that the density and viscosity of the fluid being metered are known, that calibrations such as those of figures 3 and 12 have been made, and that the properties of the fluid lie within the ranges embraced by the calibration fluids.

To illustrate the use of figure 14, assume that a fluid having $\rho = 0.740$ g/cm^3 and $\mu = 0.924$ centipoise is flowing through tube 4 at an indicated flow rate of 310 lb/hr. From figure 12, $E = 1.4$, so that $M_r = 311.4$ lb/hr. From figure 2, $X = 2.258$. The value of μ/X is 0.409. From figure 14, by interpolation to $\mu/X = 0.409$, at $M_r = 311.4$, $2.3M/X - M_r = -1.5$. The actual flow rate is

$$M = [(AM/X - M_r) + M_r]X/A$$

$$= (-1.5 + 311.4)(2.258/2.3) = 304.2 \text{ lb/hr.}$$

It will be noted that this is identical with the value computed by a different method in table 4.

A procedure has been described whereby a float-type flowmeter may be used to meter any fluid having a value of μ/X within that range embraced by those fluids used to calibrate the meter. Questions concerning the extent of the calibration and the accuracy of the procedure naturally arise. These cannot be answered explicitly, because much depends upon the characteristics of the instrument under consideration. For a meter already calibrated and scaled, the accuracy of previous work is also involved. Still another factor that varies from meter to meter is the extent and manner in which M/X changes with μ/X. If, for example, the curves of figures 3 through 7 were approximately straight lines over the range of interest, calibration with three fluids would suffice. Another design might show sudden changes in the relation between M/X and μ/X, particularly at high values of μ/X. In this case five or even more calibration fluids would be required. Since this relation can be determined only by experiment, these curves should never be extended beyond those values of μ/X for which experimental data are available.

For the meter used in the present study it appears that calibration with 4 or 5 fluids instead of 11 would have sufficed to define the curves of figures 3 to 7. It also seems, because of the smoothness of the curves of figures 13 and 14, that calibration of each tube at four float positions would have been ample. Posi-

UNIVERSITY OF MICHIGAN LIBRARIES

tions close to both top and bottom of the tube should be included, because of the effects of entrance and exit flow conditions. When the flow pattern within the tube is influenced by the connections to the meter, the same connections should be used during calibration and service.

For the reference calibration yielding figures 11 and 12, approximately one-third the number of points taken would have sufficed for a meter of this quality. However, if the tube and its scale had been crudely made, it might have been necessary to calibrate at intervals of less than 1 cm.

7. Summary

The float-type flowmeter is very convenient for measuring instantaneous rates of flow. Results accurate to within a few tenths of 1 percent can be attained with the meter used in the present study, provided adequate corrections are applied for the effects of the density and viscosity of the test liquid, and for imperfections in the original calibration and scale.

Usually such meters are calibrated and scaled at the factory in mass flow rate units for a liquid of specified properties. The present work was undertaken in an effort to develop means whereby the meter need not be calibrated directly with each liquid that is to be metered. The results show that this can be accomplished for meters of the quality used in these tests by calibrating each tube initially at four positions of the float with four or five fluids having physical properties embracing the ranges of future interest. Calibration with one liquid at a greater number of float positions is also required to eliminate errors due to possible imperfections in the tube and its scale. With such calibrations available, methods are presented whereby correction charts or calibration curves applicable to all fluids having properties within the ranges of those used in the calibration may be computed.

The present analysis expresses flowmeter performance as a functional relation between the parameters M/X and μ/X. These parameters are developed by dimensional analysis, supplemented by experimental verification of the fact that no quantity that has a significant effect on the flow of fluid past the float of the meter has been omitted. The analysis is general, in that it applies to all kinds of float-type flowmeters, regardless of the configuration of tube or float. The derived relations apply for all incompressible fluids and for gases under the limited condition that the drop in pressure across the float shall not be an appreciable fraction of the absolute pressure.

The analysis also indicates why previous attempts to develop theoretical equations applicable throughout the entire length of one flowmeter tube, or for more than one meter, were not markedly successful Actually it is not to be expected that a single theoretical equation can express accurately the performance of a single flowmeter over its entire length under all conditions likely to be encountered in service.

Experimental values of the parameters M/X and μ/X, obtained from calibrations with a series of fluids at selected positions of the float, are shown to be useful, not only in determining corrections that must be applied when fluids having other properties are metered, but also in evaluating the separate effects of density and viscosity on meter performance.

Most of the results presented apply specifically to tube 4 of the meter actually used in these tests. Similar results with other tubes confirm the soundness of the proposed method of correction, but do not require presentation in detail. Whereas the calibration procedure and the methods suggested for its subsequent use, as outlined here, are believed applicable to float-type flowmeters in general, it is emphasized that the numerical values quoted apply only to the specific meter used, and that the correction charts are intended as examples, and not for use with any other instrument.

The suggestions and assistance of H. N. Eaton, Chief of the Hydraulics Section, in applying the methods of dimensional analysis to the present problem are gratefully acknowledged.

8. References

[1] E. M. Schoenborn, Jr. and A. P. Colburn, The flow mechanism and performance of the rotameter, Trans. Am. Inst. Chem. Engr. **35,** 359 (1939).
[2] J. C. Whitwell and D. S. Plumb, Correlation of rotameter flow rates, Ind. Eng. Chem. **31,** 451 (1939).
[3] L. E. Stout and A. R. Rowe, A new type of fluid rate flowmeter, Trans. Amer. Inst. Chem. Engr. **34,** 1 (1938).
[4] K. Fischer, S. Bleckman, and E. Lipstein, The elimination of viscosity as a factor in determining rotameter calibration, Trans. Am. Inst. Chem. Engr. **36,** 857 (1940).
[5] R. C. Kintner, Visual fluid flowmeters with straight-walled tubes, Ind. Eng. Chem., Anal. Ed. **14,** 261 (1942).
[6] E. Buckingham, Notes on the method of dimensions, Phil. Mag. **42,** 696 (1921).
[7] E. Buckingham, On physically similar systems; illustrations of the use of dimensional equations, Phys. Rev. **4,** 345 (1914).
[8] J. J. Martin, Calibration of Rotameters, Chem. Eng. Prog. **45,** 338 (1949).

Washington, February 20, 1950.

Journal of Research of the National Bureau of Standards Vol. 47, No. 4, October 1951 Research Paper 2248

Mutarotation, Hydrolysis, and Structure of D-Galactosylamines

Harriet L. Frush and Horace S. Isbell

Of the two previously described galactosylamines, one has been shown to be a mixture. A pure compound has now been isolated from it, thus making available for the first time two pure modifications of a glycosylamine. The structure and properties of these compounds and of certain derivatives have been determined. The new substances constitute a group of reference compounds useful for the assignment of structure in this field. The mutarotation and hydrolysis of the two galactosylamines were studied and found to be in harmony with mechanisms previously advanced by us.

1. Introduction

Reaction of ammonia or suitable amines with sugars produces glycosylamines by replacement of one amino hydrogen with a glycosyl group. The compounds are of interest, because, like many biologically important substances such as nucleic acids and certain coenzymes, they contain an *N*-glycosyl linkage. In a previous publication [1],[1] it was shown that in solution L-arabinosylamine, I, undergoes a mutarotation reaction that is followed or accompanied by hydrolysis of the amino group. The mutarotation is strongly catalyzed by acids; the hydrolysis, like certain enzyme reactions, is rapid only in the pH range 3 to 7. Mechanisms were advanced to account for these unusual properties, through the intermediate formation of the imonium ion $-\overset{|}{C}=\overset{+}{N}H_2$. Hydrolysis was conceived as involving combination of the imonium ion with hydroxyl ion, and decomposition of the resulting aldehyde ammonia. Lack of reaction in highly acid solution was ascribed to low hydroxyl ion concentration, and lack of reaction in alkaline solution to low imonium ion concentration. To provide additional support for the mechanisms, a study has now been made of the D-galactosylamines.

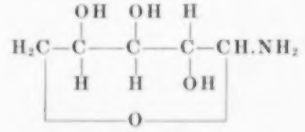

(I)

L-Arabinosylamine.

2. Preparation and Structure of the Galactosylamines

By treatment of galactose with ammonia and methanol, de Bruyn and Van Leent [2] obtained two galactosylamines of unknown structure. One of the amines had an initial specific rotation of +87°, and contained a mole of loosely bound ammonia; the other had an initial specific rotation of +64°, and was ammonia free. These compounds have now been prepared and their structures determined. By repeated recrystallization of the ammonia complex, the initial rotation was raised from +87° to +138°. Inasmuch as the optical rotation could not be further increased, it is believed that this material is a pure modification of the galactosylamine. Preparation of the amonia-free form of galactosylamine by a number of methods, and repeated recrystallization of the product, gave a substance having an initial specific rotation of +62° in comparison with the value of +64° reported in [2]. The two modifications of galactosylamine were acetylated, and yielded crystalline pentaacetates, which differed in properties. By deacetylation of the pentaacetates, the corresponding crystalline N-acetylgalactosylamines were obtained, and the latter compounds were shown by periodate oxidation and study of the dialdehydes to be an alpha-beta pyranose pair. Since mild conditions of acetylation and deacetylation were employed, it appears reasonably certain that the parent galactosylamines as well as the corresponding pentaacetates are also alpha-beta pyranose pairs. The mutarotation and hydrolysis of the two galactosylamines have been studied, and found to be in harmony with the mechanisms previously advanced.

In accordance with convention, the more dextrorotatory amine II (known in the form of the ammonia complex) is designated alpha; the less dextrorotatory amine III is designated beta, even though it does not exhibit normal mutarotation. The lack of mutarotation might suggest that the compound is an isomeric mixture. Such a mixture, however, on mild acetylation, would have yielded a mixed acetate. The fact that a high yield of a nearly pure acetate was obtained supports the conclusion that the parent glycosylamine is a single modification and that the equilibrium mixture for D-galactosylamine consists almost entirely of the beta form.

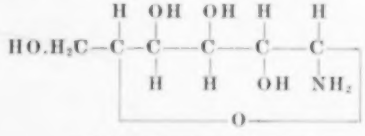

(II)

α-D-Galactopyranosylamine.

[1] Figures in brackets indicate the literature references at the end of this paper.

UNIVERSITY OF MICHIGAN LIBRARIES

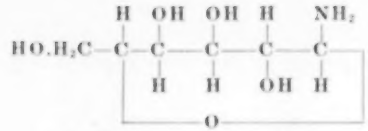

(III)

β-D-Galactopyranosylamine.

3. Mutarotation of α-D-Galactosylamine Ammonia Complex and β-D-Galactosylamine

The changes that occur when α-D-galactosylamine ammonia complex is dissolved in water are given in table 1. The behavior of the substance resembles that of L-arabinosylamine in that the optical rotation, $[\alpha]_D^{20}$, drops to a minimum and then rises slowly. The first change may be ascribed to the mutarotation reaction and the second to hydrolysis. Table 2 gives a comparison of the behavior of α-D-galactosylamine ammonia complex and of β-D-galactosylamine in water and in aqueous 2.5 *N* HCl. At the time of the earliest reading in acid solution the two substances exhibit within experimental error the same optical rotation (+63.0°). This value is presumably that of the alpha-beta equilibrium mixture, since in acid solution equilibrium is established quickly. The subsequent rise in optical rotation is attributed to slight hydrolysis. The mutarotation of the beta isomer in water and in water containing ammonia appears anomalous, in that the change in optical rotation, although small, is in the same direction as that of the alpha isomer. It is believed that this change is not due to the establishment of the alpha-beta equilibrium, but rather to a side reaction, the formation of a less dextrorotatory substance, presumably the digalactosylamine having a specific rotation of +22° [3].

As shown by the experiment given in table 3, the side reaction causing the optical rotation to fall below the equilibrium value is enhanced by the presence of general acid catalysts, in this case the ammonium ion. A similar reaction was observed concurrently with the mutorotation of L-arabinosylamine [1]. We believe that the reaction involves the condensation of the amine with the imonium cation essentially as represented below:

TABLE 1. *Mutarotation of α-D-galactosylamine* [a]

[0.5 g α-D-galactosylamine ammonia complex dissolved in water to give a volume of 25 ml at 20°C]

Time	$[\alpha]_D^{20}$	$[\alpha]_D^{20}$ (ammonia-free basis)	pH	Mutarotation constant, [b] k_m	Hydrolysis rate constant, [c] $k_{hydrol.}$
Minutes					
0	[d](+138)	[d](+151.1)	.....	.....	.....
2.8	135.9	148.8	10.9	.....	.....
15.8	129.4	141.7	.....	0.0029	.....
30.0	115.3	126.3	.....	.0048	.....
70	94.7	103.7	.....	.0048	.....
136	73.0	79.9	10.8	.0052	.....
280	56.8	62.9	10.7	.....	.....
20.3 hr	59.2	64.8	10.6	.....	.....
29	60.0	65.7	.....	.....	0.00005
45	61.8	67.7	10.8	.....	.00006
∞	[e](73.0)	[e](79.9)	.....	.....	.....
			Avg.....	0.0044	0.00006

[a] Experiment 1, see table 4.
[b] $k_m = 1/t \log (r_0 - r_\infty)/(r_1 - r_\infty)$.
[c] $k_{hydrol.} = 1/(t_2 - t_1) \log (r_1 - r_\infty)/(r_2 - r_\infty)$.
[d] Calculated initial rotation.
[e] Calculated rotation for complete hydrolysis.

TABLE 2. *Changes in optical rotation of α-D-galactosylamine ammonia complex and of β-D-galactosylamine on dissolution in water and in 2.5 N HCl*

Alpha modification		Beta modification	
Time	$[\alpha]_D^{20}$	Time	$[\alpha]_D^{20}$
Experiment 2 solution in 2.5 *N* HCl		Experiment 3 solution in 2.5 *N* HCl	
Min.			
3.0	+63.0	3	+63.1
10.3	63.3	60	63.2
225	63.5	90	64.3
360	63.9	215	64.6
22 hr	64.3	72 hr	66.6
Experiment 1 solution in water pH 10.9		Experiment 4 solution in water + NH_3 [b] pH 10.9	
2.8	+148.8	3.1	+62.7
15.8	141.7	30	62.7
30	126.3	60	62.7
136	79.9	180	62.5
280	62.9	24 hr	62.4
20.3 hr	64.8		
		Experiment 5 solution in water pH 9.2	
		2.1	+62.2
		5.1	61.9
		10.5	61.2
		21.1	60.8
		60	60.5
		120	60.4

[a] Ammonia-free basis.
[b] The solution of α-D-galactosylamine ammonia complex in water had a pH of 10.9. For comparison, measurements of the rotation of β-D-galactosylamine also were made in the presence of NH_3 at this pH.

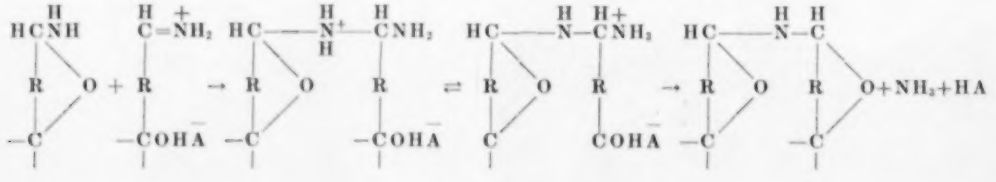

This mechanism requires the presence of both the free amine and the imonium cation. Relatively high concentrations of both constituents exist in alkaline solution in the presence of general acid catalysts, and hence the side reaction is of importance under these conditions. As pointed out in [1], the mechanism also accounts for the variation in the amount of the side reaction with the manner of mixing the glycosylamine and acid. Slow addition of the acid permits the amine present in excess to react with the imonium cation as it is formed.

TABLE 3. *Change in optical rotation of β-D-galactosylamine in the presence of 1 N $NH_4Cl + NH_3$ at pH 10.9* [a]

Time	$[\alpha]_D^{20}$
min	
2.4	+58.2°
10.7	57.5
60	55.8
120	55.3
300	54.5
460	54.9

[a] Experiment 6.

4. Acid-Base Catalysis in the Mutarotation of α-D-Galactosylamine

Solutions of α-D-galactosylamine ammonia complex in water react alkaline and contain free ammonia. A 0.1-molar solution has a pH of about 10.9. To study the variation in the rate of mutarotation with pH, measurements were made in solutions containing either additional base or an acid. The data are presented in table 4 and figure 1. In figure 1, curve 1 shows the mutarotation of the substance in water free from carbon dioxide, and curves 2 and 3 show the effect of increasing the alkalinity by the use of ammonia and sodium hydroxide, respectively. Curve 4 shows the effect of a substantial quantity of ammonium chloride and curve 5 of strong acid. In the presence of strong acid the optical rotation drops to the equilibrium value before the first measurement can be made. In the pH range 8.7 to 11.5, solutions buffered with ammonium chloride and ammonia gave satisfactory rate constants (table 4). In some cases the muta-

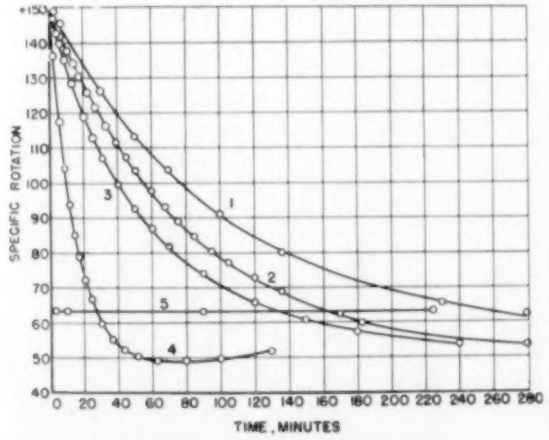

FIGURE 1. *Mutarotation of α-D-galactosylamine ammonia complex.*

1. In water, pH 10.9 (experiment 1); 2. in water + NH_3, pH 11.5 (experiment 8); 3. in 0.01 N NaOH (experiment 7); 4. in 0.5 N $NH_4Cl + NH_3$, pH 10.9 (experiment 9); 5. in 2.5 N HCl (experiment 2).

TABLE 4. *Mutarotation of α-D-galactosylamine*

[0.5 g α-D-galactopyranosylamine ammonia complex dissolved in sufficient acid base or buffer to give a volume of 25 ml at 20° C, and the solvent composition listed opposite the experiment number. pH given is that of solution]

Time	$[\alpha]_D^{20}$ [a]	Time	$[\alpha]_D^{20}$ [a]	k_m [b]
Experiment 7. 0.01 N NaOH. pH 12.1 [c]				
min		*min*		
10	+132.5	70	+82.1	
30	108.0	90	74.5	0.009
50	92.5	110	68.7	.007
			Avg	0.008
Experiment 8. Water + NH_3 pH 11.5				
10	+138.3	110	+75.5	
30	119.4	130	70.6	0.0055
50	104.6	150	66.8	.0055
			Avg	0.005
Experiment 1. Water pH 10.9 (See table 1) 0.004				
Experiment 9. 0.5 N $NH_4Cl + NH_3$ pH 10.9				
2	+136.3	18	+77.2	
6	114.4	22	69.8	0.030
10	97.8	26	64.3	.031
			Avg	0.030
Experiment 10. 0.04 N $NH_4Cl + NH_3$ pH 9.6				
2	+128.7	100	+75.8	
10	120.4	108	74.0	0.007
18	113.3	116	72.5	.007
			Avg	0.007
Experiment 11. 0.08 N $NH_4Cl + NH_3$ pH 9.0				
5	+138.0	95	+75.3	
15	115.0	105	73.7	0.018
25	103.3	115	72.4	.013
			Avg	0.016
Experiment 12. 0.1 N $NH_4Cl + NH_3$ pH 8.7				
2	+127.9	12	+78.2	
4	109.5	14	75.0	0.079
6	96.4	16	72.4	.079
			Avg	0.079
Experiment 13. 0.25 N $(NH_4)_2HPO_4 + NH_3$ pH 9.9				
1	+121.3	5	+76.5	
2	109.3	6	73.3	0.220
3	88.5	7	70.8	.183
			Avg	0.202
Experiment 2. 2.5 N HCl (See table 2) ∞				

[a] Specific rotations expressed on ammonia-free basis.
[b] Determined by the method of Brönsted and Guggenheim [4].
[c] Approximate pH.

rotation appears to be caused not only by the establishment of the alpha-beta equilibrium, but also to some extent by the side reation discussed in the preceding paragraph.

The side reaction accounts for the drop in rotation below the equilibrium value of +63° (strikingly shown in curve 4 of fig. 1). It seems to be favored by the presence of general acid catalysts, particularly in alkaline solution. Presumably both the mutarotation and the slide reaction involve the intermediate formation of the imonium cation, and since separate treatment of the reactions does not seem feasible, no attempt was made to determine separate rate constants; rather, a rate constant k_m was calculated for the over-all process.

TABLE 5. *Mutarotation constants for α-D-galactosylamine ammonia complex*

Experiment	pH	$[H^+]$	$[OH^-]$	$[NH_4^+]$	k_m	k_m(corrected)[a]
7	12.0	10^{-12}	10^{-2}	.....	0.008	0.008
8	11.5	3.2×10^{-12}	3.2×10^{-3}	.....	.005	.005
1	10.9	1.3×10^{-11}	7.9×10^{-4}	.....	.004	.004
9	10.9	1.3×10^{-11}	7.9×10^{-4}	0.5	.030	.004
10	9.6	2.5×10^{-10}	4.0×10^{-5}	.04	.007	.005
11	9.0	1.0×10^{-9}	1.0×10^{-5}	.08	.016	.012
12	8.7	4.8×10^{-9}	8.5×10^{-6}	1.0	.079	.027
13	9.0	1.0×10^{-9}	1.0×10^{-5}	0.5	.202	[b] 176
2	2.5NHCl	.....	.....	.....	[c] ∞	.....

[a] Corrected for the catalytic effect of ammonium ion.
[b] Higher constant due to catalytic effect of the phosphate used as a buffer.
[c] Too rapid to measure.

To evaluate the effect of acid and base catalysts on the mutarotation, the rate constants reported in tables 4 and 5 were determined by the method of Brönsted and Guggenheim [4]. This method was used because it does not require the final, or equilibrium rotation. A comparison of the data of experiments 1 and 9 and of 11 and 13 show that the process is catalyzed by ammonium ion, and by acid phosphate, respectively. Thus the reactions clearly show general acid catalysis. If, for simplicity, the system is restricted to solutions containing water and ammonium salts of strong acids, the rate constant is given by the following expression:

$$k_m = k_{H_2O} + k_H[H^+] + k_{OH}[OH^-] + k_{NH_4}[NH_4^+].$$

From equations representing the rate constants for experiments 1 and 9, k_{NH_4} was found to be 0.052. By use of this value, k_m was corrected for the catalytic effect of the ammonium ion. The corrected values are given in the right-hand column of table 5 and are plotted in figure 2. It will be seen from the figure that in acid solution the mutarotation is too rapid to measure; with reduction in the oxonium ion concentration the rate decreases to a minimum and then increases. With the assumption that in highly alkaline solution the catalytic effect due to oxonium ion becomes small and may be neglected, the rate constants of experiments 1 and 7 give values of 0.004 and 0.4, respectively, for k_{H_2O} and k_{OH}. Use of these values in equations representing the data from experiments 11 and 12, and solution of the equations, gives for k_H an average value of 6×10^6.

Thus, in the absence of ammonium ion,

$$k_m = 0.004 + 6\times10^6[H^+] + 0.4[OH^-].$$

The dotted curve of figure 2 corresponds to this equation.

It was suggested in [1] that the mutarotations of both the sugars and the glycosylamines take place by several mechanisms. The mechanism of eq 1 was shown to be promoted by acids in general and to be of importance for the mutarotation of both the sugars and the glycosylamines. It was pointed out that a base-catalyzed mechanism such as that of eq 2 is of first importance for the mutarotation of the sugars, but that base catalysis could not be demonstrated in the case of L-arabinosylamine. However, the data of table 5 and figure 2 show that the mutarotation constants of α-D-galactosylamine ammonia complex rise in highly alkaline solution, and hence the over-all change due to the mutarotation and the side reaction is catalyzed not only by acids, but also by hydroxyl ion.

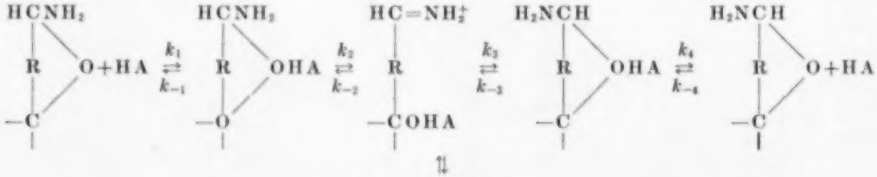

(1)

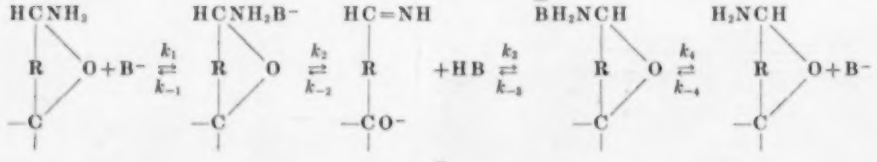

(2)

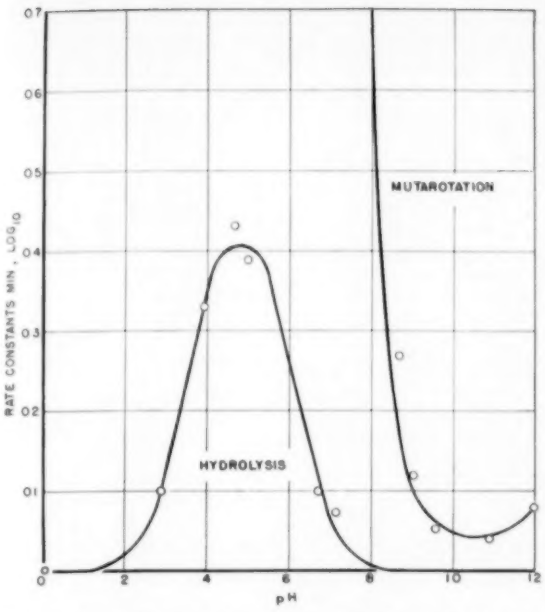

FIGURE 2. *Rate constants for the mutarotation and hydrolysis of α-D-galactosylamine.*

5. Hydrolysis Reaction

To study the hydrolysis of D-galactosylamine, measurements of optical rotation were made largely in the pH range in which equilibrium of the anomeric forms of the amine is established rapidly. Under these conditions, the change in optical rotation can be ascribed exclusively to the hydrolysis reaction, and the rate constant can be obtained by application of the conventional first-order formula:

$$k_{\text{hydrol}}=\frac{1}{t_2-t_1}\log\frac{r_{t_1}-r_\infty}{r_{t_2}-r_\infty},$$

where r_{t_1} and r_{t_2} are the rotations at times t_1 and t_2, respectively, and r_∞ is the specific rotation of the fully hydrolyzed material. The hydrolysis rate constants obtained at various pH levels are given in table 6 and figure 2.

We have shown previously from theoretical considerations [1] that the effect of the oxonium and hydroxyl ion concentrations on the hydrolysis constant should conform to an equation of the type:

$$k_{\text{hydrol}}=\frac{1}{K_1+K_2[H^+]+K_3[OH^-]}.$$

When the data of experiments 15, 18, and 19 were applied to this equation, K_1, K_2, and K_3 were found to be 22.5, 6.16×10^4 and 1.55×10^9, respectively. Thus,

$$k_{\text{hydrol}}=\frac{1}{22.5+6.16\times10^4[H^+]+1.55\times10^9[OH^-]}.$$

The solid curve of figure 2 represents a plot of this expression; the circles represent the experimentally determined rate constants given in table 6. The calculated maximum rate is at pH 4.8.

The data of experiment 16 of table 6 show an effect that requires explanation. The optical rotation of the material on hydrolysis increases to a value higher than the equilibrium value corresponding to the

TABLE 6. *Hydrolysis of α-D-galactosylamine*

[0.5 g α-D-galactosylamine ammonia complex dissolved in sufficient acid, base or buffer to give a volume of 25 ml at 20° C. Solvents are listed with experiment numbers]

Time	$[\alpha]_D^{20}$ [a]	pH	k_{hydrol}
Experiment 1. Water See table 1		10.9	0.00006
Experiment 14. 5 volumes of *M* KH_2PO_4+ 2 volumes *N* NaOH diluted to 10 volumes			
min 15.3 75 150 26 hr	+62.9 72.3 76.9 78.5	7.1	0.007 .007
		Avg.	0.007
Experiment 15. 5 volumes of *M* KH_2PO_4+ 1 volume *N* NaOH diluted to 10 volumes			
10.8 26.6 60.1 20 hr	+64.6 69.3 75.8 80.2	6.7	0.010 .011
		Avg.	0.010
Experiment 16. 5 volumes *N* acetic acid+ 2 volumes *N* NaOH diluted to 10 volumes			
2.2 3.4 6.0 9.8 12.8 32.7 71 90 150	+58.5 60.4 64.8 70.7 74.1 82.0 81.1 80.5 79.7	5.0	0.031 .036 .042 .045
		Avg.	0.039
Experiment 17. 5 volumes of *N* acetic acid +1 volume *N* NaOH diluted to 10 volumes			
1.7 7.5 10.3 18.6 32.3 60 200	+54.9 63.7 67.6 74.3 77.4 76.0 [b] 74.6	4.7	0.037 .042 .051
		Avg.	0.043
Experiment 18. 1 *N* acetic acid			
2.4 10.1 15.1 30.0 60 380 25 hr	+57.5 65.4 68.5 73.9 75.8 75.2 74.6	3.9	0.032 .031 .036
		Avg.	0.033

TABLE 6.—*Hydrolysis of α-D-galactosylamine*—Continued

0.5 g α-D-galactosylamine ammonia complex dissolved in sufficient acid, base or buffer to give a volume of 25 ml at 20° C. Solvents are listed with experiment numbers]

Time	$[\alpha]_D^{20}$ [a]	pH	k_{hydrol}
Experiment 19. 5 *N* acetic acid			
2.4	+62.4	2.9	.....
16.3	67.3		0.011
30.7	69.8		.009
60	74.4		.009
23 hr	79.3		.....
		Avg.	0.010
Experiment 2. 2.5 *N* HCl			
3.0	+63.0	.....	.....
225	63.5	.....	0.00006
22 hr	64.3	.....	.00003
∞	[c] 79.9	.....	.....
		Avg.	0.00004

[a] Expressed on the ammonia-free basis.
[b] Constant.
[c] Calculated rotation for complete hydrolysis.

TABLE 7. *Mutarotation of hydrolysis product* [a] *before and after the addition of α-D-galactose* [b]

Time	Observed rotation, °S	k_m
min		
32.7	+17.31	.....
71	17.12	[c] 0.008
90	16.98	.015
150	[d] 16.93	.....
[e] 200	.....	.....
202.8	+18.22	.....
207.2	18.13	0.020
215.2	18.00	.020
240.3	17.80	.021
260	[d] 17.72	.....

[a] Experiment 16, table 6.
[b] 0.5 g of α-D-galactosylamine ammonia complex in 25 ml of solution. After equilibrium was reached, 0.0170 g of α-D-galactose was added to 20 ml of the solution, and the resulting mutarotation was observed in a 4-dm tube.
[c] As hydrolysis is not entirely complete, the mutarotation constant would be expected to be low and to increase with time.
[d] Constant.
[e] α-D-Galactose added to solution.

sugar presumably formed, and then slowly decreases. A similar drop in rotation was observed in experiments 17 and 18. The phenomenon was studied further by the addition of α-D-galactose to the solution of experiment 16 after hydrolysis had taken place. It will be seen from table 7 that the slow decrease in optical rotation observed in experiment 16 is comparable to that caused by the mutarotation of α-D-galactose in the same solution. The effect is detected only when conditions are such that the rate of hydrolysis is high and the rate of mutarotation of the free sugar is low. Thus it appears that under these conditions the proportion of the alpha pyranose modification of the sugar temporarily exceeds the equilibrium proportion, and that restoration of the equilibrium is accompanied by a decrease in optical rotation. A simple explanation for the effect is that the rate constants for the system

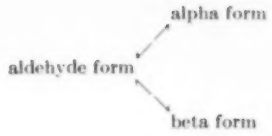

are such that the equilibrium between the aldehyde and the alpha modification is attained more quickly than that between the aldehyde and the beta modification. Thus, the proportion of the alpha form increases until equilibrium is established with the aldehyde, after which the beta form continues to increase at the expense of the alpha until finally all modifications are in equilibrium.

6. Periodate Oxidation of the *N*-Acetyl-D-Galactosylamines

On periodate oxidation, essentially as employed by Niemann and Hays [5] in the study of *N*-acetyl-D-glucosylamine, the specific rotation of *N*-acetyl-α-D-galactosylamine decreased rapidly from the initial value of +194.9° to about +60° and then decreased slowly, whereas the specific rotation of *N*-acetyl-β-D-galactosylamine changed rapidly from +9.8° to about −96°. In each case 2 moles of periodate were consumed rapidly. Both of the oxidation products, after bromine oxidation and hydrolysis, yielded glyceric acid, identified colorimetrically [6]. The consumption of 2 moles of periodate and the identification of a three-carbon fragment after subsequent oxidation and hydrolysis, show that both compounds are pyranoses and hence they must constitute an alpha-beta pyranose pair. Presumably the products having rotations [2] of +60° and −96° are, respectively, D′-acetamido-D-hydroxymethyldiglycolic aldehyde IV and L′-acetamido-D-hydroxymethyldiglycolic aldehyde V. The alpha and beta modifications of all *N*-acetyl-D-aldohexopyranosylamines will give one or the other of these dialdehydes, and the corresponding enantiomorphs will give products whose rotations differ from these merely in direction. Hence the optical rotations of ±60° and ±96° for the products of periodate oxidation can be used for the assignment of ring structure, as well as alpha or beta configuration for any *N*-acetyl-aldohexosylamine.

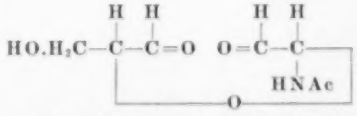

(IV)

D′-Acetamido-D-hydroxymethyl-diglycolic aldehyde.

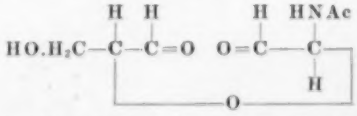

(V)

L′-Acetamido-D-hydroxymethyl-diglycolic aldehyde.

[2] The values +60° and −96° are based on the weight of the original compounds. These correspond to specific rotations of +70° and −112°, respectively, based on the corresponding weights of the resultant dialdehydes.

7. Experimental Details

7.1. α-D-Galactopyranosylamine Ammonia Complex

Forty grams of D-galactose and 1 g of ammonium chloride were suspended in 100 ml of anhydrous methanol, and ammonia was passed into the mixture until dissolution of the material was complete. The solution was stored at room temperature for several days, and finally in the refrigerator for 1 day. The product that crystallized from solution was separated, washed with methanol and dried for 2 hours over sodium hydroxide at reduced pressure. The crude yield was about 35 g, having a specific rotation of +87°. This value is in accord with that reported in [2]. The product was recrystallized by dissolving it in 10 parts of cold 3-percent aqueous ammonia and adding 10 parts of methanol saturated with ammonia at 0° C. The crystals, which formed in the course of a few minutes, were collected on a filter and washed with methanol saturated with ammonia. They were then stored in an atmosphere of ammonia in a desiccator containing sodium hydroxide. Prior to analysis or use, the excess ammonia was removed from the material by evacuation of the desiccator for 15 minutes. On repeated recrystallization $[\alpha]_D^{20}$ rose from +87° to +138° initially (water, $c=5$). Further recrystallization failed to change this value. The product contained approximately 1 mole of ammonia per mole of amine but the composition varied slightly in different preparations, apparently because of the tendency of the ammonia to escape.

Analysis: Calculated for $C_6H_{16}O_5N_2$: C, 36.7; H, 8.2; N, 14.2. Found: C, 36.5; H, 8.4; N, 12.9.

7.2. β-D-Galactopyranosylamine

Storage of α-D-galactosylamine ammonia complex over phosphoric anhydride for several months gave an amorphous residue with a specific rotation of +63°. On dissolution of this material in water, followed by the addition of ethanol to incipient turbidity, a crystalline product formed that appeared to be the same as that of de Bruyn and Van Leent [2]. The material was obtained more readily by dissolving the crude ammonia complex in two parts of warm water, and after half an hour, filtering and adding four parts of methanol and two parts of isopropanol. The large rectangular prisms that separated were washed with methanol and dried over sodium hydroxide. After two crystallizations the compound gave the following analysis: Calculated for $C_6H_{13}O_5N$: C, 40.2; H, 7.3; N, 7.8. Found: C, 40.1; H, 7.4; N, 7.8. $[\alpha]_D^{20}=+62.2°$ (2.1 min, water, $c=2$).

7.3. Pentaacetyl-α-D-Galactopyranosylamine

Ten grams of finely powdered α-D-galactosylamine ammonia complex was added to a previously cooled mixture of 100 ml of pyridine and 50 ml of acetic anhydride in a flask equipped with a mechanical stirrer and immersed in a mixture of ice and salt. Stirring was continued for 3 days in the ice-salt bath and for 1 day at room temperature. The reaction mixture was diluted with several volumes of petroleum ether, which precipitated a sirup. The liquid was decanted and the sirup brought to crystallization by the addition of isoamyl alcohol. The crystals weighed 3.5 g and had a specific rotation of +112°. After several recrystallizations from 95-percent ethanol, the product, pentaacetyl-α-D-galactopyranosylamine, melted at 172° to 173° C; $[\alpha]_D^{20}=+117.4°$ ($CHCl_3$, $c=2$).

Analysis: Calculated for $C_{16}H_{23}O_{10}N$: C, 49.35; H, 5.95; N, 3.60; found: C, 49.6; H, 6.0; N, 3.6.

7.4. Pentaacetyl-β-D-Galactopyranosylamine

Ten grams of ammonia-free galactosylamine of specific rotation +62° was treated with a mixture of pyridine and acetic anhydride as described for the acetylation of the alpha isomer. The amine dissolved in the acetylation mixture in the course of several hours, and the solution was then poured into ice and water. The crystals that formed were separated by filtration, and the aqueous filtrate was extracted with chloroform to recover additional material. The combined yield of crude pentaacetyl-galactosylamine was 18 g, having a specific rotation of +35°. After recrystallization from chloroform with the addition of petroleum ether, and two recrystallizations from ethanol, the product, pure pentaacetyl-β-D-galactopyranosylamine, melted at 173°C. $[\alpha]_D^{20}=+34.7°$ ($CHCl_3$, $c=2$). The constants were unchanged by further recrystallization.

Analysis: Calculated for $C_{16}H_{23}O_{10}N$: C, 49.35; H, 5.95; N, 3.60; found: C, 49.6; H, 6.1; N, 3.6.

7.5. N-Acetyl-α-D-Galactopyranosylamine and N-Acetyl-β-D-Galactopyranosylamine

Both the alpha and beta forms of pentaacetyl-D-galactosylamine were deacetylated by the catalytic barium methylate method [7] in the following manner: Ten grams of the material was dissolved in 100 ml of anhydrous methanol containing 10 ml of 0.4 *N* barium methylate. The mixture was allowed to stand for 1 hr and was then treated with an exactly equivalent amount of 0.4 *N* sulfuric acid. Barium sulfate was removed by filtration of the mixture on a Büchner funnel heavily coated with diatomaceous earth and decolorizing carbon, and the residue was washed with water. The filtrate was concentrated under reduced pressure to a sirup from which the *N*-acetylgalactosylamine crystallized. The crystals were separated and washed with ethanol.

N-Acetyl-α-D-galactopyranosylamine. The crystalline product, obtained from 10 g of pentaacetyl-α-D-galactopyranosylamine by the process outlined above, weighed 5.5 g and had a specific rotation of +193°. After two recrystallizations from warm methanol with the addition of isopropanol, pure *N*-acetyl-α-D-galactopyranosylamine was obtained, $[\alpha]_D^{20}=+194.9°$ (water, $c=2$); mp 179° to 180°C.

Analysis: Calculated for $C_8H_{15}O_6N$: C, 43.43; H, 6.84; N, 6.33. Found: C, 43.5; H, 6.8; N, 6.3.

N-Acetyl-β-D-galactopyranosylamine. The product from 10 g of pentaacetyl-β-D-galactopyranosylamine (5.5 g) having a specific rotation of +10° was recrystallized twice from 20 parts of warm water by concentration in vacuum. The pure material, *N*-acetyl-β-D-galactopyranosylamine, melted at 233° C; $[\alpha]_D^{20} = +9.8°$ (water, $c=2$).

Analysis: Calculated for $C_8H_{15}O_5N$: C, 43.43; H, 6.84; N, 6.33. Found: C, 43.3; H, 6.9; N, 6.2.

7.6. Periodate Oxidation of *N*-Acetyl-α-D-Galactopyranosylamine and *N*-Acetyl-β-D-Galactopyranosylamine.

A 1-g sample of either *N*-acetyl-α-D-galactopyranosylamine or *N*-acetyl-β-D-galactopyranosylamine was dissolved at 20° C in sufficient 0.29 *M* sodium metaperiodate to give a volume of 50 ml, and the course of the oxidation was followed by the change in optical rotation. The results, given in table 8 and figure 3, show that in each case there was a rapid change followed by a slower change. At points near and after the termination of the rapid change, 10-ml aliquots of the solution were pipetted into glass-stoppered flasks containing 20 ml of 0.1 *N* sodium arsenite, 10 ml of a saturated solution of $NaHCO_3$, and 1 ml of a 20-percent solution of KI. After 15 min. the excess arsenite was titrated with 0.1 *N* iodine. In both cases, substantially 2 moles of periodate per mole of *N*-acetylgalactosylamine had been used at the termination of the rapid change.

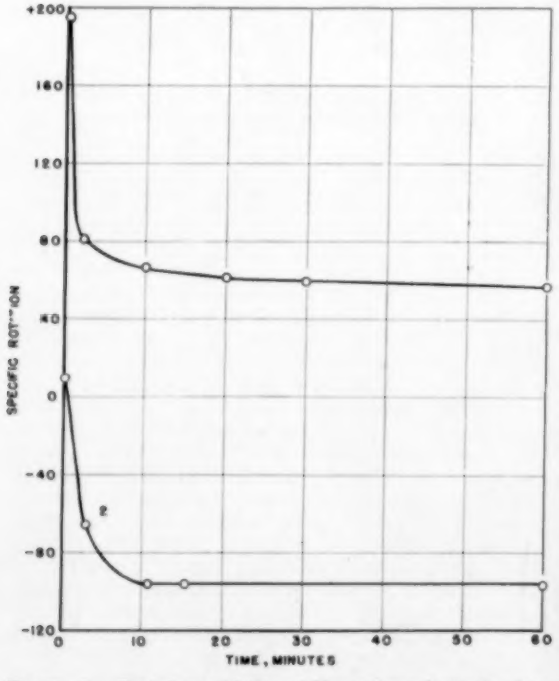

FIGURE 3. *Periodate oxidation of N-acetyl-D-galactosylamines.*
1. N-Acetyl-α-D-galactosylamine; 2. *N*-Acetyl-β-D-galactosylamine.

TABLE 8. *Periodate oxidation of N-acetyl-D-galactosylamines* [a]

Reaction time	Optical rotation		Moles periodate per mole amine
	°S [b]	$[\alpha]_D^{20°}$	
N-acetyl-α-D-galactosylamine			
min			
0	(+22.52)	(+194.9)	.....
2.2	+9.46	+81.4	.....
10.1	7.77	+66.9	.....
20.0	7.07	+60.8	.....
30.0	6.89	+59.3	2.04
60.0	6.59	+56.7	2.04
N-acetyl-β-D-galactosylamine			
0	(+1.13)	(+9.8)	.....
3.0	−7.55	−65.1	.....
10.7	−10.97	−94.5	.....
15.4	−11.13	−95.9	2.04
60.0	−11.07	−95.4	2.04

[a] 1 g of *N*-acetylgalactosylamine in 50 ml of 0.29 *M* sodium metaperiodate.
[b] Read in a 2-dm tube.
[c] Based on the weight of *N*-acetylgalactosylamine.

7.7. Mutarotation and Hydrolysis Measurements

The mutarotation and hydrolysis reactions were followed by measurement of the changes in optical rotation that occurred in solutions of the compounds in water containing known amounts of acids and bases essentially as described in [1]. In each experiment 0.5 g of crystalline amine was placed in a volumetric flask, and sufficient acid, base or buffer solution at 20° C was added to give a volume of 25 ml. Because of the ammonia present in α-galactosylamine ammonia complex, its aqueous solution was highly alkaline. To obtain less alkaline solutions, the substance was dissolved in sufficient aqueous hydrochloric acid to give the quantities of NH_4Cl reported in experiments 10, 11, and 12. In experiments 6 and 9, ammoniacal solutions of NH_4Cl were added to the compounds. The rate constants are expressed in common logarithms and minutes.

8. Summary

A study of the reactions and properties of the products obtained by reaction of ammonia with galactose has revealed that one of the two previously known galactosylamines is a mixture. The crude material, by recrystallization from aqueous ammonia gave an isomer containing 1 mole of loosely bound ammonia, and having a specific rotation of +138°, and the previously known galactosylamine of specific rotation +62.2°. The two modifications of galactosylamine, on acetylation, gave crystalline pentaacetates of specific rotation +117.4° and +34.7°, respectively. By partial deacetylation of the acetates there were obtained two crystalline *N*-acetyl derivatives, namely, *N*-acetyl-α-D-galactopyranosylamine, $[\alpha]_D^{20}$ +194.9°, m. p. 179° to 180° C, and *N*-acetyl-β-D-galactopyranosylamine $[\alpha]_D^{20}$ +9.8°, m. p. 233° C. The *N*-acetyl derivatives, by periodate oxidation and study of the resultant dialdehydes,

were shown to be an alpha-beta pyranose pair. Since a shift in ring structure seems improbable, the corresponding pentaacetates and the parent galactosylamines can be tentatively classified also as pyranoses.

The mutarotation and hydrolysis of the two galactosylamines were studied and found to be in harmony with the mechanisms previously advanced by us. The mutarotation constant for α-D-galactosylamine ammonia complex at various pH levels may be expressed by the following equation:

$$k_m = 0.004 + 6 \times 10^6 [H^+] + 0.4 [OH^-].$$

The hydrolysis of D-galactosylamine, like the previously studied hydrolysis of L-arabinosylamine, takes place rapidly only in a limited pH range. The maximum rate is at pH 4.8, and the rate constant is given by the expression

$$k_{hydrol} = \frac{1}{22.5 + 616 \times 10^4 [H^+] + 1.55 \times 10^9 [OH^-]}.$$

The work establishes experimentally for the first time the existence of the alpha and beta modifications of a glycosylamine. The existence of these compounds supports the interpretation of the mutarotation of the glycosylamines as consisting of the interconversion of alpha and beta isomers. The optical rotations of the new compounds and of the products of periodate oxidation can be used in various ways for the assignment of structures to compounds in this field.

The authors greatly appreciate the assistance of Nancy B. Holt, who made most of the optical measurements and assisted in other experimental work and of Rolf A. Paulson, who analyzed the compounds reported.

9. References

[1] H. S. Isbell and H. L. Frush, J. Research NBS **46,** 132 (1951) RP 2186.
[2] C. A. Lobry de Bruyn and F. H. Van Leent, Rec. trav. Pays-Bas **14,** 134 (1895).
[3] C. A. Lobry de Bruyn and F. H. Van Leent, Rec. trav. Pays-Bas **15,** 81 (1896).
[4] J. N. Brönsted and E. A. Guggenheim, J. Am. Chem. Soc. **49,** 2554 (1927).
[5] C. Niemann and J. T. Hays, J. Am. Chem. Soc. **62,** 2960 (1940).
[6] S. Rapoport, Biochem. Z. **289,** 406 (1937).
[7] H. S. Isbell, BS J. Research **5,** 1179 (1930) RP 253.

WASHINGTON, February 26, 1951

Journal of Research of the National Bureau of Standards Vol. 47, No. 4, October 1951 Research Paper 2249

Near Infrared Absorption Spectra of Deuterated Acetylene

Earle K. Plyler and Norman Gailar

The bands of C_2D_2 at 1.96 and 2.39 microns have been measured under high resolution so that the moments of inertia of this molecule could be compared with that of C_2H_2 and C_2HD. From the measurement of the rotational structure the ground rotational constant, B_0, is found to be 0.8471 cm^{-1}. The center of the $\omega_1+\omega_3$ band is 5097.07 cm^{-1}, and the center of $\omega_2+\omega_3$ is 4190.46 cm^{-1}.

The absorption spectra of C_2H_2 and of C_2HD have been studied in detail, and internuclear distances have been calculated.[1] Inasmuch as further comparisons can be made by a study of C_2D_2, an investigation in the near infrared has been made of this molecule. In the course of this study the results of a similar investigation were made known by Talley and Nielsen.[2] Their B_0 will be compared with ours.

For a given vibrational state, linear molecules have a single moment of inertia, and their rotational fine structure is composed of a series of nearly equally spaced lines. By a comparison of the moments of inertia of the three acetylenes the C—H and C—D distances are, theoretically, calculable. In order to calculate these distances to one part in 10,000, it is required to measure the rotational lines to 0.03 cm^{-1} in the 2-μ region. To approach such accuracy a high resolution instrument that would reproduce spectra faithfully would be required.

These measurements were made on an infrared grating spectrometer, which was constructed at the National Bureau of Standards. A lead sulfide cell was used as the detecting element. The grating was ruled at Johns Hopkins University in the aluminum film on an optically flat quartz blank 9 in. in diameter. The spacing was 15,000 lines/in., and the lines, about 5 in. long, extended over 7½ in. The grating produces very sharp images and is almost free of ghosts. The precision slits and cone bearings for the grating were constructed in the physics shop of the University of Michigan.

The spectrometer with the cover removed is shown in figure 1. In front of the entrance slit is a chopper, which modulates the radiant energy 1,080 times a second. The amplifier is a narrow band pass type and has been described by Nelson and Wilson.[3] The detector is a PbS cell, and with the present arrangement the resolution is about 0.1 cm^{-1} at 2 μ. The optical system is of the conventional design. The radiant energy from the entrance slit, S_1, falls on an off-axis paraboloidal mirror, M_1, which is 7 in. in diameter and 102 cm in focal length. The mirror is 10° off axis and allows the grating, G, to be mounted sufficiently to the side so as not to intercept the incident beam. After the parallel beam falls on the grating, different wavelengths, depending on the grating position, are diffracted back to the paraboloidal mirror. Then this energy is focused on the second slit, S_2, by means of a small plane mirror set at 45° to the impinging beam. After the energy passes through the second slit, another plane mirror is used to cause the radiation to fall on the ellipsoidal mirror, M_2, which focuses the image of the second slit on the PbS cell, D. The image is greatly reduced in size because of the 7 to 1 ratio of the foci of the ellipsoidal mirror.

The source of the energy is a tungsten ribbon filament lamp, drawing about 37 amp and operating at about 2,700° K.

The grating is mounted on a cone bearing and is rotated by means of a worm and gear. Reduction gears allow the spectrum to be scanned at four different speeds. A microswitch, operated by the teeth of one of these gears, activates a pen of the recorder, which places fiducial marks at constant angular intervals. The spectrum is recorded by a Leeds & Northrup Speedomax, type A. Weights are hung on the recorder paper to provide constant tension. The spectrometer is calibrated by superimposing on the record appropriate emission lines known to an accuracy of ±0.01 A or better.

In the 2-μ region this instrument can resolve lines separated by slightly less than 0.1 cm^{-1} when the slit width is 0.02 mm. The centers of absorption lines, when reasonably strong, are reproduced in successive

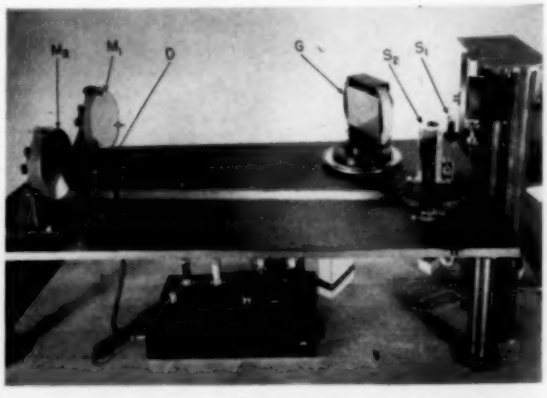

FIGURE 1. *Granting spectrometer.*
The letters refer to the various elements of the instrument.

[1] G. Herzberg, Infrared and Raman spectra of polyatomic molecules, p. 290 to 292 (D. Van Nostrand Co., New York, N. Y., 1945).
[2] R. M. Talley and A. H. Nielsen, Bul. APS **26**, 51 (Feb. 1, 1951).
[3] R. C. Nelson and W. R. Wilson, Proc. Nat. Elec. Conf. **3**, (1947).

runs to about 0.1 cm^{-1}. This will permit calculation of the moment of inertia of C_2D_2 to 1 part in 4,000, but will not allow the detection of any small difference that may exist between the C—D and the C—H distances.

The deuterated acetylene, 3 liters at atmospheric pressure, was obtained from the Atomic Energy Commission. Mass spectrograph tests at the Bureau show that about 94 percent of the gas was C_2D_2. The balance was C_2HD and C_2H_2. The gas was placed in a 60-cm cell with windows of glass. The cell was made from a brass tube 8 cm in diameter.

In analyzing the spectrum of a molecule such as C_2D_2, the ideal procedure would be to study several bands either originating in or ending in a common state averaging the results of several measurements of each band, to minimize random errors. In the present work several factors, short cell lengths, the explosive quality of compressed acetylene, and the limited range of the PbS detector, limited the number of bands that could be used to two. The $\omega_1+\omega_3$ band at 1.96 μ was measured four times, and the $\omega_2+\omega_3$ band at 2.39 μ was measured five times. Each band was measured at several pressures and several grating speeds.

To find the rotational constants and moments of inertia, use was made of the well known relations [4]

$$\Delta_2F(J)=R(J-1)-P(J+1)=4B''(J+\tfrac{1}{2})-8D(J+\tfrac{1}{2})^3 \quad (1)$$

$$R(J)+P(J)=2\nu_0+2B'+2(B''-B')J^2. \quad (2)$$

When D is negligibly small, B'', the lower state rotational constant, can be obtained from the slope of the straight line that results when $\Delta_2F(J)$ is plotted against J. $B'-B''$, the difference between the rotational constants of the upper and lower states, can be found in an analogous manner, as can ν_0, the band origin.

When eq 1 is plotted a straight line results, the slope of which is about 3.5 cm^{-1}. This approximate value is now used in the plot of $\Delta_2F(J)-3.5(J+\frac{1}{2})$ against J. This, too, results in a straight line of slope m, and B' can be found from the relation

$$B'=(3.5-m)/4. \quad (3)$$

The results of this investigation are presented in figures 2 to 4 and in table 1. Figure 2 is a reproduction of the $\omega_2+\omega_3$ band (with three of the kyrpton emission lines that establish the calibration). The intensity of the absorption lines of C_2D_2 shows the 2:1 alternation pattern expected of molecules that follow Bosé statistics. Faint indications can be seen of a superimposed band of a higher state. Figure 3 is a reproduction of the $\omega_1+\omega_3$ band. Two C_2HD bands [5] are present and prevent the 2:1 intensity ratio from being observed. In the P branch, however, at $J=19$ to 24 this intensity ratio is noticeable.

In analyzing the spectra, values of $\Delta_2F(J)$ from the nine records were averaged and the results are tabulated in column 1 of table 1. This average value, divided by $J+\frac{1}{2}$, appears in column 2. Column 3 presents the value of $\Delta_2F(J)-3.5(J+\frac{1}{2})$. Figure 4 is a plot of this value against J. Two lines are drawn through the values of $\Delta_2F(J)-3.5(J+\frac{1}{2})$ representing the minimum and maximum probable slope. Line A results in $B_0=0.8470$ cm^{-1}; line B in $B_0=0.8473$ cm^{-1}. Taking the mean of the values

[4] G. Herzberg, Infrared and Raman spectra of polyatomic molecules, chap. IV (D. Van Nostrand Co., New York, N. Y., 1945)

[5] F. Stitt, J. Chem Phys. 8, 56 (1940).

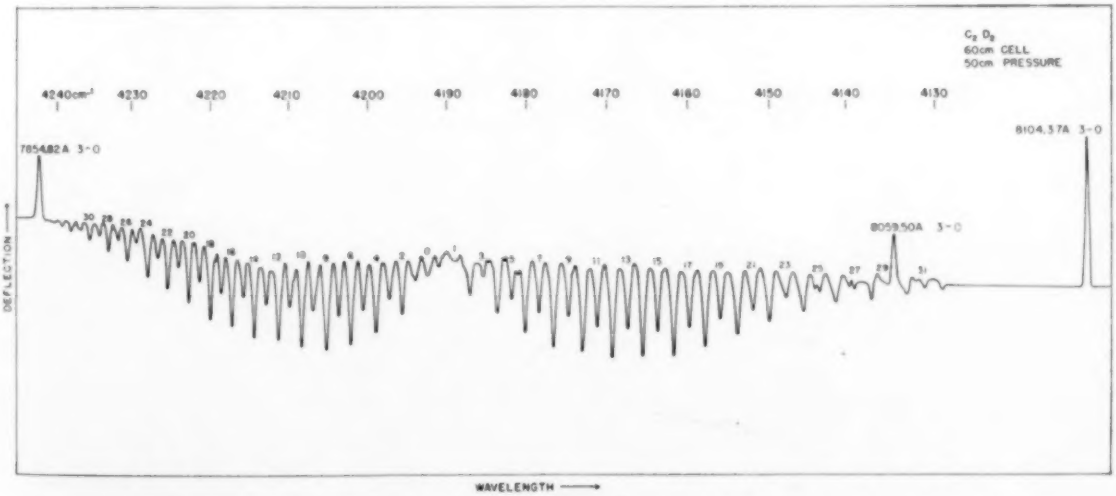

FIGURE 2. *Absorption spectrum of the $\omega_2+\omega_3$ band of C_2D_2 at 2.39 μ, $\nu_0=4190.46$ cm^{-1}.*

The numbers accompanying the various absorption lines are the J numbers of the lines. The three emission lines are Kr lines.

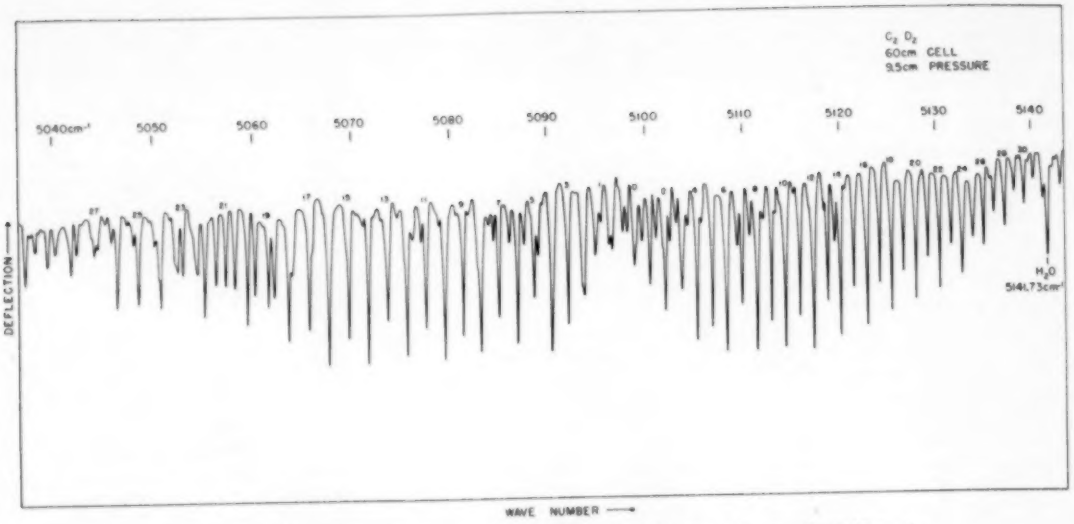

FIGURE 3. *Absorption spectrum of the $\omega_1+\omega_3$ band of C_2D_2 at 1.96 μ, ν_0=5097.07 cm^{-1}.*

The numbers accompanying the various absorption lines are the J numbers of the lines.

TABLE 1. *Measured values of quantities used in determination of B_0 for the J values from 1 through 30*

J	$\overline{\Delta_2 F(J)}$ = Average $R(J-1)-P(J+1)$	$\overline{\frac{\Delta_2 F(J)}{J+\frac{1}{2}}}$	$\Delta\nu=\Delta_2 F(J)-3.5(J+\frac{1}{2})$	$\Delta\nu-$ average $\Delta\nu$
	cm^{-1}	cm^{-1}	cm^{-1}	cm^{-1}
1	5.11	3.407	−0.14	−0.02
2	8.50	3.400	−.16	+.09
3	11.90	3.400	−.35	0
4	15.31	3.402	−.44	+.04
5	18.66	3.393	−.59	+.01
6	22.01	3.386	−.74	−.04
7	25.34	3.379	−.91	−.10
8	28.79	3.387	−.96	0
9	32.15	3.384	−1.10	−.04
10	35.54	3.385	−1.21	−.04
11	38.95	3.387	−1.30	0
12	42.39	3.391	−1.36	+.04
13	45.70	3.385	−1.55	−.02
14	49.13	3.388	−1.62	+.01
15	52.49	3.386	−1.76	0
16	55.91	3.388	−1.84	+.01
17	59.32	3.390	−1.93	+.04
18	62.65	3.386	−2.10	−.01
19	66.05	3.387	−2.20	0
20	69.44	3.387	−2.31	+.01
21	72.89	3.390	−2.36	+.08
22	76.20	3.387	−2.55	0
23	79.64	3.389	−2.61	+.06
24	83.04	3.389	−2.71	−.04
25	86.31	3.385	−2.94	−.04
26	89.78	3.388	−2.62	+.40
27	93.07	3.384	−3.18	−.06
28	96.46	3.384	−3.29	−.04
29	99.84	3.384	−3.41	−.05
30	103.22	3.384	−3.53	−.06

of $\Delta_2 F(J)/(J+\frac{1}{2})$ in column 2 of table 1 yields a value of B_0=0.8469 cm^{-1}. Averaging these three values of B_0 gives the results B_0=0.8471 ± 0.0003 cm^{-1}. Column 4 of table 1 shows the deviation of the individual values of $\Delta_2 F(J)-3.5(J+\frac{1}{2})$ from the values indicated by the resultant B_0=0.8471 cm^{-1}. This value can be compared with that of B_0=

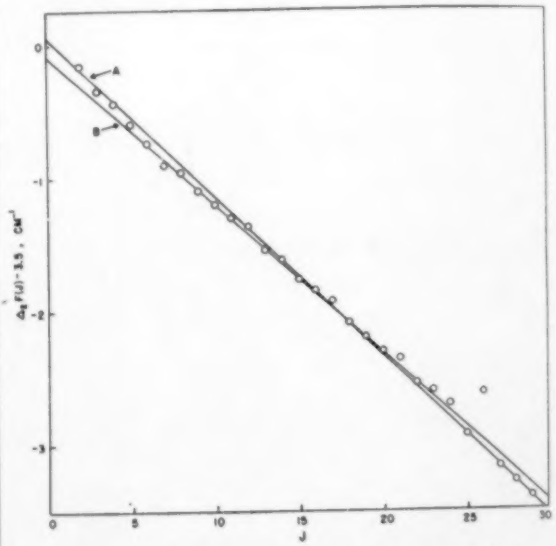

FIGURE 4. *Plot of $\Delta_2(J)-3.5(J+\frac{1}{2})$ as a function of J values.*

Lines A and B are the minimum and maximum probable slopes.

0.84827 cm^{-1} reported by Talley and Nielsen (see footnote 2).

To calculate internuclear distances, the value of B_e, the equilibrium rotation constant, is necessary. From B_e can be found the various r_e's, the equilibrium distances. To find B_e, however, each normal mode must be represented at least once in the bands studied; we cannot find B_e from the two bands studied.

The equilibrium distances C−H and C−D should be equal, with a slight variance for the zero-order state. If this variance is ignored, the zero-order distances reported by Herzberg (see footnote 3) can be used to calculate a B_0. This has a value of 0.8474 cm^{-1}.

Again ignoring the difference between r_0 of C−H and r_0 of C−D, our value of B_0 can be combined with that for C_2H_2 of Herzberg (see footnote 3) to find the internuclear zero state distances. The values of the distances are C−D and C−H $=1.0611\times10^{-8}$ cm, and C≡C$=1.2067\times10^{-8}$ cm. Combining the B_0 of C_2HD of Herzberg (see footnote 3) with our C_2D_2 value gives C−H and C−D $=1.0630\times10^{-8}$ cm and C≡C$=1.2054\times10^{-8}$ cm. When the values of the constants of C_2H_2 and C_2HD are used, one finds C−H and C−D$=1.0595\times10^{-8}$ cm and C≡C$=1.2073\times10^{-8}$ cm. Theoretically, the rotational constants of C_2H_2, C_2HD, and C_2D_2 can be used to solve for the values of the three internuclear distances C≡C, C−H, and C−D; unfortunately, the precision of measurement of these constants is not sufficient to detect any differences between C−H and C−D distances.

The upper state rotational constants were found by plotting eq 2. They are:

$$B_{10100}=0.8574\pm0.0003\ cm^{-1},$$

$$B_{01100}=0.8547\pm0.0003\ cm^{-1}.$$

The centrifugal stretching has been ignored, as it is negligible. The effect on the value of $[\Delta_2F(J)-3.5(J+\frac{1}{2})]/(J+\frac{1}{2})$ would be equal to $8(J+\frac{1}{2})^3D$, where $D=4B^3(\delta_1/\omega_1^2+\delta_2/\omega_2^2)$ and where $\delta_1^2+\delta_2^2=1$.[6] The largest possible value of D would be for $\delta_1=0$ and $\delta_2=1$. Thus $D=4\times.85^3\times1/1760^2\simeq10^{-6}$, and for $J=30$, the centrifugal stretching $\leq8\times27{,}000\times10^{-6}\simeq0.014$ cm^{-1}. This is much less than the experimental error.

WASHINGTON, March 20, 1951

[6] W. Schaffer and A. Nielsen, J. Chem. Phys. **9**, 847 (1941).

Journal of Research of the National Bureau of Standards Vol. 47, No. 4, October 1951 Research Paper 225

Spectrophotometric Determination of Bismuth in Lead-Base and Tin-Base Alloys

Bruce B. Bendigo, Rosemond K. Bell, and Harry A. Bright

A method is described for the determination of bismuth in lead-base and tin-base alloys. Tin, arsenic, and antimony are volatilized as the bromides from a perchloric acid solution. The bismuth is then precipitated as the oxychloride in a perchloric-nitric acid solution. The precipitate is dissolved in nitric acid, and the bismuth is treated with thiourea to form a yellow complex. The absorbancy of the colored solution is measured with a filter photometer at approximately 425 millimicrons, and the amount of bismuth is read from a curve prepared by treating known amounts of bismuth with thiourea. An accuracy of ±0.002 percent of bismuth is indicated for lead-base and tin-base alloys containing from 0.02 to 0.10 percent.

1. Introduction

Bismuth in lead-base and tin-base alloys can be precipitated as the oxychloride or as the carbonate, subsequent to an alkali-sulfide treatment to remove tin, antimony, and arsenic. This method is not satisfactory in accurate work because bismuth sulfide is slightly soluble in alkali sulfides or in mixtures of the alkali sulfides and hydroxides [1].[1] If there is an appreciable amount of lead sulfide, as with lead-base alloys, some insoluble lead sulfate is usually formed when the sulfide precipitate is treated with nitric acid or a mixture of hydrochloric and nitric acids, and this interferes in the subsequent determination of bismuth.

The internal electrolysis method [2] has been used to separate bismuth and copper in solutions of lead-base and tin-base alloys. By this method the deposition of bismuth in a lead-base alloy is incomplete unless the amount of copper equals or exceeds that of bismuth, and there is considerable difficulty in obtaining adherent deposits of bismuth and copper in tin-base alloys, probably because of the hydrofluoric acid required to keep the tin in solution.

Tin, antimony, and arsenic can be removed as the volatile bromides from a sulfuric acid solution [3]. However, the solubility of tin in concentrated sulfuric acid makes it difficult to determine when all of the tin has been removed. In alloys containing considerable lead, low values for bismuth may be obtained as some bismuth is carried down with the lead sulfate [1].

After the removal of the tin, antimony, and arsenic by any of these methods, the bismuth may be precipitated as the oxychloride and the precipitate weighed, or bismuth may be precipitated as the carbonate, ignited, and weighed as bismuth trioxide, Bi_2O_3, or the precipitate of bismuth oxychloride, BiOCl, may be dissolved in a suitable acid and bismuth determined photometrically. Mahr [4] developed a thiourea-photometric method in which a soluble yellow bismuth-thiourea complex is formed. A modification of this method was proposed by Tompsett [5].

A tentative ASTM standard, E46–50T, [6] for the determination of bismuth in lead-base and tin-base solder metal and white-metal bearing alloys, calls for the separation of tin, antimony, and arsenic as the volatile bromides from a perchloric-phosphoric acid solution and the measurement of the absorbancy of the bismuth-thiourea complex in the residual solution at approximately 440 mμ. However, if copper exceeds the maximum permissible limit of 0.5 percent, this method cannot be used.

The limitations of these several methods led to the development of the procedure described in section III. In the proposed method the sample is dissolved in a mixture of hydrobromic acid and bromine, nitric and perchloric acids are added, and tin, antimony, and arsenic are removed as the volatile bromides. Bismuth in the residual solution is precipitated as the oxychloride. The precipitate is dissolved in nitric acid, and the bismuth is determined photometrically with thiourea at approximately 425 mμ.

2. Apparatus and Reagents

2.1. Apparatus

A photoelectric colorimeter of the Fisher type was used in this work. The absorption cells were matched test tubes (approximately 20 mm in diameter and 80 mm long). Measurement of the absorbancy of the solution was made with a filter having an absorption peak at approximately 425 mμ.

2.2. Reagents

Hydrobromic acid-bromine mixture. Add 10 ml of bromine to 100 ml of hydrobromic acid (48%).

Dilute nitric acid (1+1). Add 500 ml of nitric acid (sp gr 1.42) to 500 ml of water.

Hydrobromic acid (48%).

Dilute ammonium hydroxide (1+2). Add 100 ml of ammonium hydroxide (sp gr 0.9) to 200 ml of water.

Dilute hydrochloric acid (1+9). Add 10 ml of hydrochloric acid (sp gr 1.18) to 90 ml of water.

Thiourea solution (5%). Dissolve 5.00 g of thiourea, $(NH_2)_2CS$, in water. Dilute to exactly 100 ml and filter without washing. Prepare this solution daily as needed.

[1] Figures in brackets indicate the literature references at the end of this paper.

Standard bismuth nitrate solution (1 ml=0.1 mg Bi). Transfer 0.1000 g of high-purity bismuth to a 250-ml beaker and add 10 ml of dilute nitric acid (1+3). Heat gently to dissolve the sample and to expel brown fumes. Cool, transfer to a 1-liter volumetric flask, and dilute to the mark with dilute nitric acid (1+9).

3. Procedure

The weight of sample taken for analysis should be such that the bismuth content is approximately 1 to 10 mg. The optimum weight of bismuth is from 2 to 5 mg. Transfer the sample to a 250-ml wide-mouthed Erlenmeyer flask and, in a well-ventilated hood, add the hydrobromic acid-bromine mixture. For a 2-g sample use approximately 25 ml of the mixture and for 7 g use approximately 60 ml. Carry a blank through all of the operations of the procedure. Cover the flask and heat gently, avoiding excessive loss of bromine, until the sample is in solution. Cool, add 5 ml of dilute nitric acid (1+1), and cover. Heat gently until a reaction begins, indicated by effervescence, and then remove from the heat. Cool, add 15 to 25 ml of perchloric acid (70%) [2] and heat over a free flame with constant rotation until the perchloric acid refluxes on the wall of the flask.[3] Cool, wash the wall of the flask with 10 ml of hydrobromic acid and continue the heating and agitation until the perchloric acid refluxes as before. If the solution is turbid, continue the addition of hydrobromic acid and the heating until a clear solution is obtained, which indicates complete expulsion of tin, antimony, and arsenic. Cool, add 25 ml of water and 10 ml of dilute nitric acid (1+1). If the solution is turbid at this point, heat until the solution clears. Transfer the solution to a 600-ml beaker and dilute to approximately 100 ml.

Add dilute ammonium hydroxide (1+2) drop by drop from a burette while constantly stirring the solution until a faint opalescence appears or until the solution is slightly alkaline, as indicated by litmus paper. If a precipitate separates, dissolve it in dilute nitric acid (1+4) and carefully repeat the neutralization with dilute ammonium hydroxide (1+2) until a faint opalescence appears. If no turbidity is visible when the solution is alkaline, add dilute nitric acid (1+4) until the solution is faintly but distinctly acid. Then add 5 ml of dilute hydrochloric acid (1+9), dilute the solution to 400 ml with hot water, heat just to boiling, and let stand on a steam bath for 2 to 3 hours, or preferably overnight. Filter on a tight paper containing a little paper pulp and wash once with a small portion of hot water.[4] Dissolve the precipitate in 25 ml of hot dilute nitric acid (1+2) and transfer the clear solution to a 100-ml volumetric flask. Cool to room temperature, dilute to the mark, and mix.

Transfer a 10-ml aliquot portion of the solution to a 50-ml volumetric flask.[5] Add 10 ml of dilute nitric acid (1+5) and 15 ml of water and mix. Add 10 ml (±0.1 ml) of the thiourea solution, dilute to the mark, and mix thoroughly. Immediately transfer a suitable portion of the solution to the absorption cell and measure the transmittancy or absorbancy at approximately 425 mμ, using water in another cell as a reference solution for 100-percent transmittancy or zero absorbancy.

The amount of bismuth is obtained from a standard curve prepared as follows: To five 50-ml volumetric flasks transfer 1.0, 3.0, 5.0, 7.0, and 10.0 ml of the standard bismuth solution and carry a sixth flask through the procedure as a blank. Add 5 ml of the dilute nitric acid (1+1), dilute to 35 ml, and add 10 ml (±0.1 ml) of the thiourea solution. Dilute to the mark and mix thoroughly. Measure the transmittancy or absorbancy of the solution as directed for the analysis sample. Plot the absorbancy, A, against the respective concentrations on ordinary graph paper, or concentration, C, against transmittancy on semilogarithmic paper, using the semilog scale for the percentage, T, values. The results obtained with a series of known amounts of bismuth are shown graphically in figure 1.

As the color of the bismuth-thiourea complex has a significant temperature coefficient, the temperature at which the absorbancy measurements of the test solutions and standards are made should not vary more than 2° C.

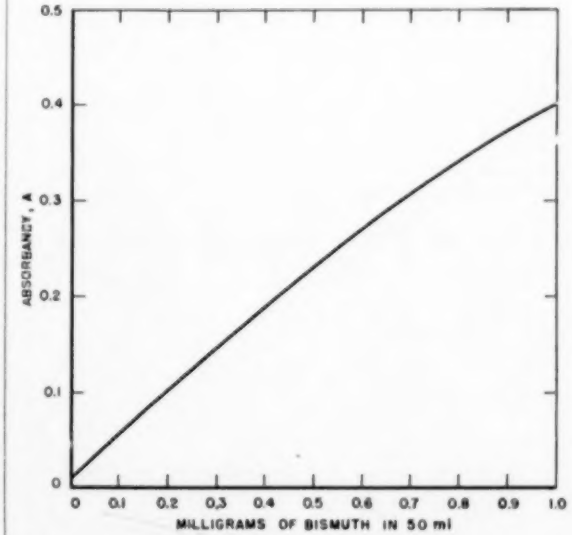

FIGURE 1. *Absorbancy-concentration curve of bismuth-thiourea complex at 425mμ.*

[2] At the temperature used in this work perchloric acid is a powerful oxidizing agent and may therefore react with explosive violence if it comes in contact with certain reducing substances, such as organic matter.

[3] When large amounts of lead are present bumping may occur, and the conversion of lead bromide to lead perchlorate should be done cautiously. If too much perchloric acid is expelled before complete removal of tin, more perchloric acid should be added.

[4] If the iron exceeds 1 mg it interferes when the color of the bismuth-thiourea complex is formed. If necessary, iron may be separated from bismuth at this point by dissolving the precipitate in hydrochloric acid and treating the solution with hydrogen sulfide.

[5] If desired, aliquot portions of other size may be used, provided the amount of bismuth and the acidity of the final solutions are within the recommended ranges.

4. Results

The results shown in table 1 indicate the accuracy that can be expected when the complete recommended procedure is applied to known amounts of bismuth.

The data in table 2 indicate the results obtained by applying the recommended procedure to solutions containing known amounts of bismuth, together with other elements likely to be present in lead-base and tin-base alloys.

TABLE 1. *Results obtained by applying the recommended procedure to known amounts of bismuth*

Bismuth		
Present	Found	Difference
mg	*mg*	*mg*
1.00	0.95	−0.05
1.00	.95	−.05
5.01	5.00	−.01
5.01	4.90	−.11
10.03	9.80	−.23
10.03	9.86	−.17
[a] 10.03	9.90	−.13
[a] 10.03	9.80	−.23

[a] In these experiments 5-ml aliquot portions were taken instead of 10 ml.

TABLE 2. *Results obtained for bismuth in solutions approximating the composition of lead-base and tin-base alloys*

Bismuth			Tin	Lead	Copper	Antimony
Added	Found	Difference				
mg	*mg*	*mg*	*mg*	*mg*	*mg*	*mg*
[a] 10.03	9.90	−0.13	860	20	50	70
[a] 10.03	10.00	−.03	860	20	50	70
[a] 10.03	10.00	−.03	860	20	50	70
[b] 10.03	10.00	−.03	860	20	50	70
[b] 10.03	10.15	+.12	860	20	50	70
[b] 10.03	10.15	+.12	860	20	50	70
[c] 10.03	9.85	−.18	50	850	5	100
[c] 10.03	9.85	−.18	50	850	5	100
[c] 10.03	9.90	−.13	50	850	5	100
[d] 10.03	9.95	−.08	50	850	5	100
[d] 10.03	10.00	−.03	50	850	5	100
[d] 10.03	10.00	−.03	50	850	5	100

[a] Set 1. [b] Set 2. [c] Set 3. [d] Set 4.

TABLE 3. *Results obtained for bismuth in tin-base and lead-base alloys*

Material	Weight of sample	Bismuth			
		Certificate value	Found	Number of determinations	Range
	g	*Percent*	*Percent*		*Percent*
Tin-base bearing metal, NBS Standard Sample 54c [a]	7	0.028	0.026	9	0.025 to 0.027
Solder, NBS Standard Sample 127 [b]	5	.041	.041	9	.039 to .043
Lead-base bearing metal, NBS Standard Sample 55c [c]	4	.093	.091	7	.090 to .091

Approximate percentages of other constituents:
[a] 86 Sn; 7 Sb; 4 Cu; 2 Pb.
[b] 64 Pb; 35 Sn; 0.7 Sb; 0.1 As.
[c] 84 Pb; 10 Sb; 5 Sn; 0.2 Cu.

The data in table 3 indicate the results obtained by applying the recommended procedure to standard samples of tin-base and lead-base alloys.

5. Discussion

Volatilization of tin, antimony, and arsenic as the bromides from a perchloric acid solution [3] offers several advantages over volatilization of these elements from a sulfuric acid solution. With perchloric acid, incomplete removal of tin and antimony is indicated by the turbidity of the solution, and the residual lead forms a soluble perchlorate. If the determination or separation of lead is desired, sulfuric acid may be added to the filtrate from the bismuth oxychloride and the solution heated until copious fumes of sulfuric acid appear, to remove the perchloric acid and to precipitate lead sulfate. Copper, nickel, and zinc in the filtrate from the lead sulfate may be determined by suitable methods.

No evidence was found in this work that bismuth was volatilized as the bromide when perchloric-hydrobromic acid solutions containing 1 to 10 mg of bismuth were heated to about 200° C. The color reaction produced by thiourea with bismuth is not sensitive enough to determine with certainty less than 10 μg of bismuth in a volume of 50 ml. If nitric acid is not present when bismuth is precipitated as the oxychloride in a perchloric acid solution containing lead, an insoluble lead compound will separate. The addition of a small amount of nitric acid prevents the formation of the insoluble lead compound and permits a quantitative separation of bismuth from lead.

Tests of a number of the filtrates from the bismuth oxychloride separation indicated slight, but practically negligible, amounts of bismuth. For example, 30, 10, and 10 μg of bismuth were found in the filtrates [6] when 1, 5, and 10 mg of bismuth were precipitated as the oxychloride.

The presence of 10 mg of silver, 3 mg of copper, and 0.1 mg of iron added as nitrates to 0.2 mg of bismuth as nitrate in a volume of 50 ml does not interfere in the color development of the bismuth-thiourea complex. These amounts of silver and copper are greater than those encountered ordinarily in the nitric acid solution of the precipitate of bismuth oxychloride. When more than 1 mg of iron is present in the bismuth oxychloride precipitate, the iron must either be removed, or the ferric iron reduced to the ferrous state [4] before the bismuth-thiourea color is developed. There is no interference in the development of color when 0.25 mg of chlorine as hydrochloric acid is added to 0.2 mg of bismuth as bismuth nitrate in a volume of 50 ml (1 mg of bismuth as bismuth oxychloride contains 0.17 mg of chlorine).

The optimum concentration of nitric acid for the development of the yellow color is in the range from 2 to 10 percent by volume [4]. In the described procedure approximately 5 percent by volume of nitric acid is used.

[6] The filtrates were extracted with a carbon tetrachloride solution of dithizone, and bismuth was determined photometrically with thiourea.

In the recommended procedure all the added thiourea is available for complexing with the bismuth, because the bismuth is isolated from the heavy metals, which also form complexes with thiourea. An attempt was made to determine if there is a minimum amount of thiourea above which the absorbancy of the bismuth-thiourea color is independent of the concentration of the thiourea. Absorption curves were obtained with a Cary Recording Spectrophotometer on five solutions each containing 2.0 mg of bismuth and from 0.25 to 2.5 g of thiourea in 100 ml of dilute nitric acid (5+95). It was found that the absorbancy, at 425 mμ, of the bismuth-thiourea color in dilute nitric acid (5+95), is relatively independent of the thiourea concentration when the solution contains 1 percent or more of thiourea. However, for accurate work it is recommended that a pipette be used to measure the volume of the thiourea solution.

A few comparison absorbancy curves, obtained by John H. Gould with the Cary Recording Spectrophotometer, of the bismuth-thiourea color in dilute nitric acid (5+95) and in perchloric-phosphoric acids [6] showed that the shape of the absorption curve is dependent on the particular acid medium in which the colored complex is developed.

6. References

[1] W. F. Hillebrand and G. E. F. Lundell, Applied inorganic analysis, p. 188 (J. Wiley and Sons Inc., New York, N. Y., 1929).
[2] Beverly L. Clarke, L. A. Wooten, and C. L. Luke, Ind. Eng. Chem., Anal. Ed. **8**, 411 (1936).
[3] J. I. Hoffman and G. E. F. Lundell, J. Research NBS **22**, 465 (1939) RP1198.
[4] C. Mahr, Z. Anal. Chem. **94**, 161 (1933); **97**, 96 (1943).
[5] S. L. Tompsett, Analyst **63**, 250 (1938).
[6] ASTM Methods of chemical analysis of metals (Am. Soc. Testing Mat., Philadelphia, Pa., 1950).

Washington, March 14, 1951.

Journal of Research of the National Bureau of Standards Vol. 47, No. 4, October 1951 Research Paper 2251

Calorimetric Properties of Benzoic Acid from 0° to 410° K

George T. Furukawa, Robert E. McCoskey, and Gerard J. King

Heat capacity, enthalpy, and entropy of benzoic acid (C_6H_5COOH) are tabulated from 0° to 410° K, using experimental heat capacities obtained by means of an adiabatic vacuum-type calorimeter. The heat of fusion was measured to be 18,000 ±100 abs j mole^{-1}. The standard entropy, heat, and free energy of formation of benzoic acid at 298.16°K are calculated.

1. Introduction

For many years benzoic acid (C_6H_5COOH) has been issued by the National Bureau of Standards as a standard for acidimetry and for determining the energy equivalent of combustion bomb calorimeters. More recently this material has been used in standard thermometric cells in which its liquid-solid equilibrium temperature is used as a reference for thermometer calibration. At the meeting on April 21, 1948, the Low Temperature Calorimetry Conference,[1] which was organized for the purpose of promoting improved calorimetric techniques and setting up standards for testing and calibrating calorimeters of various designs, selected benzoic acid along with synthetic sapphire (α-aluminum oxide) and normal heptane as standards for the intercomparison of precision heat-capacity calorimeters in the temperature ranges from 10° to 350°K, 10° to 1,800° K, and 10° to 300°K, respectively. The three materials were prepared and packaged in suitable quantities at this Bureau and are of sufficient purity and uniformity that errors arising from these sources are well within the precision of experimental measurements.

The benzoic acid for the Calorimetry Conference was purified by procedures similar to those used in the preparation of the benzoic acid for the thermometric standard cells issued by this Bureau. The purity of this material is 99.997 mole percent, as calculated from the freezing curve. The purity of benzoic acid Standard Sample 39g, presently issued for acidimetry and for the calibration of the combustion-bomb calorimeters, is 99.99 weight percent, as determined by titration. Considering the high purities, the authors believe that within the accuracy with which calorimetric measurements can now be made the calorimetric properties of these two samples are the same. In this paper there are presented the results of the measurements, with an adiabatic vacuum-type calorimeter, of the heat capacity and the heat of fusion of the sample of benzoic acid prepared for distribution by the Calorimetry Conference. The enthalpy and entropy have been calculated from the results of the measurements, and these properties are tabulated from 0° to 410°K. The calorimetric measurements above 395°K, as indicated in the following sections, are less accurate due to a slight chemical reaction of benzoic acid with the container.

[1] The Low Temperature Calorimetry Conference was renamed the Calorimetry Conference at the meeting held on Sept. 5, 1950.

2. Experimental Procedure

2.1. Apparatus and Method

This investigation on benzoic acid was carried out with an adiabatic vacuum-type calorimeter similar to that used with diphenyl ether [1].[2] Since details of the design and operation of a similar calorimeter are given in the paper on 1,3-butadiene by R. B. Scott, et al. [2], only a brief account will be given. The sample was sealed in a copper container and suspended inside an adiabatic shield system. A series of heat-capacity experiments was made over the temperature range 13° to 410° K. After making the so-called curvature correction, which transforms observed values, $\Delta Q/\Delta T$, to the desired values, dQ/dT, these were plotted on a large scale as deviations from an approximate empirical equation. A smooth curve was drawn through the deviation points, and the heat-capacity values were obtained at equally spaced integral temperatures from this deviation curve combined with the approximate empirical equation. Similar heat-capacity experiments were made with the empty container, and the data obtained were treated in the same manner. The net heat capacities were computed by subtraction, using the smoothed tabulated values for the two sets of measurements at the corresponding temperatures. The vaporization correction is negligible for benzoic acid in the temperature range reported in this paper.

2.2. Sample

The benzoic acid sample for the Calorimetry Conference was prepared by F. W. Schwab[3] of this Bureau. Details of the purification by fractional crystallization and the subsequent removal of water and air are given in previous publications [3, 4]. The final treatment for the purification and the purity tests was carried out in thermometric cells similar to those described in one of the references cited [4]. The molten benzoic acid was transferred into platinum dishes and allowed to solidify in

[2] Figures in brackets indicate the literature references at the end of this paper.
[3] Deceased.

a dessicator containing phosphorus pentoxide in order to prevent absorption of moisture from the atmosphere. The solid benzoic acid thus obtained was crushed and sieved; the particle sizes between number 10 and 50 sieves were thoroughly mixed and bottled in 70-g units. All units are considered to have a purity and identity well within the precision of heat-capacity measurements. The purity of this material from freezing-temperature studies was calculated to be 99.997 mole percent [5]. In order to determine whether the crushing and sieving processes would introduce any impurities, a crushed sample of benzoic acid was sieved 20 times. Spectrographic analysis by B. F. Scribner of this Bureau showed an increase of five parts per million of metallic impurities. It is considered, therefore, that a single sieving would introduce negligible amounts of impurities.

A sample (79.2409-g mass) of benzoic acid from two units was sealed in a copper container under pressure of helium of about 0.2 atm (0.0020 g). All heat-capacity experiments were completed below 320° K before the material was heated above this temperature for any further heat-capacity experiments or for the determination of the heat of fusion and purity by melting-temperature studies. This precaution was taken because the tests at 100° C performed by F. W. Schwab indicated that benzoic acid reacts slightly with copper and tin. The sample container, as described in the references cited [1, 2], is constructed with copper and coated with tin on the inside.

3. Results

3.1. Heat-Capacity Results

The heat capacity of the empty container was measured from 14° to 386° K. The deviation of individual experiments from the smoothed heat capacities is shown in figure 1. The heat capacities of the container plus benzoic acid were measured over the temperature range 13° to 410° K. The deviations of the experimental values from the smoothed heat capacities are given in figures 2 and 3. The deviation boundary of ±0.05 percent in the solid range and ±0.25 percent in the liquid range are expressed in terms of net heat capacities. The precision of ±0.02 percent obtained with the empty container arises from the high net heat capacity. The smoothed heat-capacity values of the empty container were extrapolated from 385° to 410° K in order to obtain the net heat capacities in this range. It is believed that the error in the extrapolation is less than the experimental precision. The heat capacity of benzoic acid was extrapolated below the experimental temperature range to 0° K by means of the Debye function,

$$C_{sat.} = 38.97 D\left(\frac{116.1}{T}\right), \qquad (1)$$

which was fitted to the experimental values at 14°, 18°, and 22° K. The heat-capacity values are tabulated in table 1 at intervals of 2 deg from 0° to 50° K and at intervals of 5 deg from 50° to 410° K.

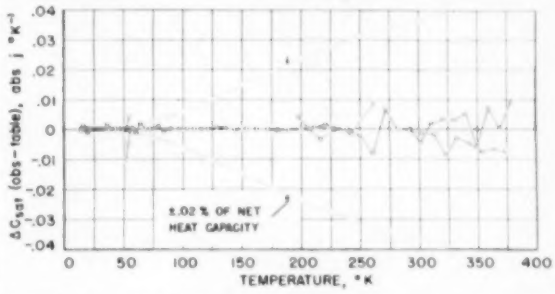

FIGURE 1. *Deviations of the experimental heat capacities (corrected for curvature) from smoothed values for the empty container.*

Experiments in a single series are connected by lines.

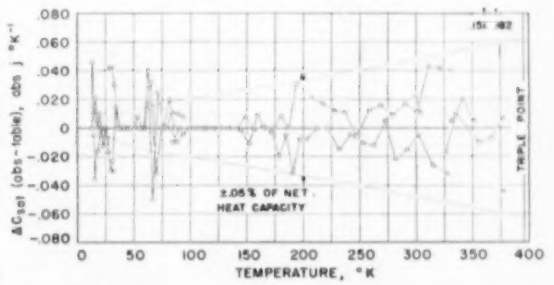

FIGURE 2. *Deviations of the experimental heat capacities (corrected for curvature) from smoothed values for the container plus benzoic acid in the solid range.*

Experiments in a single series are connected by lines. The heat-capacity experiments after melting are indicated by ⊖.

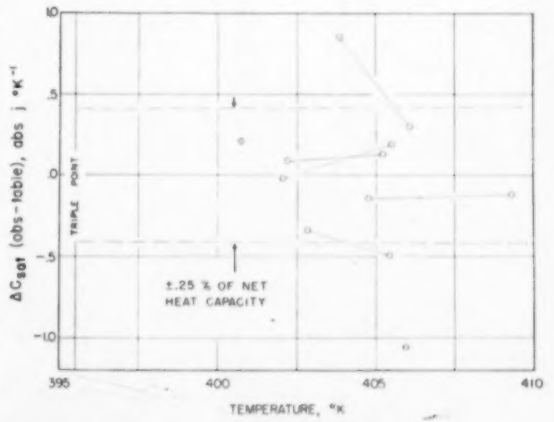

FIGURE 3. *Deviations of the experimental heat capacities from smoothed values for the container plus benzoic acid in the liquid range.*

Experiments in a single series are connected by lines. The points indicated by ⊕ and ⊖ are single separate measurements.

TABLE 1. *Heat capacity, enthalpy, and entropy of benzoic acid at saturation pressure*

T	$C_{sat.}$	$(H_{sat.}-E_0^0)$	$(S_{sat.}-S_0^0)$
		Solid	
°K	*abs j °K⁻¹ mole⁻¹*	*abs j mole⁻¹*	*abs j °K⁻¹ mole⁻¹*
0.0	0.0	0.0	0.0
2	.0155	.0078	.0052
4	.1242	.1242	.0414
6	.4191	.6287	.1397
8	.9924	1.987	.3313
10	1.923	4.838	.6454
12	3.242	9.978	1.107
14	4.932	18.063	1.729
16	6.824	29.790	2.509
18	8.854	45.446	3.429
20	11.00	65.294	4.473
22	13.17	89.458	5.623
24	15.46	118.09	6.867
26	17.61	151.16	8.189
28	19.78	188.56	9.574
30	21.92	230.26	11.012
32	24.03	276.22	12.494
34	26.08	326.33	14.012
36	28.05	380.48	15.560
38	29.91	438.46	17.126
40	31.68	500.06	18.706
42	33.36	565.12	20.293
44	34.98	633.48	21.882
46	36.55	705.02	23.472
48	38.06	779.63	25.060
50	39.50	857.20	26.643
55	42.81	1063.1	30.565
60	45.88	1284.9	34.424
65	48.65	1521.4	38.207
70	51.24	1771.2	41.908
75	53.52	2033.1	45.522
80	55.85	2306.5	49.050
85	58.13	2591.5	52.505
90	60.14	2887.3	55.886
95	62.04	3192.8	59.189
100	63.93	3507.7	62.419
105	65.82	3832.1	65.584
110	67.69	4165.8	68.689
115	69.60	4509.1	71.740
120	71.51	4861.8	74.742
125	73.38	5224.1	77.700
130	75.27	5595.7	80.614
135	77.18	5976.8	83.491
140	79.09	6367.5	86.332
145	80.99	6767.7	89.141
150	82.90	7177.4	91.919
155	84.81	7596.7	94.668
160	86.75	8025.6	97.391
165	88.72	8464.2	100.09
170	90.70	8912.8	102.77
175	92.69	9371.3	105.43
180	94.70	9839.7	108.07
185	96.72	10318	110.69
190	98.75	10807	113.29
195	100.80	11306	115.89
200	102.89	11815	118.46
205	104.99	12335	121.03
210	107.11	12865	123.59
215	109.25	13406	126.13
220	111.40	13958	128.67
225	113.58	14520	131.20
230	115.78	15093	133.72
235	117.99	15678	136.23
240	120.22	16273	138.74
245	122.46	16880	141.24
250	124.71	17498	143.74
255	126.97	18127	146.23
260	129.24	18768	148.71
265	131.52	19419	151.20
270	133.81	20083	153.68
273.16	135.26	20508	155.24
275	136.10	20758	156.15
280	138.40	21444	158.63
285	140.71	22142	161.10
290	143.03	22851	163.56
295	145.35	23572	166.03
298.16	146.81	24033	167.59
300	147.66	24304	168.49
305	149.98	25049	170.95
310	152.30	25804	173.41

TABLE 1. *Heat capacity, enthalpy, and entropy of benzoic acid at saturation pressure*—Continued

T	$C_{sat.}$	$(H_{sat.}-E_0^0)$	$(S_{sat.}-S_0^0)$
		Solid	
°K	*abs j °K⁻¹ mole⁻¹*	*abs j mole⁻¹*	*abs j °K⁻¹ mole⁻¹*
315	154.63	26572	175.86
320	156.96	27351	178.32
325	159.28	28141	180.77
330	161.60	28943	183.22
335	163.91	29757	185.67
340	166.22	30582	188.11
345	168.53	31419	190.56
350	170.84	32268	193.00
355	173.17	33128	195.44
360	175.52	34000	197.88
365	177.90	34883	200.31
370	180.34	35779	202.75
375	182.81	36687	205.19
380	185.25	37607	207.62
385	187.64	38539	210.06
390	190.05	39483	212.50
395	192.47	40440	214.93
395.522	192.74	40541	215.19
		LIQUID	
395.522	250.60	58541	260.70
400	253.33	59669	263.54
405	256.59	60944	266.70
410	259.86	62235	269.87

3.2. Reliability of the Heat-Capacity Results

The possible sources of errors in the adiabatic calorimeter were discussed previously [1]. As a test on the performance of the calorimeter, the heat capacity of water was measured between 274° and 332° K under conditions as nearly identical as possible to those of the benzoic acid experiments. These results agree within 0.02 percent of the values previously published [6]. Considering the precision and the various known sources of errors a probable error [4] of ±0.2 percent is assigned to the heat-capacity values from 60° to 395° K. Above 395° K the probable error is ±0.3 percent, due to the increased uncertainty arising from the chemical reaction of benzoic acid with the container. In order to determine the effect of the chemical reaction on the heat capacity of benzoic acid, a series of heat-capacity measurements was carried out after two experiments in which the material had been melted. Figure 2 shows, except for the two points indicated by the deviations of 0.151 and 0.182 abs j deg^{-1}, which are considered to be experimental errors, the results for the solid benzoic acid are essentially the same as prior to melting. No unusual thermal drifts were observed in the higher temperature range to indicate the evolution of a large heat of chemical reaction. Below 60° K the probable error increases to ±1 percent at 14° K because of the greatly diminished absolute heat capacity and uncertainties in the measurement of temperature.

[4] For these experiments a true probable error cannot be computed statistically. The values given are estimates reached by examining contributions to the inaccuracy from all known sources. The authors estimate that there is a fifty-fifty chance that the error is no larger than that indicated.

3.3. Purity and Heat of Fusion

In order to follow the extent of chemical reaction when the material was melted, three purity determinations were made with two meltings before each measurement. The purity was calculated from the equilibrium melting curves [1]. The results in the order of the measurements were 99.93, 99.92, and 99.92 mole percent purity, indicating that the purity did not change greatly with the number of meltings. These figures are considerably lower than the value, 99.997 mole percent, obtained from the freezing-point curve. Judging from the appearance of the interior surface of the container and the fact that the container lost about 0.45-g mass, it seems the purity determined is higher than expected. It is possible, however, that the reaction products are insoluble in benzoic acid. This method only gives liquid soluble-solid insoluble impurities.

The heat of fusion was determined by the usual method of heating continuously from a temperature slightly below the triple point to just above it [1]. The total heat input was corrected for the heat capacity of the container and sample below and above the triple point and for the premelting of the sample due to impurities. Three determinations were made, and the results were 18,006, 18,003, and 18,011 abs j $mole^{-1}$. The heat of fusion is taken to be 18,000 abs j $mole^{-1}$. It is believed, upon considering the chemical reaction that took place with the container, the uncertainty in the heat-capacity correction, and the uncertainty in the premelting correction, that the probable error in the heat of fusion may be as much as 100 abs j $mole^{-1}$. In the temperature range of this investigation the amount of benzoic anhydride formed was probably not greater than 0.03 mole percent, as estimated from the work of Schwab and Wichers [4, 7]. It is considered that the error in the heat of fusion from this source is negligible.

4. Derived Thermal Properties

4.1. Enthalpy and Entropy

The enthalpy and entropy of solid and liquid benzoic acid are given in columns 3 and 4 of table 1, respectively, at 2-degree intervals from 0° to 50° K and at 5-degree intervals from 50° to 410° K. The enthalpy was evaluated using the relation

$$(H_{\text{sat.}}-E_0^\circ)=\int_0^T C_{\text{sat.}}\,dT+L_f, \qquad (2)$$

in which $(H_{\text{sat.}}-E_0^\circ)$ is the enthalpy along the saturation curve relative to the internal energy of the solid benzoic acid at absolute zero; and L_f is the heat of fusion. The entropy was evaluated using the relation

$$(S_{\text{sat.}}-S_0^\circ)=\int_0^T \frac{C_{\text{sat.}}}{T}\,dT+\frac{L_f}{T_t}, \qquad (3)$$

in which $(S_{\text{sat.}}-S_0^\circ)$ is the entropy of the solid benzoic acid along the saturation curve relative to absolute zero (S_0° is considered to be zero in all calculations made in this work); and T_t is the triple-point temperature. The equations were evaluated above 12° K by numerical integration, using four-point Lagrangian integration coefficients [8] and below this temperature by analytical methods. The integrations were checked by evaluating the thermodynamic identity

$$\int_0^T (S_{\text{sat.}}-S_0^\circ)\,dT=T(S_{\text{sat.}}-S_0^\circ)-(H_{\text{sat.}}-E_0^\circ). \qquad (4)$$

The tabulated enthalpy values are considered to have a probable error of ±0.2 percent between 60° and 395° K, ±1 percent below 60° K, and ±0.3 percent above 395° K. The entropy values have a probable error of ±0.1 abs j $°K^{-1}$ $mole^{-1}$ in the temperature range below 395° K and ±0.5 abs j $°K^{-1}$ $mole^{-1}$ above this temperature. The increase in uncertainty above 395° K as previously stated is due to the chemical reaction of benzoic acid with the container. In all calculations the triple-point temperature was taken to be 395.522°K,[5] as given by Schwab and Wichers [4].

4.2. The Standard Entropy, Heat, and Free Energy of Formation

The standard entropy of formation of benzoic acid at 298.16° K was calculated by using the entropy value directly from table 1 without correction to standard state, since this correction is negligible for all practical purposes. The standard entropies of graphite, hydrogen, and oxygen used in the calculation are 5.720 ±0.050 [9], 130.574 ±0.010 [10, 11] and 205.073±0.010 [12, 13] abs j $°K^{-1}$ $mole^{-1}$, respectively. The value so obtained is

$$\Delta S^\circ_{f,\,298.16°\text{K}}=-469.25\pm0.37 \text{ abs j } °\text{K}^{-1} \text{ mole}^{-1}.$$

The standard heat of formation was calculated using the standard heat of combustion of benzoic acid, −3226.92±0.32 abs kj $mole^{-1}$ [14, 15, 16] with the standard heats of formation of carbon dioxide, −393.513±0.045 abs kj $mole^{-1}$ [17], and liquid water, −285.840±0.042 abs kj $mole^{-1}$ [17]. The value obtained is

$$\Delta H^\circ_{f,\,298.16°\text{K}}=-385.19\pm0.46 \text{ abs kj mole}^{-1}.$$

The standard free energy of formation was calculated using the above values of standard entropy and heat of formation. The result is

$$\Delta F^\circ_{f,\,298.16°\text{K}}=-245.28\pm0.47 \text{ abs kj mole}^{-1}.$$

The probable error given with each of these values was obtained from a statistical combination of the probable errors of the data used in computing the value.

[5] Temperatures in degrees Kelvin were obtained from the relation °K = °C + 273.160.

5. Comparison With Other Results

Hess [18] measured the enthalpy of benzoic acid relative to 0° C, using a Bunsen ice calorimeter and formulated a linear heat-capacity equation to fit the interval from 0° to 122° C. His heat-capacity values are 25 percent lower at 275° K and 32 percent higher at 395° K than the values in table 1. Andrews, et al. [19], using a drop method similar to Hess but with the receiving vessel at 22° C, obtained linear relations for the heat capacity of solid and liquid benzoic acid in the temperature range 22° to 200° C. Comparing their work in the range of this work, their values are about 5.4 percent higher at 300° K and 6.7 percent lower at 395° K. Using a cooling method Hrynakowski and Smoczkiewiczowa [20] measured the heat capacity at 25° C. This value is 6.5 percent higher than the value in table 1. Parks, et al. [21], using an aneroid type calorimeter, measured the heat capacities from 90° to 295° K. These values are within 1 percent of the values in table 1. Jessup [14] measured the heat capacity of benzoic acid at 28.5° C; this value is 0.4 percent lower. The heat-capacity values obtained by Andrews, et al., Parks, et al., and Jessup are compared in figure 4 with the values in table 1.

A few authors have published their experimental values in terms of mean heat capacities. These are compared in table 2 with the values in table 1. The comparisons were made by interpolating the tabulated enthalpies at the proper temperature intervals. Hess [18] and Satoh and Sogabe [22] used ice calorimeters in their experiments.

The heats of fusion of benzoic acid obtained by previous investigators are compared in table 3. Hess [18] obtained mean heat capacities of solid and liquid benzoic acid at the melting point relative to 0° C and from these values calculated the heat of fusion. Garelli and Montanari [23] determined the cryoscopic constant of benzoic acid using different solutes at various concentrations and from the average of the cryoscopic constants calculated the heat of fusion. Mathews [24] similarly calculated the heat of fusion from the cryoscopic constant

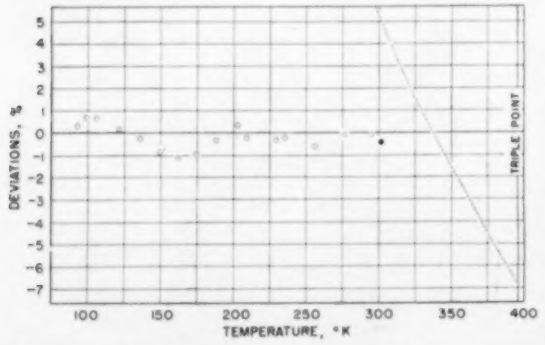

FIGURE 4. *Comparison of heat capacities of benzoic acid with those from other investigators.*

The base-line represents the values in table 1. ○, Parks, Hoffman, and Barmore; ●, Jessup; ——, Andrews, Lynn, and Johnston.

TABLE 2. *Comparison of mean heat capacities of benzoic acid with the values obtained by other investigators*

Investigator	Temperature interval	Mean heat capacity	
		Other investigator	This work
	°C	*abs j deg⁻¹ mole⁻¹*	*abs j deg⁻¹ mole⁻¹*
Hess [18]	0 to 50	131.4	146.82
Do	0 to 94	159.3	157.03
Do	0 to 110	169.6	160.79
Satoh and Sogabe [22]	0 to 99.6	160.2	158.34

TABLE 3. *Comparison of heat of fusion of benzoic acid with the values obtained by other investigators*

Investigator	L_f
	abs j mole⁻¹
Hess [18]	9,810
Garelli and Montanari [23]	20,260
Mathews [24]	17,780
Andrews, et al. [19]	17,320
Klosky, et al. [25]	16,760
Hrynakowski and Smoczkiewiczowa [26]	15,530
This work	18,000

obtained using anthracene as a solute at different concentrations. Andrews, et al. [19] obtained their value for the heat of fusion from the enthalpy curves for the solid and liquid benzoic acid determined by the drop method. Klosky, et al. [25] calculated the heat of fusion from the vapor pressure curves for solid and liquid benzoic acid. Hrynakowski and Smoczkiewiczowa [26] determined the heat of fusion by a cooling method.

6. Discussion

The results of this investigation show that benzoic acid is a suitable heat-capacity standard in the temperature range 10° to 350° K prescribed by the Calorimetry Conference. As this material becomes corrosive above the upper temperature limit, particularly in the liquid state, it should be used only below 350° K. The benzoic acid, packaged in 70-g units in particle sizes between number 10 and 50 sieves, can be easily poured into calorimeter sample containers. As long as this material is used below 350° K, most of it can be poured out after use, but once fused the task of removing the sample becomes more difficult.

The original purpose of the benzoic acid standard as proposed by the Calorimetry Conference is for the intercomparison of precision heat-capacity calorimeters. It seems appropriate that the heat capacity of benzoic acid be determined by other laboratories so that calorimeters of various design and the results obtained with them can be compared.

7. References

[1] G. T. Furukawa, D. C. Ginnings, R. E. McCoskey, and R. A. Nelson, J. Research NBS **46**, 195 (1951) RP2191.

[2] R. B. Scott, C. H. Meyers, R. D. Rands, Jr., F. G. Brickwedde, and N. Bekkedahl, J. Research NBS **35**, 39 (1945) RP1661.

[3] F. W. Schwab and E. Wichers, J. Research NBS **32,** 253 (1944) RP1588.
[4] F. W. Schwab and E. Wichers, J. Research NBS **34,** 333 (1945) RP1647.
[5] The Fourth Meeting of the Conference on Low Temperature Calorimetry, Chem. Eng. News **27,** 2772 (1949).
[6] N. S. Osborne, H. F. Stimson, and D. C. Ginnings, J. Research NBS, **23,** 197 (1939) RP1228.
[7] F. W. Schwab and E. Wichers, J. Research NBS **25,** 747 (1940) RP1351.
[8] Tables of Lagrangian interpolation coefficients (Columbia Univ. Press, New York, N. Y., 1944).
[9] F. G. Brickwedde, M. Moskow, and J. G. Aston, J. Research NBS **37,** 263 (1946) RP1747.
[10] The NBS-NACA Tables of thermal properties of gases, Table 7.10, Molecular hydrogen, ideal gas properties.
[11] H. W. Woolley, R. B. Scott, and F. G. Brickwedde, J. Research NBS **41,** 379 (1948) RP1932.
[12] The NBS-NACA Tables of thermal properties of gases, Table 9.10, Molecular oxygen, ideal gas properties.
[13] H. W. Woolley, J. Research NBS **40,** 163 (1948) RP1864.
[14] R. S. Jessup, J. Research NBS **29,** 247 (1942) RP1499.
[15] R. S. Jessup, J. Research NBS **36,** 421 (1946) RP1711.
[16] F. B. Silsbee, NBS Circular 475, p. 22 (June 30, 1949).
[17] Selected values of chemical thermodynamic properties, NBS Circular 500 (1950).
[18] H. Hess, Ann. Physik und Chemie **35,** 410 (1888).
[19] D. H. Andrews, G. Lynn, and J. Johnston, J. Am. Chem. Soc. **48,** 1274 (1926).
[20] K. Hrynakowski and A. Smoczkiewiczowa, Roczniki Chem. **17,** 140 (1937).
[21] G. S. Parks, H. M. Huffman, and M. Barmore, J. Am. Chem. Soc. **55,** 2733 (1933).
[22] S. Satoh and T. Sogabe, Sci. Papers Inst. Phys. Chem. Res. (Tokyo) **36,** 449 (1939).
[23] F. Garelli and C. Montanari, Gazz. chim. ital. **24,** [2], 229 (1894).
[24] J. H. Mathews, J. Am. Chem. Soc. **39,** 1125 (1917).
[25] S. Klosky, L. P. L. Woo and R. J. Flanigan, J. Am. Chem. Soc. **49,** 1280 (1927).
[26] K. Hrynakowski and A. Smoczkiewiczowa, Roczniki Chem. **17,** 165 (1937).

WASHINGTON, February 2, 1951

964065—51——4

Journal of Research of the National Bureau of Standards Vol. 47, No. 4, October 1951 Research Paper 2252

Infrared Emission Spectrum of Calcium[1]

Curtis J. Humphreys

The spectrum of neutral calcium excited in alternating-current and direct-current arcs, using carbon electrodes cored with CaO, has been observed with high resolution, in the interval between 12816 and 22655 Angstroms. A total of 36 lines has been observed, of which all but one have been classified. The long-sought term, $3d^2\ ^3F$, has been found and established on the basis of two complete multiplets, $3d\cdot4p\ ^3F^\circ - 3d^2\ ^3F$, and $3d\cdot4p\ ^3D^\circ - 3d^2\ ^3F$, and two intersystem lines $3d\cdot4p\ ^1D^\circ - 3d^2\ ^3F_{2,3}$. Most of the infrared energy is radiated in the multiplet $4p\ ^3P^\circ - 3d\ ^3D$. These lines are suggested for use as wavelength standards for the 2-micron region.

1. Introduction

The study of infrared atomic emission spectra has been given new impetus as a result of the utilization of photo-conducting cells in conjunction with high-resolution grating spectrometers for observation in the region just beyond the limit of response of infrared-sensitive photographic emulsions. Previous to this recent renewal of activity there had been an almost complete cessation of work on infrared atomic emission spectra for a period of about 25 years, following the work of Paschen and his pupils. The explanation lies mainly in the relative insensitivity of thermal detectors, such as thermopiles, bolometers, and radiometers, as compared with photographic emulsions in regions where they could be used. In order to observe infrared emission spectra at all, it was necessary to work with optical slits so wide that the precision of wavelength determinations was insufficient to distinguish between real and fortuitous regularities, with the result that the observational data were not of much value for term analyses. It was also impossible to observe lines other than those of very high intensity, thus providing an insufficient number of wavelengths for use in establishing regularities.

The use of photoconducting detectors now provides essentially the same advantages as photography, as regards both volume of attainable data and precision of observations, particularly for the region between 1 and 3 μ where lead sulfide cells may be used. It is obviously possible to observe infrared lines for most if not all atoms in this region. Many of these lines can be predicted in position on the basis of term analyses already made with varying degrees of completeness. Three criteria are suggested as the basis of selection of spectra for study; first, gaps in the term system that can be filled in only by finding regularities involving infrared data; second, astrophysical interest, such as questions of identification of elements in the solar spectrum on the basis of excitation in the laboratory, and, finally, usefulness in providing wavelength standards that may assist in the measurement of wavelengths in other spectra, either atomic or molecular.

Observations have been completed or are now in progress on several infrared emission spectra in the Radiometry Laboratory. Ca I has been selected for the first detailed report because it is probably the most conspicuous example of a spectrum in urgent need of observation on the basis of all three suggested criteria.

[1] Reported, in part, at the meeting of the Optical Society of America, Washington, D. C., March 1, 1951.

2. Energy Levels of Ca I

Ca I is an example of a relatively simple spectrum, the term system comprising singlets and triplets, arising from two valence electrons outside of closed shells. Table 1 lists the electron configurations with designations of predicted terms appropriate to each. A more detailed table is to be found on page XXXV of Bureau Circular 467 [1].[2] The numerical values of all energy levels of Ca I previously known are listed in the same book, together with references to the sources of the material.

TABLE 1. *Electron configurations and terms of* Ca I

Configuration	Predicted terms
$4s^2$	^1S
$4s(^2S)5s$	^1S , ^3S
$4s(^2S)4p$	$^1P^\circ$, $^3P^\circ$
$4s(^2S)3d$	^1D , ^3D
$4s(^2S)4f$	$^1F^\circ$, $^3F^\circ$
$3d(^2D)4p$	$^1(P,D,F)^\circ$, $^3(P,D,F)^\circ$
$4p^2$	$^1(S,D)$, ^3P
$3d^2$	$^1(S,D,G)$, $^3(P,F)$

The regular series, resulting from the displacement of one electron from the normal $4s^2$ configuration to successively higher states, have been known almost from the first discovery of spectral regularities. The information is summarized in the well-known monographs by Paschen and Götze [2] and by A. Fowler [3]. It was pointed out in 1925 by Russell and Saunders [4] that, in Ca I and other alkaline-earth spectra, features of these spectra not accounted for by regular series could be explained as transitions between terms arising from electron configurations in which both electrons are displaced from the normal configuration. This paper, which preceded the formal presentation of the Hund theory [5], served in a sense as an introduction to the theory of complex spectra.

[2] Figures in brackets indicate the literature references at the end of this paper.

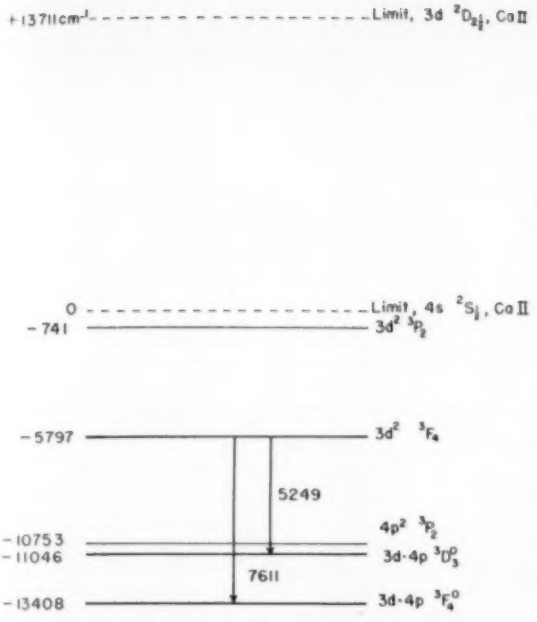

FIGURE 1. *Partial term diagram of* Ca I.

In spite of extensive efforts that had been made to complete the analysis of Ca I, there remained, previous to the observations reported in this paper, a conspicuous gap in the term array, namely, that, with the exception of ^{3}P, all terms from the $3d^2$ configuration were missing. The $3d^2\,^3$P term is abnormally high, possibly because of a perturbation by $4p^2\,^3$P, another term of even parity. This perturbation has the effect of a repulsion, producing a separation of terms that would otherwise be at about the same elevation. Combinations of $3d^2\,^3$P with lower odd terms yield photographically observable lines, permitting evaluation of the term. There is no such perturbing term to affect the position of $3d^2\,^4$F. Its location was predicted by H. N. Russell in accordance with the following considerations, communicated privately. The higher members of this series, converging to the $3d\,^2$D limit in Ca II, are known, permitting evaluation of total quantum numbers and the values of Δn. Assuming Δn to be a little greater than 1 for the first two members of the ^{3}F series, the absolute value of $3d^2\,^3F_4$ was predicted to be 20700 cm^{-1} with respect to its own limit. Taking into account the elevation of this limit, 13711 cm^{-1} above $4s\,^2$S in Ca II, the ionization limit of the regular series, the $^3F_4$ level is expected about 7000 cm^{-1} below the usual ionization limit in Ca I. Translating this into the usual system, as employed in Circular 467 [1], in which the ground level is given the value zero, the predicted value of $3d^2\,^3F_4$ becomes approximately 42300. This is accomplished by subtracting 7000 from 49304.80, the value of the first ionization limit. Actually, $3d^2\,F_4$ was found to be 43508.11, or 5797 cm^{-1} below this limit, in excellent agreement with the prediction, considering the uncertainty in the estimate of Δn. Figure 1 is introduced to assist in visualizing the relative positions of the terms that are of significance in determining the location of $3d^2\,^3$F. For simplicity, only a single level, that of highest J-value, is drawn in the position of each term. The displacements indicated are with reference to the limit of the regular series, that is the $4s\,^2$S ground level of Ca II. The diagram includes the $3d\,4p\,^3D^\circ_3$ and $^3F^\circ_4$ levels, representing the terms that give the strongest combinations with $3d^2\,^3$F. The experimental material completely establishing all the levels comprising this term will be presented in a later section of this paper.

3. Observations

The development of photoconducting detectors and of amplifying and recording equipment has now advanced sufficiently that energy detection no longer represents the principal difficulty in infrared observation. The high-resolution spectrometer recently completed and put in use in the radiometry laboratory of the Bureau has been described previously [6]. A 15,000 lines-per-inch plane grating, 7½ in. wide, supplied by Johns Hopkins University, is used for observations in the region between 1 and 3 μ. Where one must obtain the record of the spectrum on a paper chart by continuous scanning, the most serious problem in observing line spectra is to find a source combining sufficient excitation of high-energy states with operation steady enough to give a smooth development of line profiles, permitting precise location of the peaks for wavelength determinations. An enclosed source, such as a Geissler tube, or the various metal vapor lamps utilizing relatively volatile metals, for example, mercury, cadmium, or the alkalis, is ideal for such use. Calcium unfortunately does not lend itself readily to such use because it has a fairly high melting point and combines readily with the glass enclosures at elevated temperatures.

The reasonably smooth operation of open flame alternating-current arcs, using carbons cored with various salts in order to increase emission in selected spectral regions, suggested that a satisfactory calcium source might be developed by using this principle. Unfortunately, no commercially prepared carbons cored with calcium salts were available. The problem was, however, brought to the attention of the National Carbon Co., and this company generously offered to supply experimental carbons cored with calcium salts and other metallic compounds to be used in other investigations now on our program. A supply of these carbons has been received, but so far has been used only to a limited extent. Most of the observations reported in this paper had been completed before the arrival of these carbons. Inasmuch as subsequent work on this and other elements requiring similar sources will probably utilize the electrodes supplied by the National Carbon Co., an extremely brief report will be given of the preparation of cored carbons in the laboratory and of methods of use.

Fadometer carbons one-half in. in diameter were used in these experiments. The arc was assembled with one plain electrode and one cored with a salt of the element under study. Operation of the arc on alternating-current supply was abandoned after early trials when it was found that satisfactorily smooth operation could be obtained on direct current, and that, as might be expected, greatly improved excitation resulted when the cored carbon was made positive. Most of the cored electrodes were made by drilling a 3/16-in. opening in a plain carbon along the axis and packing with a mixture of calcium oxide and carbon dust. The calcium oxide was the most satisfactory of a number of compounds tried, but, in view of the development work by the National Carbon Co., no exhaustive study was made. The hand-operated arc was powered by the 220-v direct-current supply available in the laboratory, ballasted by sufficient resistance to maintain the current in the range between 15 and 25 amp. This was close to the maximum operating load of the circuits as assembled. It did not necessarily represent the optimum conditions for smooth arc operation or excitation of desired energy levels. However, operating conditions were adequate to permit attainment of the primary objectives of the experiments.

One troublesome experimental difficulty arose in connection with the operation of the carbon arcs. The entire spectral region extending from about 1.1 to beyond 1.6μ, except for a short gap near 1.3μ, is covered by two sets of band progressions of the CN system, corresponding to two vibrational transitions. Wavelengths of the (0, 0) band heads were reported by Kiess [7] from photographic observations, and the entire infrared system was observed with relatively low dispersion by Herzberg and Phillips [8]. These bands were completely resolved in these experiments and will be reported in a subsequent publication. This band structure is so intense and closely packed that other spectral structures cannot be distinguished if they fall within these bands. One of the multiplets involving the newly found ^{3}F term, $3d(^2\mathrm{D})4p\ ^3\mathrm{F}^\circ$—$3d^2\ ^3\mathrm{F}$, is within the gap between the two bands. There is, however, enough weak band structure to prevent observation of the satellite lines. It was found possible to eliminate most of the band structure by using an enclosed water-cooled arc, circulating helium through the arc chamber at a rapid rate. To offset the suppression of the excitation accompanying the introduction of helium, the positive carbon was cored with a slug of calcium metal replacing the CaO. This permitted the tracing of satisfactory records over short ranges. The calcium is used up rapidly in the enclosed arc and does not operate in controllable fashion in the open arc because of extremely rapid conversion to oxide. The enclosed arc, used for many years in the Spectroscopy Laboratory, was originally designed by H. D. Curtis [9], and kindly loaned for these experiments by William F. Meggers.

The optical system in front of the entrance slit of the spectrometer was set up in order to satisfy two conditions in addition to full illumination of the collimating mirror. These were elimination of continuous emission from the electrodes and provision for introduction of a source of standard wavelengths. The arrangement of components is sketched in figure 2, as seen from above. A quartz lens and a concave mirror were lined up on the optic axis. These were at such distances that a slightly magnified image of the source, set up slightly off axis, was formed by the concave mirror on the axis at a point such that a sharp image of the first image was projected onto the slit. A horizontal diaphragm was mounted between the lens and mirror, so that the images of the electrodes could be seen on the upper and lower jaws of the diaphragm with the arc stream between. The length of the arc and the diaphragm opening were adjusted to give the best operating conditions. In general, arcs of about 6-mm length gave the most satisfactory operation. A Corning 2540 filter was attached to the back of this diaphragm to eliminate higher orders of spectra. Actually, this diaphragm-filter combination was placed a little out of focus nearer the mirror. This permitted inserting the source of standard wavelengths at the common focus of the mirror and lens, making possible the use of wavelengths of any desired order. The Corning filter begins to transmit at about 0.9 μ. A neon discharge tube was used as a source of comparison spectra for determining the wavelengths of most of the observed lines, because second or third orders of the intense red lines happened to be most favorably located with reference to calcium lines. The neon tube was brought into position as required while the spectrum was being scanned. In a few instances, determined by the wavelengths to be measured, a krypton source was used.

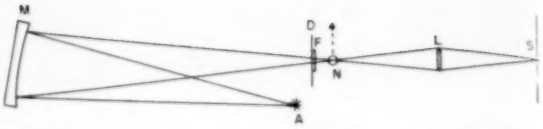

FIGURE 2. *Arrangement for projecting image of source upon slit of spectrometer.*

A, Arc lamp; N, neon tube; M, concave mirror; D, diaphragm with horizontal slot; F, filter; L, quartz lens; S, spectrometer slit.

The records used for wavelength determinations were run at the slowest scanning speed, approximately 16 A a minute at 20000 A, insofar as operating conditions permitted. It was found possible to introduce standards close enough together in all instances that a linear interpolation could be used for reduction.

The shortest wavelength measured was of 12816 A. This is barely within the range of photography. It is just at the beginning of the intense portion of the (0,0) CN band. For these reasons and also because the transitions especially sought had been found, it did not appear profitable to extend the measurements to shorter wavelengths. The spectrum was explored out to the limit of sensitivity of the lead sulfide cell near 27000 A, but no first-order lines of appreciable intensity were found beyond 22655 A. The $3d\ ^2\mathrm{D}$—$4p\ ^2\mathrm{P}^\circ$ doublet of Ca II near 8600 A appeared with such intensity in the second and third orders that the

lines were recorded even with the cutoff filters used to exclude higher orders.

4. Discussion of Results

The observation of the infrared spectrum of calcium was included in the very early work previously mentioned. Such observations were reported by Paschen [10], by Randall [11], and by Sandvik and Spence [12]. These observations were subject to the limitations in precision already mentioned, and, although most of the lines reported appear to be real, the levels represented in the transitions could be determined more precisely by other combinations in regions more favorable to observation. None of the lines involving combinations of the heretofore missing $3d^2\,{}^3F$ term was reported in any previous work. Having in mind that an entirely different order of precision of wavelength measurement has now been realized, a completely new description of the infrared spectrum has been prepared without attempting to associate any lines with probable counterparts from earlier work.

Descriptive data pertaining to 36 lines of Ca I observed and measured in these experiments are compiled in table 2. These data comprise observed

TABLE 2. *Description of* Ca I *in the infrared region*

[C, Probably confused by line at 16156.04 A; u, Unresolved with respect to adjacent strong line

Observed wavelength in air	Observed intensity	Intensity sun [14]	Wave number observed	Wave number calculated	J	Multiplet
A			*cm*$^{-1}$	*cm*$^{-1}$		
12815.69	400		7800.80	7800.56	1 – 2	$4s(^2S)5s\ {}^3S - 3d(^2D)4p\ {}^3P^\circ$
12823.46	100		7796.07	7795.81	1 – 1	
12826.60	25		7794.17	7793.86	1 – 0	
12885.21	15		7758.71	7758.76	2 – 3	$3d(^2D)4p\ {}^3F^\circ - 3d^2\ {}^3F$
12909.07	200		7744.37	7744.44	2 – 2	
13001.37	20		7689.39	7689.40	3 – 4	
13033.41	300		7670.49	7670.50	3 – 3	
13057.82	20		7656.15	7656.18	3 – 2	
13134.96	400		7611.19	7611.22	4 – 4	
13167.75	24		7592.24	7592.32	4 – 3	
13061.84	8		7653.79	7653.81	2 – 3	$3d(^2D)4p\ {}^1D^\circ - 3d^2\ {}^3F$
13086.26	50		7639.51	7639.49	2 – 2	
16135.80	20	8?	6195.71	6195.39	0 – 1	$4s(^2S)5p\ {}^3P^\circ - 4s(^2S)5d\ {}^3D$
16149.79	70	9	6190.34	6190.05	1 – 2	
	C	5		6188.34	1 – 1	
16195.33	150	14	6172.94	6172.31	2 – 3	
16202.94	10	12	6170.04	6169.64	2 – 2	
		15?		6167.93	2 – 1	
16156.04	100		6187.95	6187.45	1 – 2	$3d(^2D)4p\ {}^1P^\circ - 4s(^2S)5d\ {}^1D$
18924.96	30		5282.58	5282.52	1 – 2	$3d(^2D)4p\ {}^3D^\circ - 3d^2\ {}^3F$
18969.71	60		5270.12	5270.12	2 – 3	
19021.39	4		5255.80	5255.80	2 – 2	
19045.86	90		5249.05	5249.01	3 – 4	
19114.83	5		5230.11	5230.11	3 – 3	
				5215.79	3 – 2	
19309.43	500		5177.41	5177.43	0 – 1	$4s(^2S)4p\ {}^3P^\circ - 4s(^2S)3d\ {}^3D$
19452.82	1500		5139.24	5139.18	1 – 2	
19505.62	500		5125.33	5125.28	1 – 1	
19776.67	2000	35	5055.09	5055.04	2 – 3	
19861.70	500		5033.44	5033.30	2 – 2	
19916.34	50	11	5019.63	5019.40	2 – 1	
19620.75		10	5095.23			$4s(^2S)4d\ {}^1D - 4s(^2S)4f\ {}^1F^\circ$
19815.14	30	20	5045.27	5045.24	2 – 3	
19852.96	250	21	5035.66	5035.62	1 – 2	$4s(^2S)5s\ {}^3S - 4s(^2S)5p\ {}^3P^\circ$
19932.94	100	20	5015.45	5015.21	1 – 1	
19961.37	40		5008.31	5008.16	1 – 0	
22608.39	10	12	4421.93	4421.99	1 – 2	$4s(^2S)4d\ {}^3D - 4s(^2S)4f\ {}^3F^\circ$
22625.51	20	14	4418.58	4418.65	2 – 3	
	u	9		4418.30	2 – 2	
22651.30	30	18	4413.55	4413.55	3 – 4	
	u	9		4413.07	3 – 3	
	u			4412.72	3 – 2	

wavelengths at atmospheric pressure, corresponding wave numbers in vacuum, calculated wave numbers, intensity estimates, and classification where determined, as shown by multiplet designations. The reduction to wave numbers for wavelengths greater than 10000 A is accomplished by inversion of the Kayser "Tabelle der Schwingungszahlen", as suggested by Babcock [13] and applying the required correction. There is some uncertainty regarding the index of refraction of air for this region, but there is no evidence that this uncertainty introduces an error into wave-number reductions as large as the random errors inherent in the observational procedures. The wavelengths are carried out to seven figures in the table, that is to hundredths of angstroms. On the basis of experimental checking of known constant term differences, considerable confidence is felt in the sixth digit for all lines. The seventh is very uncertain but is retained for uniformity throughout the table, since it is regarded as probably significant for the best determined wavelengths. In most instances the listed wavelengths represent averages of from four to six measurements each on separate records. In a few cases ten or more measurements are included.

The indicated intensities may be regarded as semi-quantitative. A precision technique for evaluating intensities has not been developed for the equipment in use, but such a development appears feasible. Intensity estimates are rendered somewhat uncertain for an arc source, because on the basis of repeated runs it appears to be subject to slow variation in energy output even when apparently steady. The relative intensities are much more reliable within multiplets than in the intercomparison of multiplets. Spectral sensitivity of the detector must be considered in any precise intercomparison over wide ranges. As is to be expected, the intensity distribution in multiplet patterns points to a very close realization of the *LS*-coupling scheme for Ca I.

One column of table 2 contains a listing of the intensities of lines in the solar spectrum observed by Goldberg, Mohler, Pierce, and McMath [14], where coincidences occur with the laboratory observations here reported. Calcium is one of the abundant metallic elements in the sun and is outstanding in the emission spectrum of the chromosphere and prominences. The laboratory observation and description of the infrared-calcium spectrum is expected to aid in the identification of calcium lines in this portion of the solar spectrum.

The most important result of this work, representing the attainment of the principal objective of the investigation, was the discovery of the multiplets comprising the combinations of $3d^2\ ^3F$. The identification and interpretation of these multiplets are based on the observed fact that they involve combinations with the previously known levels from the $3d\text{-}4p$ configuration, also that such combinations are expected in these regions in accordance with the discussion of the level scheme already given. These multiplets are displayed in table 3. The adopted

TABLE 3. *Multiplet combinations of* $3d^2\ ^3F$ *in* Ca I

	$3d^2\ ^3F_4$ 43508. 11	$^3F_3$ 43489. 21	$^3F_2$ 43474. 89
$3d\cdot 4p\ ^3F_4^\circ$ 35896. 890	13134. 96 (400) 7611. 19 7611. 22	13167. 75 (24) 7592. 24 7592. 32	
$^3F_3^\circ$ 35818. 712	13001. 37 (20) 7689. 39 7689. 40	13033. 41 (300) 7670. 49 7670. 50	13057. 82 (20) 7656. 15 7656. 18
$^3F_2^\circ$ 35730. 450	----------	12885. 21 (15) 7758. 71 7758. 76	12909. 07 (200) 7744. 37 7744. 44
$3d\cdot 4p\ ^1D_2^\circ$ 35835. 400	----------	13061. 84 (8) 7653. 79 7653. 81	13086. 26 (50) 7639. 51 7639. 49
$3d\cdot 4p\ ^3D_3^\circ$ 38259. 102	19045. 86 (90) 5249. 05 5249. 01	19114. 83 (5) 5230. 11 5230. 11	---------- 5215. 79
$^3D_2^\circ$ 38219. 094	----------	18969. 71 (60) 5270. 12 5270. 12	19021. 39 (4) 5255. 80 5255. 80
$^3D_1^\circ$ 38192. 373	----------	----------	18924. 96 (30) 5282. 58 5282. 52

values of the levels were arrived at by an adjustment to provide the best fit of the observed wave numbers into the scheme. The construction of this table should be fairly obvious, it being the familiar quadratic array frequently used in reporting spectral regularities. The entries comprise in each instance the observed wavelength followed by estimated intensity in parenthesis, just below the wavelength the corresponding observed wave number (alined with the combining level in the left column) and finally the calculated or adjusted wave number. The precision of the experimental observations may be judged by the agreement between observed and calculated wave numbers. There are several instances of exact agreement and no deviations greater than 0.08 cm^{-1}. All possible transitions are observed except the faint corner satellite $^3D_3^o - {}^3F_2$. The satellites in the $^3F^o - {}^3F$ multiplet are somewhat less precisely determined than the transitions on the diagonal, because they could be observed only by using the difficult experimental technique involving circulating helium in the enclosed arc in order to eliminate band structure.

The data compiled in table 3 were obtained from the measurement of records similar to the one reproduced in figure 3, which is an ink tracing of a chart record. The records that were actually used for wavelength reductions were obtained by scanning at speeds one-half or one-fifth as fast, permitting a corresponding greater linear dispersion. In order to exhibit the weaker lines, the deflections for the more intense lines are necessarily off scale, as indicated by the blunt maxima of the strong lines. The same statement applies to figure 4, which illustrates the extremely intense multiplet $4p\ ^3P^o - 3d\ ^3D$. For the actual wavelength determinations of the intense lines, they are kept on the scale by an attenuator utilizing a network of resistors. A setting may be chosen to give the desired attenuation factor.

By far the strongest infrared lines and among the most intense in Ca I are included in the multiplet $4p\ ^3P^o - 3d\ ^3D$. These are illustrated, together with $5s\ ^3S - 5p\ ^3P^o$ and $4d\ ^1D - 4f\ ^1F^o$, in figure 4, which is traced from an actual chart record in this region. The positions of all of these lines are predictable from the values of the combining levels, given to eight figures by Wagman [15], based on interferometric measurements of wavelengths of lines, due to other combinations of these same levels, in the photographically accessible region. The calculated wave numbers given in table 2 are obtained from these precisely determined levels where possible. The $4p\ ^3P^o - 3d\ ^3D$ multiplet can be observed under favorable conditions, that is high intensity and freedom from interference. These favorable factors strongly suggest the use of these lines as wavelength standards.

The agreement between observed and calculated wave numbers for lines of some multiplets in the 13000- to 16000-A region is not quite so good as the estimated precision of the wavelength measurements should make possible. The reason for these differences is still not fully understood, but it is suggested that the values of some of the levels may still be subject to revision. It is hardly necessary to point out that it is a prime necessity to establish a satisfactory set of standards throughout the infrared region in order that these new high-resolution techniques may be used to advantage in both atomic and molecular spectra.

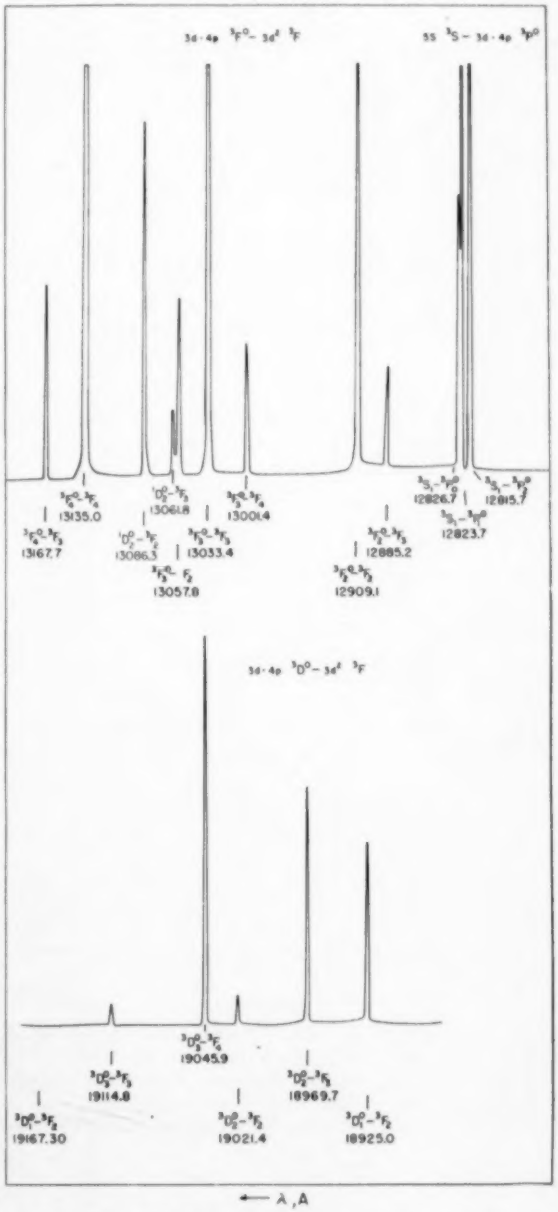

FIGURE 3. *Multiplet combinations of* $3d^2\ ^3F$ *in* Ca I.

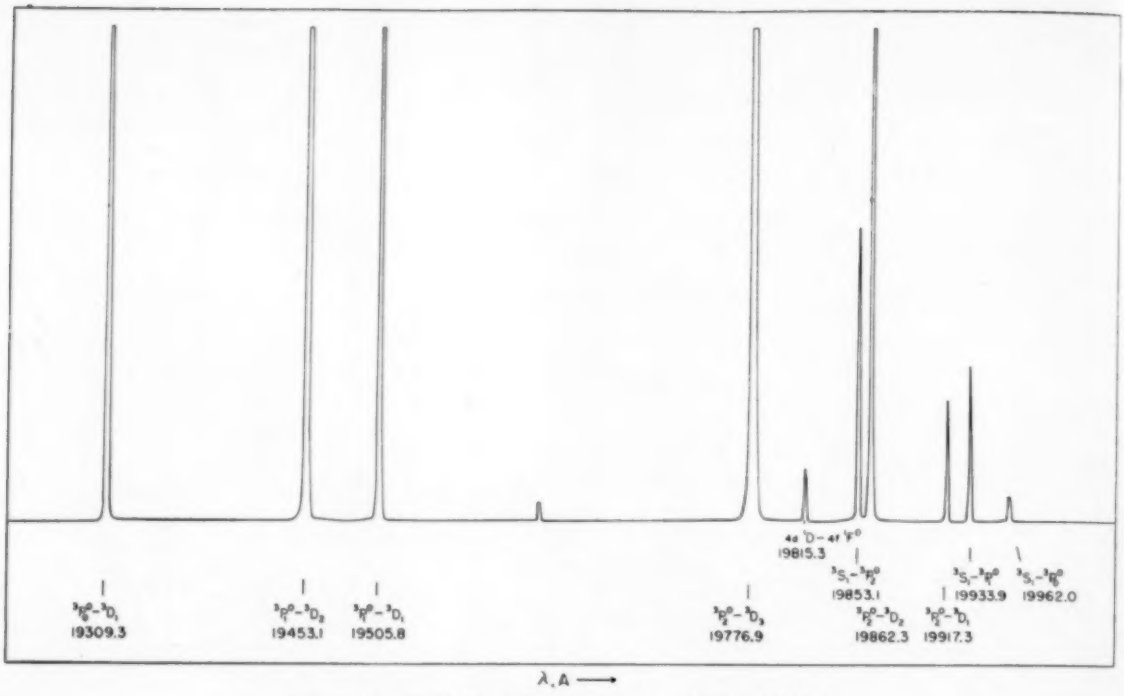

FIGURE 4. *Multiplets of* Ca I *in the region 19300 to 20000 A.*

5. Conclusion

This work can hardly be said to complete the analysis of Ca I, although it has remedied the outstanding deficiency in the term array. None of the singlets either from $3d^2$ or $3d\ 4d$ is known. It is probable that most of the required combinations are in the photographic infrared in the region obscured by the (0, 0) CN band.

Further observation in the regions free of interference does not appear profitable. These experiments were undertaken as part of a larger program including the other alkaline earths. This report on calcium was prepared because of a very urgent and long-standing need for further information regarding its term structure, having in mind especially the monograph that Professor Russell has proposed. Similar observations on strontium and possibly barium are expected to yield comparable results.

The assistance of M. E. Anderson in the preparation of drawings, reproduction of records, and reduction of data, and of A. J. Cussen, in maintaining and improving the performance of the electronic accessories of the spectrometer, is gratefully acknowledged.

6. References

[1] Charlotte E. Moore, Atomic energy levels, NBS Circular 467 **I**, 242 (1949).
[2] F. Paschen and R. Götze, Seriengesetze der Linienspektren (Springer, Berlin, 1922).
[3] A. Fowler, Report on series in line spectra (Fleetway Press, London, 1922).
[4] H. N. Russell and F. A. Saunders, Astroph. J. **61**, 38 (1925).
[5] F. Hund, Linienspektren und periodisches System der Elemente (Springer, Berlin, 1927).
[6] E. K. Plyer and M. A. Lamb, J. Research NBS **45**, 204 (1950) RP2125.
[7] C. C. Kiess, Astroph. J. **109**, 551 (1948).
[8] G. Herzberg and J. G. Phillips, Astroph. J. **108**, 163 (1948).
[9] H. D. Curtis, J. Opt. Soc. Am. and Rev. Sci. Instr. **8**, 697 (1924).
[10] F. Paschen, Ann. Physik. **29**, 625 (1909).
[11] H. M. Randall, Ann. Physik **33**, 739 (1910).
[12] O. Sandvik and B. J. Spence, Astroph. J. **62**, 265 (1925).
[13] H. D. Babcock, Phys. Rev. **46**, 382 (1934).
[14] L. Goldberg, O. C. Mohler, A. K. Pierce, and R. R. McMath, Astroph. J. **111**, 565 (1950).
[15] N. E. Wagman, Univ. Pittsburgh Bul. **34**, 1 (1937).

WASHINGTON May 4, 1951,

Journal of Research of the National Bureau of Standards Vol. 47, No. 4, October 1951 Research Paper 2253

Crystallization of Aluminum Chloride in the Hydrochloric Acid Process for Production of Alumina From Clay

Lewis Jesse Clark, Willard D. Hubbard, and James I. Hoffman

When roasted clay is treated with dilute hydrochloric acid, a solution is obtained that contains aluminum and other soluble constituents of the clay in the form of chlorides. Crystallization as the hydrated chloride, $AlCl_3 \cdot 6H_2O$, serves to separate the aluminum from the other soluble chlorides. A process is described for this crystallization on a large scale.

1. Introduction

In 1946 a hydrochloric acid process for the production of alumina from clay [1] was described, which involved the following steps: (1) roasting the clay at about 700° C, (2) digesting the roasted product in dilute hydrochloric acid, (3) filtering to separate the insoluble siliceous matter from the solution containing the aluminum and soluble impurities such as iron and alkali salts, (4) concentrating the solution, (5) precipitating the aluminum as the hydrated chloride from the concentrated solution by adding gaseous hydrogen chloride; (6) removing the crystals of hydrated aluminum chloride, (7) washing the crystals to remove adhering impurities, (8) calcining the hydrated chloride to obtain alumina, and (9) recovering hydrochloric acid from the waste products at the end of the process. The process is outlined in the flow sheet in figure 1.

Alumina of satisfactory purity was obtained, but the precipitation of aluminum chloride hexahydrate ($AlCl_3 \cdot 6H_2O$) by saturating the solution with hydrogen chloride (step 5) resulted in considerable loss of hydrochloric acid. This in turn caused an unreasonable amount of corrosion with consequent deterioration of equipment. The present discussion is concerned with an improvement of step 5, that is, the separation of the aluminum from the other constituents of clay that are soluble in hydrochloric acid.

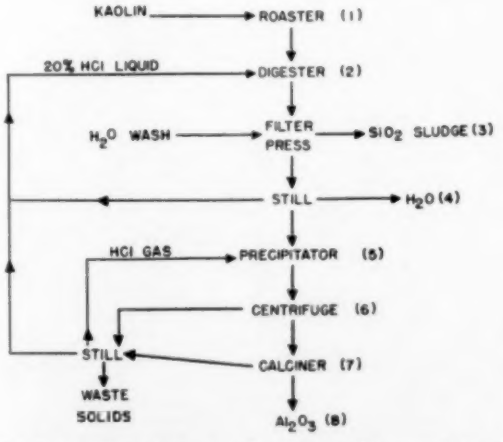

FIGURE 1. *Flow sheet of hydrochloric acid process for the extraction of alumina from clay.*

[1] James I. Hoffman, Robert T. Leslie, Harold J. Caul, Lewis Jesse Clark, and John Drake Hoffman, J. Research NBS **37**, 409 (1946) RP1756.

In the paper cited, evaporation of the solution until a slurry of crystals formed was mentioned as a means of separating the hydrated aluminum chloride, but during the war, when this work was being done, the necessary equipment was not available. Evaporation with the resultant formation of crystals in hot solution seemed especially well suited for the precipitation of hydrated aluminum chloride because its solubility does not vary much with change in temperature.[2]

2. Crystallization Without Mechanical Stirring

For good plant operation it seemed obvious that considerable agitation of the solution would be necessary during distillation and crystallization. To obtain such agitation without mechanical stirring, the evaporator shown in figure 2 was designed. It consisted of a Karbate heat exchanger, *A*, connected to a settling tank, *B*. The solution, which was nearly saturated with respect to aluminum chloride, was pumped into the heat exchanger and settling tank assembly so that the level of the solution was somewhat above the inlet of the settling tank (*C* in fig. 2). This required about 125 gal in the assembly shown. The solution was then heated by means of steam at gage pressures up to 40 lb/in^2. As soon as the steam was turned on, the solution in the Karbate tubes within the steam jacket (*D* in fig. 2) started to rise, and at the boiling temperature a vigorous circulation resulted.

[2] According to Solubilities of inorganic and metal compounds, 3d ed. **I**, by Atherton Seidell (D. Van Nostrand Co., 1940) the solubility of hydrated aluminum chloride, $AlCl_3 \cdot 6H_2O$, in water is 57.2 g per 100 g of solution at 25° C and 59.6 g per 100 g of solution at 100° C. Approximate determinations in our control laboratory indicated the following solubilities in dilute hydrochloric acid:

Temperature	Specific gravity of acid	Solubility	
		g/100 g solution	*lb/gal*
°C			
25	1.03	50.4	5.6
100	1.03	54.7	6.0
25	1.06	41.0	4.5
100	1.06	46.8	5.

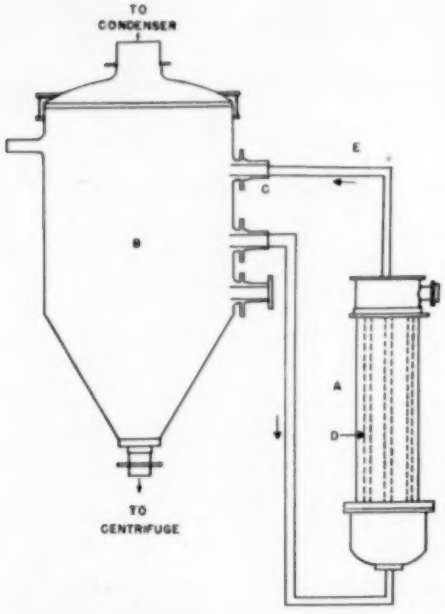

FIGURE 2. *Evaporator without mechanical stirrer.*

The boiling point of the solution remained practically constant (124° C) while crystals were separating. From a knowledge of the volume of the solution in the assembly and of the distillate, together with the concentration of aluminum chloride in the solution in the beginning and at the time of filtration, the approximate weight of crystals could be calculated. With the assembly described, the intention was to evaporate a sufficient volume of acid to produce about 200 lb of the hydrated chloride before separating the crystals from the mother liquor, but an unforeseen difficulty arose. In the glass pipe leading from the heat exchanger to the settling tank (*E* in fig. 2) bubbles broke, and vapor escaped so rapidly that crystals formed on the inside surface. By the time approximately 100 lb of chloride had separated, this pipe became completely clogged and the distillation had to be discontinued. In addition to the clogging just described, crystals had a tendency to deposit on the gaskets in the pipe lines throughout the system. These deposits on the gaskets resembled doughnuts. If the distillation was continued long enough, the holes in these doughnut-like deposits closed up entirely, and the circulation stopped. In attempts to prevent the formation of these deposits, gaskets, joints, and right angles were entirely eliminated at critical points (*E* to *C* in fig. 2). Pipes of Karbate, Haveg, and glass were selected for smoothness of inside surface, but in all cases the deposits eventually stopped the circulation.

This system of producing crystals was quite satisfactory up to the point where clogging occurred, but because of this difficulty, this evaporator was abandoned in favor of the evaporator described in the next section.

3. Crystallization With Mechanical Stirring

The glass-lined steam-jacketed evaporator, shown in figure 3, is commercially available [3] and is provided with a motor-driven mechanical stirrer. The nearly saturated solution was pumped into the evaporator, and steam at 10 to 40 lb/in.^{2} was maintained in the jacket while the solution was mechanically agitated. The approximate quantity of crystals was calculated, as was done in operating the first evaporator. Experience showed that the best slurry for filtering was one that contained 3 to 3.6 lb of aluminum chloride, $AlCl_3 \cdot 6H_2O$, in a gallon of liquid. In this evaporator no clogging occurred during evaporation. The process is entirely satisfactory if the slurry is cooled and immediately filtered. For best operation, the slurry should not stand overnight because of dense packing of crystals in the bottom of the evaporator and consequent difficulty of starting the flow to the centrifuge.

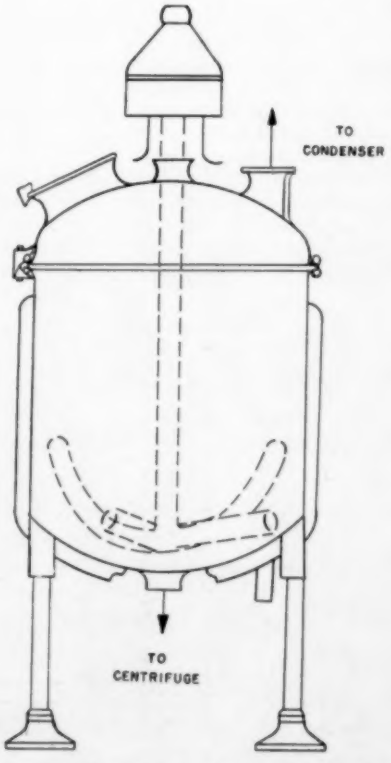

FIGURE 3. *Evaporator with a mechanical stirrer.*

[3] The evaporator used in our plant has a capacity of 100 gal and was purchased from the Pfaudler Co., Rochester, N. Y. Similar equipment can be purchased from Glascote Co., Cleveland, Ohio.

The acid distillate obtained with this, as well as with the Karbate evaporator, had a specific gravity of about 1.03.

4. Separation of the Crystals From the Mother Liquor

The crystals of aluminum chloride were separated from the mother liquor by means of a rubber-coated centrifuge in the manner described in the original article (see footnote 1). Before filtration, the slurry was cooled to about 40°C, because rubber-coated equipment deteriorates more rapidly at higher temperatures, and because filtration without preliminary cooling usually results in a glaze over the filter cloth, which slows the flow of the liquid through the cloth. The cooling in both crystallizers was accomplished by cutting off the steam and running tap water through the steam jacket.

The purity of the crystals obtained was about the same as in the process described in the original article.

5. Cost of Precipitating Aluminum Chloride Hexahydrate

During the evaporation of the solutions, the steam condensate was collected and the heat input calculated. This value is undoubtedly higher than it should be in good plant operation because the evaporators were not insulated. The results are as follows:

The first evaporator required 16,800,000 Btu a ton of alumina, equivalent to $6.75 on the basis of coal. The second evaporator required 18,336,000 Btu a ton of alumina, equivalent to $7.36 on the basis of coal.

In the original process 4,980,000 Btu were required for producing the gaseous hydrogen chloride used in step 5. This was equivalent to $2.00 a ton of alumina on the basis of coal at $6.00 a ton. In addition, there was a loss of hydrochloric acid in step 5 amounting to $29.85 a ton of alumina. The loss of acid in this step is entirely eliminated by the process just described. With the glass-lined evaporator the cost of crystallizing aluminum chloride, equivalent to 1 ton of alumina, is therefore only $7.36 as compared with $31.85 by the original process ($29.85 for loss of acid and $2.00 for heat in step 5). This represents a saving of $24.49. The total cost for all the steps in the original process is $109.13. This improvement in step 5 therefore represents a saving of 22.4 percent.[4] With reasonable insulation of the equipment the saving may easily be 25 percent.

The authors acknowledge the assistance of Herbert Lowey for his contributions to the mechanical operation of the plant, to George Derbyshire for his assistance in the operation of the Karbate evaporator, and to John Drake Hoffman, who did the laboratory work on which the process is based.

[4] For original figures on cost, see J. Research NBS 37, 425 (1946) RP1756.

Washington, May 8, 1951

Journal of Research of the National Bureau of Standards Vol. 47, No. 4, October 1951 Research Paper 2254

Creep of Annealed and Cold-Drawn High-Purity Copper

William D. Jenkins and Thomas G. Digges

A study was made of the effect of temperature and stress on the creep behavior at 110°, 250°, and 300° F of high-purity oxygen-free high-conductivity copper initially as annealed and as cold-drawn 40-percent reduction of area. The resistance to creep and to fracture at all these test temperatures was increased by cold-drawing the copper prior to testing in creep; however, this superiority in creep properties was accompanied by a decrease in ductility and time to rupture. Dissociation of parent grains into crystals of microscopic dimensions and the presence of strain markings were evidenced in all specimens carried to complete fracture in creep. Correlations are made of these changes in structure with time, stress, temperature, and the discontinuous flow, as evidenced by the creep rate-extension curves.

1. Introduction

The results of creep tests made at different temperatures on annealed high-purity (OFHC) copper were described in a recent paper [1].[1] It was found that the strain rate in the second stage was not constant, and the formation of cracks of microscopic dimensions often accompanied but was not necessarily a prerequisite for the initiation of the third stage of creep in this material. Furthermore, the original grains of the annealed copper broke down into subsize grains under varying test conditions, and strain markings were present in all specimens fractured in creep. As a part of a continuing study of the creep behavior of high-purity metals and binary alloys, additional creep tests have been completed on specimens prepared from this same lot of copper in the initial conditions both as annealed and as cold-drawn 40-percent reduction in area. The creep tests were made at different strain rates and at temperatures of 110°, 250°, and 300° F. The creep tests were supplemented by hardness and tensile tests at room temperature and by a metallographic examination of specimens representative of the initial conditions of the copper and of the different stages of creep and fracture. These results are summarized in the present report.

2. Material and Testing Procedures

Some of the properties at room temperature of the high-purity copper (99.99+% of copper) in the initial conditions as annealed and as cold-drawn 40-percent reduction in area are given in table 1.

All specimens of the annealed material were prepared from the same bar as that used previously [1], and the test specimens of the cold-drawn copper were prepared from another bar, originally from the same heat. The testing procedures and apparatus have been already described in some detail [1, 2]. Essentially, the creep specimens were machined to 0.505-in. diameter and 2.0-in. gage length. Each specimen was held at a test temperature of 110°, 250°, or 300° F for 48 hrs before loading to the desired creep stress at a controlled rate of 3,200[2] psi/hr for the annealed and 5,333 psi for the cold-drawn specimens (3,200 or 5,333 psi added at 1-hr intervals); each creep test was made at a constant load. The temperatures of the creep furnaces were controlled within the range of about ±1° F of the desired temperatures, and the probable error in measuring the extensions was less than 0.00002 in.

TABLE 1. *Grain size and mechanical properties at room temperature of the copper used*

[The tensile tests were made at a rate of extension of approximately 1 percent per minute]

Property	Initial condition	
	Annealed	Cold-drawn (40% reduction in area)
Average grain diameter, mm	0.025	
Average hardness, Rockwell F	34	86
Tensile strength, 1,000 psi	31.9	51.1
Yield strength (0.2% offset), 1,000 psi	12.2	50.3
Elongation in 2 in., percent at maximum load	39	0.7
Elongation in 2 in., percent at fracture	51	11
Reduction of area, percent at maximum load	28	0.68
Reduction of area, percent at fracture	88	80

Hardness tests were made at room temperature on all specimens fractured in creep. Two flats 180° apart were prepared parallel to the longitudinal axis of the specimen after fracturing and Rockwell readings (F scale, 60-kg load, 1/16-in. diameter ball) were made at various points along the center line of these flats. Metallographic examinations were made of specimens representative of the copper as annealed, cold-drawn, and deformed in creep.

3. Results and Discussion

3.1. Influence of Temperature, Stress, and Rate of Loading of Creep Behavior

The resistance to flow of the cold-drawn copper decreased as the test temperature was increased

[1] Figures in brackets indicate the literature references at the end of this paper.

[2] A rate of loading of 3,200 psi/hr (a load of 3,200 psi, added at 1-hr intervals) was selected as a standard rate for the annealed copper previously tested in creep [1]. As the area of an annealed specimen is reduced to three-fifths of its original area by cold-drawing 40-percent reduction of area, the cold-drawn specimens were loaded in intervals of 3,200×5/3=5,333 psi.

(fig. 1); the stress-strain curves for specimens tested at 250° and 300° F were nearly alike for stresses ranging up to about 15,000 psi.

Extension-time curves for specimens prepared from cold-drawn copper and annealed copper are given in figures 2 to 6.

It is a common belief that the extension at fracture of a metal or alloy tested in creep usually increases as the time to initiate each stage and to fracture decreases. However, with the high-purity copper, the extension-time relationship varied depending upon the test conditions (temperature, strain rate, history, etc.) For example, with the initially cold-drawn copper at 110° F, two specimens (fig. 2, tests 4 and 3) had the same extension at fractures, but the times to fracture were 28 and 236 hr, respectively. At 250° F (fig. 3), the extension in two specimens increased as the time to fracture increased (tests 8 and 7), and then the extension in another specimen decreased with a further increase in time to fracture (tests 7 and 6). At 300° F (fig. 4), the extension at fracture decreased continuously as the time to fracture increased. At 80° F (table 1), the extensions at the maximum load and at fracture were less than the extensions at the beginning of the third stage and at fracture, respectively, of many of the specimens tested under creep conditions; at 80° F, the time to fracture was only about 1 hr. At constant temperature, reversals also were observed in the extension-time relationship at the beginning of the third stage (table 2), but the time to the beginning of the third stage and to fracture increased continuously with decrease in creep stress. At constant creep rate (average in second stage), the time to attain the third stage and the extent of this stage both increased with increase in test temperature. These features should be considered in the commercial application under conditions of creep of cold-drawn copper and the interpretation of stress-rupture data.

With annealed copper, the characteristics of the extension-time curves were similar to those previously described [1]. In the present tests (fig. 5), the extensions at the beginning of the second stage, third stage, and at fracture usually decreased with increase in the duration of the creep test at each temperature investigated. An important feature, however, was shown in the creep behavior after the beginning of the third stage of a specimen tested at 110° F and with a relatively slow rate (2.75%/1,000

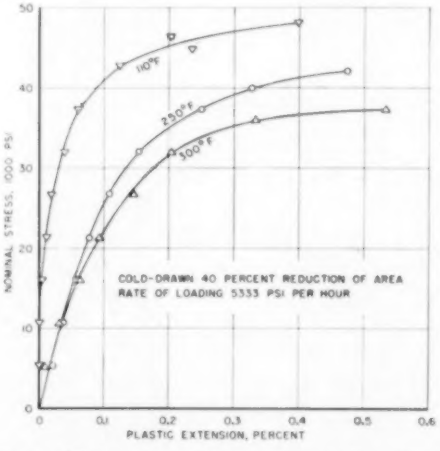

FIGURE 1. *Effect of nominal stress on plastic extension of cold-drawn copper at different temperatures.*

The values for extension are those obtained after the application of the loads for a period of 1 hour

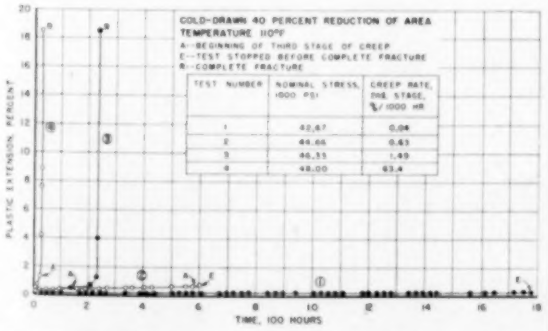

TEST NUMBER	NOMINAL STRESS, 1000 PSI	CREEP RATE, 2ND STAGE, %/1000 HR
1	42.67	0.04
2	44.66	0.63
3	46.33	1.49
4	48.00	63.4

FIGURE 2. *Extension-time curves for cold-drawn copper specimens tested in creep at 110° F.*

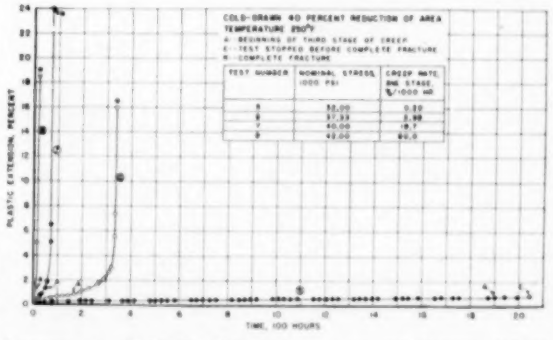

TEST NUMBER	NOMINAL STRESS, 1000 PSI	CREEP RATE, 2ND STAGE, %/1000 HR
9	32.00	0.39
8	37.33	3.98
7	40.00	19.7
6	42.00	80.0

FIGURE 3. *Extension-time curves for cold-drawn copper specimens tested in creep at 250° F.*

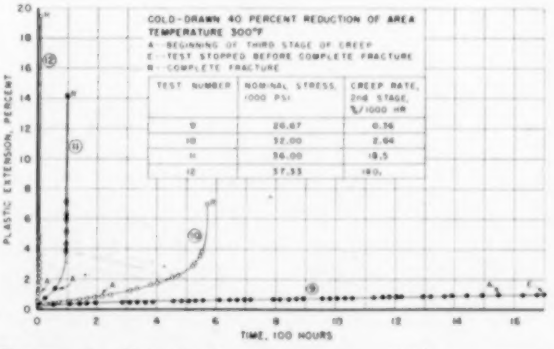

TEST NUMBER	NOMINAL STRESS, 1000 PSI	CREEP RATE, 2ND STAGE, %/1000 HR
9	26.67	0.36
10	32.00	2.94
11	36.00	18.5
12	37.33	190.

FIGURE 4. *Extension-time curves for cold-drawn copper specimens tested in creep at 300° F.*

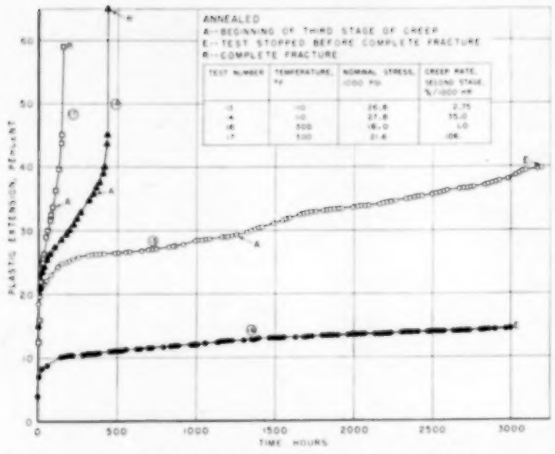

FIGURE 5. *Extension-time curves for annealed copper specimens tested in creep at 110° and 300° F.*

hr, test 13). After the beginning of the third stage (point A), the creep rate materially increased and continued in excess of the average rate in the second stage for a period of about 500 hr. At the end of this period the specimen attained an average creep rate of 3.8 percent per 1,000 hr for a period of about 1,000 hr before again increasing rapidly.

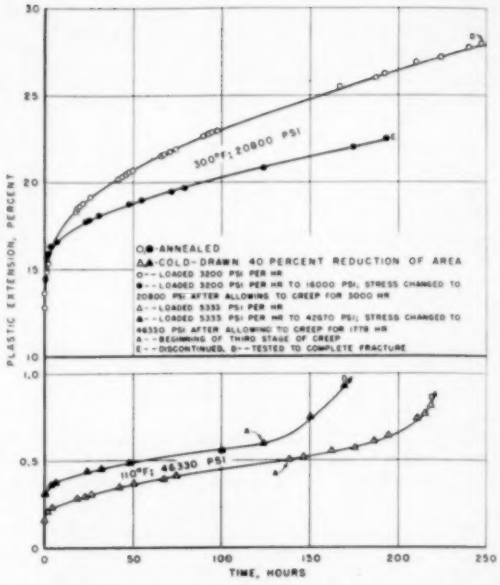

FIGURE 6. *Effect of rate of loading on creep of annealed copper at 300° F and of cold-drawn copper at 110° F.*

TABLE 2. *Results of creep tests on high-purity copper initially as bright annealed and as cold-drawn 40-percent reduction of area*

Number	Test temperature	Nominal creep stress	Average creep rate, second stage	Beginning of third stage			End of test				Remarks
				Time	Plastic extension	True stress	Time	Plastic extension	Reduction of area	True stress	
A. Annealed; rate of loading, 3,200 psi/hr											
	°F	1,000 psi	%/1,000 hr	hr	% in 2 in.	1,000 psi	hr	% in 2 in.	%	1,000 psi	
18	110	25.6	1.08	------	------	------	943	19	16	30.5	Test stopped in second stage.
13	110	26.8	2.75	1,250	29.2	34.6	3,194	39.7	28.1	37.3	Test stopped in third stage.
14	110	27.8	35	340	35.7	37.7	435	65	90	289	Tested to complete fracture.
19	110	28.8	165	105	42.2	40.9	123	62.5	89.7	278.6	Do.
21	250	16	0.33	------	------	------	2,472	8.94	8.19	17.4	Test stopped in second stage.
15	250	19.2	1.04	------	------	------	8,454	23.14	18.8	23.6	Do.
22	250	22.4	10.1	1,248	35.7	30	1,824	48.9	34.3	34.1	Test stopped in third stage.
23	250	24	130	134	41.2	33.9	168	59.4	78.7	112.4	Tested to complete fracture.
16	300	16	1	------	------	------	3,000	14.43	12.6	18.3	Tested into second stage. Stress changed to 20,800 psi and test continued as 16A.
[a] 16A	300	20.8	24.5	------	------	------	193	22.5	16.7	21.4	Test stopped in second stage.
24	300	19.2	8.3	990	25.4	24.1	1,522	36.5	33	28.8	Tested to complete fracture.
20	300	20.8	36.4	335	31.4	27.5	439	46	46.7	39	Do.
17	300	21.6	106	90	33.5	28.9	154	59	61.1	55.5	Do.
B. Cold-drawn, 40-percent reduction of area; rate of loading, 5,333 psi/hr											
1	110	42.67	0.04	------	------	------	1,778	0.25	0.25	42.8	Tested into second stage. Stress changed to 46,330 psi and test continued as 1A.
[b] 1A	110	46.33	1.6	125	0.6	46.9	194	20	83.6	282.5	Tested to complete fracture.
2	110	44.66	0.63	587	.69	45	600	0.73	0.7	45.1	Tested stopped in third stage.
3	110	46.33	1.49	140	.50	46.6	236	18.5	84.2	293.6	Tested to complete fracture.
4	110	48	63.4	20	1.3	48.6	28	18.5	83.2	285.6	Do.
5	250	32	0.20	1,900	0.72	32.3	2,041	0.73	0.89	33	Test stopped in second stage.
6	250	37.33	2.98	160	.85	37.8	335	16	52.3	78.2	Tested to complete fracture.
7	250	40	19.7	50	1.3	40.6	74	24	67.2	122	Do.
8	250	42	80	13	1.38	42.6	18	18.5	78.1	193.9	Do.
9	300	26.67	0.36	1,550	0.94	26.9	1,701	0.98	0.79	26.9	Test stopped in second stage.
10	300	32	2.64	220	.85	32.3	569	7	12.3	36.5	Tested to complete fracture.
11	300	36	18.5	60	1.4	36.5	98	14.2	41.5	61.5	Do.
12	300	37.33	180	4	1.03	37.7	7	19.5	78.3	172.2	Do.

[a] For prior thermal-mechanical history, see test 16. Final stress of 4,800 psi applied instantaneously. Temperature unchanged throughout the test.
[b] For prior thermal-mechanical history, see test 1. Final stress of 3,660 psi applied instantaneously. Temperature unchanged throughout the test.

Creep curves of this type have been observed by Burghoff and Mathewson [3] with single crystals of brass, and Cottrell and Aytekin [4] with single crystals of zinc. The shape of the curve appears to indicate a localized softening effect followed by a strain hardening process that prevents further extension in that region. However, the remaining regions in which the hardening process has been not so effective continue to extend at a rate suggestive of the normal strain hardening-recovery process, which is known to exist during the third stage.

Although the resistance to creep and to fracture was significantly increased by cold-drawing, the copper (as compared to the annealed condition), the superiority in these properties as exhibited in the cold-drawn condition was attended by a marked decrease in plastic extension at each temperature used in the creep tests.

The effects of rate of loading on creep behavior of ingot iron and on annealed copper have been previously described [2, 1]. Additional data obtained on both annealed and cold-drawn copper are presented in figure 6 and table 2. The extension-time curves for the annealed specimens (fig. 6) indicate that, after an initial adjustment period (first stage) and at equal values of time, the creep rate at 300° F was greater for the specimen loaded in the usual manner than for the specimen allowed to creep for 3,000 hr before the application of the same stress (20,800 psi). The extension-time curves obtained at 110° F on cold-drawn specimens indicate that the creep rate, for equal values of time, extensions at the beginning of third stage and at fracture were greater for the specimens loaded slowly than for the specimens loaded relatively fast to a stress of 46,330 psi; the time for initiation of third stage and to fracture was greater for the specimen loaded relatively rapidly.

While the observations made on the annealed specimens appear inconsistent with some of the previous results, they also serve to emphasize the importance of the rate of loading, together with temperature and strain rate on the mechanism of deformation of high-purity copper.

3.2. Influence of Stress and Temperature on the Average Creep Rate in the Second Stage

The relation between nominal [3] stress and creep rate (average in the second stage) at 110°, 250°, and 300° F for both annealed and cold-drawn copper is shown by the curves of figure 7. The smooth curves connecting the experimental values as plotted on a semilog basis (fig. 7) or on a log-log basis (not shown) are nonlinear. The sigmoidal curves obtained for some of the test conditions (110° F) indicate the existence of threshold stresses below which the resulting creep rates are nil. At relatively high stresses, the rate of creep at each temperature increased markedly with a further increase in stress.

Obviously the resistance to creep was materially increased by cold-drawing the copper 40-percent

[3] The nominal stress is defined as the stress obtained by dividing the current load by the original area of the specimen.

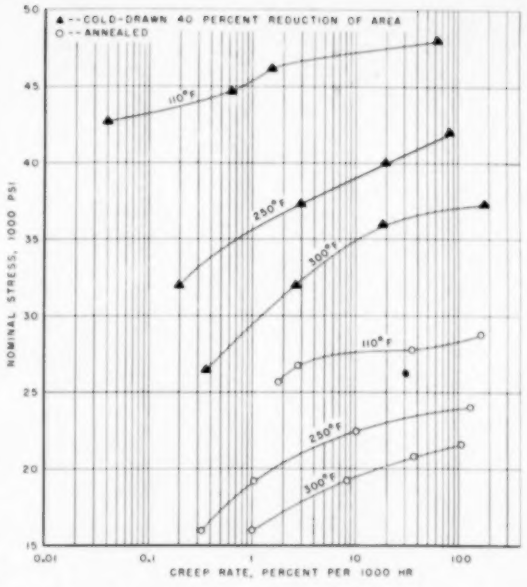

FIGURE 7. *Relation between nominal stress and creep rate at different temperatures.*

reduction in area (fig. 7). This superiority of the copper in the initially cold-drawn condition increased as the test temperature was decreased. Thus, prestraining at a fast rate at room temperature (cold-drawing) improves the creep strength of high-purity copper, and this or other cold-working processes might be very useful in certain commercial applications.

The greater resistance to creep of the cold-drawn copper is still manifested even where comparison of the creep rates of the two initial conditions is made on the basis of equivalent [4] stress values (fig. 8). If the second-stage creep rates of the copper were independent of the prior strain history, similar or identical curves should be obtained at each test temperature for both the annealed and cold-drawn specimens. At each temperature, the strength of the cold-drawn copper is superior to that of the annealed.

Comparison of the performance of the copper also can be conveniently made on the basis of the true stress [5] at the beginning of the third stage (table 2). Again, at each temperature, the stresses required to produce equivalent creep rates were greater for the cold-drawn than for the annealed condition. As will be shown later, however, the increase in creep resistance brought about by cold-drawing the copper was attended by an appreciable decrease in creep extension at the operating temperatures.

[4] Equivalent stress is defined as the stress obtained by dividing the current load by the original area in the annealed condition (before cold-drawing).

[5] The true stress is defined as the stress obtained by dividing the current load by the current area of the specimen.

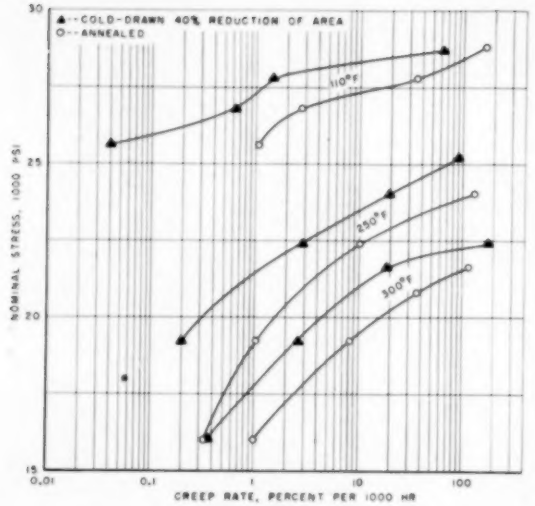

FIGURE 8. *Relation between equivalent nominal stress and creep rate at different temperatures.*

3.3. Variation in Creep Rate With Plastic Extension and Time

A number of theories have been advanced to explain the relationship between extension and time during the first stage of creep. Among the proposals that have received considerable attention are those of Andrade [5] and Mott and Nabarro [6]. Andrade's analysis postulates that in the transient portion of the creep curve (first stage) the strain varies linearly with the one-third power of the time. Application of this concept would require that all curves for metals and alloys in the transient region should have a slope of minus two-thirds when the logarithm of the creep rate is plotted against the logarithm of time. Accordingly, the slope should be independent of test temperature and applied stress. Mott and Nabarro, however, developed a theory for exhaustion creep in which the strain was found to be proportional to a value dependent on the applied shear stress, absolute temperature to the two-thirds power, and the logarithm of the time to the two-thirds power.

The relation between creep rate and time during the first stage of creep of the annealed and cold-drawn copper is shown in figure 9. The present results are consistent with those previously shown [1, 2, 7]. For any constant temperature used, the creep rate-time cycles are more evident at the lower than at higher stresses, and the slopes of the curves (as drawn through average values) tend to increase as the stress is increased. Obviously, the slopes of these curves are approximately equal only when the mechanisms of deformation for the specimens under consideration are approximately equivalent.

It has been suggested [1] that deformation during creep occurs by a discontinuous process. The relationship between creep rate and plastic extension occurring during creep of the cold-drawn copper is shown in figures 10, 11, and 12. The magnitude of the creep rate-extension cycles is greater during the second stage than in either the first or third stage. At constant temperature, moreover, the magnitude and frequency of occurrence of these cycles are decreased as the stress is raised. The rate of loading also affects the occurrence of these cycles, as is illustrated by the two curves in figure 10 for specimens tested at a stress of 46,330 psi. These results confirm qualitatively those previously presented for ingot iron, annealed copper, and cold-drawn aluminum, and lends further credence to the belief that during second-stage creep there is a delay in the balance between strain hardening and recovery.

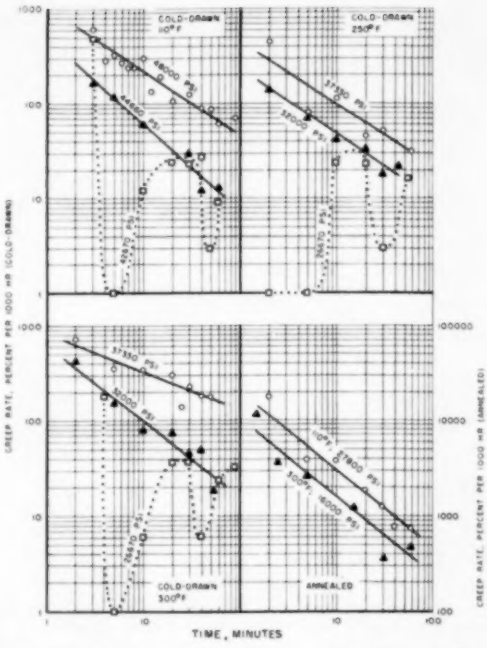

FIGURE 9. *Variation in creep rate in the first stage with time at different temperatures and with different nominal stresses.*

3.4. Effect of Creep Rate on Ductility

Previous results [1] of creep tests made with annealed copper indicated that, in general, the extension at the beginning of the third stage increased with increase in creep rate (constant temperature) and with a decrease in temperature (constant creep rate). However, it was pointed out that the increase in values for extension at the beginning of the third stage approached a limit beyond which the extension would not increase with an increase in creep rate or a decrease in test temperature.

The relation between creep rate (average, second stage) and plastic extension at the beginning of the

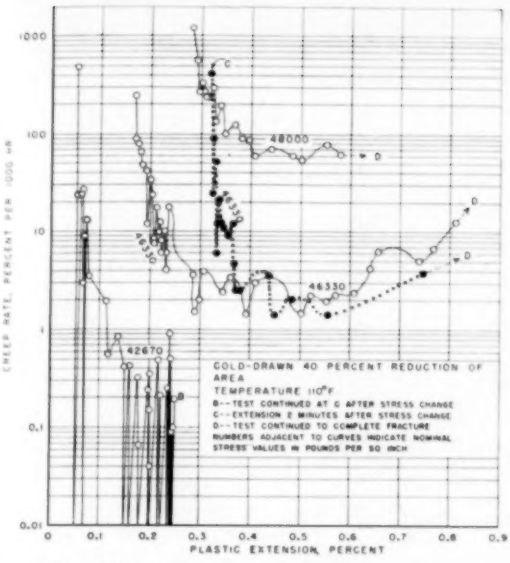
CREEP RATE, PERCENT PER 1000 HR
PLASTIC EXTENSION, PERCENT
48000
46330
42670
COLD-DRAWN 40 PERCENT REDUCTION OF AREA
TEMPERATURE 110°F
B--TEST CONTINUED AT C AFTER STRESS CHANGE
C--EXTENSION 2 MINUTES AFTER STRESS CHANGE
D--TEST CONTINUED TO COMPLETE FRACTURE
NUMBERS ADJACENT TO CURVES INDICATE NOMINAL STRESS VALUES IN POUNDS PER SQ INCH

FIGURE 10. *Variation in creep rate of cold-drawn copper with plastic extension at 110° F and with different nominal stresses.*

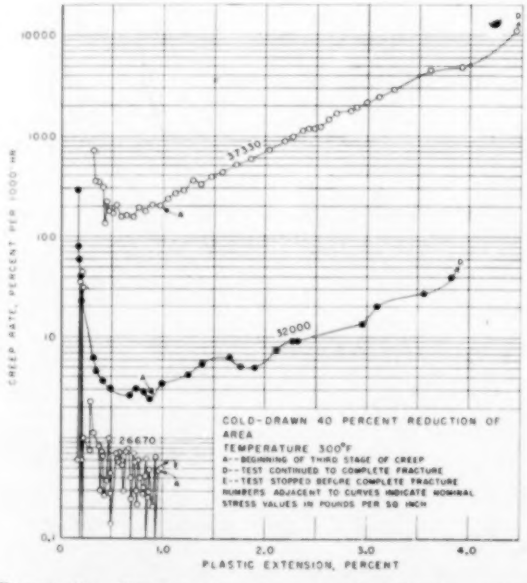
CREEP RATE, PERCENT PER 1000 HR
PLASTIC EXTENSION, PERCENT
37330
32000
26670
COLD-DRAWN 40 PERCENT REDUCTION OF AREA
TEMPERATURE 300°F
A--BEGINNING OF THIRD STAGE OF CREEP
D--TEST CONTINUED TO COMPLETE FRACTURE
E--TEST STOPPED BEFORE COMPLETE FRACTURE
NUMBERS ADJACENT TO CURVES INDICATE NOMINAL STRESS VALUES IN POUNDS PER SQ INCH

FIGURE 11. *Variation in creep rate of cold-drawn copper with plastic extension at 300° F and with different nominal stresses.*

third stage of creep of the cold-drawn copper is shown in figure 13. The general pattern of these curves, similar to those already presented, shows a series of reversals that depend upon the mode of deformation

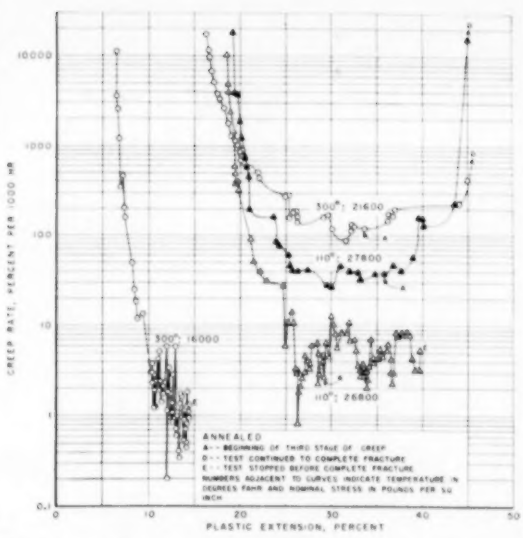
CREEP RATE, PERCENT PER 1000 HR
PLASTIC EXTENSION, PERCENT
300°; 21600
110°; 27800
300°; 16000
110°; 26800
ANNEALED
A--BEGINNING OF THIRD STAGE OF CREEP
D--TEST CONTINUED TO COMPLETE FRACTURE
E--TEST STOPPED BEFORE COMPLETE FRACTURE
NUMBERS ADJACENT TO CURVES INDICATE TEMPERATURE IN DEGREES FAHR AND NOMINAL STRESS IN POUNDS PER SQ INCH

Figure 12. Variation in creep rate of annealed copper with plastic extension at different temperatures and different nominal stresses.

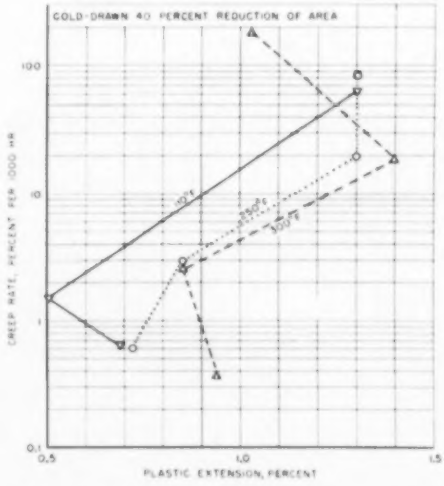

FIGURE 13. *Influence of creep rate on plastic extension at the beginning of the third stage of creep of cold-drawn copper at different temperatures.*

as affected by variations in both creep rates and in temperatures. That is, the balance between recovery and work-hardening of the initially cold-worked copper varied with the strain rate and test temperature in the creep tests. In some cases, recovery predominated, whereas in other cases work-hardening either predominated or just balanced the effect of recovery.

The effect of creep rate (average in second stage) on plastic extension and reduction of area at fracture

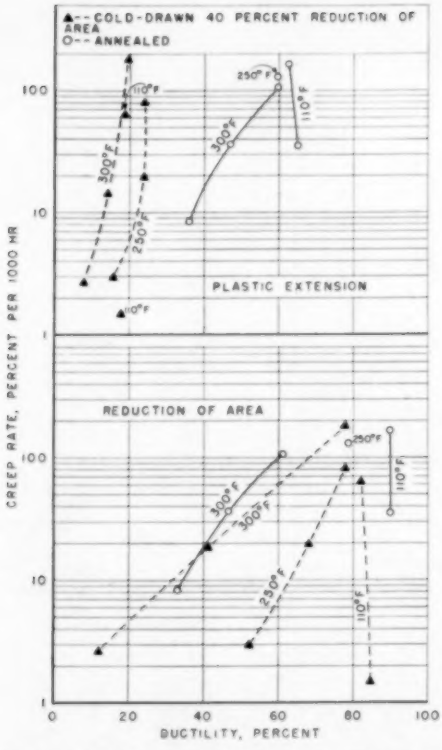

FIGURE 14. *Influence of creep rate on ductility at fracture of annealed and cold-drawn copper at different temperatures.*

(ductility) of both the annealed and cold-drawn copper is shown in figure 14. Regardless of creep rate or temperature used, the plastic extension at fracture was significantly greater for the annealed than for the cold-drawn copper, but this superiority in ductility in creep of the annealed condition was not always maintained when comparisons were made of the reduction of area values; at equivalent creep rates and a test temperature of either 250° or 300° F, the values for reduction of area were nearly alike for both conditions.

For the annealed copper, the values for plastic extension at fracture were of the same order of magnitude for all conditions used, except two tests made at 300° F. At this temperature, both the extension and reduction of area increased appreciably with an increase in creep rate. At 110° F, variations in creep rates over the range investigated had no material effect on the reduction of area.

For the cold-drawn copper, the trend was for the ductility at fracture to increase with an increase in creep rate at 250° and 300° F; the plastic extension at fracture did not materially change with an increase in creep rate from 20 to 80 percent per 1,000 hr. At 110° F, variations in creep rate had no appreciable effect on the ductility. At equivalent creep rates, the trend was for the reduction of area to

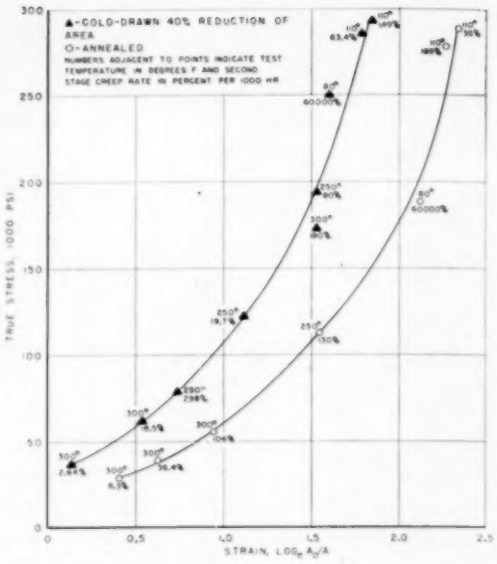
▲-COLD-DRAWN 40% REDUCTION OF AREA
O-ANNEALED
NUMBERS ADJACENT TO POINTS INDICATE TEST TEMPERATURE IN DEGREES F AND SECOND STAGE CREEP RATE IN PERCENT PER 1000 HR
TRUE STRESS, 1000 PSI
STRAIN, $\log_e A_0/A$

FIGURE 15. *Relation between true stress and strain at fracture of annealed and cold-drawn copper specimens tested at different temperatures and creep rates.*

increase as the test temperature was decreased, but no consistent relation was shown between the plastic extension at fracture and test temperature.

3.5. Relation of True Stress to True Strain at Complete Fracture

The effect of plastic deformation on the fracture stress of specimens tested at different temperatures and creep rates is shown in figure 15. At equal values for true-strain [6] in creep at fracture, the true-stress values for the cold-drawn copper are higher than those for the annealed copper. The gradual change in slopes of the smooth curves representing the locus of fracture in creep under varying conditions of temperature and strain rate indicate that there is a gradual change in mode of deformation during creep leading to fracture and in the mode of fracture of both the annealed and cold-drawn copper. However, the fact that no single displacement of values will cause the two curves to coincide supports the belief that these characteristics are affected by the prior strain history of the copper.

3.6. Influence of Strain History on Recovery

The effect of prior strain history on the stress-strain characteristics of annealed copper during unloading at the same temperature at which the creep test was carried out, was discussed in a previous paper [1]. Data obtained on additional specimens of annealed and of cold-drawn copper are

[6] True strain at fracture is the value obtained by taking the natural logarithm of the ratio of the initial cross-sectional area of the specimen prior to testing in creep to the cross-sectional area of the specimen at complete fracture.

ummarized in figure 16. The change in total extension (elastic and plastic) after completely unloading, was a maximum for the annealed specimen (curve 13) that was tested in creep with a stress of 26,700 psi. at a temperature of 110° F to an extension of approximately 40 percent. The slope of the curves for the two cold-drawn specimens (curves 5 and 9) was nearly alike (except for the somewhat greater contraction of specimen 9 upon the removal of the last stress), but their slope was different from those obtained for the annealed specimens (curves 13 and 15). This difference indicates that the recovery behavior of the high-purity copper is affected by its prior strain history.

3.7. Influence of Strain Rate, Temperature, and Deformation on Hardness at Room Temperature

The relation of hardness at room temperature and reduction of area to the distance from the fractured end of specimens tested in creep at 110°, 250°, and 300° F is given in figures 17, 18, 19, and 20. Provided necking occurs, it is to be normally expected that the hardness induced by deforming the copper in creep would attain a maximum in the vicinity of fracture (place of maximum deformation) and to decrease as the distance in the necked region is increased from the fractured surface. The present results, however, similar to those obtained previously [2], show that the hardness-distance from fracture curves and the propensity for the copper specimens to neck varied with the testing conditions (prior strain and mechanical history, strain rate, and temperature). Thus the maximum value for hard-

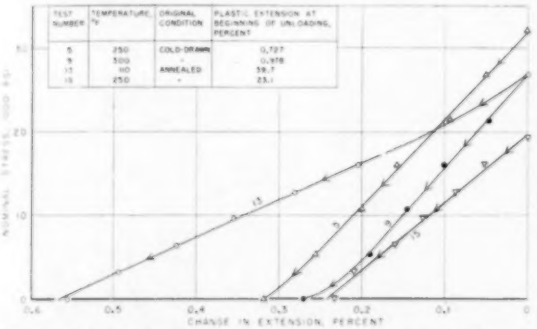

FIGURE 16. *Change in total extension during unloading of specimens of annealed and cold-drawn copper initially at different temperatures and stresses.*

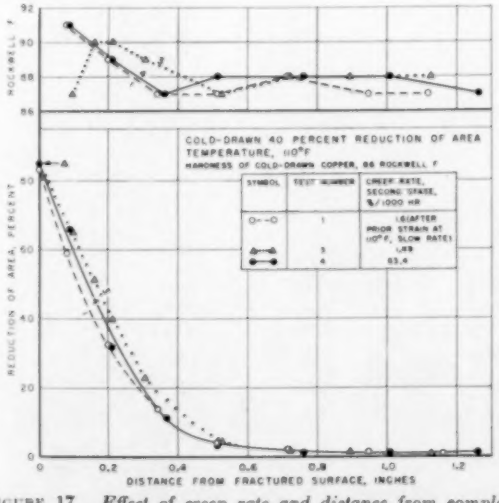

FIGURE 17. *Effect of creep rate and distance from complete fracture on reduction of area and hardness at room temperature of cold-drawn copper fractured at 110° F.*

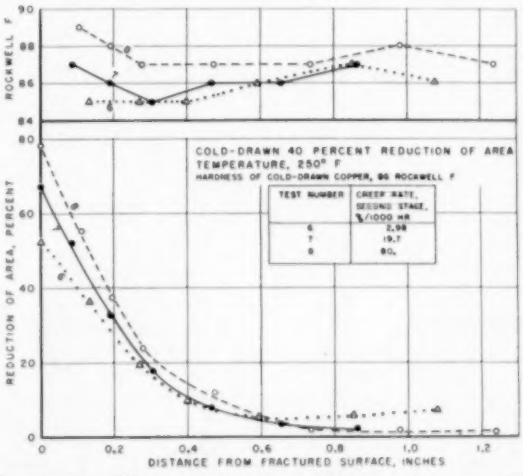

FIGURE 18. *Effect of creep rate and distance from complete fracture on reduction of area and hardness at room temperature of cold-drawn copper fractured at 250° F.*

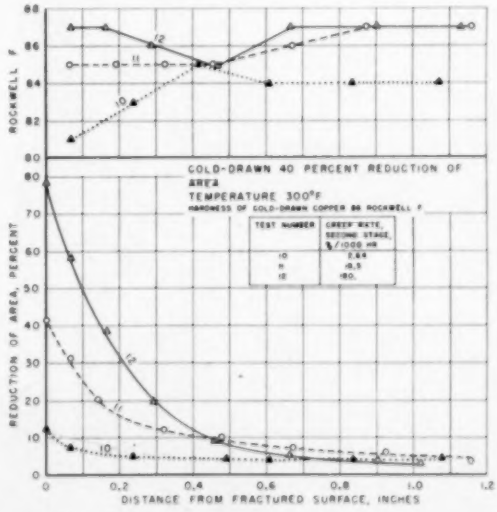

FIGURE 19. *Effect of creep rate and distance from complete fracture on reduction of area and hardness at room temperature of cold-drawn copper fractured at 300° F.*

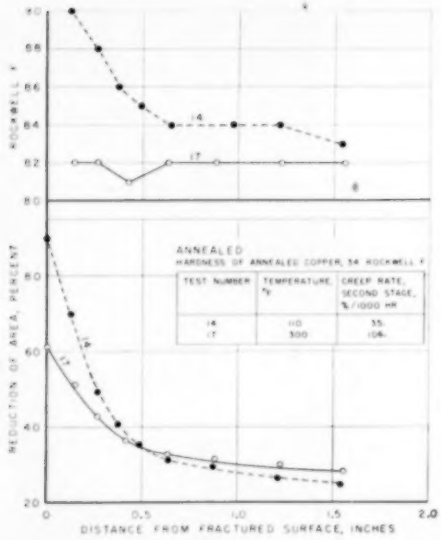

FIGURE 20. *Effect of temperature, creep rate, and distance from complete fracture on reduction of area and hardness at room temperature of annealed copper.*

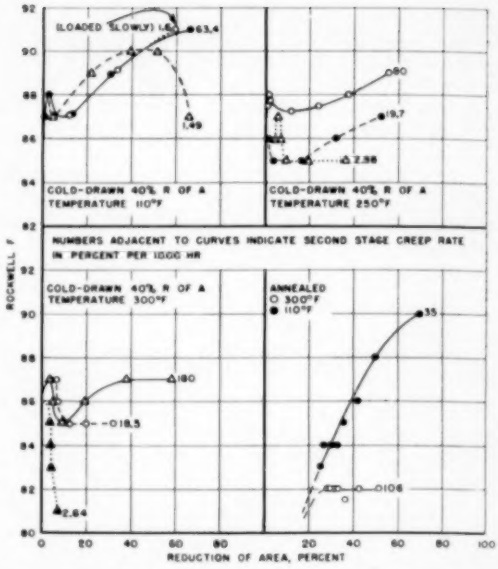
(LOADED SLOWLY) 1.6
63.4
1.49
COLD-DRAWN 40% R OF A TEMPERATURE 110°F
COLD-DRAWN 40% R OF A TEMPERATURE 250°F
NUMBERS ADJACENT TO CURVES INDICATE SECOND STAGE CREEP RATE IN PERCENT PER 1000 HR
COLD-DRAWN 40% R OF A TEMPERATURE 300°F
ANNEALED
300°F
110°F
ROCKWELL F
REDUCTION OF AREA, PERCENT

FIGURE 21. *Effect of plastic deformation at different temperatures and creep rates on hardness at room temperature.*

ness obtained in one or more specimens comprising each of the three series of cold-drawn copper (figs. 17, 18, and 19, respectively) was not at its fractured surface. In general, the degree of necking increased with an increase in creep rate and with a decrease in temperature (fig. 22).

For annealed copper (fig. 20), the hardness at room temperature was a maximum in the vicinity of the fracture of a specimen tested in creep at 110° F, but no material difference in hardness with distance from the facture end was obtained in a specimen tested at 300° F. Both of these specimens showed appreciable necking.

The change in hardness at room temperature with deformation (reduction of area) as affected by creep rate and temperature is illustrated in figure 21. The general trend was for the induced hardness to increase with creep rate and decrease in temperature.

3.8. Metallography

The influence of creep rate, temperature, and deformation on the structural and fracture characteristics of the initially cold-drawn copper is illustrated by representative photomicrographs reproduced in figures 23 to 27. The grains were elongated in the direction of drawing (figs. 23, A, and 26, A), and the elongated grains were further elongated during creep (fig. 23) in the direction of the applied stress; the degree of elongation varied with the test conditions as fast rates and low temperatures both favored this condition.

The fractures were predominantly transcrystalline in all specimens fractured in creep (fig. 23), although some intercrystalline cracking occurred at the deformation corresponding to the beginning of the third stage in a specimen tested at 300° F with a creep rate of 18.5%/1,000 hr (fig. 24, F). A general disintegration is evident even at the beginning of the third stage in this latter specimen, whereas cracks of microscopic dimensions in specimens tested at 110° or 250° F were confined principally to the vicinity of complete fracture. Thus, the beginning of the third stage of creep was attended by cracks of microscopic dimensions (fig. 24, F), but the presence of such cracks was not a prerequisite for the initiation of the third stage of creep in the initially cold-drawn copper (fig. 24, E). The evidence thus indicates that under slow creep rates cracks are nucleated at various sites in the vicinity of the axis of the specimen, and as the test continues these cracks grow and subsequently join (fig. 24, D) to form the main path of the complete fracture. In creep tests made at relatively high rates and low temperatures, cracking appears to be initiated solely at or near the axis of the specimen, and these cracks grow and extend outward to the periphery and the final fracture is that of the "rim." As the rim is the final section to fracture, the "flow lines" formed during the progress of the fracture follow the contour of the rim (figs. 24, B, and 25, A). The formation of a "neck" and the accompanying rim is accentuated by fast creep rates and low temperatures (fig. 22). Hence, the abnormal fracture stress often reported for high-purity copper can be attributed partly to this characteristic. When appreciable necking occurs, the fracture is predominantly transcrystalline (fig. 23).

The parent grains of the cold-worked copper (fig. 26, A) were also broken down during creep to subcrystals whose occurrence, size, and dimensions varied with the test conditions of temperature (fig. 26),

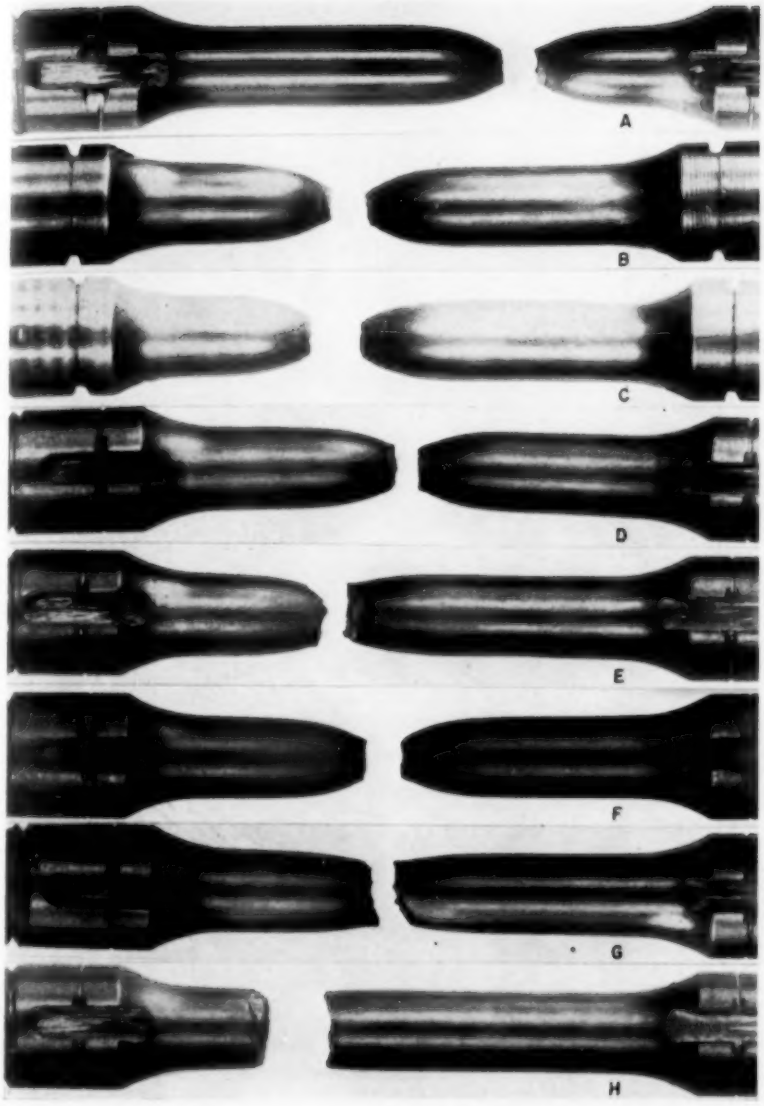

FIGURE 22. *Specimens of cold-drawn copper after fracturing at different temperatures and rates; ×1.*

	Test		Elongation in 2" in.	Reduction of area
	Temperature	Creep rate		
	°F	%/1000 hr	%	%
A	110	63.4	18.5	84.2
B	110	1.49	18.5	83.2
C	250	80	18.5	78.1
D	250	19.7	24	67.2
E	250	2.98	16	52.3
F	300	180	19.5	78.3
G	300	18.5	14.2	41.5
H	300	2.64	7	12.3

creep rate (fig. 27, A, and B) and deformation (fig. 27, C, and D). In some cases, only a portion of the parent grain broke down into subcrystals (fig. 27, B), and in other grains no subcrystals were observed (fig. 26, D). The general trend was for the size of these subcrystals to increase with the test temperature and deformation and with decrease in creep rate. For like test conditions, apparently the size of the subcrystals was appreciably smaller for initially cold-drawn than for the annealed copper. This condition is believed to be the result of the 40-percent reduction by cold-drawing prior to testing in creep.

4. Summary

Creep tests in tension were made at 110°, 250°, and 300°F on OFHC copper initially as bright annealed and as cold-drawn 40-percent reduction of area. Microscopic examination and hardness tests at room temperature were made to ascertain some of the damaging effects due to prior creep.

The period of time to initiate the third stage of creep and fracture of cold-drawn copper increased with decrease in stress (constant temperature) or with decrease in temperature (constant rate, average in second stage).

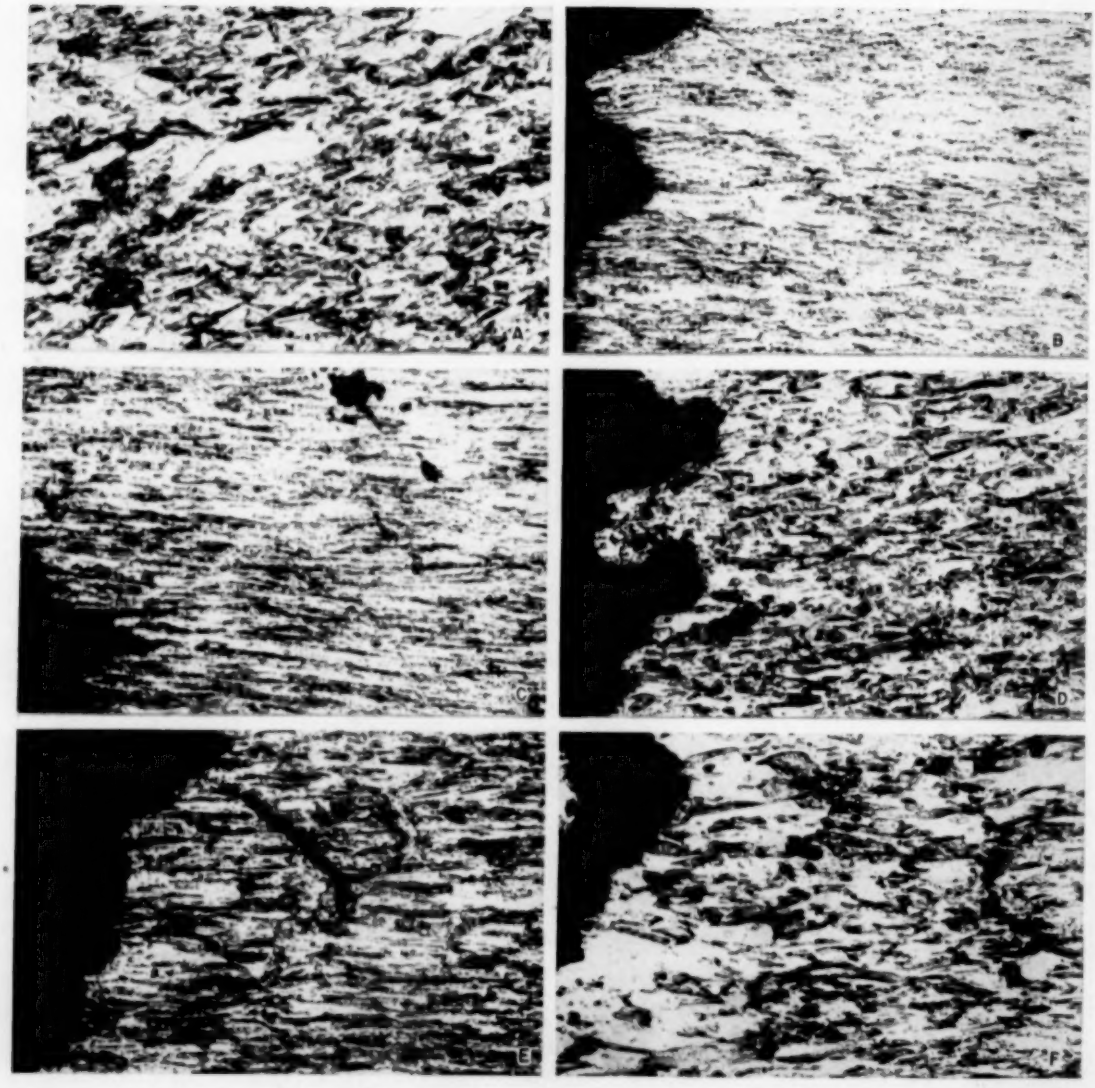

FIGURE 23. *Structure of copper initially as cold-drawn 40-percent reduction of area and structures at fracture of specimens tested at different temperatures and rates.*

Longitudinal sections etched in equal parts NH_4OH and H_2O_2 (3%).

	Test		Elongation in 2 in.	Reduction of area	Remarks
	Temperature	Creep rate			
	°F	%/1000 hr	%	%	
A					×75; as cold-drawn.
B	110	63.4	18.5	82.2	×100.
C	110	1.49	18.5	84.2	×100.
D	250	2.98	16	52.3	×100.
E	300	180	19.5	78.3	×100.
F	300	18.5	14.2	41.5	×100.

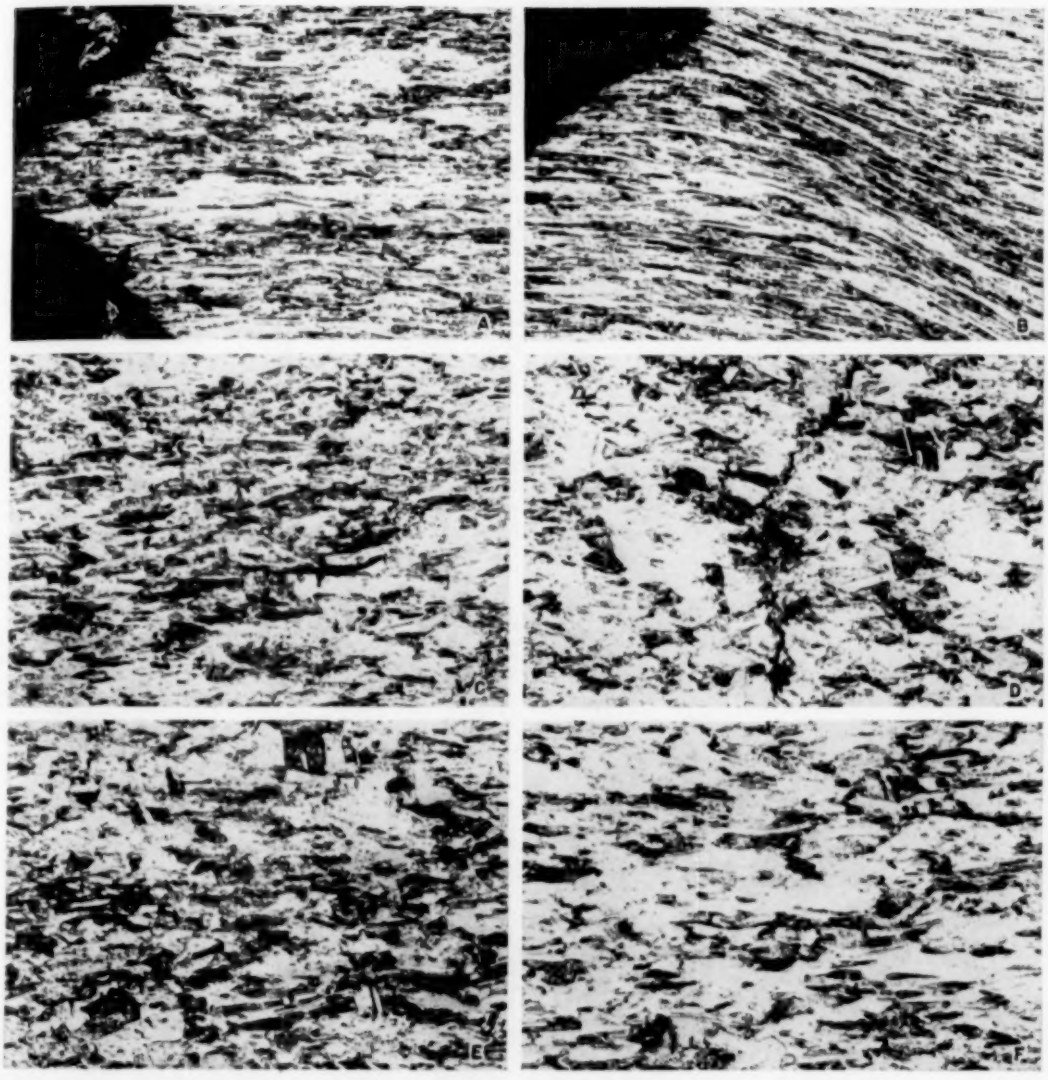

FIGURE 24. *Effect of temperature, rate, and plastic deformation on microcracking of copper initially as cold-drawn 40-percent reduction of area.*

Longitudinal sections near axis of specimen except as indicated, etched in equal parts NH_4OH and H_2O_2 (3%); × 100.

	Test		Remarks
	Temperature	Creep rate	
	°F	%/1000 hr	
A	250	19.7	Structure at fracture.
B	250	19.7	Same specimen as A; structure at "rim" surface.
C	250	2.98	Structure 0.05 in. from complete fracture.
D	300	2.64	Do.
E	300	180	Structure corresponding to deformation at beginning of third stage.
F	300	18.5	Do.

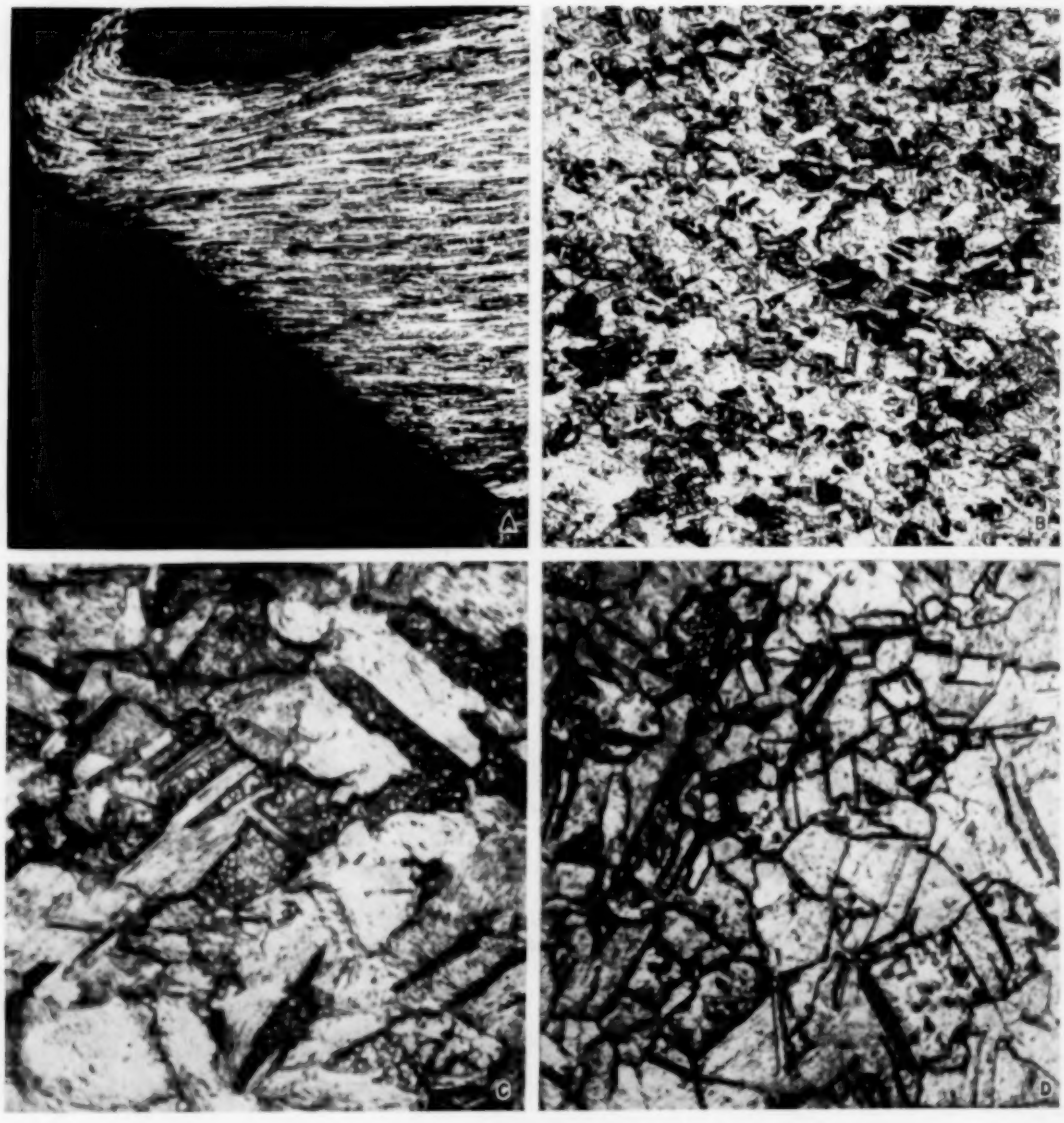

FIGURE 25. *Effect of temperature and rate on structure of copper initially as annealed.*

Longitudinal sections A and B etched in equal parts NH_4OH and H_2O_2 (3%). Longitudinal section C and transverse section D etched in 3.5 parts glacia acetic acid, 4.5 parts nitric acid (conc.) and 2 parts ethylene glycol.

	Test		Remarks
	Temperature	Creep rate	
	°F	%/1000 hr	
A	110	35	×100; structure at "rim" of fractured surface.
B	300	1.0 (a)	×100; (a) 16,000 psi for 3,000 hr; (b) 20,800 psi for 193 hr; structure at 22.5-percent extension.
		24.5 (b)	
C	300	1.0	×750; same specimen as B; longitudinal section.
		24.5	
D	300	1.0	×750; same specimen as B; transverse section.
		24.5	

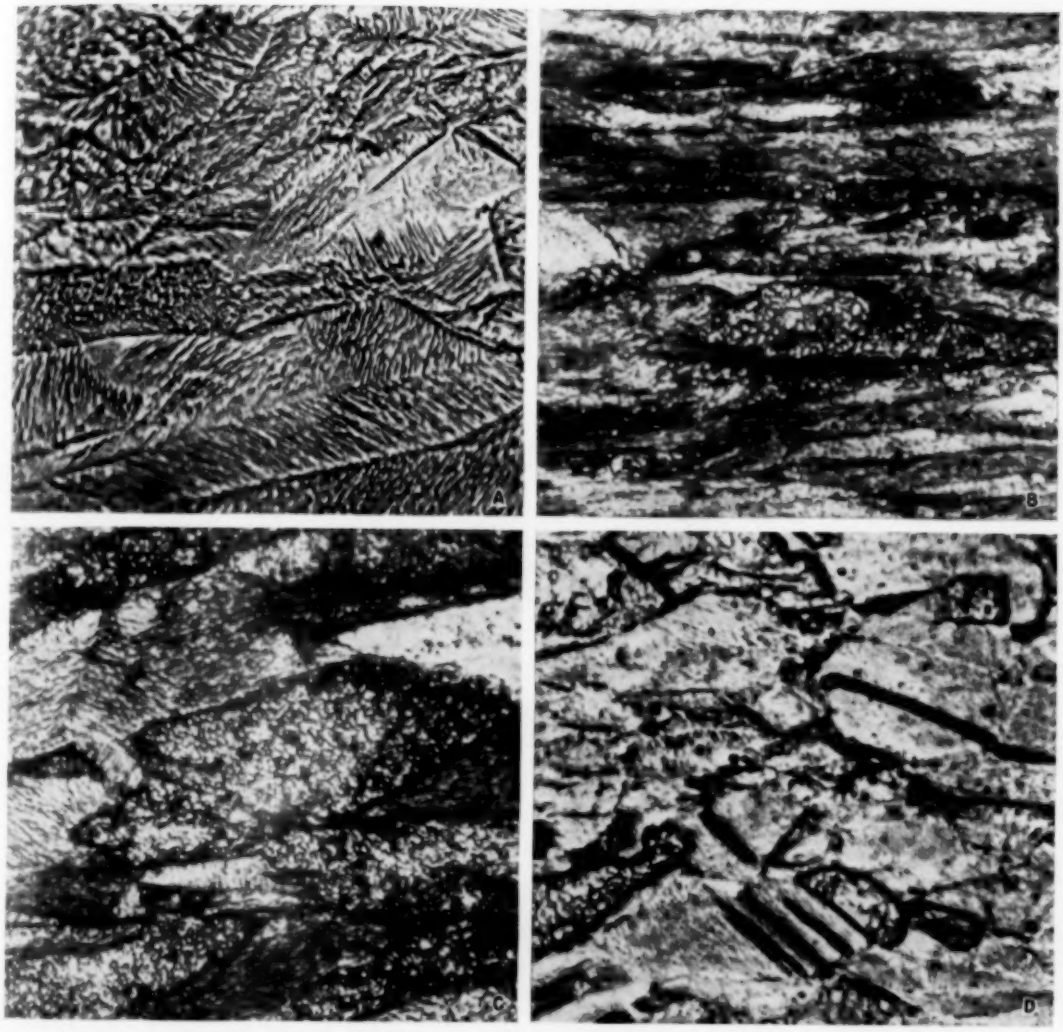

FIGURE 26. *Effect of testing conditions on the structure of copper initially as cold-drawn 40-percent reduction of area.*
Longitudinal sections etched in 3.5 parts glacial acetic acid, 4.5 parts nitric acid (conc.), and 2 parts ethylene glycol, ×750.

	Test		Remarks
	Temperature	Creep rate	
	°F	%/1000 hr	
A	.....	.....	As cold-drawn 40-percent reduction of area.
B	110	1.49	Structure near axis of specimen 0.1 in. from complete fracture.
C	250	2.98	Do.
D	300	2.64	Do.

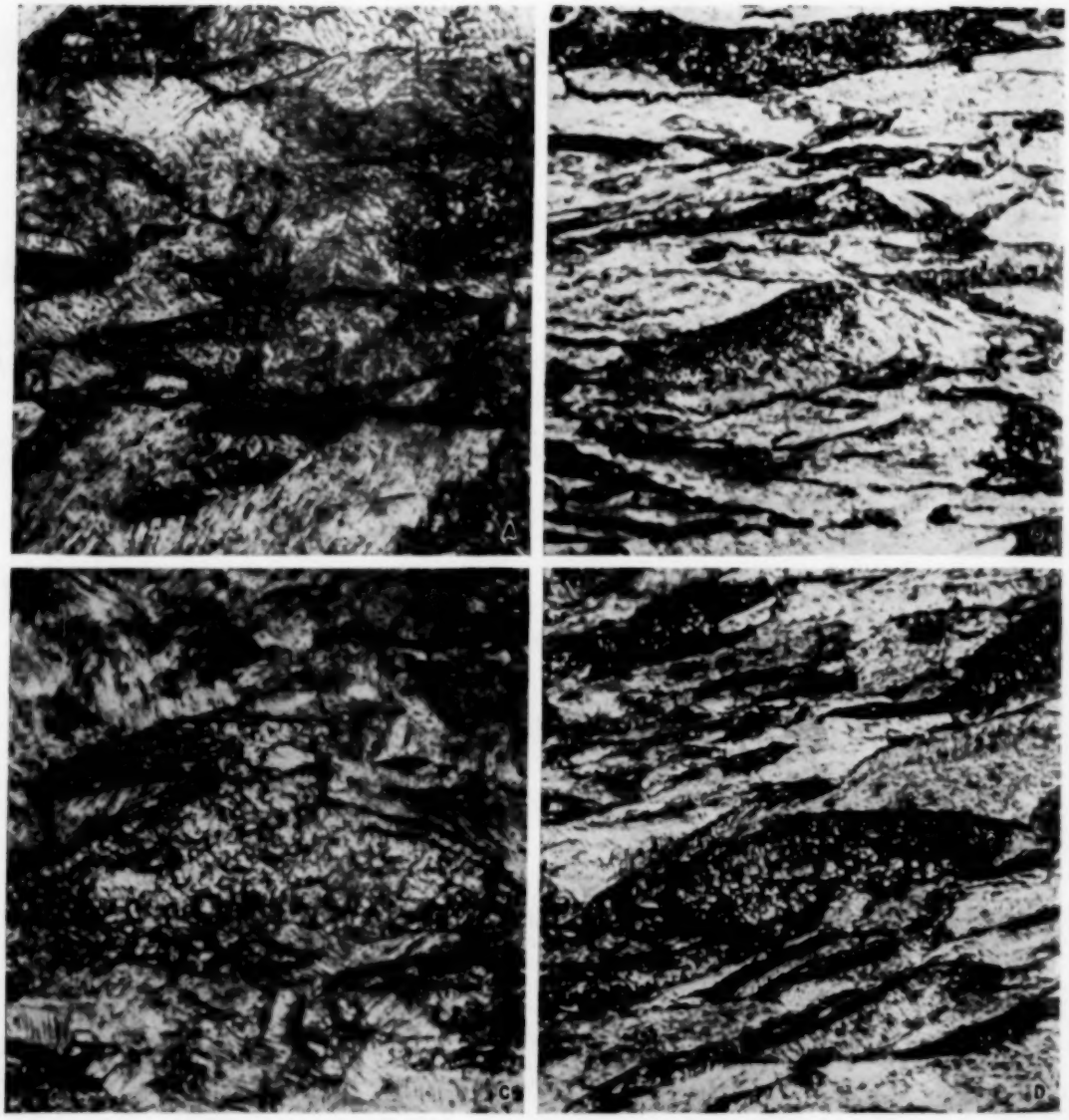

FIGURE 27. *Effect of testing conditions and plastic deformation on structure of copper initially as cold-drawn 40-percent reduction of area.*

Longitudinal sections etched in 3.5 parts glacial acetic acid, 4.5 parts nitric acid (conc.), and 2 parts ethylene glycol, ×750.

	Test		Remarks
	Temperature	Creep rate	
	°F	%/1000 hr	
A	300	18.5	Structure at axis 0.1 in. from position of complete fracture.
B	300	180	Do.
C	300	18.5	Same specimen as A; structure at axis 0.2 in. from position of complete fracture.
D	110	1.49	Structure at axis 0.2 in. from position of complete fracture.

The effect of rate of loading on creep characteristics was influenced by the prior thermal-mechanical history of the copper.

The resistance to creep at all the temperatures used was increased by cold-drawing the copper prior to testing. This superiority in creep properties was more evident at relatively low than at high temperatures and creep rates. Plastic extension at the beginning of the third stage and at fracture was greater for the annealed than for the cold-drawn copper, but the reduction of area values at fracture were similar.

Conformance to existing theories of transient flow (first stage) was found only in a limited number of cases, as the form of the extension-time curve in the first stage of creep was dependent on the applied stress and the test temperature.

Discontinuous flow was evidenced in each of the stages of creep and was found to be dependent on the test conditions, prior thermal-mechanical history, and stage of test.

The general trend was for the fracture stress to increase as the true strain at fracture increased. Fracture stress at equal strain value was materially increased by prior cold-drawing.

Increase in creep rate or decrease in test temperature generally caused an increase in hardness at room temperature.

The degree of necking; the tendency toward the formation of a rim at fracture; the tendency toward transcrystalline separation of the parent grains; the absence of cracks in regions away from complete fracture; the number and prominence of strain markings; and the tendency toward formation of subcrystals of smaller size as a result of plastic deformation; all increase with decrease in test temperature or increase in creep rate.

Cold-drawing prior to the creep test appears to alter the region in which transcrystalline fracture occurs. That is, transcrystalline fracture predominates at higher temperatures and lower creep rates for the cold-drawn than for the annealed copper. Furthermore, for similar test conditions, the size and number of subcrystals evident in the grains after the creep tests are decreased by cold-drawing the copper prior to testing in creep.

The authors are indebted to C. R. Johnson for assistance in this investigation.

5. References

[1] W. D. Jenkins and T. G. Digges, Creep of high-purity copper, J. Research NBS **45,** 153 (1950) RP2121.

[2] W. D. Jenkins and T. G. Digges, Influence of strain rate and temperature on the creep of cold-drawn ingot iron, J. Research NBS **43,** 117 (1949) RP2013.

[3] H. Burghoff and C. H. Mathewson, Time and temperature effects in the deformation of brass crystals, Trans. Am. Inst. Mining Met. Engr. (Inst. of Metals Div.) **143,** 45 (1941).

[4] A. H. Cottrell and V. Aytekin, The flow of zinc under constant stress, J. Inst. Metals **77,** 389 (July 1950).

[5] E. N. da C. Andrade, The creep of metals, Report of a conference on the strength of solids, The Physical Society, page 20 (1948).

[6] N. F. Mott and F. R. N. Nabarro, Dislocation theory and transient creep, Report of a conference on the strength of solids, The Physical Society, page 1 (1948).

[7] W. D. Jenkins, Creep of high-purity aluminum, J. Research NBS **46,** 310 (1950) RP2201.

Washington, April 3, 1951.

Journal of Research of the National Bureau of Standards Vol. 47, No. 4, October 1951 Research Paper 225

Tables of the Functions $\int_0^\phi \sin^{1/3} x\,dx$ and $(4/3)\sin^{-4/3}\phi\int_0^\phi \sin^{1/3} x\,dx$

Milton Abramowitz

This article concerns itself with the tabulation of the functions $\int_0^\phi \sin^{1/3} x\,dx$ and $4/3\sin^{-4/3}\phi\int_0^\phi \sin^{1/3} x\,dx$, which are important in the theory of condensation of vapor at rest on cylindric surfaces. The series expansion for the latter function is given, and certain functional relations useful for interpolation are mentioned. Instructions for interpolation with Lagrangian interpolations are given for the user.

This article concerns itself with the tabulation of the functions

$$I_1(\phi)=\int_0^\phi \sin^{1/3} x\,dx, \qquad \phi=0°(1°)90°, \tag{1}$$

$$I_2(\phi)=(4/3)\sin^{-4/3}\phi\int_0^\phi \sin^{1/3} x\,dx, \qquad \phi=0°(30')180°, \tag{2}$$

which are important in the theory of condensation of vapor at rest on cylindric surfaces.[1,2]

The integral $I_1(\phi)$ may be expressed in terms of the Incomplete Beta function, namely $I_1(\phi)=\frac{1}{2}B_{\sqrt{\sin\phi}}(\frac{2}{3},\frac{1}{2})$. However, the existing tables of the Incomplete Beta function are not convenient for interpolation.

When $\phi=\pi/2$, we have

$$I_1(90°)=\int_0^{\pi/2}\sin^{1/3} x\,dx=\frac{\Gamma(2/3)\Gamma(3/2)}{\Gamma(7/6)}$$
$$=1.2935\ 5478 \quad \text{(to 8 decimals)}. \tag{3}$$

Integrating by parts, one obtains for $I_2(\phi)$ the expression

$$I_2(\phi)=\sec\phi\left[1-1\left(\frac{3}{10}\right)\tan^2\phi+1.3\left(\frac{3}{10}\right)\left(\frac{3}{16}\right)\tan^4\phi\right.$$
$$\left.-1.3.5\left(\frac{3}{10}\right)\left(\frac{3}{16}\right)\left(\frac{3}{22}\right)\tan^6\phi+\ldots+R_n\right], \tag{4}$$

where R_n is the remainder after n terms and is given by

$$R_n=\frac{(-1)^n 3^{n-1}[1.3.5\ldots(2n-1)]}{10.16.22\ldots(6n-2)}$$
$$\cdot[\cos\phi\sin^{-4/3}\phi]\int_0^\phi \tan^{2n} x\,\sin^{1/3} x\,dx.$$

It may be shown that if $n\to\infty$, the resulting infinite series converges for $\phi\leq\pi/4$. When $\phi<\pi/4$ the convergence follows from the ordinary ratio test and when $\phi=\pi/4$ by application of Raabe's test since

$$\lim_{n\to\infty} n\{|U_n|/|U_{n+1}|-1\}=7/6, \text{ where } |U_n|$$
$$=\frac{1.3.5\ldots(2n-3)3^{n-1}}{10.16\ldots(6n-2)}.$$

Furthermore, it is clear that $|R_n|\to 0$ as $n\to\infty$; since

$$|R_n|<(2n-1)|U_n|\cos\phi\sin^{-4/3}\phi\int_0^{\pi/4}\tan^{2n} x\,dx$$
$$=(2n-1)|U_n|\cos\phi\sin^{-4/3}\phi\int_0^1\frac{t^{2n}}{1+t^2}\,dt$$

(setting $\tan x=t$), and therefore

$$|R_n|<(2n-1)|U_n|\cos\phi\sin^{-4/3}\phi\int_0^1 t^{2n}dt$$
$$<|U_n|\cos\phi\sin^{-4/3}\phi.$$

Thus if $0<\phi\leq\pi/4$, $R_n\to 0$, since $|U_n|\to 0$; establishing the fact that (4) represents $I_2(\phi)$ for $0<\phi\leq\pi/4$.

The function $I_1(\phi)$ has been tabulated only in the range from 0° to 90°, since the values for $90°\leq\phi\leq 180°$ may be obtained from the relation

$$I_1(\phi)=2I_1(90°)-I_1(180-\phi). \tag{5}$$

The corresponding relation for $I_2(\phi)$ is

$$I_2(\phi)=2I_2(90°)\sin^{-4/3}\phi-I_2(180°-\phi). \tag{6}$$

The table of $I_1(\phi)$ in the range from 0° to 20° was obtained with the aid of the expression for $I_2(\phi)$ given in (4) and multiplication by the factor $(3/4)\sin^{4/3}\phi$. From 20° to 90° the values were obtained by numerical integration. The function $I_2(\phi)$ in the range from 20° to 90° was obtained from the previously computed values of $I_1(\phi)$ and multiplication

[1] L. M. K. Boelter and others, Heat transfer notes (Univ. California Press, Berkeley, Calif., 1948).
[2] M. Jakob, Heat transfer 1 (John Wiley & Sons, Inc., New York, N. Y., 1949).

by the factor $(4/3)\sin^{-4/3}\phi$. The values at intervals of 30′ were obtained by interpolation. The relation (6) was then employed to extend the table to 180°.

The following information has been given so that interpolation with tables of Lagrangian interpolation coefficients [3] will yield the full accuracy provided by the table.

In the case of $I_1(\phi)$ in the range from 0° to 15° it will be advisable to interpolate in the table of $I_2(\phi)$ and multiply by $(3/4)\sin^{4/3}\phi$. From 15° to 90° the five-point Lagrangian interpolation formula will be adequate. In the case of $I_2(\phi)$, the three-point Lagrangian formula may be used from 0° to 15°, the four-point formula from 15° to 30°, the five-point formula from 30° to 135°, and the six-point formula from 135° to 165°. In the range from 165° to 180° the relation (6) given above should be used.

$$I_1(\phi) = \int_0^\phi \sin^{\frac{1}{3}} x\, dx$$

$\phi°$	$I_1(\phi)$	$\phi°$	$I_1(\phi)$
0	0.0000 0000	45	0.5360 1006
1	.0033 9543	46	.5516 0397
2	.0095 5577	47	.5672 8574
3	.0146 9038	48	.5830 5283
4	.0215 5745	49	.5989 0273
5	.0290 2580	50	.6148 3300
6	.0370 1067	51	.6308 4124
7	.0454 5180	52	.6469 2507
8	.0543 0371	53	.6630 8218
9	.0635 3059	54	.6793 1028
10	.0731 0330	55	.6956 0713
11	.0829 9758	56	.7119 7050
12	.0931 9282	57	.7283 9822
13	.1036 7125	58	.7448 8812
14	.1144 1731	59	.7614 3808
15	.1254 1726	60	.7780 4600
16	.1366 5880	61	.7947 0980
17	.1481 3088	62	.8114 2743
18	.1598 2346	63	.8281 9686
19	.1717 2738	64	.8450 1607
20	.1838 3423	65	.8618 8308
21	.1961 3621	66	.8787 9590
22	.2086 2613	67	.8957 5260
23	.2212 9724	68	.9127 5122
24	.2341 4327	69	.9297 8985
25	.2471 5831	70	.9468 6658
26	.2603 3677	71	.9639 7950
27	.2736 7341	72	.9811 2674
28	.2871 6324	73	.9983 0643
29	.3008 0150	74	1.0155 1670
30	.3145 8368	75	1.0327 5571
31	.3285 0547	76	1.0500 2161
32	.3425 6272	77	1.0673 1258
33	.3567 5149	78	1.0846 2679
34	.3710 6786	79	1.1019 6242
35	.3855 0846	80	1.1193 1767
36	.4000 6946	81	1.1366 9074
37	.4147 4754	82	1.1540 7981
38	.4295 3939	83	1.1714 8312
39	.4444 4181	84	1.1888 9886
40	.4594 5169	85	1.2063 2525
41	.4745 6601	86	1.2237 6052
42	.4897 8183	87	1.2412 0288
43	.5050 9630	88	1.2586 5056
44	.5205 0662	89	1.2761 0178
45	.5360 1006	90	1.2935 5478

[3] National Bureau of Standards, Tables of Lagrangian interpolation coefficients (Columbia University Press, New York, N. Y., 1944)

$$I_2(\phi) = (4/3)\sin^{-4/3}\phi \int_0^\phi \sin^{1/3} x\, dx$$

$\phi°$	$I_2(\phi)$	$\phi°$	$I_2(\phi)$	$\phi°$	$I_2(\phi)$
0 00	1.0000 0000	45 00	1.1344 8391	90 00	1.7247 3971
30	1.0000 1523	30	1.1377 6325	30	1.7304 6333
1 00	1.0000 6093	46 00	1.1410 9202	91 00	1.7483 654
30	1.0001 3709	30	1.1444 7070	30	1.7604 493
2 00	1.0002 4373	47 00	1.1478 9982	92 00	1.7727 184
30	1.0003 8087	30	1.1513 7990	30	1.7851 763
3 00	1.0005 4851	48 00	1.1549 1149	93 00	1.7978 266
30	1.0007 4669	30	1.1584 9511	30	1.8106 731
4 00	1.0009 7542	49 00	1.1621 3134	94 00	1.8237 196
30	1.0012 3473	30	1.1658 2075	30	1.8369 700
5 00	1.0015 2466	50 00	1.1695 6390	95 00	1.8504 284
30	1.0018 4524	30	1.1733 6139	30	1.8640 988
6 00	1.0021 9651	51 00	1.1772 1382	96 00	1.8779 855
30	1.0025 7851	30	1.1811 2181	30	1.8920 928
7 00	1.0029 9130	52 00	1.1850 8597	97 00	1.9064 253
30	1.0034 3491	30	1.1891 0686	30	1.9209 875
8 00	1.0039 0942	53 00	1.1931 8542	98 00	1.9357 841
30	1.0044 1487	30	1.1973 2201	30	1.9508 199
9 00	1.0049 5134	54 00	1.2015 1740	99 00	1.9661 000
30	1.0055 1888	30	1.2057 7230	30	1.9816 294
10 00	1.0061 1757	55 00	1.2100 8739	100 00	1.9974 133
30	1.0067 4748	30	1.2144 6340	30	2.0134 572
11 00	1.0074 0870	56 00	1.2189 0106	101 00	2.0297 667
30	1.0081 0130	30	1.2234 0116	30	2.0463 473
12 00	1.0088 2537	57 00	1.2279 6430	102 00	2.0632 050
30	1.0095 8100	30	1.2325 9143	30	2.0803 458
13 00	1.0103 6829	58 00	1.2372 8327	103 00	2.0977 758
30	1.0111 8733	30	1.2420 4064	30	2.1155 015
14 00	1.0120 3823	59 00	1.2468 6434	104 00	2.1335 294
30	1.0129 2110	30	1.2517 5523	30	2.1518 662
15 00	1.0138 3605	60 00	1.2567 1415	105 00	2.1705 190
30	1.0147 8319	30	1.2617 4198	30	2.1894 948
16 00	1.0157 6265	61 00	1.2668 3960	106 00	2.2088 011
30	1.0167 7454	30	1.2720 0792	30	2.2284 453
17 00	1.0178 1899	62 00	1.2772 4787	107 00	2.2484 353
30	1.0188 9615	30	1.2825 6039	30	2.2687 793
18 00	1.0200 0614	63 00	1.2879 4644	108 00	2.2894 853
30	1.0211 4911	30	1.2934 0701	30	2.3105 621
19 00	1.0223 2521	64 00	1.2989 4308	109 00	2.3320 184
30	1.0235 3458	30	1.3045 5570	30	2.3538 633
20 00	1.0247 7737	65 00	1.3102 4589	110 00	2.3761 061
30	1.0260 5376	30	1.3160 1473	30	2.3987 566
21 00	1.0273 6390	66 00	1.3218 6330	111 00	2.4218 248
30	1.0287 0797	30	1.3277 9270	30	2.4453 208
22 00	1.0300 8613	67 00	1.3338 0407	112 00	2.4692 553
30	1.0314 9857	30	1.3398 9855	30	2.4936 394
23 00	1.0329 4546	68 00	1.3460 7734	113 00	2.5184 842
30	1.0344 2700	30	1.3523 4162	30	2.5438 016
24 00	1.0359 4339	69 00	1.3586 9264	114 00	2.5696 036
30	1.0374 9481	30	1.3651 3163	30	2.5959 027
25 00	1.0390 8147	70 00	1.3716 5988	115 00	2.6227 118
30	1.0407 0359	30	1.3782 7869	30	2.6500 443
26 00	1.0423 6137	71 00	1.3849 8940	116 00	2.6779 139
30	1.0440 5503	30	1.3917 9336	30	2.7063 350
27 00	1.0457 8481	72 00	1.3986 9197	117 00	2.7353 223
30	1.0475 5091	30	1.4056 8665	30	2.7648 912
28 00	1.0493 5359	73 00	1.4127 7885	118 00	2.7950 574
30	1.0511 9309	30	1.4199 7004	30	2.8258 373
29 00	1.0530 6964	74 00	1.4272 6174	119 00	2.8572 480
30	1.0549 8350	30	1.4346 5550	30	2.8893 070
30 00	1.0569 3493	75 00	1.4421 5289	120 00	2.9220 326
30	1.0589 2419	30	1.4497 5552	30	2.9554 436
31 00	1.0609 5156	76 00	1.4574 6505	121 00	2.9895 598
30	1.0630 1730	30	1.4652 8316	30	3.0244 013
32 00	1.0651 2169	77 00	1.4732 1157	122 00	3.0599 894
30	1.0672 6503	30	1.4812 5204	30	3.0963 459
33 00	1.0694 4761	78 00	1.4894 0636	123 00	3.1334 936
30	1.0716 6973	30	1.4976 7638	30	3.1714 561
34 00	1.0739 3169	79 00	1.5060 6397	124 00	3.2102 580
30	1.0762 3381	30	1.5145 7106	30	3.2499 247
35 00	1.0785 7641	80 00	1.5231 9961	125 00	3.2904 827
30	1.0809 5981	30	1.5319 5162	30	3.3319 597
36 00	1.0833 8435	81 00	1.5408 2915	126 00	3.3743 844
30	1.0858 5036	30	1.5498 3431	30	3.4177 866
37 00	1.0883 5820	82 00	1.5589 6925	127 00	3.4621 974
30	1.0909 0821	30	1.5682 3615	30	3.5076 492
38 00	1.0935 0076	83 00	1.5776 3727	128 00	3.5541 758
30	1.0961 3623	30	1.5871 7492	30	3.6018 123
39 00	1.0988 1497	84 00	1.5968 5144	129 00	3.6505 954
30	1.1015 3739	30	1.6066 6925	30	3.7005 633
40 00	1.1043 0386	85 00	1.6166 3082	130 00	3.7517 561
30	1.1071 1480	30	1.6267 3867	30	3.8042 153
41 00	1.1099 7060	86 00	1.6369 9538	131 00	3.8579 845
30	1.1128 7168	30	1.6474 0361	30	3.9131 093
42 00	1.1158 1848	87 00	1.6579 6606	132 00	3.9696 371
30	1.1188 1141	30	1.6686 8551	30	4.0276 177
43 00	1.1218 5092	88 00	1.6795 6480	133 00	4.0871 032
30	1.1249 3746	30	1.6906 0684	30	4.1481 481
44 00	1.1280 7150	89 00	1.7018 1463	134 00	4.2108 094
30	1.1312 5349	30	1.7131 9120	30	4.2751 469
45 00	1.1344 8391	90 00	1.7247 3971	135 00	4.3412 233

$I_2(\phi) = (4/3)\sin^{-4/3}\phi \int_0^{\phi} \sin^{1/3} x\, dx$—*Continued*

ϕ°	$I_2(\phi)$	ϕ°	$I_2(\phi)$	ϕ°	$I_2(\phi)$
135 00	4. 3412 233	150 00	7. 6352 085	165 00	19. 8995 93
30	4. 4091 045	30	7. 8159 323	30	20. 8455 96
136 00	4. 4788 593	151 00	8. 0040 878	166 00	21. 8713 32
30	4. 5505 602	30	8. 2001 124	30	22. 9867 12
137 00	4. 6242 835	152 00	8. 4044 774	167 00	24. 2033 08
30	4. 7001 092	30	8. 6176 916	30	25. 5347 16
138 00	4. 7781 213	153 00	8. 8403 047	168 00	26. 9969 98
30	4. 8584 087	30	9. 0729 114	30	28. 6092 68
139 00	4. 9410 644	154 00	9. 3161 562	169 00	30. 3944 31
30	5. 0261 870	30	9. 5707 389	30	32. 3801 58
140 00	5. 1138 800	155 00	9. 8374 197	170 00	34. 6001 61
30	5. 2042 529	30	10. 1170 27	30	37. 0959 09
141 00	5. 2974 211	156 00	10. 4104 63	171 00	39. 9189 44
30	5. 3935 067	30	10. 7187 15	30	43. 1340 72
142 00	5. 4926 386	157 00	11. 0428 63	172 00	46. 8238 26
30	5. 5949 535	30	11. 3840 91	30	51. 0948 39
143 00	5. 7005 957	158 00	11. 7437 01	173 00	56. 0871 25
30	5. 8097 184	30	12. 1231 26	30	61. 9879 45
144 00	5. 9224 841	159 00	12. 5239 48	174 00	69. 0530 72
30	6. 0390 650	30	12. 9479 17	30	77. 6404 89
145 00	6. 1596 443	160 00	13. 3969 73	175 00	88. 2657 37
30	6. 2844 165	30	13. 8732 73	30	101. 6068 9
146 00	6. 4135 898	161 00	14. 3792 21	176 00	119. 1260 9
30	6. 5473 815	30	14. 9175 04	30	142. 4996 8
147 00	6. 6860 298	162 00	15. 4911 34	177 00	175. 2051 7
30	6. 8297 844	30	16. 1034 98	30	223. 6536 1
148 00	6. 9789 132	163 00	16. 7584 16	178 00	301. 4551 5
30	7. 1337 025	30	17. 4602 12	30	442. 8076 0
149 00	7. 2944 586	164 00	18. 2138 02	179 00	760. 9850 1
30	7. 4615 100	30	19. 0247 90	30	1918. 9846
150 00	7. 6352 085	165 00	19. 8995 93	180 00	∞

WASHINGTON, November 1, 1950.

Journal of Research of the National Bureau of Standards Vol. 47, No. 4, October 1951 Research Paper 2256

Separation of Close Eigenvalues of a Real Symmetric Matrix[1]

J. B. Rosser, C. Lanczos, M. R. Hestenes, and W. Karush

In order to test two methods, one proposed by C. Lanczos and the other by M. R. Hestenes and W. Karush, for the numerical calculation of eigenvalues of symmetric matrices, an 8 by 8 matrix is constructed that has several sets of eigenvalues close together. The application of the two methods to this test matrix is described, and in addition, a third method for dealing with such problems is proposed.

In recent publications [2] [3] two methods have been proposed for finding eigenvalues of real symmetric matrices. In order to make a numerical comparison between the methods, an 8 by 8 matrix was especially designed (see appendix 1) and the two methods were used independently to get all eight eigenvalues and eigenvectors of the matrix. In order that the test be a severe one, the matrix was designed with several sets of eigenvalues very close together. In order to separate these eigenvalues, special modifications of the two methods were developed for the separation of close eigenvalues (see appendixes 2 and 3).

The method of Lanczos (see footnote 2 and appendix 2) seems best adapted for use by a hand computer using a desk computing machine. In the present case, the computation according to Lanczos' method was carried out by a hand computer, and required of the order of 100 hours computing time.

The method of Hestenes and Karush (see footnote 3 and appendix 3) seems best adapted for use by machine computation. In the present case, the computation according to the method of Hestenes and Karush was carried out on an IBM Card-Programed Electronic Calculator. Considerable time was spent by Karush in becoming familiar with the machine, so that it is difficult to say just how long the computation would require of an experienced operator. Probably 3 or 4 days would be ample.

During and since the computations described above, there has been much discussion of the problem of separating close eigenvalues of a real symmetric matrix. Besides the methods offered in appendices 2 and 3, we wish to offer the following modifications of the familiar power method.

First let us consider the case where only the numerically largest eigenvalue, λ_1, and the corresponding eigenvector, v_1, of a matrix A are desired. We may assume λ_1 to be positive, since otherwise we treat $-\mathbf{A}$.

Suppose $\lambda_1, \ldots, \lambda_n$ are the eigenvalues of A in decreasing order, and $v_1, \ldots, v_n$ are the corresponding eigenvectors. If no other eigenvalue is near λ_1, one can find λ_1 and v_1 by the standard power method. In order to be able to compare the modifications for the case where another eigenvalue is near λ_1, we review the power method.

First, one chooses a vector x. This has a representation

$$x=c_1v_1+c_2v_2+ \ldots +c_nv_n,$$

but as yet we do not know the c's or v's. By iterations of the step of operating on a vector with a matrix, we form Ax, A^2x, A^3x, ... The representation of A^Nx is

$$A^Nx=c_1\lambda_1^N v_1+c_2\lambda_2^N v_2+ \ldots +c_n\lambda_n^N v_n.$$

If $c_1 \neq 0$ (which is the case except in very extraordinary circumstances), then for sufficiently large N, $c_1\lambda_1^N$ will be much greater than $c_i\lambda_i^N (i>1)$, since $\lambda_1 > |\lambda_i| \ (i>1)$. Thus A^Nx is nearly a multiple of v_1. By normalizing in the desired fashion, an approximation (of any desired degree of accuracy) for v_1 is obtained, from which an approximation to λ_1 can be obtained.

In case $\lambda_2=\lambda_1$, any linear combination of v_1 and v_2 will serve perfectly well as an eigenvector corresponding to λ_1. The power method just outlined will yield a linear combination of v_1 and v_2 in such a case, and so no difficulty arises.

Suppose λ_2 is nearly as great as λ_1, but all other λ's are appreciably smaller. Then one will have to take N excessively large before $c_2\lambda_2^N$ is small compared to $c_1\lambda_1^N$. Two possible procedures for curtailing the labor are as follows.

In the first, we take N large enough so that $c_i\lambda_i^N$ is small compared to $c_1\lambda_1^N$ or $c_2\lambda_2^N$ for $i>2$. Then approximately,

$$A^Nx=c_1\lambda_1^N v_1+c_2\lambda_2^N v_2.$$

Choose two vectors y and z. Put

$$a_{2j}=(y, A^{N+j-1}x)$$

$$a_{3j}=(z, A^{N+j-1}x),$$

where (u,v) denotes the inner product of the vectors u and v. Then λ_1 and λ_2 are the two roots of the quadratic equation

$$\begin{vmatrix} 1 & a_{21} & a_{31} \\ \lambda & a_{22} & a_{32} \\ \lambda^2 & a_{23} & a_{33} \end{vmatrix} = 0. \qquad (1)$$

[1] The preparation of this paper was sponsored (in part) by the Office of Naval Research.

[2] C. Lanczos, An iteration method for the solution of the eigenvalue problem of linear differential and integral operators, J. Research NBS 45, 255 (1950) RP2133.

[3] M. R. Hestenes and W. Karush, A method of gradients for the calculation of the characteristic roots and vectors of a real symmetric matrix, J. Research NBS 47, 45 (1951) RP2227.

To prove this, write

$$a=(y,c_1\lambda_1^N v_1)$$

$$b=(z,c_1\lambda_1^N v_1)$$

$$c=(y,c_2\lambda_2^N v_2)$$

$$d=(z,c_2\lambda_2^N v_2).$$

Then

$$\begin{vmatrix} 1 & a_{21} & a_{31} \\ \lambda & a_{22} & a_{32} \\ \lambda_2 & a_{23} & a_{33} \end{vmatrix} = \begin{vmatrix} 1 & 1 & 1 \\ \lambda & \lambda_1 & \lambda_2 \\ \lambda^2 & \lambda_1^2 & \lambda_2^2 \end{vmatrix} \times \begin{vmatrix} 1 & 0 & 0 \\ 0 & a & b \\ 0 & c & d \end{vmatrix}.$$

Then clearly the determinant is zero whenever $\lambda=\lambda_2$ or $\lambda=\lambda_2$, so that λ_1 and λ_2 are roots of (1).

In exceptional cases, the coefficients of (1) are all zero. This can happen if $\lambda_1=\lambda_2$, or $c_1=0$, or $c_2=0$, or in case the projections of y and z are not independent on the subspace spanned by v_1 and v_2 (this is the case where

$$\begin{vmatrix} a & b \\ c & d \end{vmatrix} = 0,$$

and can generally be treated by merely choosing a different y and z).

The case where λ_1, λ_2, and λ_3 are all nearly equal but the remaining λ's are small can be handled similarly, and leads to a third-degree equation defined by a fourth-order determinant.

Returning to the case where λ_1 and λ_2 are nearly equal, and other λ's are smaller, an alternative procedure makes use of Chebyshev polynomials. Suppose that a sufficiently high value of N has been used in order to establish that there are one or more roots in the vicinity of some value μ (which is approximately λ_1, and hence also approximately λ_2, since λ_1 and λ_2 are nearly equal), and that the other roots are appreciably less than μ in absolute value. In particular, $-\mu$ is a lower bound for the roots. Now instead of taking powers of A, we take powers of a polynomial in A, noting that

$$(P(A))^N x=c_1(P(\lambda_1))^N v_1+\ \ldots\ +c_n(P(\lambda_n))^N v_n.$$

If now we choose $P(\lambda)$ so that $P(\lambda_1)$ and $P(\lambda_2)$ are near 1, and $P(\lambda)$ has a large slope in the neighborhood of λ_1 and λ_2, then $P(\lambda_1)$ and $P(\lambda_2)$ will have a ratio appreciably less than λ_1/λ_2, and hence powers of $P(A)$ will eliminate v_2 relative to v_1 faster than powers of A.

We first apply A enough times to eliminate all v's except v_1 and v_2, and then apply $P(A)$. In order to insure that $P(A)$ does not bring back the v's already eliminated, it suffices that $|P(\lambda)|\leq 1$ for $-\mu\leq\lambda\leq\mu$. To do this and simlutaneously maximize the slope of $P(\lambda)$ at $\lambda=\mu$ for $P(\lambda)$ a polynomial of degree M, it suffices to take

$$P(\lambda)=T_M\left(\frac{\lambda}{\mu}\right),$$

where T_M is the Chebyshev polynomial of degree M.[4]

Actually, it may be more efficient to use different polynomials at different stages in the proceedings. The optimum choices of the polynomials will depend on the distribution of the λ's, naturally. As this is not known ahead of time in a given case, one must depend on a combination of experience and alert improvisation to get a good choice of polynomials.

We now turn to the case where one wishes to find all eigenvalues and eigenvectors. If any sort of fast computing machinery is available, one can probably proceed best by a combination of the power method plus orthogonalization on the eigenvectors already known. In particular, suppose λ_1 and v_1 are known. We can start with x and orthogonalize it with respect to v_1. That is, we replace x by

$$x-\frac{(v_1,x)}{(v_1,v_1)}v_1.$$

For the resulting vector, we have $c_1=0$. Hence, if we apply powers of A to it, we get the eigenvector corresponding to the eigenvalue next greatest after λ_1 in absolute value. Unfortunately, since we do not know v_1 exactly, we cannot in general determine x to be exactly orthogonal to v_1, and so cannot insure $c_1=0$. We thus face the possibility that $c_1\lambda_1^N$ may again be large. If, however, we orthogonalize with respect to v_1 from time to time, we repeatedly cut down the size of $c_1\lambda_1^N$. On a fast machine, orthogonalization is a quick procedure, and it is probably worthwhile to alternate the steps of orthogonalization and operating with A.

If λ_1 and λ_2 and v_1 and v_2 are known, one orthogonalizes with respect to both v_1 and v_2 between each time that one operates with A.

If at any point in the procedure, one encounters two close eigenvalues, one is trying to find the largest unknown eigenvalue, and so can apply the methods noted above (which are not disturbed by the frequent orthogonalizations). However, now that one plans to find all eigenvalues, alternative quicker methods are available for separation of close eigenvalues, depending upon knowing all other eigenvalues and eigenvectors. For example, suppose A has eigenvalues 1, 2, 2.95, 3.05, 4, and 5. Successively getting the largest eigenvalue twice by the power method plus orthogonalization, we readily get the eigenvalues 5 and 4, and their eigenvectors. We now discover that there are troubles in the neighborhood of 3. Essentially, we "postpone" treatment of this point by putting $B=3I-A$. Then the eigenvalues 1, 2, 2.95, 3.05 of A lead to the eigenvalues 2, 1, 0.05, -0.05 of B. Going now for the largest eigenvalues of B, we quickly get 2 and 1. We now have all eigenvalues and eigenvectors of A except 2.95 and 3.05 and their eigenvectors. Also we now know that there are just two remaining eigenvalues, and that both are near 3. We now consider $C=A-2.9I$. This has eigenvalues 0.05 and 0.15, and the power

[4] G. Pólya and G. Szegö, Aufgaben und Lehrsätze aus der Analysis II, p. 91 (Dover Publications, New York, N. Y., 1945).

method plus orthogonalization quickly gives the larger of these.

This method will run into difficulties if there are two pairs of close eigenvalues. An alternative procedure that will take care even of this case is the following. Suppose we have eigenvalues $\lambda_1=5$, $\lambda_2=4.05$, $\lambda_3=3.95$, $\lambda_4=3$, $\lambda_5=2.05$, $\lambda_6=1.95$, and $\lambda_7=1$. We quickly find λ_1 and v_1. Trying for λ_2, we find trouble. By starting with some x and alternately orthogonalizing with respect to v_1 and operating with A, we keep v_1 out, and eventually eliminate v_4, v_5, v_6, and v_7. We now have a certain linear combination of v_2 and v_3, which we may as well call u_2. We now repeat the procedure, except for starting with a different x. We then get a u_3 that is also a linear combination of v_2 and v_3. Except in the most extraordinarily unfortunate cases, u_3 will be independent of u_2. One can insure this independence by orthogonalizing with respect to u_2 throughout the computation of u_3. However, it is scarcely worth while, except perhaps in the choice of the initial x.

Since u_2 and u_3 are independent linear combinations of v_2 and v_3, it follows that a vector is orthogonal to both of v_2 and v_3 if and only if it is orthogonal to both of u_2 and u_3. To find λ_4 and v_4, we would wish to orthogonalize with respect to all of v_1, v_2, v_3. We can get the same effect if we instead orthogonalize with respect to v_1, u_2, and u_3 (this is most conveniently done if u_3 is taken orthogonal to u_2). Thus we can now proceed to get λ_4 and v_4, although we do not yet know λ_2, λ_3, v_2, or v_3. We again encounter difficulty with v_5, and v_6 because λ_5 and λ_6 are near together. However, we can get a u_5 and a u_6, which will suffice to let us obtain λ_7 and v_7. Now, by orthogonalizing with respect to v_1, v_4, u_5, u_6, and v_7, we can readily separate λ_2 and λ_3 by working with powers of $A-3.9I$. Then we get λ_5 and λ_6 by working with powers of $A-1.9I$.

Appendix 1. Construction of a Test Matrix

In order to get eigenvalues very close together without using many significant digits in the coefficients, it seemed necessary to use irrational numbers. Accordingly, a search was made for 2 by 2 symmetric matrices with eigenvalues, some of which were near together. We decided on the following four, where the eigenvalues are written to the right of the matrices:

$$\begin{Vmatrix} 102 & 1 \\ 1 & -102 \end{Vmatrix} \quad \pm\sqrt{(102)^2+1}$$

$$\begin{Vmatrix} 101 & 1 \\ 1 & 101 \end{Vmatrix} \quad 101 \pm 1$$

$$\begin{Vmatrix} 1 & 10 \\ 10 & 101 \end{Vmatrix} \quad 51 \pm \sqrt{(51)^2-1}$$

$$\begin{Vmatrix} 98 & 14 \\ 14 & 2 \end{Vmatrix} \quad 100,\ 0$$

The approximate numerical values of these eight eigenvalues, written in descending order are:

102.005
102.000
101.990
100.000
100.000
0.010
0.000
−102.005

One eigenvalue, namely 100, is exactly repeated. These 2 by 2 matrices were then mixed together into an 8 by 8 matrix as follows:

$$\begin{Vmatrix} 102 & 0 & 0 & 0 & 0 & 1 & 0 & 0 \\ 0 & 101 & 0 & 0 & 0 & 0 & 0 & 1 \\ 0 & 0 & 98 & 0 & 0 & 0 & 14 & 0 \\ 0 & 0 & 0 & 1 & 10 & 0 & 0 & 0 \\ 0 & 0 & 0 & 10 & 101 & 0 & 0 & 0 \\ 1 & 0 & 0 & 0 & 0 & -102 & 0 & 0 \\ 0 & 0 & 14 & 0 & 0 & 0 & 2 & 0 \\ 0 & 1 & 0 & 0 & 0 & 0 & 0 & 101 \end{Vmatrix}$$

Temporarily call this matrix B, and let P denote

$$\begin{Vmatrix} 2 & 1 & 1 & 2 & 0 & 0 & 0 & 0 \\ 1 & -2 & -2 & 1 & 0 & 0 & 0 & 0 \\ 1 & 2 & -2 & -1 & 0 & 0 & 0 & 0 \\ 2 & -1 & 1 & -2 & 0 & 0 & 0 & 0 \\ 0 & 0 & 0 & 0 & 1 & -1 & -2 & 2 \\ 0 & 0 & 0 & 0 & -1 & -1 & 2 & 2 \\ 0 & 0 & 0 & 0 & -2 & -2 & -1 & -1 \\ 0 & 0 & 0 & 0 & 2 & -2 & 1 & -1 \end{Vmatrix}$$

The two 4 by 4 matrices occurring in the corners of P were made by a scheme due to Sylvester, [1] with the result that P has the property

$$P^TP=10I$$

(we use P^T to denote the transpose of P). We then defined A to be P^TBP. The matrix A is then

$$\begin{Vmatrix} 611 & 196 & -192 & 407 & -8 & -52 & -49 & 29 \\ 196 & 899 & 113 & -192 & -71 & -43 & -8 & -44 \\ -192 & 113 & 899 & 196 & 61 & 49 & 8 & 52 \\ 407 & -192 & 196 & 611 & 8 & 44 & 59 & -23 \\ -8 & -71 & 61 & 8 & 411 & -599 & 208 & 208 \\ -52 & -43 & 49 & 44 & -599 & 411 & 208 & 208 \\ -49 & -8 & 8 & 59 & 208 & 208 & 99 & -911 \\ 29 & -44 & 52 & -23 & 208 & 208 & -911 & 99 \end{Vmatrix}$$

[1] T. Muir, History of determinants **III**, 289 (Macmillan and Co., Ltd., London, 1920).

with the eigenvalues and eigenvectors

$$\lambda_1 = 10\sqrt{10405} = 1020.04901843$$

$$v_1 = (2,\ 1,\ 1,\ 2,\ 102 - \sqrt{10405},\ 102 - \sqrt{10405},\ -204 + 2\sqrt{10405},\ -204 + 2\sqrt{10405})$$

$$= (2,\ 1,\ 1,\ 2,\ -0.004901843,\ -0.004901843,\ 0.009803686,\ 0.009803686)$$

$$\lambda_2 = 1020$$

$$v_2 = (1,\ -2,\ -2,\ 1,\ 2,\ -2,\ 1,\ -1)$$

$$\lambda_3 = 510 + 100\sqrt{26} = 1019.90195136$$

$$v_3 = (2,\ -1,\ 1,\ -2,\ \sqrt{26},\ -5 - \sqrt{26},\ -10 - 2\sqrt{26},\ 10 + 2\sqrt{26})$$

$$= (2,\ -1,\ 1,\ -2,\ 10.09901951,\ -10.09901951,\ -20.19803903,\ 20.19803903)$$

$$\lambda_4 = \lambda_5 = 1000$$

$$v_4 = (1,\ -2,\ -2,\ 1,\ -2,\ 2,\ -1,\ 1)$$

$$v_5 = (7,\ 14,\ -14,\ -7,\ -2,\ -2,\ -1,\ -1)$$

$$\lambda_6 = 510 - 100\sqrt{26} = 0.09804864072$$

$$v_6 = (2,\ -1,\ 1,\ -2,\ 5 - \sqrt{26},\ -5 + \sqrt{26},\ -10 + 2\sqrt{26},\ 10 - 2\sqrt{26})$$

$$= (2,\ -1,\ 1,\ -2,\ -0.099019514,\ 0.099019514,\ 0.198039027,\ -0.198039027)$$

$$\lambda_7 = 0$$

$$v_7 = (1,\ 2,\ -2,\ -1,\ 14,\ 14,\ 7,\ 7)$$

$$\lambda_8 = -10\sqrt{10405} = -1020.04901843$$

$$v_8 = (2,\ 1,\ 1,\ 2,\ 102 + \sqrt{10405},\ 102 + \sqrt{10405},\ -204 - 2\sqrt{10405},\ -204 - 2\sqrt{10405})$$

$$= (2,\ 1,\ 1,\ 2,\ 204.0049018,\ 204.0049018,\ -408.0098037,\ -408.0098037).$$

Appendix 2. Determination of the Characteristic Roots in the Method of Lanczos

The method of minimized iterations (cf. footnote 2) leads to the construction of a successive set of orthogonal vectors

$$b_0, b_1, \ldots, b_n \tag{1}$$

starting with the trial vector b_0. Each iteration is associated with two scalars α_i and β_i; they become the pivotal elements of the eigenvalue problem.

If the vectors (1) are introduced as an auxiliary reference system, the original matrix A is transformed into the following "codiagonal" form (omitting the zero elements):[6]

$$C = \begin{pmatrix} \alpha_0 & 1 & & & & \\ \beta_1 & \alpha_1 & 1 & & & \\ & \beta_2 & \alpha_2 & 1 & & \\ & & & \cdot & & \\ & & & & \cdot & \\ & & & & & \cdot \\ & & & & \beta_{n-1} & \alpha_{n-1} \end{pmatrix} \tag{2}$$

The solution of the principal axis problem requires the construction of a set of polynomials $p_i(x)$ on the basis of the recurrence relations

$$p_{i+1}(x) = (x - \alpha_i)p_i(x) - \beta_i p_{i-1}(x) \tag{3}$$

starting with

$$p_0(x) = 1$$

$$p_1(x) = x - \alpha_0$$

and ending with $p_n(x)$. The roots of the algebraic equation

$$p_n(x) = 0 \tag{4}$$

yield the n eigenvalues

$$x = \lambda_1, \lambda_2, \ldots, \lambda_n. \tag{5}$$

The matrix (2) is not symmetric because the vectors b_i are not normalized in length. In order to normalize b_i and thus symmetrize the matrix C, we introduce the quantities

$$\gamma_i = \sqrt{\beta_i}. \tag{6}$$

If the original matrix A is symmetric, then the β_i are all positive and the γ_i all real. The sign of the γ_i shall be taken as positive.

The normfactors

$$\omega_i = \sqrt{b_i^2} \tag{7}$$

are now expressible in terms of the γ_i. Assuming that the original trial vector b_0 was chosen of the length 1—that is, $\omega_0 = 1$—we obtain

$$\omega_i = \gamma_1 \gamma_2 \cdot \cdot \cdot \gamma_i. \tag{8}$$

The matrix A, if analyzed in the reference system of the normalized

$$b = \frac{b_i}{\omega_i} \tag{9}$$

[6] The β_i of the present report corresponds to the β_{i-1} of the reference cited in footnote 2.

ppears in the following symmetric form:

$$C' = \begin{pmatrix} \alpha_0 & \gamma_1 & & & & \\ \gamma_1 & \alpha_1 & \gamma_2 & & & \\ & \gamma_2 & \alpha_2 & \gamma_3 & & \\ & & & \cdot & & \\ & & & & \cdot & \\ & & & & & \cdot \\ & & & & \gamma_{n-1} & \alpha_{n-1} \end{pmatrix} \tag{10}$$

The quantities α_i and β_i, obtained by the method of minimized iterations, contain the entire solution of the eigenvalue problem. The eigenvalues are contained in the solution of the algebraic equation (4), while the components of the eigenvector u_i, analyzed in the b_i-system, become:

$$p_0(\lambda_i), p_1(\lambda_i), \ldots, p_{n-1}(\lambda_i). \tag{11}$$

If we construct the matrix

$$P = \begin{pmatrix} p_0(\lambda_1), p_1(\lambda_1), \ldots, p_{n-1}(\lambda_1) \\ \cdot \\ \cdot \\ \cdot \\ p_0(\lambda_n), p_1(\lambda_n), \ldots, p_{n-1}(\lambda_n) \end{pmatrix} \tag{12}$$

then the matrix product

$$U = PB, \tag{13}$$

where B is the matrix of the b_i, gives the matrix of the eigenvectors u_i, associated with the original matrix A.

The orthogonality of the eigenvectors u_i finds expression in the following relation:

$$1 + \sum_{\alpha=1}^{n-1} \frac{p_\alpha(\lambda_i) p_\alpha(\lambda_j)}{\beta_1 \beta_2 \ \ldots \ \beta_\alpha} = 0 \qquad (i \neq j) \tag{14}$$

In the given test-matrix a preliminary investigation of the matrix revealed that the largest eigenvalue is of the order of magnitude ± 1000. Hence all the elements of A were divided by 1000, thus obtaining a new matrix

$$A_0 = \frac{A}{1000},$$

whose largest eigenvalue was of the order ± 1.

The trial vector b_0 was chosen to be

$$0, 1, 0, 0, \ldots, 0$$

Then the method of minimized iterations was applied, obtaining the B matrix by putting the components of the vectors $b_0, b_1, b_2, \ldots, b_{n-1}$ in successive rows. Each one of these vectors was corrected during the process of generation to become strictly orthogonal to the previous vectors. Hence b_n must come out as identically zero, in spite of rounding errors. The associated α_i and β_i, together with the $\gamma_i = \sqrt{\beta_i}$, are tabulated as follows:

i	α_i	β_i	γ_i
0	0.869		
1	.1086626633	0.090839	0.3113502850
2	.7859177671	.0395179948848	.0308511731 5
3	−.7935214279	.4088977136	.6394511034
4	.0839683115517	.0520498144977	.0014317173 25
5	1.0160663075	.0940210090703	.0634121416 1
6	1.0199110708	.0*10704211101	.0327172805 5
7	1.0000000030	.0*7048359779	.0839545101 8

We will now discuss the problem of obtaining the roots of the algebraic equation (4). Our procedure will be to obtain a good first approximation and then improve this approximation to the full accuracy obtainable by 10 digit calculations.[7]

The separation of nearly equal roots is frequently a rather cumbersome task. In the present method the existence of nearly equal roots is an asset rather than a liability. The orthogonality relation (14) shows that exactly equal or nearly equal roots are only possible under singular conditions. If none of the β_k are small, then λ_i and λ_j cannot be essentially equal since a sum of all positive terms cannot vanish. If, on the other hand, a certain β_i is zero or very small, this means that the polynomial $p_n(x)$ separates into the product of two independent polynomials of lower order, which greatly simplifies the evaluation of the roots.

The given numerical example is well adapted to demonstrate the behavior of equal or nearly equal roots. Since nearly equal roots operate as practically *one* root in the successive reduction of the trial vector b_0, we will obtain a very small b_m already after m steps, where m is the number of essentially different roots. In the present problem we have only three essentially different roots. Owing to an accidental degeneracy, only *two* of these roots were strongly represented in b_0. Hence β_2 is already small. The remaining vector again contained essentially but two roots, and thus β_4 is again small. Furthermore, we notice that β_6 is very small and β_7 almost negligible.

Indeed, the fact that two roots of the given problem coincide has the consequence that b_8 should get reduced to zero in already *seven* steps, thus making β_7 *exactly* zero. That β_7 is not exactly zero, but only to 9 decimal places, is due to rounding errors.

The associated α_7 should give the double root $\lambda = 1$. Actually

$$\alpha_7 = 1.00000000030$$

is a very close approximation of the exact root.

We also notice that already β_6 is very small, although 15 times larger than β_7. The associated

$$\alpha_6 = 1.0199110708$$

is a close approximation of another of the nearly equal roots, namely

$$\lambda = 1.0199019514.$$

These specific properties of the β_i have the consequence that the original equation of 8th order separates into equations of the order

$$2 + 2 + 2 + 1 + 1.$$

This yields eight approximate roots of our problem, without solving equations of higher than second order.

The question is now, how to improve the accuracy of these approximations. The application of Newton's method for correcting a root is here out of question since we cannot construct the actual polynomial $p_n(x)$ without such rounding errors, which completely annihilate the desired accuracy. We can construct the successive polynomials $p_i(\lambda)$ for any *given* λ by the recurrence relations (2), but for *arbitrary* λ the coefficients of the final polynomial are marred by intolerably large errors.

The following perturbation method has quick convergence and operates numerically very satisfactorily. Let us assume that we possess a vector y, which approximates the solution of the eigenvalue problem.

$$Ay - \lambda y = 0. \tag{15}$$

Then

$$\lambda = \frac{yAy}{y^2} \tag{16}$$

is a very satisfactory approximation of a certain λ_i, because an error of first order in y causes an error of only second order in λ.

[7] This means 10 decimal places if the largest eigenvalue is normalized to 1. The absolutely smallest eigenvalue may be zero or arbitrarily near to zero. This zero, however, cannot be ascertained to more than 10 decimal places. The *relative* accuracy of the smallest eigenvalue may thus become arbitrarily bad.

We will apply this principle to our problem in the following sense. Let us assume that $\bar{\lambda}$ is an approximate root of the polynomial $p_n(\lambda)$. We now construct the components of the vector y by evaluating the following recurrent sequence:

$$y_0 = 1$$

$$y_1 = \frac{(\bar{\lambda} - \alpha_0) y_0}{\gamma_1}$$

$$y_2 = \frac{(\bar{\lambda} - \alpha_1) y_1 - \gamma_1 y_0}{\gamma_2}$$

$$\cdot \quad \cdot \quad \cdot$$

$$y_{n-1} = \frac{(\bar{\lambda} - \alpha_{n-2}) y_{n-2} - \gamma_{n-2} y_{n-3}}{\gamma_{n-1}}$$

$$y_n = (\bar{\lambda} - \alpha_{n-1}) y_{n-1} - \gamma_{n-1} y_{n-2}. \tag{17}$$

The vector

$$y = (y_0, y_1, \ldots, y_{n-1}) \tag{18}$$

taken in the reference system of the b_i', satisfies the equation

$$Ay - \bar{\lambda} y = 0$$

in all its components except the *last* one, where we get

$$(Ay - \bar{\lambda} y)_{n-1} = -y_n.$$

Hence

$$yAy = \bar{\lambda} y^2 - y_n y_{n-1}.$$

Substitution in (16) gives

$$\lambda = \bar{\lambda} - \frac{y_n y_{n-1}}{\Sigma y_\alpha^2}$$

Actually it is entirely accidental that the equation where the error occurs shall be the *last* one. We can start our recurrences from *both* ends of the matrix and join the two sets at an arbitrary point i. The error will then occur in the ith rather than the last equation.

Now the correction of the error of $\bar{\lambda}$ will be most effective if the error of the equation (15) appears in that particular component i that is associated with the absolutely largest y_i. We designate this particular y_i and add to the sequence (17) another sequence that starts from the other end and proceeds in opposite direction:

$$y_{n-1}' = 1$$

$$y_{n-2}' = \frac{(\bar{\lambda} - \alpha_{n-1}) y_{n-1}'}{\gamma_{n-1}}$$

$$y_{n-3}' = \frac{(\bar{\lambda} - \alpha_{n-2}) y_{n-2}' - \gamma_{n-1} y_{n-1}'}{\gamma_{n-2}}$$

$$\cdot \quad \cdot \quad \cdot$$

$$y_{i-1}' = \frac{(\bar{\lambda} - \alpha_i) y_i' - \gamma_{i+1} y_{i+1}'}{\gamma_i} \tag{19}$$

We adjust this sequence to the sequence (17) by multiplying every component by

$$\rho = \frac{y_i}{y_i'}. \tag{20}$$

We now construct our vector y by choosing its components from the y_k series up to $k=i$, and from the y_k' series from $k=i$ on:

$$\left.\begin{aligned} \bar{y}_0 &= y_0,\ \bar{y}_1 = y_1, \ldots, \bar{y}_i = y_i = \rho y_i' \\ \bar{y}_{i+1} &= \rho y_{i+1}', \ldots, \bar{y}_{n-1} = \rho y_{n-1}' \end{aligned}\right\} \tag{21}$$

The error occurs in the ith equation and we obtain

$$\lambda = \bar{\lambda} + \frac{\gamma_i (y_{i-1} - \rho y_{i-1}') y_i}{\Sigma \bar{y}_\alpha^2}. \tag{22}$$

The entire process can now be repeated, by replacing $\bar{\lambda}$ by the new λ. This process had such good convergence that after two steps the error was already pushed out beyond the 10th decimal place. The entire set of λ_i was thus obtained with relatively little difficulty and without involved calculations.

After obtaining the λ_i, the P matrix was obtained by recursions. Finally, the product PB gave the matrix U' of the eigenvectors u_i'. This matrix was then normalized by dividing each row by the square root of the sum of the squares of the elements of each row.

The resultant normalized matrix U' was now tested for orthogonality and for its eigenvector property. Under exact conditions we should get

$$u_i' u_k' = 0 \qquad (i \neq k) \tag{23}$$

$$u_i' A u_k' = 0 \qquad (i \neq k)$$

Actually, in view of the rounding errors, we do not get zero on the right side but two symmetric matrices

$$\rho_{ik} = \rho_{ki} \tag{24}$$

and

$$\sigma_{ik} = \sigma_{ki} \tag{25}$$

composed of small elements. We use these ρ_{ik} and σ_{ik} quantities to correct our solution. We evaluate

$$\epsilon_{ik} = \frac{\sigma_{ik} - \lambda_i \rho_{ik}}{\lambda_i - \lambda_k}. \tag{26}$$

In view of the extreme closeness of some of the eigenvalues, the denominator of (26) becomes small for some i, k, and the corresponding ϵ_{ik} not negligible. We now form the matrix E, composed of the non-negligible elements ϵ_{ik}, while the diagonal elements and the negligible ϵ_{ik} are replaced by zero. The corrected U' matrix becomes:

$$\overline{U}' = U' + E U' \tag{27}$$

The rows of the corrected matrix give us the proper eigenvectors with an accuracy of six decimal places. The λ_i, evaluated from these vectors, agreed with the previous λ_i to 10 decimal places. Comparison with the known exact values showed that all the 10 decimal places came out correctly for each one of the roots.[8]

Appendix 3. Modification of the Method of Hestenes and Karush

The method of fixed α (see footnote 3) was used in the calculation. This consists in passing from one approximation x for a characteristic vector to the next approximation x' by means of the formula

$$x' = x + \alpha \xi(x)$$

where

$$\xi(x) = Ax - \mu(x) x, \qquad \mu(x) = \frac{(x, Ax)}{(x, x)}.$$

Here α is a positive constant (independent of x) of the form

$$\alpha = \frac{\beta}{\lambda_1 - \lambda_n}, \qquad 0 < \beta < 1,$$

[8] The entire numerical work was carried out by Miss Fannie M. Gordon.

where β is optimally near 1. The above formula for x' is used to obtain convergence to an eigenvector v_1 belonging to λ_1 the largest (algebraically) eigenvalue. For an eigenvector v_n belonging to λ_n, the smallest eigenvalue, the formula

$$x' = x - \alpha\xi(x)$$

is to be used. In practice α is at the disposal of the computer, and he may change its value at different stages of the calculation according to his disposition and insight. The changes are easily made by having at hand several punched cards carrying different values of α and replacing at any time the single card in the deck carrying the value of α by another such card.

The fixed α method is closely related to the power method. To illustrate this, suppose we are computing the least value λ_n. After a certain number of steps the value of $\mu(x)$ will be essentially constant from step to step, this constant representing our computed value of λ_n. Continued calculation leads to improvement in the vector x. The iteration formula with $\xi(x)$ replaced by its expression in terms of Ax and x becomes

$$x' = \alpha\left\{\left(\frac{1}{\alpha}+\mu\right)I - A\right\}x,$$

with I the identity matrix. That is, approximately,

$$x' = \alpha\{(\beta'\lambda_1 + (1-\beta')\lambda_n)I - A\}x,$$

where $\beta' = 1/\beta$ is near 1. Thus, except for a normalization factor α, this is the power method applied to $\lambda_1' I - A$ with λ_1' near λ_1. In essence we have shifted the origin close to λ_1, thereby making λ_n the dominating eigenvalue in absolute value. The normalizing factor α guarantees that the lengths $|x|$ will increase and converge.

The above procedure was used to calculate all eigenvalues and eigenvectors by the technique of orthogonalizing to eigenvectors already known, in the manner described in the text. As more eigenvectors are obtained the parameter α is allowed to assume a greater value, this value in each new case being of the form β/M, where M is the spread of the eigenvalues for the subspace in question. Thus if λ_n and v_n are known, the iteration operates in the 7-dimensional subspace orthogonal to v_n, where the appropriate value of M is $\lambda_1 - \lambda_2$.

Multiple roots offer no difficulty. Thus in the case of $\lambda_4 = \lambda_5 = 1000$, the iteration first leads to the eigenvalue $\lambda_4 = 1000$ and to some corresponding eigenvectors v_4. Running orthogonal to v_4 (and other known eigenvectors) we obtain $\lambda_5 = 1000$ and the eigenvector v_5 orthogonal to v_4.

Close roots may be treated as follows. At first the close roots are ignored and because λ_1, λ_2, λ_3 are nearly equal and λ_6, λ_7 are nearly equal one obtains by the orthogonalization technique eight independent vectors

$$u_1, u_2, u_3, v_4, v_5, u_6, u_7, v_8$$

instead of the true eigenvectors

$$v_1, v_2, v_3, v_4, v_5, v_6, v_7, v_8.$$

Here u_1, u_2, u_3 are linear combinations of v_1, v_2, v_3 and u_6, u_7 are linear combinations of v_6, v_7 (see text). To find the first vector v_1 we apply our iteration procedure in the 3-space spanned by these vectors. That is, we run orthogonal to v_4, v_5, u_6, u_7, v_8 and use a (large) α appropriate to the 3-space. Having obtained v_1 we run orthogonal to v_1 to obtain v_2. To obtain v_3 we do not require the α iteration method; we need only orthogonalize to v_1 and v_2 in the 3-space. Notice that this procedure of obtaining v_1, v_2, v_3 does not require knowing u_1, u_2, u_3. Of course if one decided to separate v_6 and v_7 first, one would need to know these last three vectors but not u_6 and u_7.

In connection with orthogonalizing to known eigenvectors we remark that if x is already orthogonal to such vectors then in theory x' and all successive approximations will be. In practice however the orthogonality is lost by round-off and must be regularly restored by direct calculation.

The preceding method was, in the main, the one used in the computation. However, there is a variation of the procedure that is of interest. It takes advantage of the fact that we may make the iteration scheme move upward or downward on the scale of eigenvalues and enables us to reduce the number of orthogonalizations. Consider the problem of finding v_1, v_2, v_3. We first apply the iteration procedure that increases $\mu(x)$, that is, $x' = x + \alpha\xi$, with an α appropriate to the whole space. After a certain number of steps we have eliminated the lower eigenvectors and are operating in the invariant 3-space of v_1, v_2, v_3. We now increase α to a value corresponding to the three space. In this way we separate out v_1. In order to avoid the introduction of higher eigenvectors through round-off, we intersperse use of the larger value of α with use of the older smaller value (this replaces the orthogonalization to v_4, v_5, u_6, u_7, u_8 of the preceding method). The next vector v_2 is obtained in the same way, maintaining orthogonality to v_1. The vector v_2 is found by orthogonalizing to v_1 and v_2. To apply this technique to v_6 and v_7 we first find v_8 and then use the α iteration with decreasing μ, that is, $x' = x - \alpha\xi$. Then v_7 is found by orthogonalizing only to v_8, and v_6 by orthogonalizing to v_8 and v_7.

If we analyze either of the above methods of separation in the way we earlier compared the fixed α method with the power method, we find again that in the later stages of the iteration we are applying the power method. We first eliminate all but the invariant subspace corresponding to the close eigenvalues, and then, in essence we use the power method on a linear combination of A and I that will separate out the desired vectors. Thus, this method is closely related to that explained at the end of the text.

The final eigenvalues were found with a relative error of 10^{-8}. The absolute in the components of each eigenvector were determined with an absolute error of 10^{-8}, when the largest component of each vector is taken to be 1.

Los Angeles, September 28, 1950.

Journal of Research of the National Bureau of Standards Vol. 47, No. 4, October 1951 Research Paper 2257

Viscosity of Dilute and Moderately Concentrated Polymer Solutions[1]

S. G. Weissberg, Robert Simha, and S. Rothman

The viscosities of solutions of three polystyrene fractions in three solvents of varying solvent power were measured at two temperatures. The relative viscosities of the systems investigated ranged from 1.03 to 43.

The applicability of two empirical expressions for the concentration dependence, namely the Martin equation and the Baker relation, is examined. In addition, the results are represented by means of polynomials of suitable degree. The numerical procedures for the evaluation of the coefficients are discussed in detail. In the concentration range investigated, the introduction of a reduced concentration scale $S=[\eta]c$, places the viscosity-concentration curves for different molecular weights in the same solvent on a more nearly common scale. This scale, S, is simply related to another reduced scale c/c_0. Here c_0 represents the concentration at which the equivalent spheres of the coiling molecules, as defined at infinite dilution, would just begin to overlap. At $c/c_0 \ll 1$, the concentration dependence can be described in terms of hydrodynamic interaction. This interaction involves single molecules and can also involve the intrinsic viscosity and interactions of aggregates of low order. An attempt is made to deduce from the viscosity data and on the basis of certain hydrodynamic results, the equilibrium constants and relative populations of such aggregates. Reasonable values are obtained. On approaching c_0, the average volume available to a chain molecule in a good solvent is reduced because of the cage formed by its nearest neighbors. The effective pressure is just the internal osmotic pressure. This leads to an expression for the concentration dependence of the viscosity, in terms of the virial coefficients of osmotic pressure, molecular weight, and size. These equations are shown to be in satisfactory agreement with the experimental data. In particular, in the neighborhood of c_0 one obtains reasonable values for the molecular extension factors of the chain.

1. Introduction

A knowledge of the viscosity of a polymer solution and its dependence on such variables as temperature, nature of solvent, concentration, and molecular weight of solute is of technical and scientific importance. A large amount of effort has been devoted to theoretical studies of the intrinsic viscosities of both compact and flexible macromolecules. This work has been successful in that it is possible to deduce from these theories, in conjunction with the proper measurements, the dimensions of the solute molecules. Furthermore, the dependence of the intrinsic viscosity on thermodynamic conditions and on molecular weight has been examined for a variety of polymer-solvent systems. Thus we have a rather adequate picture of the behavior of the isolated molecule in solution.

The relation between viscosity and concentration becomes much more complicated when, with increasing concentration, the molecules begin to interact with each other, first through hydrodynamic interaction, that is a long range effect, and then by forming actual contacts, aggregates, and networks. Again there are available some theoretical treatments and a number of experimental investigations of the concentration dependence of the viscosity together with empirical expressions to describe this dependence. However, in few of the experimental studies have the effects of molecular weight or solvent power on the behavior in the moderately or highly concentrated range been critically examined. Although representation by equations of a prescribed type with two or three available parameters may be useful as an overall interpolation formula, such representations are not always readily amenable to physical interpretations.

In this paper, the results of precise measurements of moderately concentrated solutions (up to 9 g/dl) of three polystyrene fractions in three different solvents are described. The data are expressed analytically by means of customary empirical expressions, as well as by power series developments in the concentration, in order to seek theoretical conclusions. In section 2, the experimental procedures and the materials used are reviewed. In section 3, the experimental results are tabulated, and in section 4 they are described in terms of various concentration functions. The numerical procedures for evaluating the power series expansions are discussed in detail in section 5 and the results given. In the last section a discussion of the physical aspects, together with certain theoretical relations is presented.

2. Experimental Procedure

Materials; purification. Three fractions of polystyrene were selected from a set of fractions that had been prepared from styrene polymerized in bulk without catalyst at 120° C. The polymerization was nearly complete in 48 hours. We are indebted to A. N. Roche, of the Dow Chemical Co., for preparing this sample of polystyrene. The unfractionated polymer was purified and made homogeneous before its use by twice precipitating it in a large volume of methanol from a benzene solution. The precipitate

[1] Presented at the Twelfth International Congress of Pure and Applied Chemistry, New York, N. Y. (Sept. 9 to 13, 1951).

was redissolved in benzene and placed under reduced pressure (<1 mm Hg) at approximately −10° C. After practically all the volatile materials were removed, the polymer was raised to room temperature and kept under reduced pressure until there was no further loss of volatiles. The remaining material was a white, foamy, homogeneous mass.

The solvents employed were once distilled laboratory stock. The mixed solvent, 90-percent methyl ethyl ketone (2-butanone) and 10-percent isopropyl alcohol, was prepared volumetrically at 27.2° C. The physical constants of the solvents are given in table 1.

TABLE 1. *Physical constants of solvents*

Solvent	Density		Kinematic viscosity	
	30°C	48.2°C	30°C	48.2°C
	g/ml	*g/ml*	*Centistokes*	*Centistokes*
Toluene	0.857	0.839	0.608	0.510
Butanone	.794	.776	.450	.391
Mixed solvent	.792	.773	.484	.412

Fractionation. A predetermined quantity of isopropyl alcohol was added dropwise at 30°C to a 1-percent solution in butanone of the unfractionated polymer. The slightly cloudy system was then heated to approximately 60°C, or until complete solution occurred. It was then cooled slowly to 30°C and held at this temperature ±0.02°C until the precipitate had settled. The precipitate was redissolved in a small quantity of butanone and the solution centrifuged to remove all insolubles. The polymer was reprecipitated by adding the clear solution in a thin stream to a large quantity of isopropyl alcohol. Material that remained suspended in the liquid was separated with a Sharples supercentrifuge. The fraction was dried under reduced pressure at room temperature. It was redissolved in butanone to form a 1-percent solution. The entire fractionation procedure was then repeated, using this first broad fraction. Five narrower fractions resulted from this second fractionation. The highest molecular weight of these five subfractions (1.1) was used for these measurements. In addition, two singly precipitated fractions, 3.0 and 5.0, were used. The molecular weights of these fractions as given in table 2 were estimated by linear extrapolation of a differentiated curve of osmotic pressure versus concentration. The measurements of osmotic pressure were made by G. A. Hanks, of this laboratory, using a small static equilibrium osmometer. The description of this instrument designed by G. A. Hanks and one of the authors (S. G. Weissberg) will be given elsewhere.

TABLE 2. *Molecular weights*

Fraction	M_n
1.1	600,000
3.0	146,000
5.0	58,000

Viscosity measurements. The viscosity measurements were made in calibrated Ubbelohde suspended level viscometers, similar to those used previously in our laboratory [1, 2].[2] The reservoirs of these had been enlarged to hold approximately 100 ml of liquid without disturbing the suspended level. This modification makes possible dilutions within the viscometer. The constants of the instruments used are summarized in table 3. The solutions of highest polymer concentration were prepared volumetrically, but the dilutions were performed in the viscometers. When the capacity of the instrument was reached, an aliquot of solution was transferred to another viscometer and the measurements were continued. At each transfer point, viscosity measurements were made in both instruments to ascertain that there had been no concentration change in the transfer. In this manner it was possible to cover an entire concentration range with a single master solution.

For measurements of very dilute solutions, below relative viscosities of 1.2, a special Ubbelohde suspended level viscometer was made for which all corrections, including those for kinetic energy, were negligible. The small bore capillary of this viscometer, however, was easily clogged and therefore weighed amounts of filtered liquid were transferred to the instrument [3]. Most measurements of the toluene system at 30°C were made so as to have data from more than one viscometer in any given concentration range. This overlapping served as an internal check on the precision of the measurements, and as a measure of the extent of deviation from Newtonian flow, since the shearing stresses at the walls of the several capillaries varied by a factor of three. The fact that the overlapping portions were all continuous may be regarded as evidence that the deviations from Newtonian flow for the solutions studied are so small that they can be neglected. Some measurements made with a Bingham viscometer, in which the pressure could be varied over a range of an atmosphere, showed the deviation from Newtonian behavior to be less than 1 percent for a 3.5-percent solution in toluene in a viscometer in which the shearing stress at the capillary wall was 25 dynes/cm^2, corresponding to a velocity gradient of 140 sec^{-1}.

The viscometers were adapted to operate in a closed system [2]. The temperature of the thermostated water bath was kept constant to ±0.02°C. Flow times were measured with a manually switched electric stopclock graduated to 0.01 sec.

3. Experimental Results

The data obtained are shown in tables 4 to 10. The quantities listed are defined as follows:

c = polymer concentration in grams per 100 ml of solution.

η_r = relative viscosity = η/η_0, where η is the viscosity of the solution and η_0 that of the solvent.

[2] Figures in brackets indicate the literature references at the end of this paper.

$\frac{\eta_{sp}}{c}$ = reduced specific viscosity $= (\eta_r - 1)/c$.

$\Delta\left(\frac{\eta_{sp}}{c}\right) = \left(\frac{\eta_{sp}}{c}\right)_{calc.} - \left(\frac{\eta_{sp}}{c}\right)_{exp}$, where $\left(\frac{\eta_{sp}}{c}\right)_{calc.} = \sum_i A_i c^i$.

The details of the calculation are discussed in section 5.

$$S = A_0 c = [\eta]\, c,$$

where $[\eta]$ is the intrinsic viscosity defined as $\lim_{c \to 0} \eta_{sp}/c$.

c_0 is a particular concentration, the physical significance of which is discussed in section 6.

Constants for the viscometers used for the concentrations indicated are given in table 3.

TABLE 3. *Characteristics of viscometers*

Viscometer	Length of capillary	Radius of capillary	ΔP	$r\Delta P/2l$	Flow time, toluene (30° C)	A [a]	B [a]
	cm	*cm*	*Dynes/cm²*		*sec*	*Centistokes sec⁻¹*	
R	8.8	0.030	1.02×10^{-4}	17.4	70.82	8.897×10^{3}	2.02
G	9.0	.032	1.05	18.7	56.59	11.31	1.79
S	8.8	.031	1.04	18.3	64.53	10.07	2.09
U_1	10.5	.035	1.08	18.0	[b]	19.77	0.435
U_2	10.5	.050	1.08	25.7	[b]	71.70	5.37
J_1	35.0	.020	3.12	8.9	469.38	[c]	[c]
J_2	35.0	.021	3.12	9.4	370.76	[c]	[c]

[a] $\eta/\rho = At - B/t$.

[b] Flow time too short to get precision measurements. Viscometers used only for concentrated solutions.

[c] Kinetic energy correction negligible.

TABLE 4. *Toluene viscosity data for molecular weight: 600,000*

Temperature, 30°C							Temperature, 48.2°C						
c	η_r	η_{sp}/c	$\Delta(\eta_{sp}/c)$	$\frac{S}{[\eta]c}$	$\frac{c}{c_0}$	Viscometer	c	η_r	η_{sp}/c	$\Delta(\eta_{sp}/c)$	$\frac{S}{[\eta]c}$	$\frac{c}{c_0}$	Viscometer
g/dl		*dl/g*	*dl/g*				*g/dl*		*dl/g*	*dl/g*			
0.0175	1.0358	2.0457	0.0216	0.0357	0.039	J_2	0.1414	1.3065	2.1676	−0.0030	0.2783	0.310	S
.0238	1.0503	2.1134	−.0363	.0486	.053	J_2	.1962	1.4376	2.2304	.0102	.3862	.430	S
.0375	1.0783	2.0880	.0105	.0766	.084	J_2	.3199	1.7750	2.4226	−.0008	.6297	.701	S
.0610	1.1991	2.1879	−.0062	.1858	.204	J_2	.4674	2.2236	2.6180	.0017	.9200	1.02	R, S
.3384	1.8717	2.5759	−.0008	.6908	.759	R	.5978	2.6714	2.7959	.0063	1.177	1.31	R
.3618	1.9537	2.6360	−.0334	.7386	.811	S	.8291	3.5919	3.1262	.0165	1.632	1.82	R
.4230	2.1445	2.7057	−.0075	.8635	.948	R	1.0280	4.5266	3.4305	.0173	2.023	2.25	R
.4380	2.1771	2.6874	.0344	.8942	.982	R	1.3524	6.3789	3.9773	−.0148	2.662	2.97	R
.4824	2.3596	2.8184	−.0270	.9848	1.08	S	1.9759	11.2265	4.7756	−.0481	3.889	4.33	R, U_1
.5602	2.6157	2.8841	.0303	1.144	1.26	R	2.5691	18.4112	6.0899	−.0691	5.116	5.70	U_1
.5640	2.6488	2.9234	−.0030	1.151	1.26	R	3.0859	28.0056	8.1052	−.0991	6.074	6.77	U_1
.6367	2.9216	3.0181	.0181	1.299	1.43	G	3.7971	41.6402	10.7030	.0502	7.474	8.33	U_1
.7256	3.3361	3.2284	−.0521	1.477	1.62	S							
.7769	3.4871	3.2013	.0619	1.586	1.74	R							
.8460	3.8716	3.3943	−.0173	1.727	1.90	R							
.9196	4.2048	3.4850	.0148	1.877	2.06	G							
1.1824	5.6533	3.9355	.0193	2.414	2.65	G							
1.2671	6.1429	4.0588	.0493	2.587	2.84	R							
1.3795	6.9543	4.3163	.0008	2.816	3.09	G							
1.6554	9.0648	4.8718	−.0089	3.379	3.71	G							
1.8512	10.7467	5.2650	.0149	3.779	4.15	R, U_2							
2.0692	13.0331	5.8153	−.0343	4.224	4.64	G							
2.2626	15.2059	6.2786	−.0179	4.619	5.07	U_2							
2.5454	19.0082	7.0748	−.0457	5.196	5.71	U_2							
2.9090	24.7480	8.1636	−.0144	5.939	6.52	U_2							
3.3039	34.7996	9.9589	−.0479	6.929	7.61	U_2							

TABLE 5. *Methyl ethyl ketone viscosity data for molecular weight: 600,000*

Temperature, 30°C							Temperature, 48.2°C						
c	η_r	η_{sp}/c	$\Delta(\eta_{sp}/c)$	$\frac{S}{[\eta]c}$	$\frac{c}{c_0}$	Viscometer	c	η_r	η_{sp}/c	$\Delta(\eta_{sp}/c)$	$\frac{S}{[\eta]c}$	$\frac{c}{c_0}$	Viscometer
g/dl		*dl/g*	*dl/g*				*g/dl*		*dl/g*	*dl/g*			
0.0541	1.0558	1.0314	0.0167	0.0552	0.043	G	0.2493	1.2769	1.1069	0.0045	0.244	0.187	R, S
.0696	1.0735	1.0560	−.0050	.0710	.055	G	.3188	1.3678	1.1537	−.0042	.311	.240	R
.0975	1.1032	1.0586	.0123	.0994	.077	G	.4421	1.5321	1.2035	.0146	.432	.332	R
.1219	1.1339	1.0684	−.0147	.124	.096	G	.5482	1.6958	1.2692	.0091	.536	.412	R
.1625	1.1828	1.1249	−.0243	.166	.128	G	.7211	1.9855	1.3667	.0127	.704	.542	R, U_1
.2437	1.2795	1.1471	.0016	.249	.192	G	1.0535	2.7008	1.6145	−.0281	1.029	.792	U_1
.3380	1.4032	1.1929	.0089	.345	.266	G	1.3004	3.4906	1.8187	−.0154	1.338	1.03	U_1
.4191	1.5173	1.2343	.0102	.427	.330	G	1.9560	5.4472	2.2736	.0016	1.911	1.47	U_1
.5514	1.7191	1.3041	.0153	.562	.434	G	2.4890	7.9723	2.8012	.0039	2.432	1.87	U_1
.8055	2.2024	1.4927	−.0224	.822	.634	G, U_1	3.4214	14.8777	4.0561	−.0178	3.343	2.57	U_1
.9913	2.6085	1.6226	−.0347	1.011	.780	U_1	4.2099	24.0196	5.4680	.0008	4.113	3.16	U_1, U_2
1.2886	3.3230	1.8027	−.0113	1.314	1.01	U_1	5.2624	43.3556	8.0487	.0199	5.141	3.96	U_2
1.8405	5.0797	2.2166	.0148	1.877	1.45	U_1							
2.3420	7.3137	2.6959	.0231	2.389	1.84	U_1							
3.2193	13.2714	3.8118	.0199	3.284	2.53	U_1							
3.9913	21.1484	5.0860	.0081	4.040	3.12	U_1, U_2							
4.9516	37.4558	7.3624	−.0117	5.051	3.90	U_2							

TABLE 6. *90-percent methyl ethyl ketone–10-percent isopropyl alcohol viscosity data for molecular weight: 600,000*

Temperature, 30°C							Temperature, 48.2°C						
c	η_r	η_{sp}/c	$\Delta(\eta_{sp}/c)$	$\frac{S}{[\eta]c}$	$\frac{c}{c_0}$	Viscometer	c	η_r	η_{sp}/c	$\Delta(\eta_{sp}/c)$	$\frac{S}{[\eta]c}$	$\frac{c}{c_0}$	Viscometer
g/dl		*dl/g*	*dl/g*				*g/dl*		*dl/g*	*dl/g*			
0.1081	1.0913	0.8446	−0.0391	0.0833	0.049	R	0.2247	1.2108	0.9381	−0.0054	0.1964	0.115	G
.2433	1.2162	.8886	−.0155	.1876	.111	R	.4494	1.4460	.9924	−.0115	.3928	.232	S, G
.4866	1.4792	.9846	−.0017	.3752	.221	R, S	.5651	1.6357	1.0182	−.0112	.5201	.307	S
.6439	1.6765	1.0511	.0067	.4962	.292	S	.8935	2.0233	1.1021	.0140	.7696	.454	S
.9501	2.1332	1.1927	.0205	.7325	.432	S	1.1584	2.5097	1.3033	.0083	1.012	.597	S
1.2470	2.6952	1.3594	.0160	.9614	.567	S	1.3753	2.9867	1.4445	−.0137	1.202	.709	S
1.4779	3.2109	1.4960	−.0045	1.139	.672	S	1.6923	3.7580	1.6297	−.0034	1.479	.872	S
1.8138	4.1019	1.7102	.0115	1.398	.824	S	2.0308	4.7703	1.8566	.0061	1.775	1.05	R
1.9952	4.6569	1.8328	.0019	1.538	.907	S							

TABLE 7. *Toluene viscosity data for molecular weight: 146,000*

Temperature, 30°C							Temperature, 48.2°C						
c	η_r	η_{sp}/c	$\Delta(\eta_{sp}/c)$	$\frac{S}{[\eta]c}$	$\frac{c}{c_0}$	Viscometer	c	η_r	η_{sp}/c	$\Delta(\eta_{sp}/c)$	$\frac{S}{[\eta]c}$	$\frac{c}{c_0}$	Viscometer
g/dl		*dl/g*	*dl/g*				*g/dl*		*dl/g*	*dl/g*			
0.0433	1.0309	0.7135	−0.0005	0.0305	0.034	J_1	0.1360	1.0868	0.6382	−0.0022	0.0842	0.093	J_1
.0477	1.0338	.7083	−.0045	.0336	.037	J_2	.2042	1.1322	.6474	−.0029	.1264	.140	J_1
.0831	1.0451	.7143	.0023	.0445	.049	J_1	.2856	1.1873	.6569	−.0013	.1768	.196	G, J_1
.0719	1.0517	.7194	−.0012	.0507	.056	J_2	.3491	1.2300	.6588	.0040	.2161	.240	G
.1013	1.0726	.7167	.0069	.0714	.079	J_1	.4488	1.3050	.6706	−.0042	.2778	.309	G
.1155	1.0838	.7255	.0007	.0814	.090	J_2	.5236	1.3593	.6862	−.0034	.3241	.360	G
.1755	1.1301	.7413	−.0040	.1237	.137	J_1	.6283	1.4390	.6987	−.0006	.3889	.432	G
.1727	1.1309	.7366	.0011	.1253	.138	J_1	.7854	1.5615	.7149	.0034	.4862	.540	G, S
.2378	1.1786	.7510	−.0023	.1676	.185	J_1	.9179	1.6900	.7342	.0050	.5867	.652	S
.3042	1.2321	.7631	−.0023	.2145	.237	S, J_1, J_2	1.1951	1.9124	.7634	.0079	.7389	.822	S
.3891	1.3036	.7803	−.0040	.2743	.303	S	1.6167	2.3243	.8191	.0079	1.001	1.11	S
.5396	1.4370	.8098	−.0059	.3804	.421	S	1.9629	2.7126	.8725	.0014	1.215	1.35	S
.6690	1.5564	.8317	.0041	.4716	.521	S	2.4979	3.3781	.9520	−.0034	1.546	1.72	S
.8801	1.7641	.8682	−.0017	.6205	.686	S	2.8919	3.9190	1.0094	−.0037	1.780	1.99	S
1.0450	1.9368	.8864	.0004	.7367	.814	S	3.4336	4.7633	1.0960	−.0084	2.125	2.36	S
1.2858	2.2046	.9368	.0046	.9065	1.00	R, S	4.2249	6.1884	1.2280	−.0128	2.615	2.91	R, S
1.4730	2.4339	.9734	.0029	1.038	1.15	R	4.8710	7.4984	1.3341	−.0096	3.015	3.35	R
1.7239	2.7653	1.0240	−.0004	1.215	1.34	R	5.7504	9.7138	1.5154	−.0214	3.559	3.95	R
2.0779	3.2630	1.0891	.0014	1.465	1.62	R	6.1980	10.8846	1.5948	−.0096	3.836	4.26	R
2.6149	4.1321	1.1978	.0002	1.843	2.04	R	6.7212	12.4804	1.7081	−.0098	4.160	4.62	R
3.0030	4.8263	1.2748	.0034	2.117	2.34	R	7.3408	14.5544	1.8464	−.0047	4.544	5.05	R, U_1
3.5262	5.9146	1.3937	−.0022	2.486	2.75	R	7.9791	16.9546	1.9985	.0015	4.939	5.49	U_1
4.2703	7.7051	1.5762	−.0051	3.011	3.33	R	8.3418	18.4444	2.0912	.0059	5.164	5.74	U_1
4.6640	8.7200	1.6552	.0088	3.288	3.63	R, U_1	8.7390	20.3009	2.1971	.0101	5.409	6.01	U_1
5.3303	10.7928	1.8372	.0070	3.758	4.15	U_1	9.1760	22.3435	2.3260	.0085	5.680	6.31	U_1
6.2187	14.2602	2.1323	−.0190	4.384	4.85	U_1							
7.4624	20.1412	2.5650	−.0090	5.261	5.82	U_1							
8.1113	24.0575	2.8426	−.0202	5.718	6.32	U_1							
8.8838	29.1725	3.1712	.0039	6.263	6.92	U_1							
9.3280	32.4664	3.3733	.0236	6.576	7.27	U_1							

TABLE 8. *Methyl ethyl ketone viscosity data for molecular weight: 146,000*

Temperature, 30° C							Temperature, 48.2° C						
c	η_r	η_{sp}/c	$\Delta(\eta_{sp}/c)$	$\frac{S}{[\eta]c}$	$\frac{c}{c_0}$	Viscometer	c	η_r	η_{sp}/c	$\Delta(\eta_{sp}/c)$	$\frac{S}{[\eta]c}$	$\frac{c}{c_0}$	Viscometer
g/dl		*dl/g*	*dl/g*				*g/dl*		*dl/g*	*dl/g*			
0.0969	1.0442	0.4562	−0.0033	0.0432	0.033	J_2	0.2505	1.1008	0.4024	−0.0023	0.0969	0.075	J_2
.1423	1.0656	.4610	−.0044	.0634	.049	J_1	.3032	1.1228	.4050	−.0019	.1173	.090	J_2
.1751	1.0801	.4574	.0018	.0780	.060	J_1	.3763	1.1533	.4074	−.0002	.1456	.112	J_2
.2276	1.1041	.4574	.0060	.1014	.078	J_1	.4817	1.1986	.4123	.0039	.1864	.143	J_2
.3251	1.1536	.4725	−.0012	.1448	.111	J_1	.6826	1.2903	.4253	.0000	.2642	.203	J_2
.4137	1.1988	.4805	−.0022	.1843	.142	J_1	.9554	1.4261	.4469	−.0033	.3697	.284	J_2
.5686	1.2797	.4920	−.0014	.2532	.195	S, J_1	1.4932	1.7120	.4768	.0036	.5779	.444	R
.6997	1.3526	.5040	−.0029	.3116	.240	R, S	1.5398	1.7300	.4741	.0097	.5959	.458	J_2
.8711	1.4500	.5166	−.0018	.3880	.298	R	1.7821	1.8839	.5016	.0008	.6897	.530	R
1.1534	1.6191	.5368	.0009	.5137	.395	R	2.2095	2.1888	.5380	−.0006	.8551	.658	R
1.3766	1.7673	.5574	−.0009	.6131	.471	R	2.5105	2.4231	.5669	−.0031	.9716	.747	R
1.7067	2.0042	.5884	.0030	.7602	.584	R	2.9066	2.7564	.6043	−.0038	1.125	.865	R
1.9383	2.1875	.6123	−.0054	.8629	.664	R	3.4510	3.2559	.6537	.0009	1.336	1.03	R
2.2452	2.4511	.6463	−.0095	1.0000	.769	R	4.2463	4.1612	.7444	−.0032	1.643	1.26	R, U_1
2.6657	2.8409	.6906	−.0088	1.187	.913	R	4.6156	4.6242	.7852	−.0009	1.786	1.37	U_1
3.2801	3.5212	.7686	−.0128	1.461	1.12	R, U_1	5.0551	5.2608	.8429	−.0048	1.956	1.50	U_1
3.6259	3.9555	.8152	−.0487	1.615	1.24	U_1	5.5873	6.0344	.9010	.0054	2.162	1.66	U_1
4.0519	4.5422	.8742	−.0080	1.805	1.39	U_1	6.2446	7.2137	.9950	.0007	2.417	1.86	U_1
4.5922	5.4093	.9802	−.0073	2.045	1.57	U_1	6.6349	7.9739	1.0511	.0001	2.568	1.97	U_1
5.2986	6.7122	1.0780	.0036	2.360	1.81	U_1	7.0772	8.9146	1.1183	−.0020	2.739	2.11	U_1
5.6461	7.4664	1.1453	.0049	2.515	1.93	U_1							
6.0423	8.3562	1.2174	.0149	2.691	2.07	U_1							
6.4983	9.5238	1.3117	.0196	2.894	2.22	U_1							
7.0288	11.0369	1.4280	.0231	3.131	2.41	U_1							
7.6536	13.0931	1.5800	.0159	3.409	2.62	U_1							
8.4003	15.9911	1.7846	−.0143	3.741	2.88	U_1							
8.8312	17.7351	1.8950	.0287	3.933	3.02	U_1							

TABLE 9. *90-percent methyl ethyl ketone–10-percent isopropyl alcohol viscosity data for molecular weight: 146,000*

Temperature, 30°C							Temperature, 48.2°C						
c	η_r	η_{sp}/c	$\Delta(\eta_{sp}/c)$	$\frac{S}{[\eta]c}$	$\frac{c}{c_0}$	Viscometer	c	η_r	η_{sp}/c	$\Delta(\eta_{sp}/c)$	$\frac{S}{[\eta]c}$	$\frac{c}{c_0}$	Viscometer
g/dl		*dl/g*	*dl/g*				*g/dl*		*dl/g*	*dl/g*			
0.0555	1.0183	0.3291	−0.0028	0.0179	0.011	J_1	0.2501	1.0909	0.3934	0.0019	0.0878	0.052	J_1
.0838	1.0305	.3251	.0035	.0303	.018	J_1	.4355	1.1649	.3786	−.0029	.1529	.090	J_1
.1848	1.0615	.3328	.0010	.0597	.035	J_1	.6083	1.2343	.3852	.0005	.2135	.126	J_2
.2408	1.0814	.3380	−.0009	.0778	.046	J_2	.9349	1.3787	.4051	−.0008	.3281	.193	R, J_2
.3509	1.1211	.3451	−.0018	.1131	.067	J_2	1.2575	1.5304	.4218	.0011	.4414	.260	R
.4969	1.1758	.3538	−.0021	.1605	.095	J_2	1.5196	1.6661	.4393	.0001	.5334	.314	R
.7282	1.2662	.3655	−.0008	.2352	.138	J_2	1.9198	1.8914	.4643	−.0016	.6738	.397	R
1.0013	1.3826	.3821	−.0023	.3234	.190	J_2	2.2110	2.0672	.4827	−.0016	.7761	.457	R
1.3191	1.5270	.3995	−.0016	.4261	.251	R, J_2	2.6063	2.3234	.5078	−.0006	.9148	.538	R
1.5438	1.6388	.4138	−.0027	.4986	.293	R	3.1737	2.7474	.5306	.0168	1.114	.656	R
1.8609	1.8101	.4353	−.0051	.6011	.354	R	3.4764	2.9744	.5679	.0027	1.220	.718	R
2.0738	1.9300	.4484	−.0044	.6698	.394	R	3.6505	3.1135	.5790	.0055	1.281	.754	R
2.3418	2.0979	.4688	−.0070	.7564	.445	R	3.7008	3.2282	.5878	.0081	1.331	.783	R
2.6803	2.3089	.4867	−.0044	.8686	.511	R	3.8430	3.2766	.5924	.0079	1.349	.794	R
3.1579	2.6778	.5313	−.0077	1.020	.600	R	4.1402	3.5561	.6185	.0074	1.453	.855	R, U_1
3.8242	3.2651	.5923	−.0093	1.235	.727	R	4.9365	4.4778	.7045	−.0020	1.733	1.02	U_1
4.1768	3.5933	.6208	−.0028	1.349	.794	R, U_1	5.3479	5.0362	.7547	.0076	1.877	1.10	U_1
4.7569	4.2363	.6803	.0008	1.536	.904	U_1	5.8340	5.7518	.8145	−.0098	2.048	1.20	U_1
5.0367	4.5734	.7095	.0042	1.627	.957	U_1	6.4175	6.7425	.8948	−.0131	2.252	1.33	U_1
5.3515	4.9831	.7462	.0060	1.728	1.02	U_1	6.7552	7.3701	.9430	−.0125	2.371	1.40	U_1
5.7083	5.4850	.7857	.0119	1.844	1.08	U_1	7.1305	8.1035	.9962	.0075	2.503	1.47	U_1
6.1160	6.1167	.8366	.0149	1.975	1.16	U_1	7.3996	8.6413	1.0327	−.0012	2.597	1.53	U_1
6.5865	6.9181	.8985	.0176	2.127	1.25	U_1	7.4754	8.8280	1.0472	.0005	2.624	1.54	U_1
7.1353	7.9831	.9801	.0128	2.305	1.36	U_1	7.8620	9.7111	1.1080	.0068	2.760	1.62	U_1
7.7840	9.3862	1.0774	.0061	2.514	1.48	U_1	8.3800	11.0392	1.1971	.0193	2.943	1.73	U_1
8.1547	10.3064	1.1412	−.0075	2.634	1.55	U_1							
8.5624	11.3101	1.2041	−.0177	2.746	1.63	U_1							

TABLE 10. *Toluene viscosity data for molecular weight: 58,000*

Temperature, 30° C							Temperature, 48.2° C						
c	η_r	η_{sp}/c	$\Delta(\eta_{sp}/c)$	$\frac{S}{[\eta]c}$	$\frac{c}{c_0}$	Viscometer	c	η_r	η_{sp}/c	$\Delta(\eta_{sp}/c)$	$\frac{S}{[\eta]c}$	$\frac{c}{c_0}$	Viscometer
g/dl		*dl/g*	*dl/g*				*g/dl*		*dl/g*	*dl/g*			
0.0778	1.0290	0.3723	−0.0002	0.0287	0.032	J_2	0.1978	1.0663	0.3352	−0.0032	0.0639	0.071	J_1
.1172	1.0437	.3733	.0006	.0432	.048	J_2	.2683	1.0898	.3347	.0005	.0867	.096	J_1
.1900	1.0720	.3789	−.0018	.0701	.078	J_2	.4407	1.1511	.3429	.0002	.1424	.158	J_1
.2664	1.1012	.3790	.0007	.0982	.109	J_2	.9261	1.3397	.3668	−.0016	.2992	.332	J_1
.3652	1.1400	.3833	.0018	.1347	.150	J_2	1.0823	1.4060	.3751	−.0028	.3497	.388	R
.4866	1.1900	.3905	.0001	.1795	.199	J_2	1.2547	1.4784	.3813	−.0011	.4054	.450	J_1
.6067	1.2399	.3954	.0007	.2237	.249	J_2	1.4067	1.5416	.3850	.0021	.4545	.504	R
.8170	1.3314	.4056	.0003	.3013	.335	J_2	1.6548	1.6558	.3963	.0022	.5347	.593	R
1.0409	1.4305	.4136	.0029	.3839	.427	S, J_2	2.0092	1.8291	.4126	.0020	.6492	.720	R
1.1699	1.4934	.4217	.0009	.4315	.479	S	2.2501	1.9537	.4238	.0018	.7270	.806	R
1.3354	1.5691	.4262	.0044	.4925	.547	S	2.5567	2.1159	.4365	.0031	.8261	.916	R
1.5554	1.6821	.4385	.0029	.5736	.637	S	2.9601	2.3557	.4580	.0030	.9564	1.06	R
1.6950	1.7553	.4456	.0027	.6251	.695	S	3.5145	2.7010	.4840	−.0007	1.135	1.26	R
1.8622	1.8460	.4543	.0024	.6868	.763	S	3.7991	2.8849	.4961	.0001	1.227	1.36	R
2.0659	1.9658	.4680	−.0010	.7619	.847	S	4.1339	3.1155	.5117	−.0002	1.336	1.48	R
2.3198	2.1242	.4846	−.0045	.8555	.951	S	4.3245	3.2555	.5215	−.0013	1.397	1.55	R, U_1
2.6447	2.3140	.4968	.0002	.9754	1.08	S	4.7364	3.5660	.5418	−.0028	1.530	1.70	U_1
3.0755	2.5929	.5179	.0021	1.134	1.26	S	4.9732	3.7305	.5490	.0008	1.607	1.78	U_1
3.6740	3.0317	.5530	−.0004	1.355	1.51	S							
3.9841	3.2773	.5716	−.0018	1.469	1.63	S							
4.3514	3.5751	.5918	.0013	1.605	1.78	R, S							
4.7187	3.8886	.6122	−.0007	1.740	1.93	R							
5.1537	4.2928	.6389	.0043	1.901	2.11	R, U_1							
5.6446	4.7715	.6682	.0030	2.082	2.31	U_1							
5.9268	5.0714	.6869	.0050	2.186	2.43	U_1							

4. Viscosity Concentration Functions

Although one must be on guard not to attach undue significance to the form of closed analytical expressions that appear to be valid over a more or less wide range, some viscosity-concentration functions are quite useful for certain purposes. Two such are the Martin equation [4]:

$$\frac{\eta_{sp}}{c}=[\eta]\exp(k_1[\eta]c), \tag{1}$$

and the Baker equation [5]:

$$\eta_r=\left(1+\frac{[\eta]c}{n}\right)^n. \tag{2}$$

Besides $[\eta]$, the parameters n and k_1 depend on the polymer-solvent system.

The Martin equation has been applied to a large number of systems. In particular, Spencer and Williams [6] have shown it to represent the viscosities of solutions of polystyrene in toluene from 3 to 20 percent of polymer. Streeter and Boyer [7] have found the Martin equation to be reasonably good for polystyrene in a number of solvents from 1 to 12 percent polymer concentration.

The viscosity data for fraction 1.1 in toluene at 30°C previously exhibited [1] as a plot of η_{sp}/c versus c are shown in figure 1 as a Martin plot. Only above a concentration of about 1.25 g/dl is the Martin representation satisfactory. The solid curve in the inset

of figure 1 to the left of the arrow has been drawn on the basis of a least squares straight line obtained from the plot of η_{sp}/c versus c for concentrations between $c=0.1$ and 1.0 g/dl. The arrow points to the abscissa at which the slopes are the same as in the Martin plot. Figure 2 shows a similar deviation in butanone.

This example points to the uncertainty arising from extension to low concentrations of a representation like Martin's, which is found adequate in a particular concentration range (here 1 to 5 g/dl). The values of $[\eta]$ and k_1 derived from a Martin plot may thus be only mathematical fictions and not represent at all the intercept and initial slope of the viscosity-concentration function, $[\eta]$ being overestimated and k_1 underestimated (cf. [7]).

Where a system is adequately represented by a Martin equation down to low concentrations, the corresponding η_{sp}/c versus c plot is, of course, nowhere linear. For example, the data for fraction 1.1 in methyl ethyl ketone at 30°C and in the mixed solvent at 30°C (figs. 3 and 4) are well represented by a Martin equation over the entire range examined.

In fitting the Baker function to viscosity data, one need not be restricted to integral values of the parameter n for an optimum fit. In any event, only a compromise fit is achieved, and the labor of selecting a representative n may become prohibitive. If, as is here the case, it is of interest to find the variation of n with temperature and with the nature of the polymer-solvent system, the following convenient graphical method for a rapid estimate of n has been found quite useful.

The Baker equation is written in the "reduced" form:

$$\frac{\eta_{sp}}{S}=\frac{1}{S}\left[\left(1+\frac{S}{n}\right)^{n}-1\right], \qquad (2a)$$

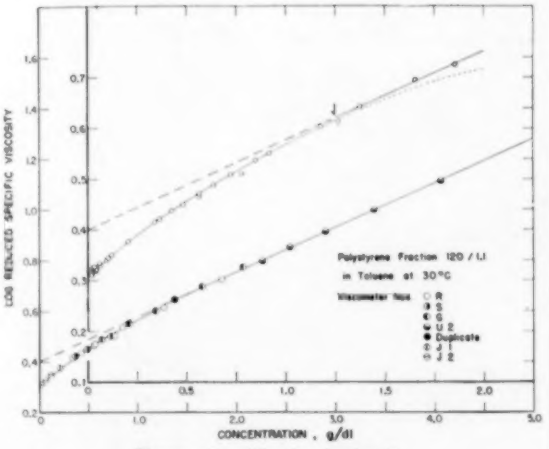

FIGURE 1. *Martin plot (eq 1).*

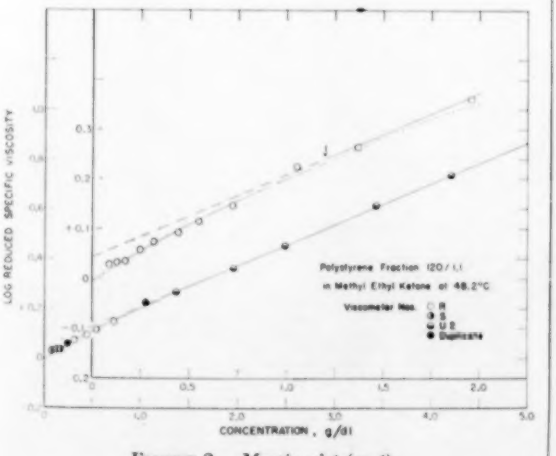

FIGURE 2. *Martin plot (eq 1).*

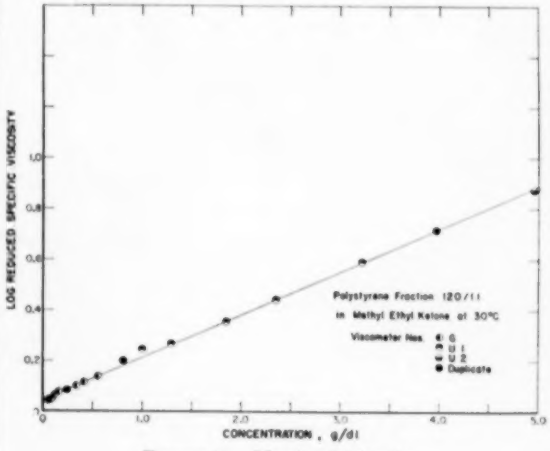

FIGURE 3. *Martin plot (eq 1).*

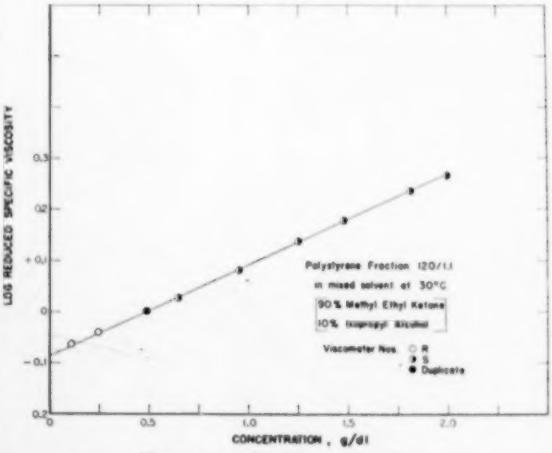

FIGURE 4. *Martin plot (eq 1).*

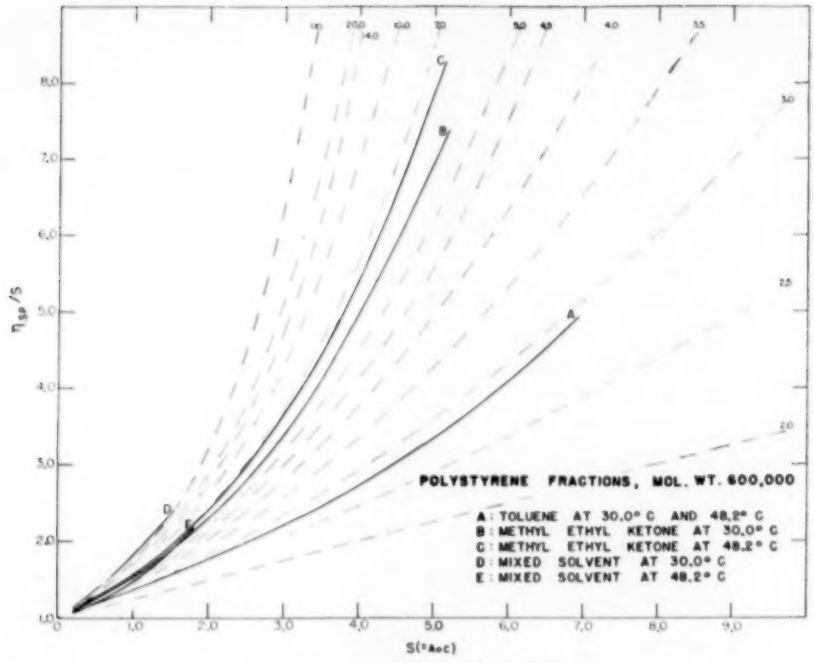
POLYSTYRENE FRACTIONS, MOL. WT. 600,000
A : TOLUENE AT 30.0° C AND 48.2° C
B : METHYL ETHYL KETONE AT 30.0° C
C : METHYL ETHYL KETONE AT 48.2° C
D : MIXED SOLVENT AT 30.0° C
E : MIXED SOLVENT AT 48.2° C
η_{sp}/S
S(°Aoc)

FIGURE 5. *Reduced Baker network (eq 2a).*
The indices, n, are shown at the termini of the dashed lines.

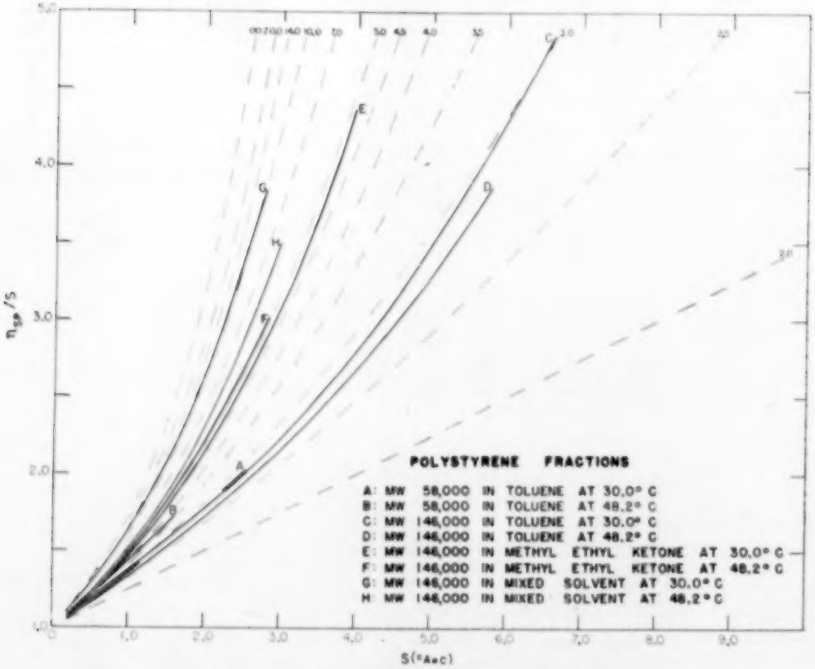
POLYSTYRENE FRACTIONS
A: MW 58,000 IN TOLUENE AT 30.0° C
B: MW 58,000 IN TOLUENE AT 48.2° C
C: MW 146,000 IN TOLUENE AT 30.0° C
D: MW 146,000 IN TOLUENE AT 48.2° C
E: MW 146,000 IN METHYL ETHYL KETONE AT 30.0° C
F: MW 146,000 IN METHYL ETHYL KETONE AT 48.2° C
G: MW 146,000 IN MIXED SOLVENT AT 30.0° C
H: MW 146,000 IN MIXED SOLVENT AT 48.2° C
η_{sp}/S
S(°Aoc)

FIGURE 6. *Reduced Baker network (eq 2a).*
The indices, n, are shown at the termini of the dashed lines.

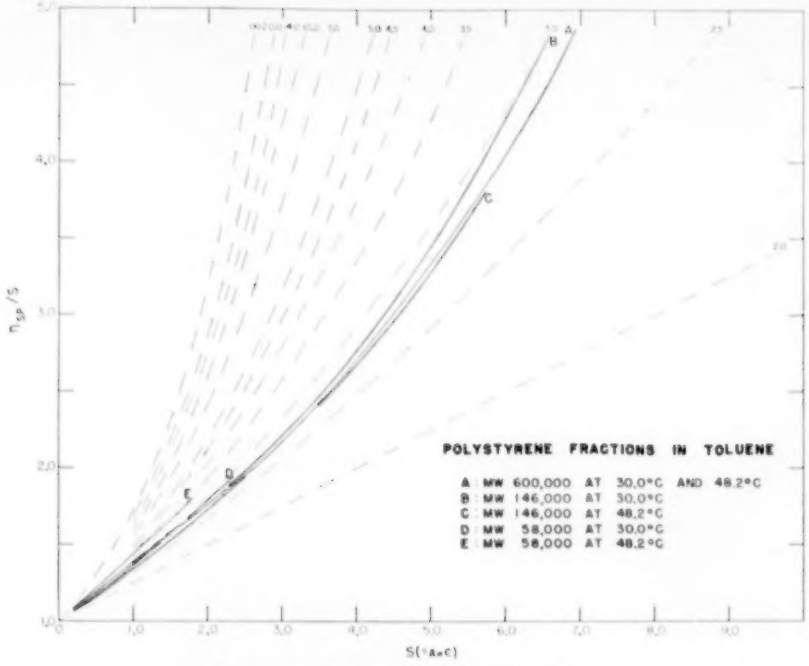

FIGURE 7. *Reduced Baker network (eq 2a).*
The indices, n, are shown at the termini of the dashed lines.

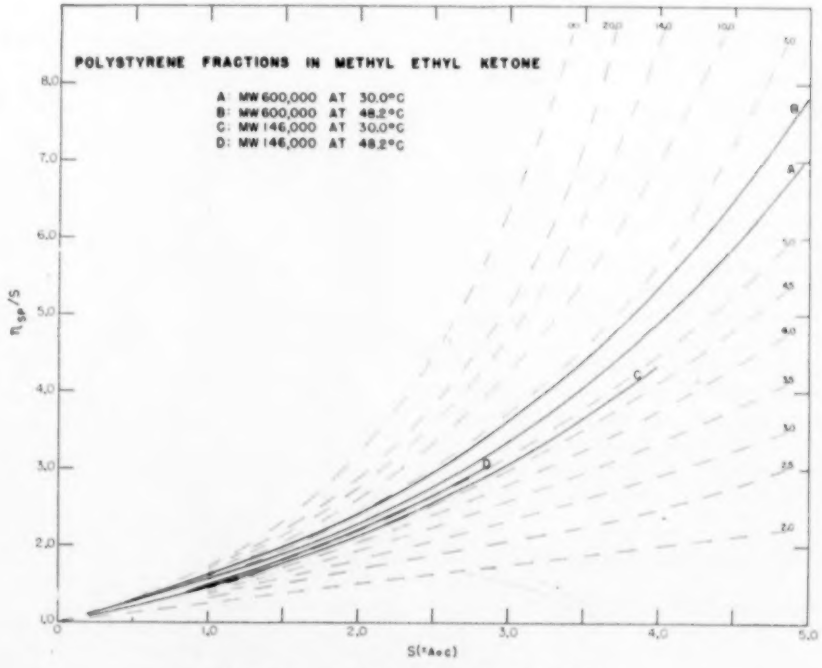

FIGURE 8. *Reduced Baker network (eq 2a).*
The indices, n, are shown at the termini of the dashed lines.

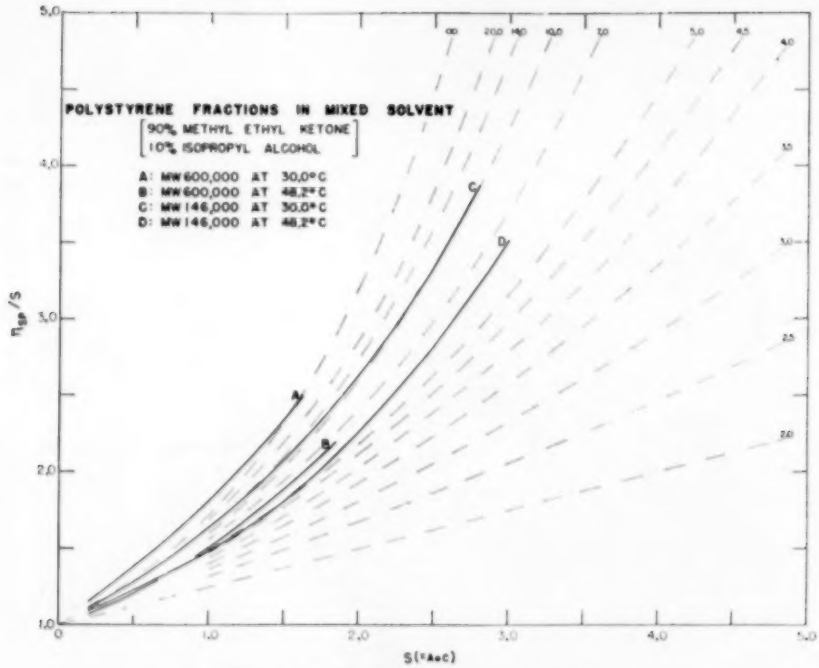

FIGURE 9. *Reduced Baker network (eq 2a).*
The indices, n, are shown at the termini of the dashed lines.

where $S=[\eta]c$. A value of $[\eta]$ is taken from a graph of η_{sp}/c versus c, and the experimental data plotted as η_{sp}/S versus S. Over the set of plotted points is placed a transparent sheet on which are drawn to the same scale a family of curves of the function (2a) for integral or any other desired values of n. The best value of n in the concentration range of interest is then easily obtained by interpolation. The data for our systems are included in the reduced Baker networks in figures 5 to 9.

This representation shows strikingly the relatively slight dependence of n on temperature and on molecular weight in the good solvent and the greater dependence of n on temperature and molecular weight in the mixed (very poor) solvent (figs. 5, 6, 7, 9). In addition, the dependence of n on the nature of the solvent is brought out in figures 5 and 6. The relative constancy of n over a range of concentrations for any one polymer-solvent system shows the utility of the Baker representation.

5. Polynomial Representation

For the purpose of characterizing and comparing systems, the viscosity data were fitted to polynomials as:

$$\eta_{sp}/c=\sum_i A_i c^i, \qquad (3)$$

$A_0=[\eta]$ being the intrinsic viscosity. In the concentration range below 1.0 g/dl, most of the plots of η_{sp}/c versus c (figs. 10 to 15) showed practically no curvature. A polynomial of a reasonable degree found by straightforward application of least squares methods to a range of data that includes a long linear portion must result in a poor fit everywhere. Had the purpose been only to find interpolation formulas, it would have sufficed to use two functions, one for the linear portion, the other for the curved portion. However, it was desired to obtain, as nearly as possible, a representation by means of a single function, at least in a restricted range. The following procedure was therefore adopted as a workable compromise, to bring the labor of calculation within reasonable limits.[3]

A least squares straight line was fitted to the data (as η_{sp}/c versus c) with zero error assumed in c, over a concentration range limited to values of c less than c_1 (see table 11). Where the deviations of the experimental points from this straight line were random in sign, the region was regarded as linear; where the deviation showed systematic changes in sign, the region was regarded as nonlinear, and the calculation repeated for a smaller range. In 11 of the 14 systems a linear region was found. For the linear cases, the intercept and slope were then used as the first two polynomial coefficients, those of the higher powers being obtained by the method of

[3] We wish to acknowledge at this point helpful discussions with John Mandel.

TABLE 11. *Coefficients of polynomials: equation 3*

Molecular weight	Solvent	Temperature, 30° C						Temperature, 48.2° C					
		c_0 [a]	c_1 [b]	A_0	A_1	$A_2\times10^2$	$A_3\times10^3$	$A_4\times10^3$	c_0 [a]	c_1 [b]	A_0	A_1	$A_2\times10^2$	$A_3\times10^3$
		g/dl	g/dl						g/dl	g/dl				
600,000	Toluene	0.45	0.92	[c] 2.04	1.56	−42.4	78.4	.....	0.46	0.8	[c] 1.97	1.389	−25.8	70.8
				[d] 2.04	1.59	[d]	.....	.....			[d] 1.95	1.45	.....	.....
	Methyl ethyl ketone	1.37	.8	[c] 1.02	0.519	29.6	23.0	.....	1.33	.8	[c] 0.977	0.534	14.1	26.7
				[d] 1.02	.519	2.55	62.9	.....			[c] .977	.534	−36.4	75.8
	90-percent methyl ethyl ketone–10-percent isopropyl alcohol	2.20	(e)	[f] 0.771	.404	64.7	.....	.....	1.94	.....	[f] .874	.233	125	.....
				[f] .771	.404	64.7	.....	.....			[f] .874	.233	125	.....
146,000	Toluene	1.28	1.05	[c] .705	.184	−1.94	1.41	.....	1.45	1.20	[c] .619	.125	1.31	0.593
				[d] .704	.188	.....	.....	.....			[c] .623	.118	.....	.....
	Methyl ethyl ketone	2.92	0.9	[c] .445	.0821	−5.13	3.42	−0.207	3.36	.....	[f] .387	.0504	8.28	−.119
				[d] .445	.0821	−2.22	2.18	.....		.....	[f] .392	.0404	11.4	.....
	90-percent methyl ethyl ketone–10-percent isopropyl alcohol	5.26	1.0	[c] .323	.0597	−5.36	2.60	−.165	4.84	1.6	[c] .351	.0572	−0.956	.768
				[d] .323	.0597	−2.96	1.38	.....			[c] .351	.0572	−.783	.672
58,000	Toluene	2.44	1.4	[c] .369	.0438	1.97	−0.0763	.....	2.79	≧5.0	[c] .323	.0456	.....	.....
				[d] .369	.0438	−2.02	1.88	.....			[c] .325	.0437	.....	.....

[a] For definition of c_0, see eq 5.

[b] c_1 is the maximum measured value of concentration below which the reduced specific viscosity is linear.

[c] A_0 and A_1 are based on the initial linear portion. The higher coefficients A_2, were obtained by a least squares calculation, using all the data but holding A_0 and A_1 fixed.

[d] The column entries left blank signify that the best fit was obtained by using only the coefficients indicated.

[e] A_0 and A_1 are based on the initial linear portion, but higher coefficients were obtained by a least squares calculation using only the data for concentrations less than the concentration c_0.

[f] No observed linear portion within the limits of measurement. The coefficients are based on a least squares calculation of all the data to the degree indicated.

least squares, treating the expression $(\eta_{sp}/c - A_0 - A_1 c)$ as dependent variable, and assuming no error in c. For the nonlinear cases, all coefficients in the polynomial were calculated directly by least squares, treating η_{sp}/c as the dependent variable. The upper limit c_1 of the linear range is shown in table 11.

In the fitting of polynomials there is frequently a question as to the degree of polynomial required to give optimum representation of the data. In the present work the degree was chosen by the Gauss criterion [8] according to which the variance

$$\Omega = \frac{\sum_i d_i^2}{n-m},$$

is minimized. Here n is the number of observations, $(m-1)$ the degree of the polynomial, and d_i are the deviations of experimental from calculated values.

In some instances the Gauss criterion was not decisive in that for two consecutive degrees very nearly the same value of Ω was indicated. In such instances, the polynomial degree was chosen for which the algebraic sum of the deviations had the smallest absolute value. In a least squares calculation in which no restrictions (such as fixing the intercept and initial slope) are made, the algebraic sum of deviations is, of course, zero.

The values of the coefficients of the polynomials are listed in table 11. The coefficients giving the best fit over the entire range are shown, as well as coefficients calculated from a range of data for concentrations less than the limit $c=c_0$ indicated in the table. The physical significance of this limitation is discussed in section 6.

6. Discussion

In comparing the specific viscosities of the same solute under different conditions or different solutes in identical environments, it is desirable to introduce a reduced concentration scale. This has already been done in discussing the Baker expression (section 4), the quantity $S=[\eta]c=A_0c$ being such a dimensionless variable. The power series representation of η_{sp}/S in terms of S, corresponding to (3), has the coefficients $k_i=A_i/(A_0)^{i+1}$. Since S is dimensionless, it obviously represents a ratio of two concentrations. One is the weight of solute molecules per unit volume and the other is related to the mass of solute per (mean) unit volume encompassed by the coiling molecule. Thus, if we discard some multiplicative factors (see below), $S=1$ would indicate equality of the two concentrations, that is, the onset of overlapping of the average spheres of action, as determined at infinite dilution. A more accurate estimate for this particular concentration c_0 (see table 11) is arrived at in the following manner [9]. Assuming on the average hexagonal packing of the mean molecular spheres, the average distance R_{12} between two molecule centers at a concentration c and for a molecular weight M is:

$$R_{12}=\left(\frac{M}{cN}\sqrt{2}\right)^{1/3}, \tag{4}$$

where N is Avogadro's number. For $c=c_0$, $R_{12}=2R$, where R is the radius of the molecule, hence:

$$c_0=\frac{\sqrt{2}}{8N}\frac{M}{R^3}. \tag{5}$$

To estimate the radius R we have applied to the intrinsic viscosities of our fractions the theory of Debye-Bueche [10] and of Brinkman [11]. Accordingly:

$$[\eta]=\frac{4\pi}{3}\frac{R^3N}{M}\Phi(x).$$

$\Phi(x)$ is a slowly varying function of the argument. Its representative value for a particular range of

molecular weights is found by comparison with the equation:

$$[\eta]=KM^a.$$

Thus from (5):

$$S=c[\eta]=0.741\Phi(x)\frac{c}{c_0}. \tag{6}$$

The values of a used were for the three solvents respectively: 0.70, 0.60, and 0.52 [12], leading to $\Phi(x)=1.22$, 1.76, and 2.33 [10]. The exponents, a, were assumed to be temperature independent in our range. It should not be inferred that the concentration c_0 represents a "critical" point. However, on approaching it, new molecular mechanisms should become important. According to (6), S and the ratio c/c_0 are in good approximation proportional to each other in a given solvent. Estimates of c_0 based on light scattering values of R are in agreement with our values of c_0 obtained from the intrinsic viscosities.

In the majority of cases our measurements extend to a lower limit of $c/c_0=0.03$ to 0.04. That is, $2R/R_{12}$ is of the order of 0.31 to 0.34. This is the region in which the hydrodynamic interaction between isolated molecules is still important and can be treated by perturbation methods. It represents a long-range effect in contrast to the interactions that determine the concentration dependence of osmotic pressure. At large distances r from a given particle, the flow disturbances decrease as $1/r^3$. It is essentially the summation of this "interaction potential," to use a familiar physical analogy, which has been considered in hydrodynamic treatments of the concentration dependence [13, 16, 17]. However, even at low concentrations, some of the (flexible) molecules have larger than average dimensions and some pairs are closer together than the assumption of a $1/r^3$-interaction admits. For these pairs the summation ought to be carried out in a more accurate manner. The problem becomes quite analogous to the calculation of the interaction potential between rigid dipoles in close proximity. Other molecules may come so close together that they entangle, or, for hydrodynamic purposes, may be considered as a single unit. As an approximation we have previously lumped all these effects into one, namely, what we may call "quasi-aggregates". Thus, in this approximation it is necessary to consider the formation of doublets and triplets that act and interact with each other hydrodynamically [13, 14, 15].

Since the relative populations of the several species depend on higher powers of the concentration than the first, their presence must contribute to the A_1, A_2, etc. terms. This has been shown previously as far as the A_1 coefficient [13]. These populations may be formally expressed in terms of "equilibrium constants". The analysis is now extended up to the A_2-term, which requires the consideration of triplets. Consider the equilibria:

$$\left.\begin{aligned} 2P_1 &\overset{k_{11}}{\rightleftharpoons} P_2 \\ 3P_1 &\overset{k_{111}}{\rightleftharpoons} P_3 \\ P_2+P_1 &\overset{k_{12}}{\rightleftharpoons} P_3 \end{aligned}\right\} \tag{7}$$

They lead to the following expressions for the relative molar concentrations of the three species:

$$\left.\begin{aligned} n_1/n &= 1-2K_1n+(8K_1^2-2K_1K_2-3K_3)n^2 \\ n_2/n &= K_1n[1-(4K_1-K_2)n] \\ n_3/n &= K_3n^2 \end{aligned}\right\} \tag{8}$$

with $n=n_1+2n_2+3n_3$. Terms higher than n^3 have been discarded. The K_i are functions of the rate constants k_i and k_{ij}. In particular, $K_1=k_{11}/k_1$ describes the equilibrium between single and double molecules, while no analogous simple relation holds for K_2 and K_3.

We can now write:

$$\eta_{sp}=A_0^{(1)}c_1+A_1^{(1)}c_1^2+A_2^{(1)}c_1^3+A_0^{(2)}c_2+A_1^{(1,2)}c_1c_2+A_0^{(3)}c_3+O(c^4),$$

where the c_i refer to weight concentrations and the upper indices in the A's to the type of molecule involved. The second and third terms represent the hydrodynamic interactions among pairs and triplets of single molecules. $A_0^{(2)}$ and $A_0^{(3)}$ are the intrinsic viscosities of double and triple molecules respectively. $A_1^{(1,2)}$ refers to the first interaction coefficient between a singlet and doublet. From (8) we find, since $n=c/M$,

$$\left.\begin{aligned} \eta_{sp}/c=A_0^{(1)}+\left[A_1^{(1)}+\frac{2K_1}{M}(A_0^{(2)}-A_0^{(1)})\right]c+\left[A_2^{(1)}-\frac{2K_1}{M^2}(4K_1-K_2)(A_0^{(2)}-A_0^{(1)})\right. \\ \left.+\frac{2K_1}{M}(A_1^{(1,2)}-2A_1^{(1)})+\frac{3K_3}{M^2}(A_0^{(3)}-A_0^{(1)})\right]c^2+O(c^3) \end{aligned}\right\} \tag{9}$$

The first two terms have been given previously [13]. This expression will be valid when the average intermolecular distances are still large in comparison with the molecular dimensions of the isolated molecules and when the number of aggregates is still comparatively small [13, 15]. It is seen that generally the various contributions can be of opposite sign, and partially cancel each other. End-to-end aggregation of rods or spheres makes $A_0^{(2)}-A_0^{(1)}$ positive. Thus in a poor solvent an increase in slope will result. In good solvents, however, the situation may be reversed.

A glance at (9) reveals the difficulty of obtaining estimates of the pertinent parameters. We must

know the intrinsic viscosities and first interaction coefficients of the aggregates, besides having the information for the single molecule, in order to arrive at estimates for the kinetic constants K_i. This requires rather stringent assumptions about the geometry of the aggregates.

Without wishing to take the values given below too literally, we make the following assumptions in the evaluation of (9) with the aid of our experimental data. First, the second step in the equilibrium (7) will be disregarded, since it should be less important in triplet formation than the third; that is $K_2=0$. Second, the hydrodynamic interaction coefficient $A_1^{(i)}$ is determined from the theory of one of the authors [13, 14], that is, $A_1^{(i)}=k_1^{(i)}(A_0^{(i)})^2$; $k_1^{(i)}=0.77$. This value has since been confirmed independently by other authors [16]. It should also be mentioned that, using a different method of attack, a different value of $k_1^{(i)}$, namely, 0.4, has been derived [18, 19]. It has been indicated that k_1 should vary with the shape of the molecule [13, 14, 15]. We shall nevertheless assume $k_1^{(i)}=k_1^{(i,2)}$. Furthermore we set $A_2^{(i)}=0.41(A_0^{(i)})^3$ [17], although this value holds only for a spherical suspension. Third, the hydrodynamic coefficients for the doublets and triplets are calculated from the equations of Zimm and Stockmayer [20] for branched molecules. This procedure assumes that the aggregate can still be treated as a random coil. Accordingly we have:

$$\left.\begin{aligned} A_0^{(2)}-A_0^{(i)}&=A_0^{(i)}\,(g_2{}^{2-a}\cdot 2^a-1)\\ A_0^{(3)}-A_0^{(i)}&=A_0^{(i)}\,(g_3{}^{2-a}\cdot 3^a-1)\end{aligned}\right\} \tag{10}$$

g_2 represents the ratio between the mean square radius of the molecule with one branch point and the linear chain of equal molecular weight, hence the factor 2. g_3 is the corresponding ratio for the molecule with two branch points. a has been previously defined. Now $0.800\geqq g_2\geqq 0.625$ [20], where the two limits refer to a random distribution of chain lengths and fixed equal chain lengths of branches, respectively. Since, in a long coiled chain, the extremities will not be available, aggregation or entanglement will occur primarily through the central portions of the chain. Hence $g_2<0.8$. We shall assume $g_2\geqq 0.625$. While the results are sensitive to the choice made, it should be noted that at $g_2=0.689$, $A_0^{(2)}-A_0^{(i)}=0$, for $a=0.7$. Similarly $0.690\geqq g_3=0.525$. Here the "branches" should be more nearly distributed at random. The value of K_3 is again sensitive to the choice of g_3. For $g_3=0.555$, $A_0^{(3)}-A_0^{(i)}$ vanishes. We shall for our estimate use $g_3\geqq 0.525$, the value corresponding to fixed equal chain lengths. Because of these choices of g_2 and g_3, the number of "aggregates" estimated below represents a minimum value. From (10) there furthermore follows with the assumptions made about the coefficient k_1:

$$A_1^{(i,2)}=A_1^{(i)}\,g_2{}^{2-a}\cdot 2^a \tag{11}$$

With these assumptions, and equating the coefficients experimentally determined for $c<c_0$ with those in equation (9), we obtain for the three fractions in toluene at 30° C, in descending order of molecular weight respectively: $2K_1/M=6.64,\ 2.32,\ 1.55$, dl/g and $3K_3/M^2=7.59,\ 1.09,\ 1.62$ $(dl/g)^2$. One finds therefrom that approximately 5 to 6 percent of all molecules are combined into doublets at a concentration $c=c_0/10$. This is reduced to 2 to 3 percent for concentrations such that two molecules can be accommodated in the empty space between particles. While the absolute magnitudes of K_1 and K_3 are sensitive to a change from 0.77 to 0.70, which is Brinkman's value for $k_1^{(i)}$ [17], the equilibrium concentrations of double molecules are insignificantly altered by this variation. Of course, more profound changes in $k_1^{(i)}$ affect the equilibrium concentrations considerably. Since we expect $k_1^{(i)}$ to increase in a poor solvent [13, 14, 15], we cannot extend these calculations to the two other solvents without additional and arbitrary assumptions.

Again it must be recalled that only a fraction of the concentration n_2 so estimated accounts for actual aggregates that make a negative (probably negligible) contribution to the second virial coefficient of osmotic pressure. Keeping this in mind, we may make an estimate of the standard free energy changes involved, realizing that they will be too high as far as true aggregates are concerned. Flory's results [21], originally derived for the case in which the free energy change $\Delta F°$ on forming a new bond in an association equilibrium is independent of chain length, can be extended to our particular case if we consider only the formation of double molecules. Thus [21]

$$\ln K_1=\frac{-\Delta F°(M)}{RT}+\ln\,[(\gamma-1)\sigma V_1].$$

γ is the coordination number of the lattice, a quantity characteristic for the type of theory from which this result is derived, σ is a symmetry number equal to two in our case and V_1 the molar volume of a chain segment. Thus, depending in the values used for γ, V_1, and on the molecular weight, we find values for $\Delta F°$ ranging between 2 to 5 kcal/mole. The latter value is somewhat high. We can make an independent estimate of the entropy change. If both the two separated chains and the doublet can be considered as random coils, as we have done above, then the entropy corresponding to an end to end distance, r, in an isolated chain of n links each of length b, equals:

$$S(r)-S(0)=-\frac{3}{2}\,k\,\frac{r^2}{nb^2},$$

or $(-3/2)\,k$ in the average configuration. Thus we obtain an entropy increase for the aggregate of $(2-g_2)3/2k$, corresponding to a free energy of the order of 1 kcal/mole.

Equation (9) is based on successive approximations by taking into account the appearance of successively more complex aggregates, which in turn interact hydrodynamically in a successively more complex way, that is by pair, triplet, and higher interactions. This picture should rapidly become untenable as the concentration c_0 is approached and

one should expect a marked increase of the influence of concentration. A glance at figures 10 to 15 indicates, at most, a moderate upswing beyond $c=c_0$. For proteins or solutions of phenolic resins, on the other hand, the concentration dependence, if expressed in a reduced scale, is more pronounced. The coefficient k_1 is generally higher than for polymer solutions and of the order of 0.7 to 1.0. This is consistent with the negative values of n indicated on the Baker plot, figure 16. The data on proteins are due to Oncley, Scatchard, and Brown [22], while those for the other polymers were taken from a summary by Bredée and de Booys [23]. It will also be noted from the graphs, that the polystyrene samples of very low molecular weight (below 20,000) yield considerably higher, or even negative, exponents n than those of large degrees of polymerization. This comparative reduction of interaction effects should in part be due to a change in shape with increasing concentration, which large flexible molecules are capable of undergoing. On close approach of two or more such molecules in a good solvent, each of them will assume configurations that correspond to a smaller average radius than at infinite dilution. In other words, the coils shrink. The magnitude of this effect varies with concentration, and it will tend to counteract the viscosity increment produced by interaction effects.

It is useful at this point to introduce an apparent

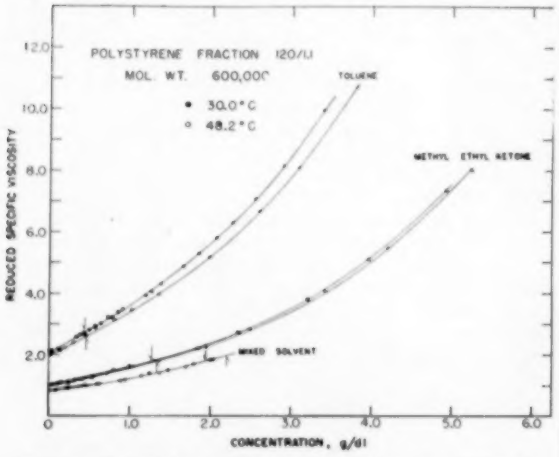

FIGURE 10. *Reduced specific viscosity versus concentration.*
Circles indicate experimental values, lines are drawn from calculated polynomials. Equation 3 and table 11. Arrows show c_0's.

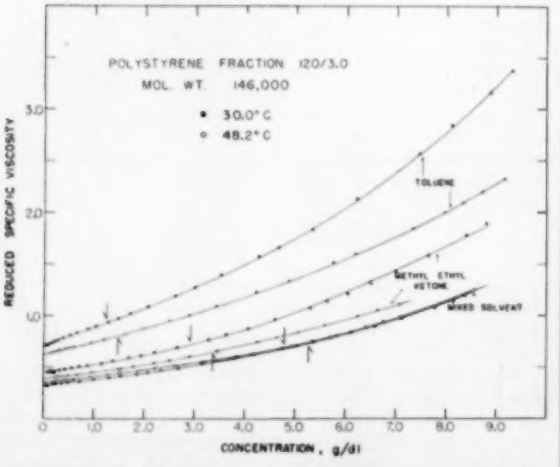

FIGURE 11. *Reduced specific viscosity versus concentration.*
Circles indicate experimental values, lines are drawn from calculated polynomials. Equation 3 and table 11. Arrows show c_0's.

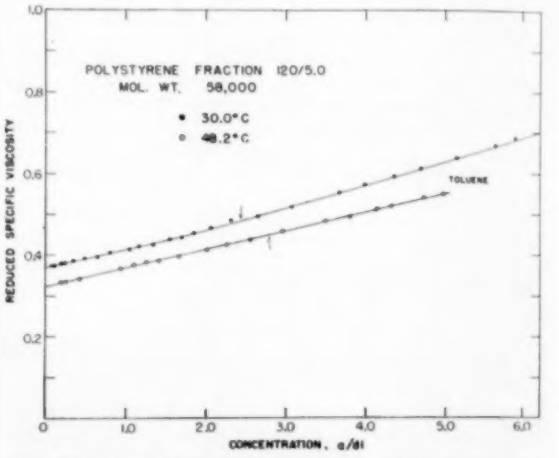

FIGURE 12. *Reduced specific viscosity versus concentration.*
Circles indicate experimental values, lines are drawn from calculated polynomials. Equation 3 and table 11. Arrows show c_0's.

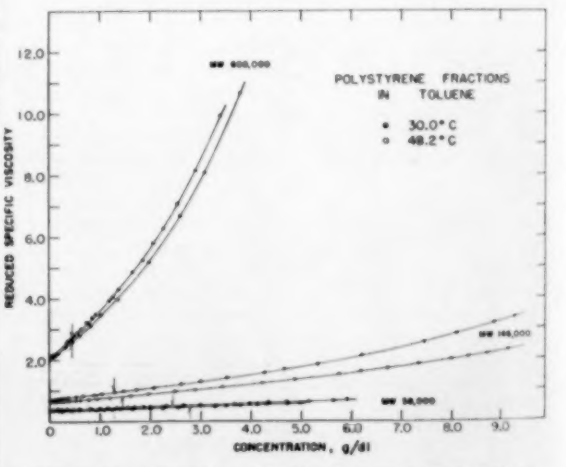

FIGURE 13. *Reduced specific viscosity versus concentration.*
Circles indicate experimental values, lines are drawn from calculated polynomials. Equation 3 and table 11. Arrows show c_0's.

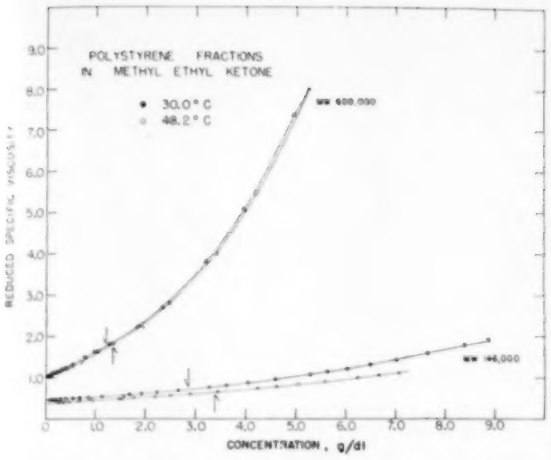

FIGURE 14. *Reduced specific viscosity versus concentration.*
Circles indicate experimental values, lines are drawn from calculated polynomials. Equation 3 and table 11. Arrows show c_0's.

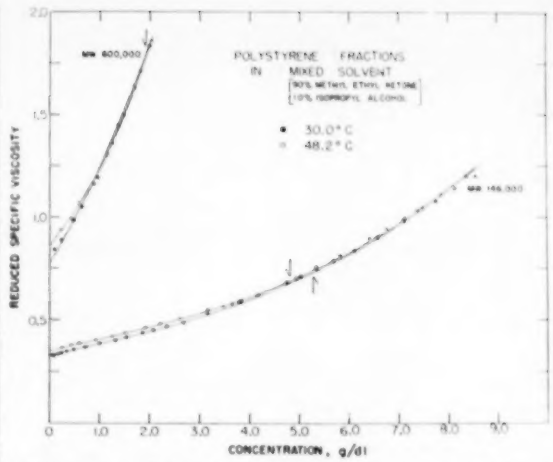

FIGURE 15. *Reduced specific viscosity versus concentration.*
Circles indicate experimental values, lines are drawn from calculated polynomials. Equation 3 and table 11. Arrows show c_0's.

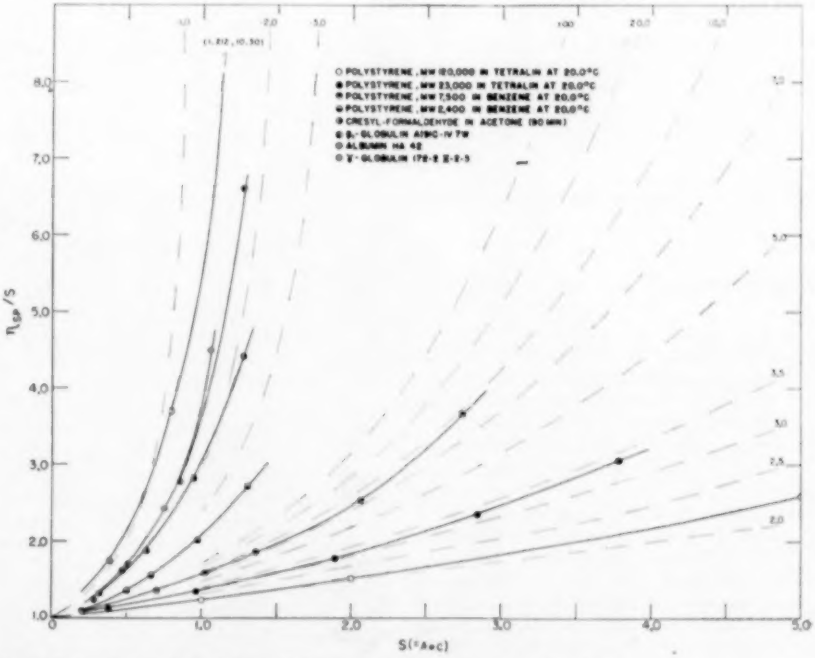
POLYSTYRENE, MW 120,000 IN TETRALIN AT 20.0°C
POLYSTYRENE, MW 23,000 IN TETRALIN AT 20.0°C
POLYSTYRENE, MW 7,500 IN BENZENE AT 20.0°C
POLYSTYRENE, MW 2,400 IN BENZENE AT 20.0°C
CRESYL-FORMALDEHYDE IN ACETONE (90 MIN)
β-GLOBULIN A1PC-IV 7W
ALBUMIN HA 42
γ-GLOBULIN 178-2 2-2-3
η_{sp}/S
$S(^2A_2c)$

FIGURE 16. *Reduced Baker Network (eq 2a) applied to various types of macromolecules.*
The indices, n, are shown at the termini of the dashed lines.

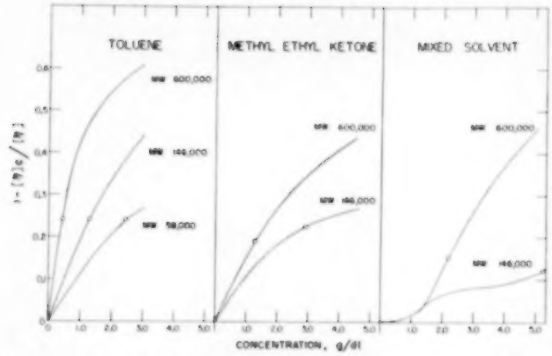

FIGURE 17. $1-([\eta]_c/[\eta])$ *calculated from polynomials and plotted versus concentration (eq 13).*

Circles indicate values for $c=c_0$.

or effective intrinsic viscosity $[\eta]_c$ at finite concentrations [4] namely,

$$[\eta]_c=\frac{1}{\eta_r}\frac{d\eta_r}{dc}=\frac{1}{\eta}\frac{d\eta}{dc}. \tag{12}$$

For $c=0$, this coincides with the customary definition of the intrinsic viscosity. The quantity $[\eta]_c$ is a measure of the relative increment in viscosity produced on adding a solute molecule to a solution of concentration c. This quantity will depend on the volume encompassed by the coiling molecule at this concentration and on its interactions with other molecules.

The concentration dependence of $[\eta]_c$ may be illustrated on the basis of the Baker equation (2). It yields

$$[\eta]_c=\frac{[\eta]}{1+\dfrac{[\eta]c}{n}}. \tag{13}$$

Thus with increasing c, for $n>0$, as is the case in all solutions of large polymers investigated, as far as we know, $[\eta]_c$ decreases, but to a lesser degree in a poor solvent in which n is large, as was shown in section 4. We may recall also that for cellulose derivatives n is larger than for polystyrene, at least in a good solvent [24].

To treat the concentration dependence in this region, two interaction effects must be evaluated. First, is the hydrodynamic interaction between the chains in close contact. It is only approximately taken care of by assuming that for each molecule added the solution can be regarded as "solvent" with a viscosity equal to that of the medium. This is inherent in the designation of $[\eta]_c$, eq 12, as an "intrinsic" viscosity. At high dilution, such an assumption leads to an overestimate of the concentration dependence.

The second effect involves the mutual influence of the chains on their internal configurations and average dimensions. Pair interaction produces an anisotropy in the previously spherically symmetrical distribution of internal configurations. Since it is difficult to treat in detail the interaction of more than two coils, we shall for our purposes simplify the analysis. At sufficiently high concentrations, we have a liquid or quasi-crystalline structure. Each solute molecule is surrounded by a "cage" formed by its neighbors, the effect of which will be approximated here by a uniform pressure, p, on the central molecule. It is furthermore assumed that the molecule can still be represented by a sphere with a given encompassed average volume.

Under the influence of such a pressure, the most probable volume V_0, will be reduced to a value V, depending on the "compressibility" of the chain. In the appendix it is shown that for a Gaussian coil, and if $pV_0/kT\ll 1$:

$$V=V_0\left[1-\frac{9}{4}\frac{pV_0}{kT}+\frac{189}{32}\left(\frac{pV_0}{kT}\right)^2\cdots\right] \tag{14}$$

Thus at vanishing pressure the compressibility $(V-V_0)/pV_0$ is proportional to V_0/kT in complete anatogy to an ideal gas. The volume effect due to the mutual repulsion of the chain segments in the isolated molecules modifies the result (14) so that for the simple model of a van der Waals gas of segments confined to the volume encompassed by the coil, the following result is derived: (see appendix)

$$V=V_0\left[1-\frac{9}{4}\frac{pV_0}{kT}\cdot\frac{2}{3}\frac{1}{\frac{5}{3}\alpha^2-1}+\cdots\right] \tag{14a}$$

α is the extension factor $r_0/r_0^{(0)}$, where r_0 is the most probable end-to-end distance at zero pressure, and $r_0^{(0)}=(\frac{2}{3}\,n\delta^2)^{1/2}$ is the corresponding quantity in the absence of the volume effect. For $\alpha=1$, (14a) reduces to (14).

The pressure, p, is the internal osmotic pressure of the solution, that is the excess $\Pi-\Pi_0$ of osmotic pressure over the van't Hoff term Π_0. Thus we make the identification:

$$\frac{p}{RT}=B_2c^2+B_3c^3+\cdots, \tag{15}$$

where the B_i represent the second and higher virial coefficients of osmotic pressure. In the present theory it would serve no purpose to introduce explicit statistical mechanical expressions for these coefficients; they are treated as experimentally known quantities. Combination of (14a), (15), and (5) leads to the following expression for the relative change in volume:

$$\frac{V}{V_0}=1-\frac{\pi^2}{8}\frac{B_2M^2}{V_0N}\frac{2}{3}\frac{1}{\frac{5}{3}\alpha^2-1}\left(\frac{c}{c_0}\right)^2+O\left(\frac{c}{c_0}\right)^3. \tag{16}$$

Since B_2 has been shown to decrease slowly with increasing molecular weight [12], while α is either constant or increases with M, the compression factor will depend only slightly on molecular weight, if

[4] The authors acknowledge at this point discussions with H. M. Spurlin

the concentration is expressed in reduced units. Furthermore, since the second virial coefficient depends on the covolume, the fourth and higher virial coefficients in the expansion (15) will contain negative contributions. Consequently the osmotic pressure in a given solvent will rise less rapidly with c than for an undeformable solute.

The connection must now be made between the viscosity and these results. Consistent with the assumption made about the hydrodynamic interaction, the ratio V/V_0 is equated to $[\eta]_c/[\eta]$. The fact that the proportionality factor between viscosity and volume also changes is not important for the moderate compressions in question. Accordingly for a poor solvent, $[\eta]_c$ is more nearly independent of concentration than for a good one, in agreement with experience. Actually, the expansion (16) is similar to an expansion of the Baker formula or to extensions of it which have been proposed [23]. Thus we can write:

$$\frac{1}{[\eta]}\frac{d\ln\eta}{dc}=1-\text{const.}\left(\frac{c}{c_0}\right)^2+\text{const.}'\left(\frac{c}{c_0}\right)^3\ldots, \quad (16a)$$

in the neighborhood of the concentration c_0.

We have calculated the quantities $1-([\eta]_c/[\eta])$ by means of our power series representations, using the coefficients for the complete range. The results for the lower temperature are shown in figure 17. As anticipated from our previous considerations, the values of the ordinates are smallest in the poorest solvent. The circles on the curves indicate the values at c_0. It is seen on comparing the three fractions in toluene, that the ordinates corresponding to the abscissae c_0, are very nearly independent of molecular weight. Using these experimental values, we obtain the results for α shown in table 12. The values for B_2 and V_0 were interpolated from the results in reference [12]. One set of coefficients B_2 applies to dichloroethane rather than toluene. However, the molecular dimensions are shown to be practically identical in these two solvents.[5] The α's so derived are reasonable. As is to be expected, they are smaller in butanone than in toluene. The absolute magnitude of α should not be taken too literally, since the hydrodynamic interaction may have been overestimated, making the present values of α too large. The inclusion of higher terms in the expansions (14a) and (15) would have the same consequence.

Thus the picture developed seems satisfactory in the neighborhood of c_0. At higher concentrations, further terms in the expansion (16a) are important. At still higher concentrations, the underlying picture must change again. Actually when the mutual particle distances become very small in comparison to the radius obtaining at infinite dilution, the coils will have the tendency to blow up again. When attempting a theoretical approach to the viscosity of highly concentrated solutions, it will be more feasible to start from the other end, namely the pure polymer, and consider an "intrinsic" viscosity of the small molecule.

[5] After the preparation of this manuscript, osmotic data for toluene became available, of C. E. H. Bawn, R. F. J. Freeman, and A. R. Kamaliddin, Trans. Faraday Soc. **46**, 862 (1950). Th. B_2's derived by these authors are smaller than those used here and lead to α-values that are smaller by about 10% than those given in table 12.

TABLE 12. *Characteristic constants of systems: equation 16*

Solvent	$M\times10^{-4}$	$B_2\times10^6$	$V_0\times10^{-5}$	$1-\frac{[\eta]_c}{[\eta]}$ at $c=c_0$	α
		cm^3g^{-2}	cm^3		
Toluene [a]	6.00	3.5	133	0.24	1.95
Do [a]	1.46	4.8	15	.24	1.72
Do [a]	0.58	5.9	3.6	.24	1.59
2-Butanone [b]	6.00	0.88	68	.19	1.62
Do [b]	1.46	1.42	9.8	.23	1.30

[a] B_2 interpolated from data of [12] for dichloroethane.
[b] B_2 interpolated from data of [12] for butanone.

We have presented a first attempt at a quantitative theory of the viscosity of moderately concentrated solutions, which shows that as at infinite dilution, there exists a parallelism between the thermodynamic and rate properties. A more rigorous theory for the range c/c_0 of the order of unity and beyond will have to overcome considerable difficulties, the nature of which has been made clear in the course of this discussion. We have also shown that one should not expect, even for a Newtonian solution, a single function with two or three parameters to provide a reasonable physical basis for the description of the solution over a wide range of concentrations, even though such empirical expressions are of practical use. The stage is, so to speak, occupied by different mechanisms in different concentration ranges which, of course, cannot be strictly separated from each other. The long linear portion of the η_{sp}/c curves, for instance, observed in several cases, is the result of a compensation of several factors.

7. Conclusions

Our viscosity data can be satisfactorily represented in poor solvents by an equation of the Martin type. The Baker equation is applicable over restricted ranges of concentration if fractional exponents are admitted. These increase in going from a good to a poor solvent and are more sensitive to changes in molecular weight and temperature in a poor than in a good solvent. In fitting polynomials to the experimental curves of η_{sp}/c one finds, as one would expect, some dependence of the coefficients of the quadratic and higher terms on the concentration range admitted for the calculation.

On the basis of the coefficients derived from the data below $c=c_0$, one can estimate the number of "aggregates" formed by entanglements or due to close proximity of two solute molecules, which effectively constitute a single kinetic unit in the field of flow. In toluene we find that 5 to 6 percent of all molecules are doublets at $c=c_0/10$. The corresponding standard free-energy changes depend on molecular weight and can be estimated to be of the order of a few kilocalories per mole. From the quantity $d\ln\eta_r/dc$ at $c=c_0$, we deduce values for the "compressibility" and the extension factor of the coil as a function of molecular weight.

It is a pleasure to acknowledge the assistance of Ruth C. MacKay and Edith L. Malin in the numerical calculations.

8. Appendix

1. Effect of External Pressure on the Dimensions of a Gaussian Coil

The distribution $W(r)dr$ of end-to-end distances r in a chain composed of n elements will have the form:

$$W(r) = \text{const.}\, r^2 e^{-\frac{3}{2}\frac{r^2}{nb^2}} \exp\left(\frac{-pV}{kT}\right). \tag{17}$$

The volume, V, is determined by the radius, R, of the coil. Although this holds strictly only for a Gaussian coil [25], we shall assume proportionality between r and R. The most probable value of r is then determined by the equation:

$$r^3 + \frac{kT}{p'nb^2} r - \frac{2}{3}\frac{kT}{p'} = 0,$$

where p' is proportional to p. For small values of pV_0/kT we expand the solution around $r^2 = r_0^2 = 2/3nb^2$ and obtain:

$$r^2 = r_0^2\left[1 - \frac{3}{2} r_0^2 \frac{p'}{kT} + \left(\frac{3}{2}\right)^3 \left(\frac{r_0^2 p'}{kT}\right)^2 - \frac{7}{4}\left(\frac{3}{2}\right)^4 \left(\frac{r_0^2 p'}{kT}\right)^3 + \cdots\right] \tag{18}$$

This leads to equation (14) in the text.

2. Volume Effect

Several methods of attack have been developed recently with very divergent results. In the following we give a simple derivation, which leads essentially to the result given by Flory [26]. Consider each of the segments to have a covolume $v_0 \sim b_0^3$ and to constitute a gas in a container of volume $\sim R^3$. That is, we assume that all links between segments have been cut. The total number of configurations originally available is then reduced by a factor:

$$\prod_{i=1}^{n-1}\left(1 - \frac{ib_0^3}{R^3}\right) \doteq 1 - \frac{b_0^3}{R^3}\sum_{i=1}^{n} i \doteq e^{-\frac{n^2}{2}\frac{b_0^3}{R^3}}. \tag{19}$$

Again we assume proportionality between r and R, and set

$$R^2 = \lambda r^2,$$

as in a Gaussian coil. Consequently:

$$W(r) \sim r^2 e^{-\frac{3}{2}\frac{r^2}{nb^2}} \exp\left\{-\frac{1}{2}\left(\frac{1}{\lambda}\right)^{\frac{3}{2}} n^2 \frac{b_0^3}{r^3}\right\}. \tag{20}$$

Differentiating (20) and defining

$$\alpha^2\left(\frac{2}{3} nb^2\right) = r^2,$$

we obtain for the most probable value of r:

$$\alpha^5 - \alpha^3 = \text{constant}\left(\frac{b_0}{b}\right)^3 n^{\frac{1}{2}}. \tag{21}$$

This is identical with the result of reference [26].

3. Effect of Pressure and Excluded Volume

Combination of equations (17) and (20) leads to

$$W(r) \sim r^2 e^{-\frac{3}{2}\frac{r^2}{nb^2}} e^{-\beta_1/r^3} e^{-\beta_2 r^2}, \tag{22}$$

where $\beta_1 \sim n^2 b_0^3$, $\beta_2 \sim p/kT$.

The most probable value of r obeys the equation:

$$\frac{3}{2nb^2} r^5 - r^3 - \frac{3}{2}\beta_1 = -\frac{3}{2}\beta_2 r^6.$$

Again we restrict the solution to small values of β_2 and find:

$$r = r_0(1 + \beta_2 \epsilon + \cdots); \qquad \epsilon = -\frac{1}{2}\frac{r_0^3}{\frac{5}{2nb^2} r_0^2 - 1}. \tag{23}$$

Introducing α, this leads to equation (14a), where now $V_0 \sim r_0^3$ represents the volume of the coil with volume effect, at $p = 0$, as given by equation (21).

9. References

[1] S. Rothman, R. Simha, and S. G. Weissberg, J. Polymer Sci. **5,** 141 (1950).
[2] J. W. McElwain, Anal. Chem. **21,** 194 (1949).
[3] S. Rothman, Anal. Chem. **22,** 367 (1950).
[4] A. F. Martin, Meeting of Am. Chem. Soc. (Memphis, April 20 to 24, 1942).
[5] F. Baker, J. Chem. Soc. London **103,** 1653 (1913).
[6] R. S. Spencer and J. L. Williams, J. Colloid Sci. **2,** 117 (1947).
[7] D. J. Streeter and R. F. Boyer, private communication, in press.
[8] A. G. Worthing and J. Geffner, Treatment of experimental data, p. 260 (John Wiley and Sons, Inc., New York, N. Y., 1943).
[9] See, for a similar analysis, R. F. Boyer and R. S. Spencer, J. Poly. Sci. **5,** 375 (1950).
[10] P. Debye and A. M. Bueche, J. Chem. Phys. **16,** 573 (1948).
[11] H. C. Brinkman, Physica **13,** 447 (1947).
[12] P. Outer, C. J. Carr, and B. H. Zimm, J. Chem. Phys. **18,** 830 (1950). The value of 0.52 for the mixed solvent was estimated and is in reasonable accord with values reported for other mixed solvents near the precipitation point.
[13] R. Simha, J. Research NBS **42,** 409 (1949) RP1981.
[14] R. Simha, Proc. Intern. Cong. of Rheology, Holland, (North Holland Publishing Co., Amsterdam, Holland, 1949).
[15] R. Simha, J. Colloid Sci. **5,** 386 (1950).
[16] J. Riseman and R. Ullman, J. Chem. Phys. **19,** 578 (1951).
[17] H. C. Brinkman, private communication, finds $k_1^{[\eta]} = 0.70$, $k_2^{[\eta]} = 0.41$.
[18] N. Saito, J. Phys. Soc. Japan **5,** 4 (1950).
[19] J. M. Burgers, private communication.
[20] B. H. Zimm and W. H. Stockmayer, J. Chem. Phys. **17,** 1301 (1949).
[21] P. J. Flory, J. Chem. Phys. **12,** 425 (1944).
[22] J. L. Oncley, G. Scatchard, and A. Brown, J. Phys. and Colloid Chem. **51,** 184 (1947).
[23] H. L. Bredée and J. de Booys, Kolloid-Z. **79,** 31 (1937).
[24] F. Howlett, E. Minshall and A. R. Urquhart, Shirley Inst. Mem. **18,** 251 (1943).
[25] J. J. Hermans and J. Th. G. Overbeek, Rec. Trav. Chim. **67,** 761 (1948).
[26] P. J. Flory, J. Chem. Phys. **17,** 303 (1949).

WASHINGTON, December 5, 1950.

Journal of Research of the National Bureau of Standards, Vol. 47, No. 4, October 1951, Research Paper 2258

An Analysis of the Effect of the Discontinuity in a Bifurcated Circular Guide Upon Plane Longitudinal Waves [1]

Louis L. Bailin*

The problem of theoretically accounting for the scattering of sound by a semi-infinite circular tube with a small diameter inserted axially, as a measuring probe, into a larger tube of infinite length, is solved in a rigorous and explicit manner when the incident plane waves are restricted to the lowest propagating mode.

The investigation follows the methods outlined by J. Schwinger and consists in solving Helmholtz's equation subject to boundary conditions on the acoustic velocity potential at rigid walls. With the aid of Green's theorem and the Green's function for a point source in the large guide, an integral representation of the desired velocity potential is obtained. The imposition of the boundary conditions leads directly to a homogeneous integral equation of the Wiener-Hopf type, which is solved by transform techniques. The results of this solution are shown to be related to a distance d, which is the length the inner guide must be extended to account for the disturbance occurring in the immediate vicinity of the discontinuity caused by the excitation of higher mode fields.

Another satisfactory method of representing the effect of the discontinuity is by the use of equivalent circuits, by means of which a discontinuity in a wave guide is replaced by a lumped parameter network in a set of transmission lines. The equivalent circuit for this network is derived, and the one essential circuit parameter is related to d and to the explicit solution of the integral equation.

Numerical results for d are given as a function of several different guide ratios and driving frequencies of the incident waves. The results are in considerable disagreement with approximation methods previously reported and indicate that these methods are unsatisfactory in the present problem.

I. Introduction

The problem of theoretically accounting for the scattering of sound by a circular tube with a small diameter inserted axially into a larger tube as a measuring probe (see fig. 1) is merely a specialization of a general class of problems dealing with the effects of obstacles on the propagating modes of both acoustic and electromagnetic waves in guides. It has been shown by J. Schwinger [1] [2], in a series of theoretical studies, that the special class of boundary-value

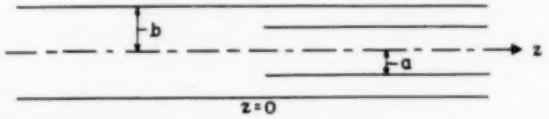

FIGURE 1.

problems, where waves are incident upon a number of semi-infinite parallel metallic structures (structures with parallel axes) of zero thickness and perfect conductivity, can be formulated mathematically as an inhomogeneous integral equation of the Wiener-Hopf type [2]. Because of the discontinuity, the imposition of the particular boundary conditions that the field components must satisfy leads directly to one or more intregral equations of the type

$$g(x)=\int_0^\infty K(x-y)f(y)\,dy, \quad x>0,$$

*Present Address, Hughes Aircraft Co., Culver City, Calif.

[1] The preparation of this paper was sponsored (in part) by the Office of Naval Research. The content of this paper was submitted as partial fulfillment of the requirements for the degree of doctor of philosophy at the University of California at Los Angeles.

[2] Figures in brackets indicate the literature references at the end of this paper.

where $f(x)$ is unknown while $K(x)$ and $g(x)$ are known functions. In the electromagnetic problems $f(x)$ is the surface current density on the obstacle while, in the acoustic case, it represents the discontinuity in the field variable on opposite sides of the obstacle. Generally $g(x)$ is determined by the boundary conditions and the incident fields; it is zero in the present acoustic problem. The components of the field vectors at all points in space can be readily related to the Fourier transform of $f(x)$, which is obtained when the above equation is solved by the transform techniques of the Wiener-Hopf method.

Schwinger [1] also points out that if incident dominant mode waves fall upon an obstacle, the effect of the obstacle is to generate a far field of scattered or reflected lowest mode waves and a local field that is a result of the excitation of the attenuated higher modes. Although a complete description would include both fields in detail, as a practical guide problem, only the far field effect on the propagating modes need be considered. Another satisfactory method of representing this effect is by the use of equivalent circuits, by means of which a discontinuity in a wave guide is replaced by a lumped parameter network in a set of transmission lines.

It will be the purpose of this paper to apply the above methods to an infinite circular guide with a concentric semi-infinite circular bifurcating cylinder and to study the effect of such a discontinuity upon plane longitudinal waves by replacing it by an equivalent circuit. By a consideration of the equations that govern them, the unknown parameter in this network will be shown to reduce to one single essential parameter. This parameter will then be related to a distance d, which is the length the inner guide must be extended to account for the disturbance occurring in the immediate vicinity of the discontinuity caused by the excitation of higher mode fields. By this extension, we are able to introduce a new reference plane, the "virtual plane of bifurcation." Here the one essential parameter vanishes, and the equivalent circuit reduces to three transmission lines in series as shown in figure 6. Thus all measurements made at a distance will indicate that the bifurcation occurs in the virtual plane that is d units from the mouth of the inner guide, provided we assume that the discontinuity produces no disturbance.

The solution to the problem will be obtained by solving Helmholtz's equation subject to boundary conditions on the acoustic velocity potential at rigid walls. This is to be done with the aid of Green's theorem and the Green's function for a point source in the large guide. From the integrals in Green's theorem, we obtain an integral representation of the desired velocity potential. This integral we shall solve in its Fourier integral form with the aid of the homogeneous integral equation that is obtained when boundary conditions on the inner guide are applied to the integral representation. The homogeneous equation is of the above-mentioned Wiener-Hopf type; since $g(x)=0$, a solution by Fourier transforms is possible and yields an explicit expression for the transform of the unknown function. As the transform of the unknown appears in the Fourier integral form of the integral representation, the solution of the Wiener-Hopf equation permits a rigorous result for the velocity potential anywhere in all three regions (large guide, small guide, and coaxial guide).

It is also noteworthy that an alternative integral equation formulation [3] of the problem can be given. This originates with the division of the space interior to the large guide into the two regions $r>a$, $r<a$, where a is the radius of the smaller guide. Green's theorem is then applied to each region with its appropriate Green's function, and each velocity potential is then expressed for $z<0$ in terms of its radial derivative on the surface $r=a$; here z is a distance along the guide with $z=0$ at the mouth of the inner guide. The requirement of continuity for the velocity potential on crossing this surface provides an inhomogeneous integral equation of the Wiener-Hopf type for the determination of the common radial derivative.

Thus if we place the inner guide at $z\geq 0$, then, for $z<0$ and large, the integral representation reduces to linear expressions involving transmission line parameters and, for $z>0$ and large, it is given in terms of expressions from the Wiener-Hopf solution as well as a linear combination of transmission line parameters appropriate to the region considered. When the solutions to the right and left are then transformed back to the reference plane at the mouth of the inner guide, we find that the discontinuity can be represented as a six terminal network and that the

one essential parameter and the distance d can be also expressed in terms of these Wiener-Hopf results.

To simplify the problem to a considerable extent we are going to restrict the driving frequency to permit only one mode plane wave propagation in all three regions. In order to insure this type of propagation in the different regions, we must carefully examine the eigenvalues that arise in the solution of Helmholtz's equation in these regions. For the present problem where the normal derivative of the velocity potential vanishes at rigid walls, such a study will indicate that if we wish the propagating mode to be the lowest "axially symmetric" mode, we must have $0<k<x_1/b$ where x_1 is the smallest zero of the Bessel function $J_1(x)$. Since $\pi<x_1=3.832, \ldots$, we may therefore select π/b as a working upper limit to guarantee only principal-mode propagation in all regions.

II. Description of Physical Quantities

In studying the effect of the discontinuity upon a plane acoustic wave in an infinite circular guide, radius b, which contains a concentric semi-infinite coaxial guide of negligible thickness, radius a, we will assume that all the walls are perfectly rigid. Accordingly, the radial component of the particle velocity vanishes on the rigid walls. Thus, the scalar velocity potential Φ satisfies the wave equation

$$\frac{\partial^2\Phi}{\partial t^2}=c^2\nabla^2\Phi, \tag{1}$$

where c is the velocity of sound propagation in free space, and the partial derivatives of Φ with respect to the coordinates are the respective components of the velocity. A solution under the assumption of harmonic time dependence and complete angular symmetry about the z-axis can be given as

$$\Phi(r,z,t)=\phi(r,z)e^{-ikct}, \tag{2}$$

where

$$k=\frac{2\pi}{\lambda}$$

and λ=free space wavelength. Equation (1) then becomes the scalar Helmholtz equation

$$(\nabla^2+k^2)\phi=\frac{\partial^2\phi}{\partial r^2}+\frac{1}{r}\frac{\partial\phi}{\partial r}+\frac{\partial^2\phi}{\partial z^2}+k^2\phi=0, \tag{3}$$

subject to the boundary condition

$$\frac{\partial\phi}{\partial r}=0 \text{ at } \begin{cases} r=b \text{ for all } z \\ r=a \text{ for } z>0. \end{cases} \tag{4}$$

Once ϕ is known, we can calculate the other important acoustic quantities from the classic relationships between the velocity potential, pressure, density of gas, and condensation.

We now formulate the equation which expresses the field variable in terms of the discontinuity of ϕ across the surface of the inner guide (surface current density in electromagnetic case). To do this, we are going to make use of Green's theorem to construct the Green's function for the structure at hand out of a more readily obtainable one, which in our problem is the one for the empty guide of radius b. Thus we are considering the inner guide as an obstacle embedded in the space of the other. The appropriate Green's function which will aid appreciably in the solution of the differential equation in ϕ satisfies a similar but inhomogeneous equation with the simpler boundary condition

$$\frac{\partial G}{\partial r}=0 \text{ at } r=b \text{ for all } z. \tag{5}$$

Therefore, Green's function for the velocity potential, with no angular dependence, satisfies the equation

$$(\nabla^2+k^2)G(r,r',z-z')=-\frac{\delta(r-r')}{r}\,\delta(z-z'). \tag{6}$$

Here $\delta(x-x')$ is the Dirac delta function and is zero everywhere save at $x-x'$, where it becomes infinite in such a fashion as to make

$$\int_{-\infty}^{\infty}\delta(x-x')dx'=1. \tag{7}$$

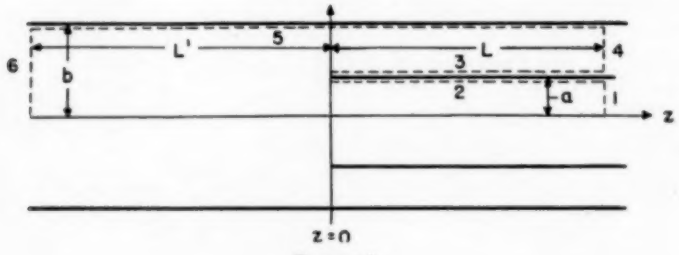

FIGURE 2.

In applying Green's theorem, we take the region under consideration as that which is enclosed by the dotted line in figure 2 and write

$$\int_{V'}[G(\nabla'^2+k^2\phi-\phi(\nabla'^2+k^2G]dV'=\int_{S'}\left(G\,\frac{\partial\phi}{\partial n'}-\phi\,\frac{\partial G}{\partial n'}\right)dS', \tag{8}$$

where n'=outward normal to the bounding surface. Although dV' represents an element of volume enclosed by the dotted line and dS' an element of surface area, the problem can be reduced to two dimensions by immediately integrating with respect to the angle, since there is complete circular symmetry. This integration merely brings in a factor of 2π on both sides of the above and removes the angle dependence from all subsequent equations. G here is an appropriate Green's function that satisfies (6) and (5).

To evaluate (8), we impose boundary conditions (4) and (5) together with (3) and (6). Since the volume integral reduces to $\phi(r,z)$, Green's identity yields

$$\phi(r,z)=\int_{S'}\left(G\,\frac{\partial\phi}{\partial n'}-\phi\,\frac{\partial G}{\partial n'}\right)dS', \tag{9}$$

where S' is determined by the six regions in figure 2 and n' measures distance along the outward normal to the surface enclosed by dotted line. By writing $G^-(r,r',z-z')$ as the asymptotic form of Green's function for z' large and negative and $G^+(r,r',z-z')$ as the asymptotic form for z' large and positive, (9) becomes the sum of the six integrals,

$$\int_1=\int_0^a\left[G^+\,\frac{\partial\phi}{\partial z'}-\phi\,\frac{\partial G^+}{\partial z'}\right]_{z'=L}r'dr'$$

$$\int_2=\int_0^L\left[-\phi(a-0,z')\,\frac{\partial G}{\partial r'}\right]_{r'=a}adz'$$

$$\int_3=\int_0^L-\left[-\phi(a+0,z')\,\frac{\partial G}{\partial r'}\right]_{r'=a}adz',$$

(minus in front since $n'=-r'$),

$$\int_4=\int_a^b\left[G^+\frac{\partial\phi}{\partial z'}-\phi\frac{\partial G^+}{\partial z'}\right]_{z'=L}r'dr'$$

$$\int_5=\int_{-L'}^{L}\left[G\frac{\partial\phi}{\partial r'}-\phi\frac{\partial G}{\partial r'}\right]_{r'=b}bdz'=0$$

$$\int_6=\int_0^b-\left[G^-\frac{\partial\phi}{\partial z'}-\phi\frac{\partial G^-}{\partial z'}\right]_{z'=-L'}r'dr', \tag{10}$$

(minus in front since $n'=-z'$).

Since it will be shown later that all integrals taken along transverse surfaces are independent of L or L' as the case may be, we may now let L and $L'\to\infty$ and write (10) as

$$\phi(r,z)=\int_0^\infty(\phi^+-\phi^-)\left(\frac{\partial G}{\partial r'}\right)_{r'=a}adz'+\lim_{\substack{L\to\infty\\L'\to\infty}}\left[\int_0^a\left(G^+\frac{\partial\phi}{\partial z'}-\phi\frac{\partial G^+}{\partial z'}\right)_{z'=L}\right.$$

$$\left.+\int_a^b\left(G^+\frac{\partial\phi}{\partial z'}-\phi\frac{\partial G^+}{\partial z'}\right)_{z'=L}r'dr'-\int_0^b\left(G^-\frac{\partial\phi}{\partial z'}-\phi\frac{\partial G^-}{\partial z'}\right)_{z'=-L'}r'dr'\right] \tag{11}$$

The difference of the velocity potential on the inner and outer surfaces of the small guide which appears in the first integral of (11) is a consequence of the oppositely directed normals at these surfaces.

III. Derivation of the Appropriate Green's Function

To obtain the solution $G(r,r',z)$ of (6) in the total space interior to the larger guide, we shall apply standard Fourier transform techniques. Thus, we transform z out of (6) by defining the Fourier transform in z as

$$\mathcal{G}(r,r',\zeta)=\int_{-\infty}^{\infty}e^{-i\zeta z}G(r,r',z)dz, \tag{12}$$

where we have written z instead of $z-z'$, since this binomial appears explicitly in the solution, $\mathcal{G}$ now satisfies the equation

$$\left(\frac{\partial^2}{\partial r^2}+\frac{1}{r}\frac{\partial}{\partial r}+\gamma^2\right)\mathcal{G}(r,r',\zeta)=\frac{-\delta(r-r')}{r}, \tag{13}$$

where $\gamma^2=k^2-\zeta^2$; $\mathcal{G}$ is subject to the boundary conditions: (1) that it be finite at the origin and (2) that its normal derivative vanish at $r=b$. Thus, we must seek a solution of Bessel's equation of order zero, since there is angular symmetry, which satisfies these boundary conditions and is continuous at $r=r'$. Following Courant-Hilbert [4], the solution of (13) can be given as

$$\left.\begin{aligned}\mathcal{G}(r,r',\zeta)&=\frac{\pi}{2}\frac{J_0(\gamma r')}{J_1(\gamma b)}\left[J_0(\gamma r)N_1(\gamma b)-N_0(\gamma r)J_1(\gamma b)\right]\qquad(r>r')\\ \mathcal{G}(r,r',\zeta)&=\frac{\pi}{2}\frac{J_0(\gamma r)}{J_1(\gamma b)}\left[J_0(\gamma r')N_1(\gamma b)-N_0(\gamma r')J_1(\gamma b)\right].\qquad(r<r')\end{aligned}\right\} \tag{14}$$

By the Mellin inversion, these then yield G in the form

$$G=\frac{1}{4}\int_{i\sigma-\infty}^{i\sigma+\infty}e^{+i\zeta z}d\zeta\frac{J_0(\gamma r_<)}{J_1(\gamma b)}\left[J_0(\lambda r_>)N_1(\gamma b)-N_0(\gamma r_>)J_1(\gamma b)\right] \tag{15}$$

where the integration contour is a straight line in the region of regularity of the Green's function transform and $r_>$, $r_<$ symbolizes the larger and smaller of the coordinates r, r', respectively.

To determine the region where the integral in (15) converges, we must first determine the form of G and then apply it to (12) which defines $\mathcal{G}(\zeta)$. From our fundamental assumption of only one mode propagation, we know that

$$G \sim Ae^{ik|z|} + \sum_{n=1}^{\infty} B_n e^{-\kappa_n |z|}. \tag{16}$$

It can be easily shown that for a G of this form, the integral in (12) has no region of regularity unless k, the propagation constant, has an arbitrarily small positive imaginary part (which is eventually set equal to zero). This corresponds to a small attenuation of the sound waves traveling in the guide. Thus, if we let $k=k_1+i\epsilon$ and introduce the coordinates in the ζ-plane as $\zeta=\xi+i\eta$, (12)| converges in the strip $|\eta|<\epsilon$ (Im k). Consequently, the inversion given in (15) can be performed, if σ is restricted to this same strip.

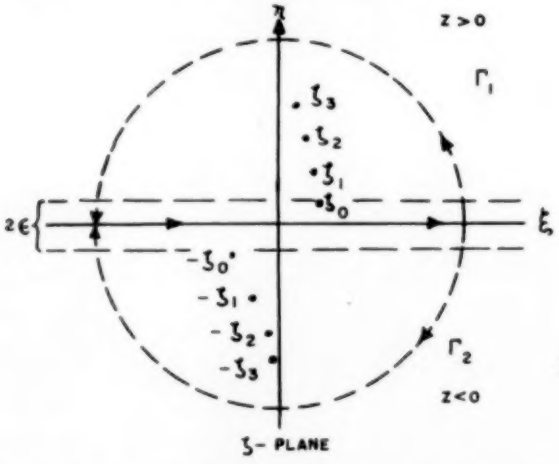

FIGURE 3.

The integral in (15) may now be evaluated by computing the residues inside the semicircular contours pictured in figure 3. The poles of (15) which are given by the zeros of $J_1(\gamma b)$ are all complex for $\epsilon>0$. Thus, if we let $J_1(\gamma_n b)=J_1(x_n)=0$ for $n=0,1,2,3,\ldots$ and $\zeta_n=k^2-\gamma_n^2$, compute the residues inside Γ_1 and Γ_2, and then let $\epsilon\to 0$, we find that the solution of (6) becomes

$$G=\frac{ie^{ik|z-z'|}}{kb^2}+\sum_{n=1}^{\infty}\frac{J_0\left(x_n\frac{r}{b}\right)J_0\left(x_n\frac{r'}{b}\right)e^{-\kappa_n|z-z'|}}{\kappa_n b^2 J_0^2(x_n)}. \tag{17}$$

Here we have insured only one mode propagation by restricting k to be less than x_1/b and defining the attenuation constants by $\kappa_n^2=(x_n/b)^2-k^2$ where $\kappa_1^2=(x_1/b)^2-k^2$ is the smallest.

The Green's function which is appropriate to this problem must give a physical description of waves incident upon and reflected from a discontinuity in a guide. Since (17) represents a wave traveling outward from a source, the appropriate Green's function requires a superposition of (17) and its complex conjugate which is the solution of (6) representing a wave traveling inward to a sink. Thus if we take one half of the sum of (17) and its conjugate and simplify the results, we obtain

$$G(r,r',z-z')=-\frac{\sin k|z-z'|}{kb^2}+\sum_{n=1}^{\infty}\frac{J_0\left(x_n\frac{r}{b}\right)J_0\left(x_n\frac{r'}{b}\right)e^{-\kappa_n|z-z'|}}{\kappa_n b^2 J_0^2(x_n)}, \tag{18}$$

which has the desired physical properties.

IV. Evaluation of Integrals

Once the appropriate Green's function has been determined, we can proceed to evaluate the integrals in (11). This is done in paragraphs (a) and (b), since the character of the results and the evaluation techniques used differ widely. Paragraph (a) is concerned with obtaining the far field contribution in terms of the transmission line parameters and paragraph (b) with the setting up of the Wiener-Hopf integral equation which is a result of the first integral in (11).

(a) In proceeding, let us temporarily ignore the first integral of (11) and examine the last three. From the explicit form of the Green's function, (18), the asymptotic forms of G can be given as

$$G^+(r, r', z-z')=G^-(r', r, z-z')=-\frac{\sin k|z-z'|}{kb^2}. \tag{19}$$

Thus, when we examine (11) for L and L' sufficiently large so that the attenuated terms may be considered negligible, only the forms in (19) need be used. It can be shown [5] that in terms of the propagation of acoustic waves in transmission tubes, the velocity potential and pressure obey analogous equations to those for currents and voltages in a transmission line. Thus, for z large, ϕ behaves as the current in a transmission line which we will denote as $I(z)$. Then, in terms of the transmission line currents and voltages measured at $z=0$, we write

$$\phi(r, z)\sim I(z)=[I\cos kz-iVY\sin kz], \tag{20}$$

where

$$Y=\frac{1}{z}=\frac{1}{\rho c}$$

is the characteristic admittance of the line and ρ is the density of the air or the gas in the tubes.

Using (20) for each of the three regions under consideration, we note that as $z\to-\infty$

$$\phi(r,z)\sim I_1(z)=[I_1\cos kz+iV_1Y_1\sin kz], \tag{21}$$

while for $z\to\infty$ and for $r<a$

$$\phi(r,z)\sim I_3(z)=[I_3\cos kz-iV_3Y_3\sin kz], \tag{22}$$

and for $z\to\infty$ and for $b>r>a$

$$\phi(r,z)\sim I_2(z)=[I_2\cos kz-iV_2Y_2\sin kz]. \tag{23}$$

Thus, the last integral of (11) becomes

$$\lim_{L'\to\infty}\left[-\int_0^b\left(G^-\frac{\partial\phi}{\partial z'}(r',z')-\phi\frac{\partial G^-}{\partial z}\right)_{z'=-L'}r'dr'\right]=\frac{I_1(z)}{2}, \tag{24}$$

since

$$\frac{\partial\phi}{\partial z'}=k(-I_1\sin kz'+iV_1Y_1\cos kz'),\quad G^-=-\frac{\sin k(z-z')}{kb^2},\quad \frac{\partial G^-}{\partial z'}=\frac{1}{b^2}\cos k(z-z').$$

Likewise,

$$\lim_{L\to\infty}\left[\int_0^a\left(G^+\frac{\partial\phi}{\partial z'}-\phi\frac{\partial G^+}{\partial z'}\right)_{z'=L}r'dr'\right]=\left(\frac{a^2}{b^2}\right)\frac{I_3(z)}{2} \tag{25}$$

and

$$\lim_{L\to\infty}\left[\int_a^b\left(G^+\frac{\partial\phi}{\partial z'}-\phi\frac{\partial G^+}{\partial z'}\right)_{z'=L}r'dr'\right]=\left(\frac{b^2-a^2}{b^2}\right)\frac{I_2(3)}{2} \tag{26}$$

since

$$\frac{\partial\phi}{\partial z'}=k(-I_3\sin kz-iV_3Y_3\cos kz'),\quad G^+=-\frac{\sin k(z'-z)}{kb^2},\quad \frac{\partial G^+}{\partial z'}=-\frac{\cos k(z'-z)}{b^2}.$$

Thus (11) becomes

$$\phi(r,z)=\int_0^\infty H(z')\left(\frac{\partial G}{\partial r'}\right)_{r'=a}dz'+\frac{1}{2}\left[I_1(z)+\left(\frac{b^2-a^2}{b^2}\right)I_2(z)+\left(\frac{a^2}{b^2}\right)I_3(z)\right], \tag{27}$$

where

$$H(z)=a\,[\phi^+(r,z)_{r=a+0}-\phi^-(r,z)_{r=a-0}]. \tag{28}$$

Since (28) is independent of L and L' we, therefore, note that all the integrals taken along transverse surfaces yield propagating terms which depend only on z. Equation (28) represents the velocity potential at all points in the large guide in terms of the potentials of the three far fields and the potential of the unknown scattered field which is given by the integral.

(b) Since $H(z)$ is as yet an unknown function, (27), the equation we referred to in our introduction as the integral representation of the desired velocity potential, is an inhomogeneous integral equation. When we impose the acoustic boundary condition

$$\left[\frac{\partial\phi}{\partial r}\right]_{r=a}=0, \qquad \text{for } z\geq 0,$$

this equation becomes readily soluble by transform methods since it is homogeneous and of the convolution type.

Thus, if we call

$$V(z)=\left(\frac{\partial\phi}{\partial r}\right)_{r=a} \qquad \text{for } z<0,$$

and since the propagating terms drop out in the differentiation, we have from (27)

$$\left.\begin{aligned} 0&=\int_{-\infty}^{\infty}K(z-z')H(z')dz', \qquad z\geq 0\\ V(z)&=\int_{-\infty}^{\infty}K(z-z')H(z')dz', \qquad z<0 \end{aligned}\right\} \tag{29}$$

where the range of integration has been extended to $-\infty$, since, from (28)

$$H(z)=\begin{cases}0, & z<0\\ H(z), & z\geq 0.\end{cases}$$

Equation (29) is a homogeneous integral equation that resembles Wiener-Hopf type, since the dependence of G and therefore the kernel,

$$K(z-z')=\left[\frac{\partial}{\partial r}\left\{\frac{\partial G}{\partial r'}(r',r,z-z')\right\}\right]_{r=r'=a},$$

upon z is of the form $(z-z')$.

V. Derivation of the Lumped Parameter Circuit and the One Essential Parameter

From equation (27), we can now derive the circuit relation of a lumped parameter network with which the discontinuity can be replaced, if we concern ourselves with fields far enough away from the mouth of the inner guide so that all attenuated modes have essentially vanished. To investigate this far field result on the left as $z\to-\infty$, we let $\phi(r,z)$ be given by the transmission line expression (21) and define the characteristic admittances as inversely proportional to the area:

$$\frac{1}{Z_1}=Y_1\sim\frac{1}{\pi b^2}; \qquad \frac{1}{Z^2}=Y_2\sim\frac{1}{\pi(b^2-a^2)}; \qquad \frac{1}{Z^3}=Y_3\sim\frac{1}{\pi a^2}. \tag{30}$$

Thus, as we shall see later, the integral in (27) vanishes for $z<0$ and large and we are left with

$$I_1(z)=\frac{1}{2}\left[I_1(z)+I_2(z)\frac{Z_2}{Z_1}+I_3(z)\frac{Z_3}{Z_1}\right],$$

which becomes

$$Z_2I_2(z)+Z_3I_3(z)-Z_1I_1(z)=0. \tag{31}$$

Now, if we rewrite the above in terms of the I's and V's at $z=0$, we have

$$Z_2(I_2\cos kz-iV_2Y_2\sin kz)+Z_3(I_3\cos kz-iV_3Y_3\sin kz)-Z_1(I_1\cos kz+iV_1Y_1\sin kz)=0$$

and since the sine and cosine are linearly independent functions, (31) becomes

$$Z_2I_2+Z_3I_3-Z_1I_1=0 \tag{32}$$

and

$$V_1+V_3+V_3=0. \tag{33}$$

These two, together with

$$Z_1=Z_2+Z_3, \tag{34}$$

a result of (30), are the defining equations for a six terminal lumped parameter circuit. Thus we have three relationships between the circuit parameters which were deduced by examining the effect on the velocity potential as $z\to-\infty$ and which represent the far field results to the left. We will presently determine the far field results to the right and then by expressing them in terms of the current and voltages at the zero reference plane, we will find that the extrapolated results coming from the left and right can be represented by same six terminal impedance network.

In general, a six terminal network contains nine impedance parameters representing the ratios of voltages to currents for all possible combinations of the three independent voltages and currents. However, if we make use of the reciprocity theorem (see Schwinger [1] or Everett [6]) of electrical circuit theory the number of impedance parameters is reduced to six. From the above three equations, we further reduce this number to three, which we will call the susceptances, B_1, B_2, and B_3. Also, from (34), we notice that they must be proportional to Y_1, Y_2, and Y_3, respectively. If this circuit is to satisfy the above equations, it must have the following delta form (fig. 4) with nondissipative pure reactive elements and with the power flow arbitrarily chosen to flow into the junction from both sides.

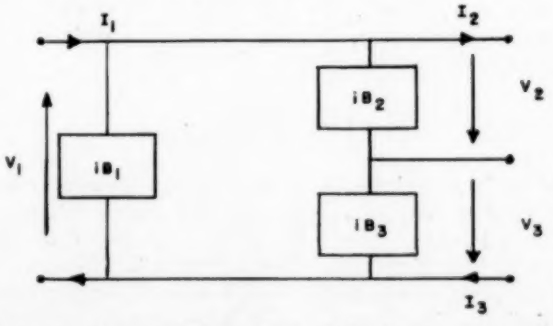

FIGURE 4.

Since the circuit parameters are independent of the impressed currents and voltages, we can now obtain independent relationships between the B's as follows:

1. Open circuit lines 2 and 3. Thus $I_2=I_3=0$ and from (32), $I_1=0$. By looking into line 1, we see B_1 in parallel with the series combination of B_2 and B_3 and we have

$$\left\{iB_1+\frac{1}{\frac{1}{iB_2}+\frac{1}{iB_3}}\right\}=0 \text{ or } \left[\frac{1}{B_1}+\frac{1}{B_2}+\frac{1}{B_3}\right]=0. \tag{35}$$

2. If we terminate lines 2 and 3 by their characteristic impedance, it can be easily shown that the impedance seen from line 1 is the characteristic impedance

$$Y_1 = iB_1 + \frac{(iB_2 + Y_2)(iB_3 + Y_3)}{(iB_2 + iB_3 + Y_2 + Y_3)}. \tag{36}$$

With the independent derivation of these last two equations, we see that the number of independent parameters is now one. Thus from the proportionality required by (34), we let

$$B_1 = b_1 Y_1,\ B_2 = b_2 Y_2, \text{ and } B_3 = b_3 Y_3.$$

Then from (36), we obtain

$$\frac{1}{Y_1(1 - ib_1)} = \frac{1}{Y_2(ib_2 + 1)} + \frac{1}{Y_3(ib_3 + 1)} \tag{37}$$

and (35) becomes

$$\left[\frac{1}{Y_1 b_1} + \frac{1}{Y_2 b_2} + \frac{1}{Y_3 b_3}\right] = 0. \tag{38}$$

By solving (37), (38), and (34) simultaneously for the three unknown parameters, we find that

$$b_1 = -b_2 = -b_3 = B \tag{39}$$

and figure 4 reduces to figure 5.

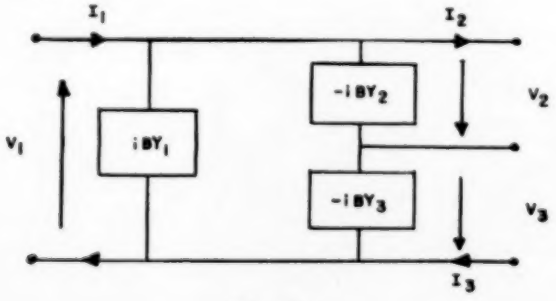

FIGURE 5.

Thus we have shown that with respect to the far field results on the left, the discontinuity can be replaced by the above network. To determine the effect on the right as $z \to +\infty$, we must first evaluate the integral in (27). A straight forward circuit analysis of figure 5 shows that B is related to the circuit parameters by

$$B = \frac{i(I_2 - I_1)}{V_1 Y_1 + V_2 Y_2}. \tag{40}$$

We have now shown that the circuit in figure 5 can be used to represent the discontinuity, when the parameters are measured from the $z=0$ reference plane which is at the mouth of the inner guide. Since, there is only one essential circuit parameter which has a known variation with driving frequency and the distance to the reference, it is possible to find a reference plane in which the equivalent circuit susceptances vanish and, consequently, the equivalent circuit reduces to three transmission lines in series as shown in figure 6.

This new reference plane is a "virtual plane of bifurcation", inasmuch as all measurements made at a distance will indicate that the bifurcation occurs in this plane, provided we neglect the effect of the discontinuity. Particularly, if one of the tubes is introduced in order to take measurements, the quantities will be measured in the virtual plane and not at the mouth of the tube.

To find this virtual plane which is at $z=-d$, or a distance d "ahead" of the actual plane of bifurcation, we follow the method outlined by Miles [7] and let $\eta = kd$ and transform the

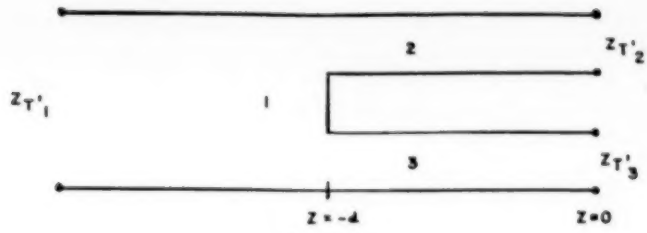

FIGURE 6.

impedance seen by the i-th tube ($i=1,2,3,$), Z_{T_i} (plane $z=0$), to Z'_{T_i} (plane $z=-d$). This transformation is effected by the use of

$$\frac{Z_{T_i}}{Z_i}=\frac{\pm\frac{Z_{T_i}}{Z_i}\cos\eta+i\sin\eta}{\pm\cos\eta+i\left(\frac{Z_{T_i}}{Z_i}\right)\sin\eta}, \tag{41}$$

but care must be taken to select the proper signs (both plus if the direction of the power flow obtained by following V_i then I_i is in the positive z direction) and to use a negative η since the reference plane is being moved to $z=-d$. Thus, if we load terminals 2 and 3 (fig. 5) with arbitrary admittances Y_{T_2} and Y_{T_3}, it can be easily shown that line 1 sees

$$Y_{T_1}=\frac{1}{Z_{T_1}}=iBY_1+\frac{[Y_{T_2}-iBY_2]\,[Y_{T_3}-iBY_3]}{[Y_{T_3}+Y_{T_2}-iB(Y_3+Y_2)]}. \tag{42}$$

Thus if

$$Z_{T_3}=0=\frac{1}{Y_{T_3}} \quad \text{and} \quad Y_{T_2}=0, \tag{43}$$

then from (42)

$$Z_{T_1}=\frac{1}{iB(Y_1-Y_2)}. \tag{44}$$

Now, if we transform the above Z_{T_i} to Z_{T_i} until the circuit can be given as the series combination (fig. 6), namely,

$$Z_{T_1}=Z_{T_2}+Z_{T_3}, \tag{45}$$

we find that

$$B=\tan\eta.$$

VI. Fourier Transform Solution of the Integral Equation

The Fourier transform solution of (29) will be undertaken as follows: In part (a) of the present section, the equation linking the transforms of the respective functions V, H, and K and the common region of regularity of these transforms will be derived. The equation follows as a direct consequence of the convolution theorem. The regions of analyticity of the transforms are obtained from the asymptotic forms of the functions themselves. Part (b) will concern itself with the decomposition of the transform of the kernel, K, into the quotient of two functions which will convert the equation of the transforms into a single integral function. This integral function will, in part (c), be shown to be constant since it satisfies the conditions of the Liouville theorem. Thus from (70), we will be able to find an expression for the transform of the heretofore unknown function $H(z)$, and thereby, in part (d), we will obtain $\phi(r,z)$ from the inversion integral.

(a) The solution of the extended Wiener-Hopf integral equation (29) by Fourier transform methods can be facilitated by the theorem of convolution which permits us to write the transform of the product of two functions as the product of the transforms. Hence, the transform of (29) becomes

$$\mathcal{V}(\zeta) = \mathcal{K}(\zeta)\mathcal{H}(\zeta), \tag{47}$$

where

$$\mathcal{K}(\zeta) = \int_{-\infty}^{\infty} e^{-i\zeta(z-z')} \left[\frac{\partial}{\partial r}\left(\frac{\partial G}{\partial r'}\right)\right]_{r=r'=a} d(z-z') = \left[\frac{\partial}{\partial r}\left(\frac{\partial}{\partial r'}\mathcal{G}\right)\right]_{r=r'=a} \tag{48}$$

and $\mathcal{K}(\zeta)$ and $\mathcal{V}(\zeta)$ denote the Fourier transforms of the respective functions, $H(z)$ and $V(z)$ in the form $f(\zeta) = \int_{-\infty}^{\infty} f(x)e^{-i\zeta x}dx$. For the transform equation (47) to have significance, there must be a common domain of analyticity of the transforms in the ζ-plane. To verify the existence and location of this domain, we examine each transform with the aid of the growth order of their corresponding functions $V(z)$, $H(z)$ and $K(z)$.

Previously, we showed that $\mathcal{G}(\zeta)$ exists only if k has an imaginary part. However, $\mathcal{K}(\zeta)$ involves differentiation with respect to r and r' which eliminates the propagating term and, consequently its region of regularity is $|\eta| < \kappa_1$.

The quantity which we have called $H(z)$, given explicitly by

$$[\phi(r,z)_{r=a+0} - \phi(r,z)_{r=a-0}]a$$

has the same asymptotic form, for $z \to \infty$, as the velocity potential on the inner and outer surfaces of the smaller guide and, therefore, can be given as $H(z) \sim Ae^{ikz} + Be^{-ikz}$. From this, we infer that $\mathcal{K}(\zeta)$ has only simple poles on the real axis at $\zeta = \pm k$, and is regular in the lower half plane $\eta < 0$, since

$$|\mathcal{K}(\zeta)| \leq \int_0^{\infty} |H(z)|e^{\eta z}dz. \tag{49}$$

is bounded in this region.

If we study the defining equation for $V(z)$, (29), by inserting the explicit expression for the asymptotic behavior of the kernel, namely $K(z-z') \sim e^{-K_1|z-z'|}$, we see that the real part of $V(z) \sim e^{K_1 z}$ as $z \to -\infty$, since $H(z)$ is the entire function (traveling wave) given above.

Thus

$$\mathcal{V}(\zeta) \sim \int_{-\infty}^{0} e^{-i\zeta z + K_1 z}dz = \int_{-\infty}^{0} e^{-i\xi z + (\eta + K_1)z}dz \tag{50}$$

and exists for $\eta > -\kappa_1$.

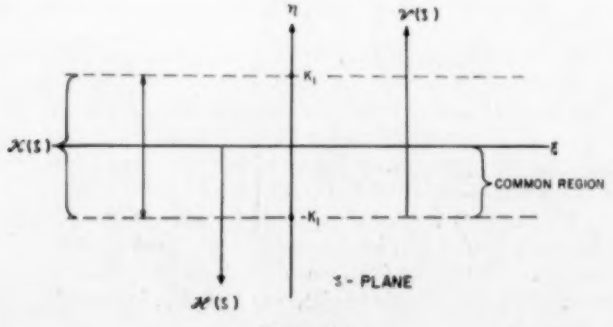

FIGURE 7.

Collecting results, we find (fig. 7) that the strip $-\kappa_1<\eta<0$ is a common region of regularity for the transform equation (47). It will now be convenient to designate the region $\eta>-\kappa_1$ and $\eta<0$ as the upper and lower half planes respectively.

(b) In order to solve the transform equation (47), we now seek to represent $\mathscr{K}(\zeta)$ as a quotient of functions $K_-(\zeta)$ and $K_+(\zeta)$ such that a simple transposition will make each side of the equation regular and not zero in separate half planes with a common strip. By writing (47) as

$$\mathscr{I}(\zeta)K_+=\mathscr{K}(\zeta)K_-=\text{integral function}, \tag{51}$$

we will see that each side of the equation is the analytic continuation of the other and therefore will represent the same function. Together they will then define an analytic function throughout the finite ζ-plane. If, in addition, this analytic integral function turns out to be bounded in the whole plane, then, as a consequence of the Liouville theorem [8], it must be equal to a constant and the transforms $\mathscr{K}(\zeta)$ and $\mathscr{I}(\zeta)$ are simply related to K_+ and K_-.

Although there are general methods for the decomposition of the kernel which are both rigorous and forceful and have been successfully [3, 9] used, in our present discussion however, a simpler and more direct approach will suffice as it has in other problems [10]. Thus we consider

$$\mathscr{K}(\zeta)=\left[\begin{matrix}\partial\\ \partial r\end{matrix}\left\{\begin{matrix}\partial\\ \partial r'\end{matrix}\mathscr{G}(\zeta)\right\}\right]_{r=r'=a}=\frac{\pi}{2}\gamma^2\left[\begin{matrix}J_1(\gamma a)\\ J_1(\gamma b)\end{matrix}\right][J_1(\gamma a)N_1(\gamma b)-J_1(\gamma b)N_1(\gamma a)] \tag{52}$$

and write each factor as an infinite product of the form (a^2-b^2) which we will simply split into terms which have simple zeros in one half plane or the other.

Thus to convert (52) to infinite products, we start by letting

$$f(\gamma)=J_1(\gamma a)N_1(\gamma b)-J_1(\gamma b)N_1(\gamma a). \tag{53}$$

From Whittaker and Watson [11], this may also be written as

$$f(\gamma)=C\prod_{n=1}^{\infty}\left(1-\frac{\gamma^2}{\gamma_n^2}\right), \tag{54}$$

where $\gamma_n=\dfrac{n\pi}{b-a}+O\left(\dfrac{1}{n}\right)$ are roots of $f(\gamma_n)=0$, provided that

(1) $f(\gamma)$ is an even function

(2) $f(0)=C$

(3) $f'(0)=0$.

A careful analysis of these restrictions will show that they are satisfied, if $c=(b^2-a^2)/(\pi a b)$. Thus, we can now write

$$f(\gamma)=\left[\frac{b^2-a^2}{\pi a b}\right]\prod_1^{\infty}\left(1-\frac{k^2}{\gamma_n^2}+\frac{\zeta^2}{\gamma_n^2}\right)$$

$$f(\gamma)=\frac{b^2-a^2}{\pi a b}\prod_1^{\infty}\left(\sqrt{1-\frac{k^2}{\gamma_n^2}}+\frac{i\zeta}{\gamma_n}\right)e^{-\frac{i\zeta(b-a)}{n\pi}}\prod_1^{\infty}\left(\sqrt{1-\frac{k^2}{\gamma_n^2}}-\frac{i\zeta}{\gamma_n}\right)e^{+\frac{i\zeta(b-a)}{n\pi}} \tag{55}$$

where $e^{\pm\frac{i\zeta(b-a)}{n\pi}}$ are inserted as absolute convergence factors, without which the infinite products are only conditionally convergent [12]. Similarly, if we expand

$$J_n(z)=\frac{(z/2)^n}{\Gamma(n+1)}\prod_{n=1}^{\infty}\left\{1-\frac{z^2}{x_n^2}\right\}, \tag{56}$$

where $J_n(x_n)=0$, then from (56)

$$J_1(\gamma a)=\frac{a\gamma}{2}\prod_1^\infty\left(1-\frac{(\gamma a)^2}{x_n^2}\right)$$

$$=\frac{a\sqrt{k^2-\zeta^2}}{2}\prod_1^\infty\left(\sqrt{1-\frac{k^2a^2}{x_n^2}}+\frac{i\zeta a}{x_n}\right)e^{-\left(\frac{i\zeta a}{n\pi}\right)}\prod_1^\infty\left(\sqrt{1-\frac{k^2a^2}{x_n^2}}-\frac{i\zeta a}{x_n}\right)e^{+\left(\frac{i\zeta a}{n\pi}\right)}$$

and

$$J_1(\gamma b)=\frac{b\sqrt{k^2-\zeta^2}}{2}\prod_1^\infty\left(\sqrt{1-\frac{k^2b^2}{x_n^2}}+\frac{i\zeta b}{x_n}\right)e^{-\frac{i\zeta b}{n\pi}}\prod_1^\infty\left(\sqrt{1-\frac{k^2b^2}{x_n^2}}-\frac{i\zeta b}{x_n}\right)e^{+\frac{i\zeta b}{n\pi}} \tag{57}$$

Hence, we may have

$$\mathscr{K}(\zeta)=\frac{\left[\begin{array}{c}\dfrac{(k^2-\zeta^2)}{2}\dfrac{(b^2-a^2)}{b^2}\displaystyle\prod_1^\infty\left\{\sqrt{1-\frac{k^2a^2}{x_n^2}}+\frac{i\zeta a}{x_n}\right\}e^{-\frac{i\zeta a}{n\pi}}\prod_1^\infty\left\{\sqrt{1-\frac{k^2a^2}{x_n^2}}-\frac{i\zeta a}{x_n}\right\}e^{+\frac{i\zeta a}{n\pi}}\\ \cdot\displaystyle\prod_1^\infty\left\{\sqrt{1-\frac{k^2}{\gamma_n^2}}+\frac{i\zeta}{\gamma_n}\right\}e^{-\frac{i\zeta(b-a)}{n\pi}}\prod_1^\infty\left\{\sqrt{1-\frac{k^2b^2}{\gamma_n^2}}-\frac{i\zeta}{\gamma_n}\right\}e^{+\frac{i\zeta(b-a)}{n\pi}}\end{array}\right]}{\left[\displaystyle\prod_1^\infty\left\{\sqrt{1-\frac{k^2b^2}{x_n^2}}+\frac{i\zeta b}{x_n}\right\}e^{-\frac{i\zeta b}{n\pi}}\prod_1^\infty\left\{\sqrt{1-\frac{k^2b^2}{x_n^2}}-\frac{i\zeta b}{x_n}\right\}e^{+\frac{i\zeta b}{n\pi}}\right]} \tag{58}$$

(c) Now, if we define, as shown in (58),

$$\mathscr{K}(\zeta)=\frac{K_-(\zeta)}{K_+(\zeta)}, \tag{59}$$

where $K_-(\zeta)$ is regular and not zero in the lower half place, $\eta<0$, and $K_+(\zeta)$ is regular and not zero in the upper half plane, $\eta>-e_1>-\kappa_1$, our transform equation (47) becomes (51) which satisfies the requirements of the Liouville theorem because $\mathscr{V}(\zeta)K_+(\zeta)$ is regular for $\eta>-e_1$, and $\mathscr{K}(\zeta)K_-(\zeta)$ is regular for $\eta<0$ and the strip $0>\eta>-e_1>\kappa_1$ preserves the continuity.

We must now study the growth order of both members of (51) as $|\zeta|\to\infty$. Thus for $\mathscr{V}(\zeta)$ and $\mathscr{K}(\zeta)$, we examine the transforms

$$\mathscr{V}(\zeta)=\int_{-\infty}^0 e^{-i\zeta z}V(z)\,dz \tag{60}$$

$$\mathscr{K}(\zeta)=\int_0^\infty e^{-i\zeta z}H(z)\,dz. \tag{61}$$

The behavior of $V(z)=\left[\dfrac{\partial\phi}{\partial r}(r,z)\right]_{r=a}$ as $z\to0$, can be obtained by examining ϕ in the region of the sharp edge (zero thickness). In this region, where the values of z are very much smaller than a wave length, ϕ satisfies Laplace's equation which can be solved by static methods. This is done by transforming the potential field about the sharp edge to the uniform region in the upper half plane with the aid of Schwarz-Christoffel [13] transformation, $W^2=2z$. From this transformation, $W\sim z^{1/2}$ and the field which corresponds to $V(z)$ as $z\to0$ at the sharp edge is $|dW/dz|\sim2z^{-1/2}$. Therefore, $V(z)$ which is related to the component of the particle velocity along the cylindrical radius at the inner pipe has an integrable singularity of the form $z^{-1/2}$ and

$$\mathscr{V}(\zeta)\sim\int_{-\infty}^0\frac{e^{-i\zeta z}}{z^{1/2}}\,dz\sim(i\zeta)^{-1/2}\text{ as }|\zeta|\to\infty\text{ for }\eta>-e_1. \tag{62}$$

Also from the above transformation, we see that $H(z)$ which behaves as the velocity potential itself can be given by $H(z)\sim z^{1/2}$ as $z\to 0$ and

$$\mathscr{H}(\zeta)\sim\int_0^\infty e^{-i\zeta z}(z^{1/2})\,dz\sim\frac{1}{(i\zeta)^{3/2}}\text{ as }|\zeta|\to\infty\text{ for }\eta<0. \tag{63}$$

Thus, from a consideration of the physical nature of V and H, we find that $\mathscr{H}$ and $\mathscr{V}$ behave in a purely algebraic manner as $|\zeta|\to\infty$. Therefore, the acceptable results of the decomposition of the kernel must behave in a similar fashion to permit the integral function to be bounded.

To properly decompose the kernel, we choose

$$K_+(\zeta)=\frac{\prod_1^\infty\left[\sqrt{1-\frac{k^2b^2}{x_n^2}}-\frac{i\zeta b}{x_n}\right]e^{+\frac{i\zeta b}{n\pi}}e^{\chi(\zeta)}}{\prod_1^\infty\left[\sqrt{1-\frac{k^2a^2}{x_n^2}}-\frac{i\zeta a}{x_n}\right]e^{+\frac{i\zeta a}{n\pi}}\prod_1^\infty\left[\sqrt{1-\frac{k^2}{\gamma_n^2}}-\frac{i\zeta}{\gamma_n}\right]e^{+\frac{i\zeta(b-a)}{n\pi}}}, \tag{63}$$

where again

$$e^{+\left(\frac{i\zeta a}{n\pi}\right)},\ e^{+\left(\frac{i\zeta b}{n\pi}\right)},\text{ and }e^{+\frac{i\zeta(b-a)}{n\pi}}$$

are inserted in each case as absolute convergence factors and the arbitrary factor $e^{\chi(\zeta)}$ is put in to remove the exponential growth and thereby insuring the algebraic behavior of the K's by the proper choice of $\chi(\zeta)$. This choice will be determined from the asymptotic form of $K_-(\zeta)$ [or $K_+(\zeta)$] as $|\zeta|\to\infty$ for $\eta<0$.

We then find that K_+ has an infinite number of poles on the negative imaginary axis for

$$\eta<-\sqrt{\kappa_1^2-\left(\frac{\pi}{b}\right)^2\left(\frac{5}{8}\right)}\equiv-\epsilon_1>-\kappa_1. \tag{64}$$

and zeros for $\eta\leq-\kappa_1$ and is therefore regular and not zero in the upper half plane $\eta>-\epsilon_1$. By removing (63) from (58), we have left

$$K_-(\zeta)=\frac{\left(\frac{k^2-\zeta^2}{2}\right)\left(\frac{b^2-a^2}{b^2}\right)\prod_1^\infty\left\{\sqrt{1-\frac{k^2a^2}{x_n^2}}+\frac{i\zeta a}{x_n}\right\}e^{-\frac{i\zeta a}{n\pi}}\prod_1^\infty\left\{\sqrt{1-\frac{k^2}{\gamma_n^2}}+\frac{i\zeta}{\gamma_n}\right\}e^{-\frac{i\zeta(b-a)}{n\pi}}e^{\chi(\zeta)}}{\prod_1^\infty\left\{\sqrt{1-\frac{k^2b^2}{x_n^2}}+\frac{i\zeta b}{x_n}\right\}e^{-\frac{i\zeta b}{n\pi}}}, \tag{65}$$

which is regular and not zero in the lower half plane, $\eta<0$, and has only simple poles and zeros in the upper half plane $\eta\geq 0$. We note, however, that K_- and K_+ have a common region which is at least as large as ϵ_1.

For the purpose of evaluating the asymptotic behaviors of K_- and K_+ we may write $\gamma_n\sim n\pi/(b-a)$ and, since Schwinger [1] proved that the infinite products in (65) must be independent of k as $|\zeta|\to\infty$, the square roots behave essentially as unity. Therefore, as $|\zeta|\to\infty$, we may use the Weirstrass [14] definition of the Γ function and the Sterling asymptotic formula [15] for $\Gamma(\zeta)$ to write, as a typical example,

$$\prod_1^\infty\left\{\sqrt{1-\frac{k^2}{\gamma_n^2}}+\frac{i\zeta}{\gamma_n}\right\}e^{-\frac{i\zeta(b-a)}{n\pi}}\sim\frac{1}{e^{(C-1)x}x^{x+1/2}\sqrt{2\pi}},\quad|\zeta|\to\infty,\quad\eta<0, \tag{66}$$

where $x=i\zeta(b-a)/\pi$ and $C=$ Euler's constant. Similarly,

$$\prod_1^\infty\left\{\sqrt{1-\frac{k^2a^2}{x_n^2}}+\frac{i\zeta a}{x_n}\right\}e^{-\frac{i\zeta a}{n\pi}}\sim\frac{\Gamma(5/4)}{e^{Cy}e^{-(y+\frac{1}{4})}(y+\frac{1}{4})^{\frac{1}{4}}\sqrt{2\pi(y+\frac{1}{4})}} \tag{67}$$

where $y=\frac{i\zeta a}{n\pi}$.

Thus as $|\zeta|\to 0$, we have

$$K_-(\zeta)=\left(\frac{k^2-\zeta^2}{2}\right)\left(\frac{b^2-a^2}{b^2}\right)\frac{b^{\left(\frac{i\zeta b}{\pi}\right)}\sqrt{2i\zeta b}\,e^{\chi(\zeta)}}{a^{\left(\frac{i\zeta a}{\pi}\right)}\sqrt{2i\zeta a}(b-a)^{\left(\frac{i\zeta(b-a)}{\pi}\right)}\sqrt{2i\zeta(b-a)}} \tag{68}$$

which approaches $(i\zeta)^{3/2}$, provides that

$$\chi(\zeta)=\frac{-i\zeta}{\pi}\left[b\ln b-a\ln a-(b-a)\ln(b-a)\right] \tag{69}$$

to insure the algebraic behavior of both K_- and K_+. Likewise, we may show that

$$K_+(\zeta)\to(-i\zeta)^{\frac{1}{2}} \text{ or that } \mathscr{K}(\zeta)\to\zeta.$$

Collecting results we see that $\mathscr{S}(\zeta)\,K_+(\zeta)$ is bounded as $|\zeta|\to\infty$ for $\eta>-\epsilon_1$ and $\mathscr{K}(\zeta)\,K_-(\zeta)$ is bounded as $|\zeta|\to\infty$ for $\eta<0$. Thus, we have shown that both sides of (51) define an analytic function which is regular everywhere including a common strip of width ϵ_1 and is bounded at infinity. Therefore, by the statement of the Liouville theorem, (51) becomes

$$\mathscr{S}(\zeta)K_+(\zeta)=\mathscr{K}(\zeta)K_-(\zeta)=C. \tag{70}$$

If we were interested in the difference of the velocity potential on either side of the inner pipe, we could now obtain it by evaluating

$$\frac{1}{2\pi i}\int_{Br}\frac{Ce^{i\zeta z}dz}{K_-(\zeta)},$$

where Br is an infinite contour within the strip of regularity $|\eta|<\kappa_1$. (d) We are now in a position to evaluate the Fourier integral form of (27), which we may write as

$$\phi(r,z)=\frac{1}{2\pi}\int_{i\sigma+\infty}^{i\sigma+\infty}d\epsilon^{i\zeta z}H(\zeta)\left[\frac{\partial\mathscr{G}}{\partial r'}(r,r',\zeta)\right]_{r'=a}, \tag{71}$$

and where we recall $\mathscr{G}$ exists in the strip $-K_1<\eta<K_1$ and $\mathscr{K}(\zeta)$ exists for $\eta<0$. Therefore the path of integration must be taken in the region $0>\eta>-K_1$.

If we concentrate for the moment on $r<r'$, we have from (14)

$$\left(\frac{\partial\mathscr{G}}{\partial r'}\right)_{r'=a}=\frac{\pi}{2}\gamma\frac{J_0(\gamma r)}{J_1(\gamma b)}\left[-J_1(\gamma a)N_1(\gamma b)+N_1(\gamma a)J_1(\gamma b)\right] \tag{72}$$

and

$$\left.\begin{aligned}\mathscr{K}(\zeta)&=\frac{\pi}{2}\gamma^2\frac{J_1(\gamma a)}{J_1(\gamma b)}\left[J_1(\gamma a)N_1(\gamma b)-N_1(\gamma a)J_1(\gamma b)\right]\\&=\frac{K_-(\zeta)}{K_+(\zeta)}.\end{aligned}\right\} \tag{73}$$

Therefore, if we form the ratio

$$\frac{\left(\frac{\partial\mathscr{G}}{\partial r'}\right)_{r'=a}}{\mathscr{K}(\zeta)}=-\frac{J_0(\gamma r)}{\gamma J_1(\gamma a)}, \tag{74}$$

then

$$\frac{\partial G}{\partial r'}=-\frac{J_0(\gamma r)}{\gamma J_1(\gamma a)}\frac{K_-(\zeta)}{K_+(\zeta)}. \tag{75}$$

Now the integral in (71) becomes

$$\frac{1}{2\pi}\int_{i\sigma-\infty}^{i\sigma+\infty} d\zeta e^{i\zeta z}\frac{\mathscr{H}(\zeta)K_-(\zeta)}{K_+(\zeta)}\frac{[-J_0'(\gamma r')]}{[J_1(\gamma a)]} \tag{76}$$

which has simple poles at $\zeta=\pm k(\gamma=0)$ and $\zeta=\pm i\kappa_n$.
The contributions at the poles on the imaginary axis vanish as $|z|\to\infty$ since they contain $e^{-\kappa_n|z|}$. For $z<0$, we closed the path of integration by an infinite contour in the lower half plane. Since the poles enclosed are all on the imaginary axis, the contribution to the integral vanishes as $z\to-\infty$ and the result claimed in section V is established. For $z>0$ and large, we use a contour in the upper half plane which encloses $\zeta=\pm k$ and (71) becomes

$$\phi(r,z)=iD\left(\frac{e^{-ikz}}{2kK_+(-k)}-\frac{e^{ikz}}{2kK_+(k)}\right)+\frac{1}{2}\left[I_1(z)+\frac{Z_2}{Z_1}I_2(z)+\frac{Z_3}{Z_1}I_3(z)\right], \tag{77}$$

since only the residues at the poles on the real axis contribute as $z\to\infty$. Likewise, if we consider $r>r'$, it can easily be verified that the result is the same as (77) with a different constant D.

VII. Expression "d" in Terms of Infinite Series

In (77), we have evaluated the integral representation (27) from its Fourier Integral form (71) and we can now obtain the far fields to the right. For now, as $z\to\infty$, $\phi(r,z)\to I_3(z)$ in region 3 and $I_2(z)$ in region 2. In terms of the parameters at $z=0$, we have similar results in regions 2 or 3 with different constants A namely

$$I_{2,3}\cos kz-iY_{2,3}V_{2,3}\sin kz=A_{2,3}\left[\frac{e^{ikz}}{K_+(-k)}-\frac{e^{ikz}}{K_+(k)}\right]+\frac{\cos kz}{2}\left[I_1+\frac{Z_2}{Z_1}I_2+\frac{Z_3}{Z_1}I_3\right]$$
$$-i\frac{\sin kz}{2}[V_3Y_3+V_2Y_2-V_1Y_1]. \tag{78}$$

If we, again, equate coefficients of sin and cos, we have the far fields results extrapolated from the right as

$$\left[I_{2,3}-\frac{1}{2}\left(I_1+\frac{Z_2}{Z_1}I_2+\frac{Z_3}{Z_1}I_3\right)\right]=A_{2,3}\left[\frac{1}{K_+(-k)}-\frac{1}{K_+(k)}\right] \tag{79}$$

and

$$\left[-iV_{2,3}Y_{2,3}+\frac{1}{2}(V_3Y_1+V_2Y_1-V_1Y_1)\right]=A_{2,3}\left[\frac{-i}{K_-(-k)}-\frac{i}{K_+(k)}\right]. \tag{80}$$

Recalling that the results from the left gave the circuit equations (32) and (33), we apply them to the above and find that

$$[I_{2,3}-I_1]=A_{2,3}\left[\frac{1}{K_+(-k)}-\frac{1}{K_+(k)}\right] \tag{81}$$

and

$$-i(V_{2,3}Y_{2,3}+V_1Y_1)=-iA_{2,3}\left[\frac{1}{K_+(-k)}+\frac{1}{K_+(k)}\right]. \tag{82}$$

By simply dividing these two equations, we see from (40), that the left side is merely the one essential circuit parameter b discussed in section V and hence with (46), we have

$$B=i\left[\frac{K_+(k)-K_+(-k)}{K_+(k)+K_+(-k)}\right]=\tan(kd), \tag{83}$$

where the reciprocal of $K_+(k)$ is

$$\frac{1}{K_+(k)}=\frac{\prod_1^\infty\left\{\sqrt{1-\frac{k^2a^2}{x_n^2}}-\frac{ika}{x_n}\right\}e^{\frac{ika}{n\pi}}\prod_1^\infty\left\{\sqrt{1-\frac{k^2}{\gamma_n^2}}-\frac{ik}{\gamma_n}\right\}e^{\frac{ik(b-a)}{n\pi}}}{\prod_1^\infty\left\{\sqrt{1-\frac{k^2b^2}{x_n^2}}-\frac{ikb}{x_n}\right\}e^{\frac{ikb}{n\pi}}e^{ik\,(a)}} \tag{84}$$

By writing the bracketed terms in (84) as exponentials, for these are of the form $\cos\theta - i\sin\theta$, we see that (83) becomes

$$\frac{\pi d}{b}=\left[\ln\alpha+\left(\frac{1}{\alpha}-1\right)\ln(\alpha-1)\right]-\frac{1}{\eta}\sum_{n=1}^{\infty}\left[\sin^{-1}\left(\frac{\eta\pi}{\alpha x_n}\right)-\left(\frac{\eta}{\alpha n}\right)-\frac{1}{\eta}\sum_{n=1}^{\infty}\left[\sin^{-1}\left(\frac{\eta\pi}{\alpha y_n}\right)-\left(\frac{\eta(\alpha-1)}{\alpha n}\right)\right]+\frac{1}{\eta}\sum_{n=1}^{\infty}\left[\sin^{-1}\left(\frac{\eta\pi}{x_n}\right)-\left(\frac{\eta}{n}\right)\right], \tag{85}$$

where y_n are the roots of

$$J_1(y_n)\,N_1(\alpha y_n)-J_1(\alpha y_n)\,N_1(y_n)=0 \tag{86}$$

and x_n are roots of $J_1(x_n)=0$. For ease in computation, we have made the following parameter changes:

1. Let $\alpha=b/a$.
2. From our initial restriction on the driving wavelength, let $k=\eta\pi/b$, where $0\leq\eta\leq 1$.
3. Let $\frac{x_n}{a}(\gamma_n a)=y_n$.

Since we now have an analytic expression for d, it is of considerable interest to determine d as a function of frequency and the radii of the tubes. To evaluate d numerically, mustwe find some way to get an accurate result for the above infinite series which is of the form

$$\sum_{n=1}^{\infty}\{[\sin^{-1}(X_n)-Y_n]\}=\sum_{n=1}^{\infty}\{[\sin^{-1}(X_n)-(X_n)+(X_n-Y_n)\}. \tag{87}$$

The first two terms can be written as

$$\sum_{n=1}^{N}[\sin^{-1}(X_n)-X_n]+R_n, \tag{88}$$

where N is some arbitrary finite number. Thus by calculating N simple values and bounding the remainder, we will be able to evaluate these sums Writing $\sin^{-1}$ as an infinite series,

$$R_n=\sum_{N+1}^{\infty}[\sin^{-1}(X_n)-X_n]=\sum_{N+1}^{\infty}\left[+\frac{1}{6}(X_n)^3+\frac{3}{40}(X_n)^5+\frac{5}{112}(X_n)^7+\ \ldots\right] \tag{89}$$

we have a series which converges rapidly for $X_n<1$.
If we now define U_{N+1} as

$$U_{n+1}=\frac{\sin^{-1}(X_{n+1})-X_{n+1}}{(X_{n+1})^3}\sim\frac{1}{6}, \tag{90}$$

we see that the numerator is the largest term in the remainder and that U_{N+1} approaches 1/6 as N grows large. Now from the series expansion, (89), it can be easily verified that

$$\frac{\sin^{-1}(X_{N+1})-X_{N+1}}{(X_{N+1})^3}\geq\frac{\sin^{-1}(X_{N+1})-X_{N+1}}{(X_{N+1})^3}, \tag{91}$$

for $i=1, 2, 3$, since $X_{N+1}\geq X_{N+i}$.

Thus from (90) and (91)

$$U_{N+1}(X_{N+1})^3 > \sin^{-1}(X_{N+1}) - X_{N+1} \tag{92}$$

which means that

$$R_n < U_{N+1} \sum_{N+1}^{\infty} (X_n)^3. \tag{93}$$

Also from the series, we have, by dropping higher order terms,

$$R_n > \sum_{N+1}^{\infty} \frac{1}{6} (X_n)^3, \tag{94}$$

which together with (93) bounds R_n as

$$\frac{1}{6} \sum_{N+1}^{\infty} (X_n)^3 < R_n < U_{N+1} \sum_{N+1}^{\infty} (X_n)^3. \tag{95}$$

Thus, we can easily determine a numerical value for R_n. The remaining sums of (87) may be easily obtained since $\lim_{n \to \infty} (X_n) = Y_n$.

The infinite sums in (85) were evaluated by the computation laboratory of the Institute for Numerical Analysis, National Bureau of Standards, for η, the frequency parameter, assuming the values of 1, .8, .6, .4, .2 and 0. Although $\eta = 0$ has no physical meaning in the present acoustic problem, for completeness the mathematical $\lim_{\eta \to 0} \pi d/b$ was evaluated to show that d is a smooth and continuous function of η for $\eta = 0$. Thus since

$$\lim_{\eta \to 0} \sin^{-1} \frac{\eta}{C} = \frac{1}{C},$$

equation (85) becomes

$$\frac{\pi d}{b} = \left[\ln \alpha + \left(\frac{1}{\alpha} - 1 \right) \ln (\alpha - 1) \right] - \sum_{n=1}^{\infty} \left[\frac{\pi}{\alpha x_n} - \frac{\pi}{x_n} + \frac{\pi}{\alpha y_n} \right] \tag{97}$$

as $\eta \to 0$. The values of α used were 1.05, 1.2, 1.5, 2, 3, 5, and 10, while $\alpha = 1.0$ and ∞ would mean that there is no inner guide; consequently $d = 0$. The computations were intended to be accurate to four decimal places, but with the methods outlined greater accuracy could have been obtained. The eigenvalues y_n (table 1) for small n were obtained from Muskat et al [16] with corrections given by Miller [17] and for large n were computed with the aid of a formula give by McMahon [18]. The results of (85) are exhibited in tables 1 and 2 and in figures 7 and 8.

TABLE 1

	F_n							y_n
n \ α	1.05	1.2	1.5	2.0	3.0	5.0	10.0	
1	62.837	15.728	6.3218	3.1966	1.6356	0.84715	0.39409	3.8317
2	125.666	31.426	12.586	6.3124	3.1789	1.6111	.73306	7.0156
3	188.497	47.131	18.863	9.4446	4.7381	2.3853	1.9748	10.1735
4	251.329	62.837	25.143	12.581	6.3028	3.1642	1.4189	13.324
5	314.160	78.544	31.424	15.720	7.8696	3.9454	1.7643	16.471
6	376.922	94.251	37.706	18.860	9.4375	4.7279	2.1107	19.616
7	439.824	109.958	43.988	21.999	11.007	5.5112	2.4578	22.760
8		125.666	50.270	25.141	12.576	6.2950	2.8052	25.904
9			56.553	28.281	14.146	7.0791	3.1529	29.047
10			62.836	31.422	15.716	7.8635	3.5010	32.190
11				34.563	17.286	8.6480	3.8492	35.332
12						9.4327	4.1975	38.475
13						10.217	4.5459	41.617
14							4.8944	44.759
15							5.2430	47.902

TABLE 2

$\frac{1}{\alpha}$ \ η	1.0	.8	.6	.4	.2	0	α
			$\left[\frac{\pi d}{b}\right]$				
0.9524	0.2061	0.1902	0.1828	0.1787	0.1767	0.1760	1.05
.8333	.4802	.4384	.4171	.4051	.3988	.3967	1.2
.6667	.6527	.5936	.5620	.5436	.5339	.5310	1.5
.5000	.6682	.6069	.5740	.5549	.5446	.5415	2.0
.3333	.5530	.5036	.4780	.4633	.4555	.4532	3.0
.2000	.3731	.3428	.3297	.3216	.3173	.3163	5.0
.1000	.1948	.1844	.1795	.1767	.1752	.1751	10.0

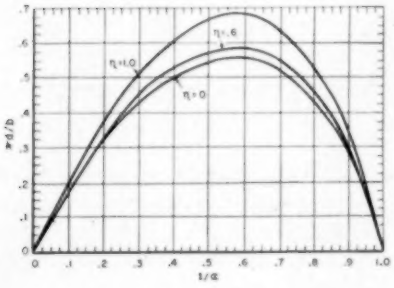

FIGURE 8.

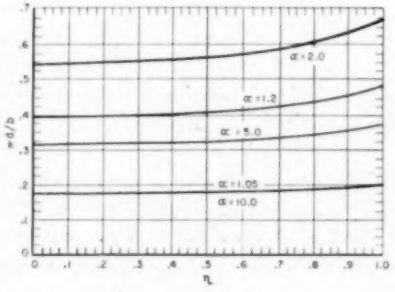

FIGURE 9.

VIII. Conclusion

In (85), we have obtained a rigorous and explicit solution for the parameter d. An approximate solution of the above problem was first reported by J. W. Miles [7], who showed by using impedance concepts developed in earlier papers and the variational principle of Schwinger's that the equivalent circuit elements can be related to the analogous change of cross section. Thus by considering the bifurcation as a mere change of cross section, he obtained his equation (53) which contained only the leading term of an infinite series. A comparison of the results given in table 2 and the values given by Miles indicates, that for this problem, this type of approximation is very poor. Attempts have been made to improve this method of approximation by considering two terms of the infinite series and only slightly better results were obtained. An explanation of these discrepancies between the exact results given here and the approximations is to be given by Miles [19].

The author is deeply indebted to Professor Alfredo Baños, Jr., for the guidance that he has so graciously given throughout all phases of this research and to Professors Baños and David S. Saxon for the suggestion of this problem, as well as the benefit of their experience in the Radiation Laboratory of Massachusetts Institute of Technology.

IX. References

[1] J. Schwinger, The theory of guided waves, Radiation Laboratory lectures. Unpublished. Communicated to the author by Professors Alfred Baños, Jr., and David S. Saxon of UCLA.

[2] R. E. A. C. Paley and N. Wiener, The Fourier transform in the complex domain, Am. Math. Soc. Colloquium Publication (1934) Vol. XIX. E. Reissner, J. Math. Phys. MIT (20) **5**, 219 (1941).

[3] Levine and Schwinger, Phys. Rev. **73,** No. 4, 383 to 406 (Feb. 1948).
[4] Courant and Hilbert, Methoden der Mathematischen Physik, **I,** Sec. Ed., p. 303 to 304 (Julius Springer, 1931).
[5] J. W. Miles, J. Acous. Soc. Am. **17,** Part I, 259 to 272 (1946).
[6] Everett, Communication Engineering, p. 52 (McGraw-Hill Book Co., Inc., New York, N. Y., 1937).
[7] J. W. Miles, J. Acous. Soc. Am **19,** No. 4, 579 to 584 (July 1947).
[8] Whittaker and Watson, A course of modern analysis, p. 105 (Am. Ed., Macmillan Co., New York, N. Y., 1945).
[9] Placzek and Seidel, Phys. Rev. **72,** No. 7, p. 550 to 555 (Oct. 1947).
[10] J. F. Carlson and A. E. Heins, Quart. Applied Math., Part I, **4,** No. 7, 313 to 329; Part II, **5,** No. 1, 82 to 88 (1947).
[11] Whittaker and Watson, Modern analysis, p. 137 (Macmillan Co., New York, N. Y., 1947).
[12] Watson.
[13] Smythe, Static and dynamic electricity, p. 82, first ed. (McGraw-Hill Book Co., Inc., New York, N. Y., 1939).
[14] Whittaker and Watson, Modern analysis, p. 236 (Macmillan Co., New York, N. Y., 1947).
[15] Whittaker and Watson, Modern analysis, p. 253 (Macmillan Co., New York, N. Y., 1947).
[16] M. Muskat, F. Morgan, and M. W. Meres, J. App. Phys. **11,** 212 (1940).
[17] Bateman and Archibald, MTAC v. 1., 7, 325 (1944). See comments by J. C. P. Miller.
[18] J. McMahon, Annals Math. **9,** 23 to 30 (1895).
[19] J. W. Miles, J. Acous. Soc. Am. **22,** No. 1, 59 to 60 (1950).

Los Angeles, November 2, 1949.